VOL. 38, 2005, Nro 3

JOURNAL OF STRUCTURAL MECHANICS

RAKENTEIDEN MEKANIIKKA

SPECIAL ISSUE FOR THE 18TH NORDIC SEMINAR ON COMPUTATIONAL MECHANICS OCTOBER, 27TH – 30TH 2005

RAKENTEIDEN MEKANIIKAN SEURA RY
FINNISH ASSOCITATION FOR STRUCTURAL MECHANICS

R A K E N T E I D E N M E K A N I I K A N S E U R A R.Y.
FINNISH ASSOCIATION FOR STRUCTURAL MECHANICS

JOHTOKUNTA **ADMINISTRATIVE BOARD**

JUHA PAAVOLA, prof. (puheenjohtaja), TKK/Rakenteiden mekaniikka
TAPIO AHO, dipl. ins., Ins.tsto Magnus Malmberg Oy
JOUNI FREUND, tekn.tri, TKK/Lujuusoppi
JUHANI KOSKI, prof., TTY/Tekn. mek. ja optimointi
KARI KOLARI, dipl. ins., TKK/Lujuusoppi
REIJO LINDGREN, dipl. ins., CSC-Tieteellinen laskenta
SEPPO ORIVUORI, tekn.lis, Enprima Oy
ILMO SIPILÄ, dipl. ins., Ins.tsto Ilmo Sipilä
JUKKA TUHKURI, prof., TKK/Lujuusoppi
MATTI RANTA, prof., kunniapuheenjohtaja

TOIMISTO OFFICE

SAMI PAJUNEN, asiamies, puh. 040 900 4501
ELSA NISSINEN-NARBRO, kanslisti/jäsenasiat, puh. (09) 451 3701

JÄSENET MEMBERS

HENKILÖJÄSENET 176
OPISKELIJAJÄSENET 3
YHTEISÖJÄSENET:

Aaro Kohonen Oy
Finnmap Consulting Oy
Ins.tsto JP-Kakko Oy
Ins.tsto Magnus Malmberg Oy
Ins. tsto Pontek Oy
Ins.tsto Pöysälä & Sandberg Oy
TKK/Laivalaboratorio
KCI Konecranes International Plc
Konecranes VLC Oy
KPM-Engineering Oy
Nokian Renkaat Oyj
Optiplan Oy
Suomalainen Insinööritoimisto SITO Oy
Pohjois-Karjalan AMK

OSOITE: Teknillinen korkeakoulu, Rakennus- ja ympäristötekniikan osasto, Rakentajanaukio 4 A, PL 2100, 02015 TKK, puh. (09) 451 3701, telefax (09) 451 3826

ADDRESS: Helsinki University of Technology, Department of Civil and Environmental Engineering, Rakentajanaukio 4 A, P.O.Box 2100, FIN-02015 HUT, Finland. tel. (358-9) 451 3701, telefax (358-9) 451 3826
http://rmseura.tkk.fi/

www.ruukki.com

If you see the name Ruukki instead of Rautaruukki, Rannila, Fundia Reinforcing, Gasell or Asva, you are actually seeing more.

ruukki
more with metals

KONECRANES

RESHAPING
the crane industry

KCI Konecranes is a world leading engineering group specialising in advanced overhead lifting solutions and maintenance services. KCI Konecranes employs 4850 people and has a presence through its own personnel, agents and other representatives in more than 35 countries and more than 300 service locations worldwide. KCI Konecranes product range covers all overhead lifting solutions and components for industries and harbours all over the world. KCI Konecranes is a forerunner in innovative lifting and maintenance technologies.

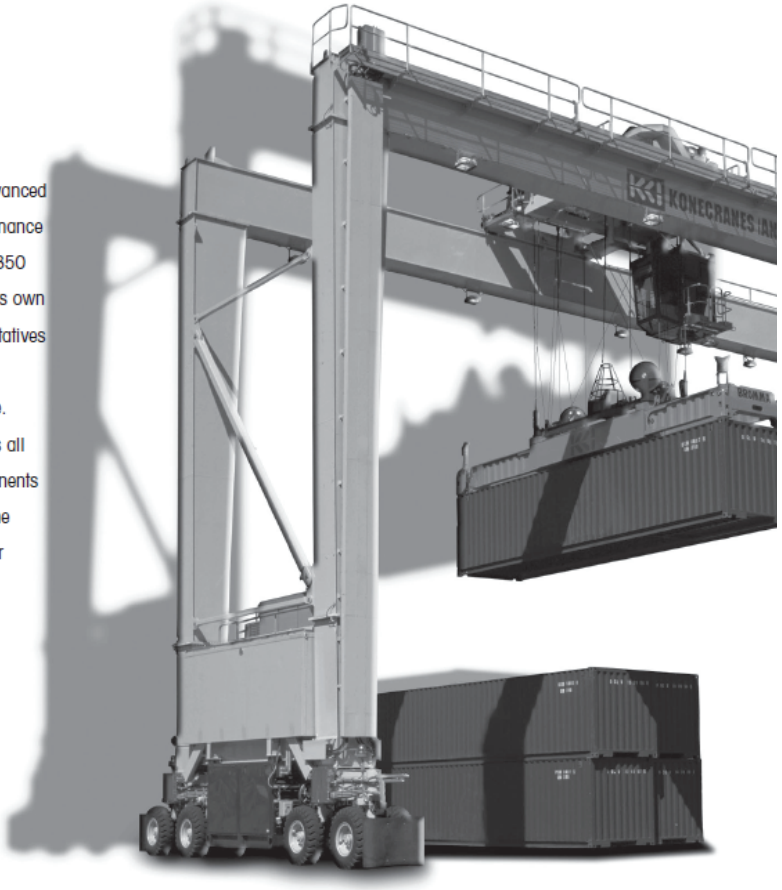

WORLD LEADING CRANE TECHNOLOGY

KCI Konecranes Plc P.O.Box 661 (Koneenkatu 8), 05801 Hyvinkää, Finland. Tel. +358-20 427 11, Fax +358-20 427 2099 **www.konecranes.com**

Call for papers

Accidents and safety in construction sector

Construction SAFETY 2006

May 10-12, 2006
Helsinki, Finland

Finnish Association of Civil Engineers

YMPÄRISTÖMINISTERIÖ
MILJÖMINISTERIET
MINISTRY OF THE ENVIRONMENT

The construction industry is one of the most hazardous workplaces in the world. Mistakes during construction often lead to very negative and unwanted results later - to loss of property or even human lives. Such situations may be caused either by natural disasters and environmental changes or human errors, whether deliberate or involuntary.

The Finnish construction industry, specialist organizations and authorities have discussed ways to improve the situation and found exchange of information, circulation of best practices, learning from cases and brainstorming with colleagues and stakeholders to be one good way to proceed. The Finnish Association of Civil Engineers RIL, as an impartial network of experts, has decided to open a time window and platform for an open discussion and exchange of views between European, Finnish and global industry members by organizing a conference where these issues can be presented and discussed .

This is an open call for experts, practioners, researchers and other professionals dealing with structural and occupational safety to step ahead, exchange their knowledge and information about these important issues and to learn, how to make construction industry a safe industry and built environment a safe place to live!

More information:
www.ril.fi/safety2006
or kaisa.venalainen@ril.fi

Proceedings of the 18th NORDIC SEMINAR ON COMPUTATIONAL MECHANICS Espoo, 27-30 October, 2005

J. Paavola, J. Freund (*editors*)

Preface

These proceedings contain the papers presented at the 18th Nordic Seminar on Computational Mechanics, held at Silja Serenade ferry travelling between Helsinki and Stockholm, the Capitals of Finland and Sweden, and hosted by Helsinki University of Technology, Espoo, Finland, on 27-30 October 2005.

The seminars are organized annually by the Nordic Association of Computational Mechanics (NoACM). The NoACM was founded in 1988 with the objective to stimulate and promote research and practice in computational mechanics, to foster the interchange of ideas among the various fields contributing to computational mechanics, and provide forums and meetings for dissemination of knowledge in computational mechanics. Younger researchers, including doctorate students etc. are especially encouraged to participate at these seminars. The member countries of NoACM are the Nordic countries (Denmark, Finland, Iceland, Norway and Sweden) and the Baltic countries (Estonia, Latvia and Lithuania). NoACM is a subchapter of the International Organization for Computational Mechanics (IAC) and the European Community on Computational Methods in Applied Sciences (ECCOMAS).

The responsibility for organizing this year's seminar was assigned by NoACM to Laboratories of Structural Mechanics and Mechanics of Materials, Helsinki University of Technology. Traditionally, the seminars have been organized in academic university circumstances. To reserve for participants more time to have with each other and to provide the common time with more comforts, this time the seminar will be arranged in the ferry. The seminar contains five invited lectures and 38 contributed presentations divided into 10 separate sessions of which some are parallel ones. In this volume, the invited keynote lectures are placed first and after that comes the contributed papers in the order of the seminar program.

On behalf of the organizers, we'd like express our gratitude to all contributors of the seminar, the invited and contributed speakers for their effort in preparing talks, presentations and papers, and to those all who have helped in practical arrangements.

Finally, we thank all the sponsors, Ruukki, KCI Konecranes PLC, VTT-Technical Research Centre of Finland, and Finnish Association of Civil Engineers, who have helped us to make this seminar true. Particularly, the Finnish Association of Structural Mechanics, deserves to be mentioned for serving a great forum to publish the seminar abstracts in the special issue devoted for the seminar.

Espoo, 21 October 2005

The editors

Program Committee

Kjell Magne Mathisen, Norway
Trond Kvamsdal, Norway
Anders Eriksson, Sweden
Göran Sandberg, Sweden
Roland Rikards, Latvia (Baltic countries)
Juha Paavola, Finland
Jouni Freund, Finland
Niels Olhoff, Denmark
Jens Sørensen, Denmark

Local Organizing Committee

Juha Paavola
Jouni Freund
Ennio Zuccaro

NSCM18 secretariat

Ennio Zuccaro
Laboratory of Structural Mechanics
Helsinki University of Technology
PO Box 2100
02015 TKK
FINLAND
Phone: +358 9 451 3711
Fax: +358 9 451 3826

Table of contents

Discrete Element Simulations in Ice Engineering

Jukka Tuhkuri
Laboratory for Mechanics of Materials
Helsinki University of Technology, Espoo, Finland
e–mail: jukka.tuhkuri@tkk.fi

Summary The ice load on an engineering structure depends on the deformation and failure process of sea ice. As several ice features and ice failure processes are discontinuous in nature, it is tempting to study the ice load problem by using a discontinuous approach. Discrete element method (DEM) is one of the techniques that model the dynamics of a system of discrete particles. This paper gives a review of a group of ice problems and their analysis with DEM.

Introduction

Determination of ice loads on ships and offshore structures is an important technical challenge. Ice forces acting on a structure are due to relative movement between the structure and ice and the sequential failure process of the ice feature. Typical sea ice features are sheets of level ice, ridges and rubble fields. Both ridges and rubble fields are piles of ice blocks, but ridges have an elongated form. Ridges and rubble fields form when two ice sheets, driven by winds and currents, collide. In the Baltic, ridges more than 10 meters deep are common.

A central hypothesis in traditional solid mechanics states that a body under consideration is continuous and remains continuous under the action of external forces. However, ice mechanics is one of the engineering fields where this continuum description may not be the most appropriate, and a discontinuum approach should be used instead. Figure 1 shows two important ice engineering problems. The key features of the ice load cases shown are the discontinuous nature of both the pile of ice blocks and the failure process of ice. When an ice sheet loads a structure as in Figure 1(a), the originally intact ice sheet breaks into discrete ice blocks which accumulate in the ice-structure interface and thus affect the failure process. On the other hand, when a structure indents a ridge or an ice rubble pile as in Figure 1(b), the load on the structure is due to rearrangement of the discrete ice blocks, in addition to possible failure of the ice blocks.

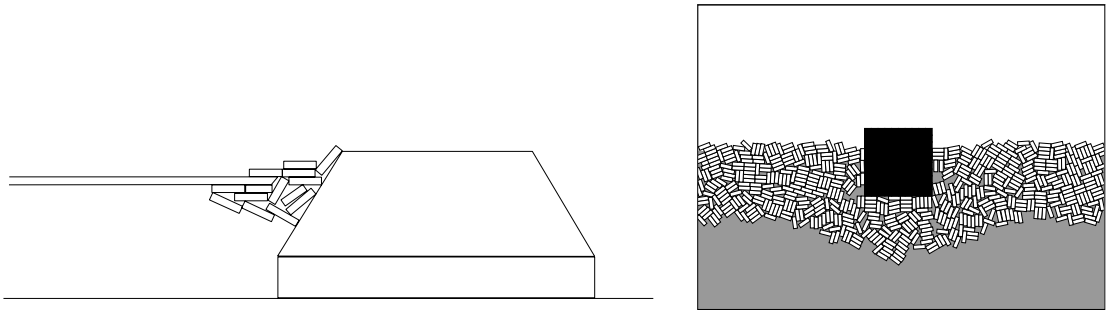

(a) (b)

Figure 1: (a) Sketch of en ice sheet failure against an inclined marine structure. (b) Snapshot of a DEM simulation of an indentor moving down into a floating layer of ice blocks [1].

The discrete element method (DEM) is a numerical tool used to simulate a system of particles. DEM is based on the concept that individual material elements are considered to be separate and,

if connected, are connected along their boundaries by appropriate interaction laws. An important aspect of the discrete element method is that the particles may fracture and fragment, thus increasing the total number of bodies during a simulation. In a discrete element simulation, the interaction and behavior of individual particles will result into emergent physical properties of the particle assembly. A DE approach can be useful in cases where the constitutive behavior of a particle assembly is not known. In addition to ice mechanics, DEM has been applied to deformation of granular materials, rock mechanics, fragmentation of solids, as well as structural failure and collapse [2][3][4]. This paper first will introduce the discrete element method and then describe some engineering problems analysed with DEM. The goal is not to give an extensive literature review, but to highlight a few important applications.

The discrete element method

In essence, a discrete element simulation is a computer program that models the nonlinear dynamics of a system of particles. The forces on each particle are calculated at each time step and the particles are moved to new locations with new velocities that depend on the forces. Newtonian mechanics is assumed to describe the particle motions. A DEM program has the following tasks:

1. Store the position, orientation, velocity, and shape of each particle.
2. Find the neighboring particles.
3. Find the contact geometry (overlapping areas) between the neighboring particles.
4. Determine the contact forces between particles, i.e. add the physical properties of the particles into the simulation.
5. Determine whether any particle will fracture into new particles.
6. Solve the equations of motion of the particles and move each to a new position with a new velocity and orientation.
7. Analyse the variables of interest and construct a visual record of the systems motion.

The second and third tasks, dealing both with contact detection, are time consuming. For radially symmetric particles (disks and spheres) it is a trivial task, but for polygonal or polyhedral particles the task is a complex exercise in computational geometry. Presumably for this reason, the majority of DE simulations have been performed by using disks or spheres. However, in many physical problems the particles are not symmetric and the particle shape is an important feature of a granular assembly [5][6][1].

The fourth task is to determine the contact forces between particles. The traditional method in DEM has been to treat each particle as a rigid body, calculate the overlap of the bodies and to relate the overlap depth δ with contact force by using simple spring and dashpot models. For example, the normal contact force F_n in compression is then

$$F_n = k_n\delta + c_n\dot{\delta} \tag{1}$$

where k_n is the contact stiffness and c_n is the contact damping. This widely used model is somewhat controversial, because it is not clear what k_n and c_n are. For elastic spheres, k_n can be

defined by using the Hertz contact model, but for other particle shapes, no general k_n exist. Thus, a more recent approach is to use a combined finite-discrete element method where each particle is modelled by using FEM [4][7].

The contact force in Equation 1 is for compression only. In problems dealing with an assembly of discrete particles, the normal force in tension vanishes. However, also tensile contact forces can be easily taken into account in DEM.

Research of ice engineering problems with DEM

Problems dealing with ice fields comprising of discrete ice floes

The early applications of DEM in ice problems concentrated in modelling the convergent behavior of systems of circular ice floes in two dimensions (2D) [6] [8]. In these studies, the goal was to examine the constitutive equations of ice cover in large scale. Engineering applications of this problem include simulations of river ice transport phenomena [9], forces exerted on a boom when it is pulled through a broken ice sheet [10] and the behavior of a ship moored in broken ice (Figure 2) [11]. Later, three dimensional (3D) simulations have shown that the floes start to overlap each other when the floes are packed on the water surface at an average concentration of about 80 % by area [12]. In other words, when the concentration reaches 80 %, the problem becomes 3D and cannot be modelled with 2D models.

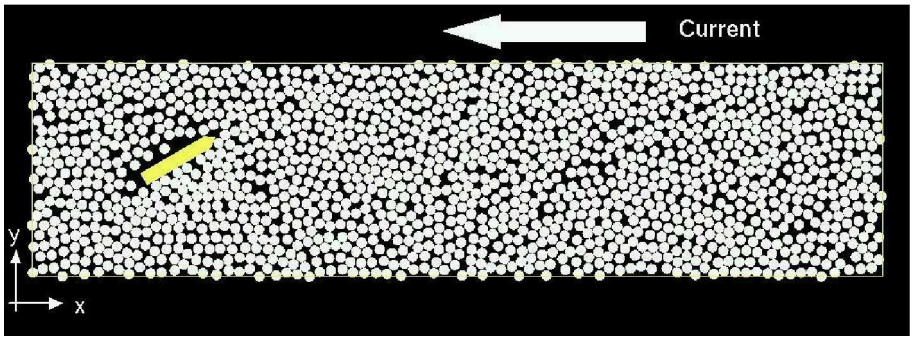

Figure 2: Snapshot of a 2D DEM simulation of a ship (left) moored in broken ice moved by a current [11].

Figure 3 shows a snapshot from 3D ice floe field simulations in which a floating layer of circular floes, confined in a rectangular channel, was compressed by a pusher moving at a constant speed [12]. The accuracy of the simulations was assessed by comparison with a series of similar physical experiments performed in a refrigerated basin. Figure 4(a) shows the forces on the pusher obtained in the experiments and simulations with two ice thicknesses. Three distinct regions are evident in the force-displacement, $F^*(X^*)$, graphs. During the first period ($X^* < 6$), the forces increase as the floes are herded toward the far end of the channel. The pusher force at $X^* = 6$ represents the strength of the 2D consolidated surface layer of horizontal floes. During the second period $6 < X^* < 35$, the $F^*(X^*)$-record is characterised by the resistance of the floes to rotation and rafting, but also to frictional contact with the channel sides. The third period, $X^* > 35$ begins when the entire initial surface layer of floes has failed. Following this comparison, the computer model was used to explore the effect of variations in channel length and width, the ratio of floe diameter to thickness, floe on floe friction coefficients, and the distribution of floe diameters on the force required to compress the floes. As an example, the frictional force at the channel sides,

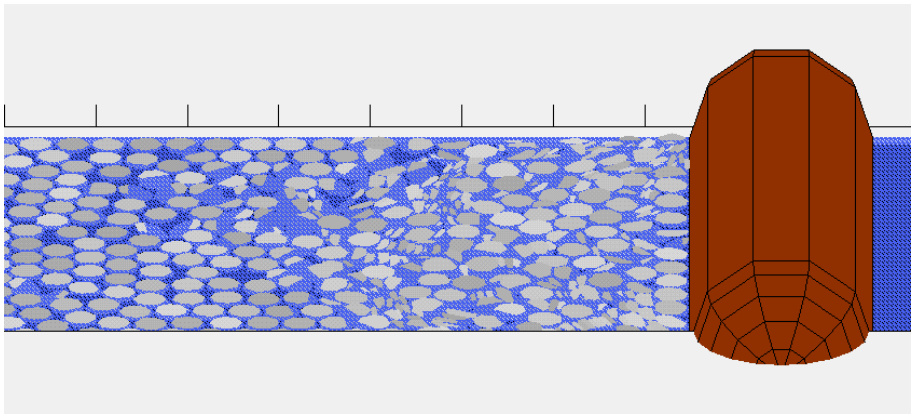

Figure 3: Snapshot of a 3D DEM simulation of a pusher (right) compressing a floating layer of ice floes [12].

which is an artifact of the experimental setup and does not appear in nature, can be removed in the DE simulations by using periodic boundary conditions. Figure 4(b) shows the simulated $F^*(X^*)$-record for two channel lengths L^* with periodic boundary conditions. Comparison between the results shown in Figures 4(a) and 4(b) suggest that the positive slope in the $F^*(X^*)$-record at $5 < X^* < 35$ in Figure 4(a) is caused by the channel edge friction.

A 3D DEM simulation of an ice floe field has also been used to model ship channel ice resistance [13]. That was done by replacing the pusher shown in Figure 3 by a ship shaped object.

The mechanical properties of ice ridge keels are important information for ridge load calculations. For over a decade, ice rubble problems have been studied with DEM in 2D [6] [14][1]. Snapshot of a simulation of ridge keel punch test was shown in Figure 1(b) and Figure 5 shows the force-displacement graph of this simulation, together with results obtained by using other particle shapes. These simulations suggest that the ridge keel indentation load is highest for the rubble pile formed from rectangular particles and lowest for a pile formed from circular particles. However, the shape of the force-displacement graph appears not to be strongly affected by the particle shape.

The differences in ice ridge analyses, performed by using a discontinuum approach (DEM) or a more traditional continuum approach, can now be highlighted. In a DE model, the ridge behavior is defined by local scale parameters through deformation, failure and interaction of individual ice blocks. These local scale parameters are, for example, the elastic modulus E of ice and the ice-ice friction coefficient μ. The traditional way to study ice ridge loads is to model the ice mass with models based on soil mechanics. For example, in the Mohr-Coulomb model the ridge strength is defined with friction angle ϕ and cohesion c. These parameters describe behavior of the ridge as a whole. It is reasonable to assume that if the number of ice floes in a ridge is high enough, the continuum approach should give acceptable results. However, the minimum number of ice blocks required to fulfill the continuum approach is not known. Another point of interest is to consider the parameters describing ridge behavior in the two approaches. Currently, it is not totally clear what are the most important local scale parameters (μ, E, block shape, etc.), nor it is known what are the relationships between the local scale parameters and the Mohr-Coulomb model.

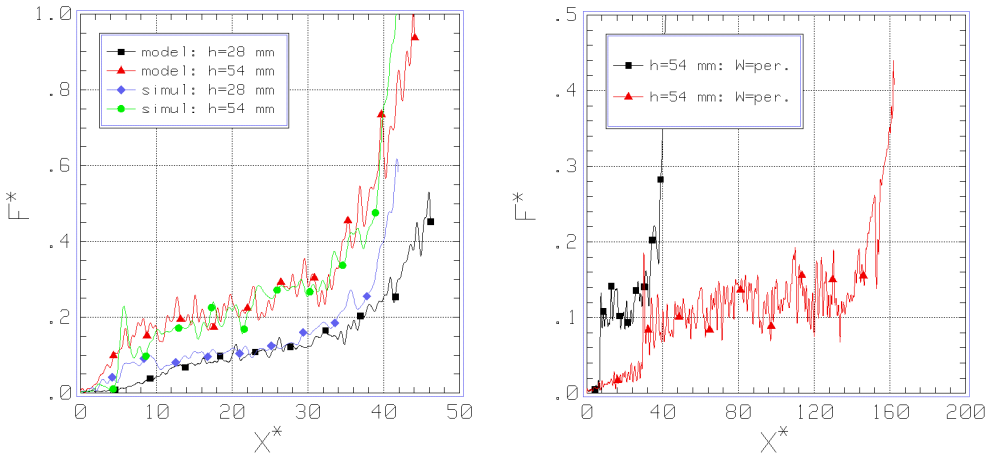

(a) (b)

Figure 4: (a) Nondimensional pusher force versus displacement as measured in experiments (model) and simulations (simul) shown in Figure 2. h is ice thickness. (b) Nondimensional pusher force versus nondimensional pusher displacement for two channel lengths L^* with periodic boundary conditions [12].

Problems dealing with ice sheets

The failure of ice cover against a marine structure is a fragmentation process where a solid disintegrates into discrete particles which then interact with each other and pile-up against the structure (Figure 1(a)). DEM appears to be well suited to this kind of problems, but only a few studies have been performed, e.g. [15][16]. Another ice pile-up process is ridging. Ice ridges form when two ice sheets are driven together, ice blocks break off the sheets and pile-up to form a ridge. Ridge formation from two thin sheets [17] as well as from a thin sheet breaking against a thick sheet [18] have been studied with DEM. Rafting is a process closely related to ridging. Rafting is the simple overriding of one ice sheet by another ice sheet.

From an engineering point of view, ridging and rafting are important processes, as they define the horizontal force an ice sheet can transmit. In other words, ridging and rafting define the horizontal strength of an ice sheet and thus give an upper limit for the ice load on a marine structure.

Figure 6 shows snapshots from DEM simulation showing rafted and ridged ice. In that two dimensional simulation [17], two identical ice sheets were pushed together. Each ice sheet was composed of two thicknesses of ice and the ratio of thicknesses was varied to obtain degrees of inhomogeneity. Again, the accuracy of the simulations was assessed by comparison with a series of similar physical model scale experiments. Both the experiments and the simulations showed that homogeneous ice sheets tend to raft and inhomogeneous ice sheets tend to form ridges. Following the comparison, the computer model was used to perform simulations to study the ridging and rafting forces and to systematically explore the effect of the thickness and thickness inhomogeneity on the likelihood of occurrence of ridging and rafting. Compared to the physical experiments, the DE simulations provided a low cost alternative to systematic parametric studies. In addition, with simulations it is easier to isolate the effect of a single variable in a physical process. Comparison of the measured and calculated forces (Figure 7) showed that the average simulation forces underestimated the average experimental forces by about 50 %. This difference is most likely due to the two dimensionality of the computer model, and highlights the need for 3D simulation tools.

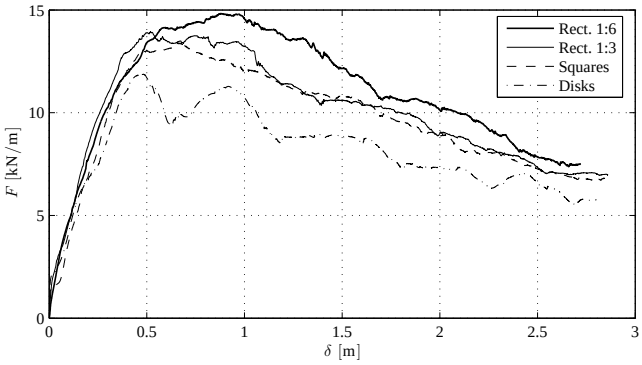

Figure 5: Force-displacement records from punch test simulations, shown in Figure 1(b), with different particle shapes [1].

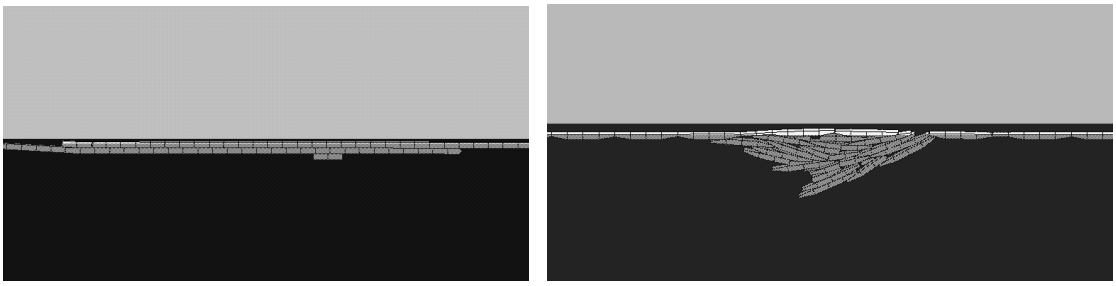

(a) (b)

Figure 6: Scenes from a DEM simulation showing (a) rafted and (b) ridged ice [17].

Summary and discussion

In this paper the discrete element method and some typical problems in ice engineering have been shortly reviewed. It was argued that there are ice engineering problems which should be analysed by using a discontinuous approach, rather than the more traditional continuum approach. First, several ice features comprise of discrete ice floes and, in addition, often the individual ice floes are large compared to the size of the ice feature. As an example, an ice ridge may be formed through stacking of less that ten layers of ice. Second, the ice failure process is a discontinuous fragmentation process. An example of this kind of problem is failure of an ice cover against a structure.

The studies reviewed have demonstrated the usefulness of DEM in ice engineering. DEM can be used in similar tasks than model scale experiments but, more importantly, DEM can be effectively used to study the effects of changing a single parameter.

While DEM is well established and has been applied to different kinds of problems, the application of DEM is still expanding, probably because of the increase in available computing power. One of the interesting new trends in DEM is the development of combined finite-discrete element method [4], where each discrete element is modelled with FEM. While this is computationally demanding, it offers possibilities to model the particle-particle contacts in a more rigorous way than can be done with a spring and dashpot model, see Equation 1.

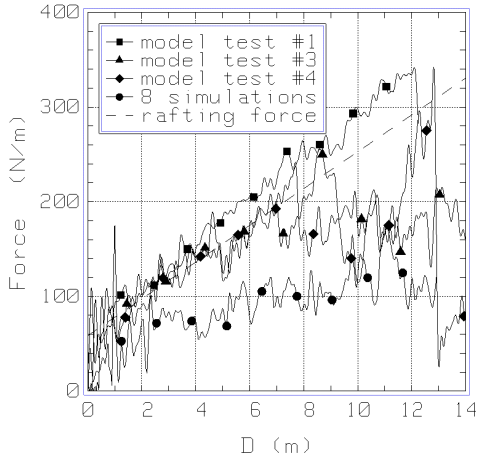

Figure 7: Force-displacement records from 3D physical experiments (model tests) and similar 2D ridge simulations shown in Figure 5(b) [17].

References

[1] J. Tuhkuri and A. Polojärvi. Effect of particle shape in 2D ridge keel deformation simulations. In Proc. 18th Int. *Conf. on Port and Ocean Engineering Under Arctic Conditions (POAC'05)*, Potsdam, New York, USA, Vol. 2, pp. 939-948, (2005).

[2] P.A. Cundall and O.D.L. Strack. A discrete numerical model for granular assemblies. *Geotechnique*, bf 29, 47–65, (1979).

[3] O.R. Walton. Explicit particle dynamics model for granular materials. In Proc. of 4th Int. Conf. on Numerical Methods in Geomechanics, Edmonton, Canada, 8 p. (1982).

[4] A. Munjiza. *The Combined Finite-Discrete Element Method*. Wiley, (2004).

[5] P.W. Cleary and M.L. Sawley. DEM modelling of industrial granular flows: 3D case studies and the effect of particle shape on hopper discharge. *Applied Mathematical Modelling*, **26**, 89–111, (2002).

[6] M.A. Hopkins and W.D. Hibler. On the strength of geophysical scale ice rubble. *Cold Regions Science and Technology*, **19**, 201–212, (1991).

[7] A. Polojärvi. Combined Finite-Discrete Element Method in 3D Ridge Keel Deformation Simulations. Thesis for the degree of M.Sc. (Eng.). Helsinki Univ. of Technology, Faculty of Mechanical Engineering, 86 p. (2005).

[8] M. Sayed, V.R. Neralla and S.B Savage. Yield conditions of an assembly of discrete ice floes. In. Proc. of the 5th Int. Offshore and Polar Engineering Conference, The Hague, The Netherlands, Vol. II, pp. 330-335, (1995).

[9] M. Babic, H.T. Shen and G. Bjedov. Discrete element simulations of river ice transport. In. Proc. of *IAHR Symposium on Ice*, Espoo, Finland, Vol. 1, pp. 564–574, (1990).

[10] S. Løset. Discrete element modelling of a broken ice field, Parts I & II. *Cold Regions Science and Technology*, **22**, 339–360, (1994).

[11] E. Hansen. A discrete element model to study marginal ice zone dynamics and the behaviour of vessels moored in broken ice. Dept. of Marine Hydrodynamics, *Norvegian Univ. of Science and Technology*, MTA-report 1998:124, 159 p. (1998).

[12] M.A. Hopkins and J. Tuhkuri. Compression of floating ice fields. *Journal of Geophysical Research*, **104**, 15,815–15,825, (1999).

[13] R. Haukioja. Simulation of ships channel ice resistance. Thesis for the degree of M.Sc. (Eng.). Helsinki Univ. of Technology, Faculty of Mechanical Engineering, 74 p. (2000).

[14] E. Evgin, R.M.W. Frederking and C. Zhan. Distinct element modelling of ice ridge formation. In Proc. 11th *OMAE Symp.*, Calgary, Canada, Vol. IV, pp. 255-260, (1992).

[15] E. Evgin and C. Zhan. Distinct element modelling in ice mechanics. Dept. of Civil Engineering, *University of Ottawa*, Report from Finnish/Canadian Joint Research Project No. 5., 80 p. (1991).

[16] M.A. Hopkins and W.D. Hibler. Onshore ice pile-up: a comparison between experiments and simulations. *Cold Regions Science and Technology*, **26**, 205–214, (1997).

[17] M.A. Hopkins, J. Tuhkuri and M. Lensu. Rafting and ridging of thin ice sheets. *Journal of Geophysical Research*, **104**, 13,605–13,613, (1999).

[18] M.A. Hopkins. On the ridging of intact lead ice. *Journal of Geophysical Research*, **99**, 16,351–16,360, (1994).

Numerical Simulation of Nano-, Meso-, Macro- and Multiscale Fluid Dynamics

J. H. Walther*
Department of Mechanical Engineering, Fluid Mechanics Section
Danish Technical University, Kgs. Lyngby, Denmark
e–mail: jhw@mek.dtu.dk
also at: Institute of Computational Science
ETH Zürich, CH-8092, Switzerland
e–mail: walther@inf.ethz.ch

P. Koumoutsakos
Institute of Computational Science
ETH Zürich, CH-8092, Switzerland
e–mail: petros@inf.ethz.ch

Summary We present algorithms and numerical simulations of fluid flow at the nano-, meso- and macroscale. The techniques involve nonequilibrium molecular dynamics simulations of fluids in nanoscale confinement, dissipative particle dynamics for fluids at the mesoscale, and smooth particle hydrodynamics and particle vortex methods for compressible and incompressible macroscale fluid dynamics. We couple the nano- and macroscale descriptions using a Schwarz alternating procedure and effective boundary wall forces to minimize the artifacts introduced by the interface between the two regions. This procedure is extended to the mesoscale model and includes the inherent fluctuations at this length scale. A unifying particle description is used thoughout in the framework of massively parallel hybrid particle-mesh library.

Introduction

Particle methods provide a powerful, unifying description of discrete and continuum mechanics [17] with applications that that range from atomistic systems using molecular dynamics (MD) simulations, through agglomerations of atoms and molecules at meso-scopic time and length scales using dissipatitive particle dynamics (DPD), and continuum description of fluid and solid mechanics using vortex particle method (VM) and smooth particle hydrodynamics (SPH), to planetary systems invoking Barnes-Hut [1] and hybrid particle-mesh methods [13].

The kinematic relations governing these different systems share many common features and may often be described in terms of short- and long-range interaction potentials. The latter includes the omnipresent $1/r$ potential governing electrostatics, gravitation, and "induced fluid motion" in vortex particle methods. The computational cost associated with the evaluation of the $1/r$-potential formally scales as $\mathcal{O}(N^2)$, where N denotes the number of computational elements/particles, and severely limits the computational efficiency of these methods. Fast Multipole Methods (FMM) [12] have been developed to reduce the computational cost to formally $\mathcal{O}(N)$, while retaining the flexibility of the $\mathcal{O}(N^2)$ algorithm, but carries in general a large prefactor, currently limiting this method to $\mathcal{O}(10^6)$. Hybrid partcle-mesh methods overlay the particle domain with a regular mesh to obtain solution for the partial differential equation corresponding to the particular interaction potential [15]. This method achieves significantly higher serial and parallel efficiency than FMM cf. [8, 24], but are currently limited to problems in simple geometries. We employ these hybrid methods to study fluids at the nano-, meso-, and macroscale, specifically the influence of confinement on the validity of the no-slip velocity boundary conditions.

The objective of the present paper is two-fold. First we describe simulations of flow at the nano- and meso-scale, and demonstrate techniques that allow us to couple the the different time and lenght scales. Second, we outline the main elements of the parallelisation of a hybrid particle-mesh library [24] designed for multi-scale problems.

Nano-scale fluid mechanics

The understanding of the static and dynamic behaviour of fluids at solid interfaces is central for the modeling and simulation of fluid mechanics problems. For nanoscale systems this is particular important as the no-slip boundary condition ($\boldsymbol{u}_{fluid} = \boldsymbol{u}_{solid}$) usually assumed in macroscale fluid mechanics is know to fail. Thus a finite fluid "slip" velocity ($u_s = |\boldsymbol{u}_{fluid} - \boldsymbol{u}_{solid}|$) has been observed in experiments of water in hydrophobic capillaries [14, 25, 7, 3], whereas the amount of slip at hydrophilic surfaces remains less clear [6, 26]. The slip is traditionally modeled by the Navier slip condition [18]:

$$u_s = L_s \frac{\partial u}{\partial n}, \tag{1}$$

where L_s denotes the slip length, and $\dfrac{\partial u}{\partial n}$ the normal component of the velocity gradient at the surface.

We study this model using large scale parallel molecular dynamics (MD) simulations of canonical flow problems including the flow past a circular cylinder, and here described by water molecules passing the surface of a carbon nanotube [27]. The water is modeled by the SPC/E model [4] with a $1/r$ potential acting between the partial charges located at the atomic sites, and a 12-6 Lennard-Jones potential (U) between the oxygen atoms

$$U(r) = 4\epsilon \left[\left(\frac{\sigma}{r} \right)^{12} - \left(\frac{\sigma}{r} \right)^{6} \right]. \tag{2}$$

ϵ and σ denote the energy and length scale of the potential. The interaction between the water and the 2.5 nm diameter rigid carbon nanotube mounted at the center of computational box is given by a Lennard-Jones potential (Eq. (2)) acting between the oxygen and carbon atoms.

A flow is imposed in the stream- and spanwize directions using an adaptive body force acting on the waters upstream of the carbon carbon nanotube. Periodic boundary conditions are imposed in all spatial direction and effective model the flow past an array of carbon nanotubes.

The time average density and velocity profiles (Fig. 1) are sampled after the decay of the initial transient at 40 ps, and throughout the remaining 340 ps of the simulation. The density profile (Fig. 1a) display a layering characteristic of water at a hydrophobic surface, and the tangential velocity profile (Fig. 1b) a negligible slip length of $\mathcal{O}(1\,\mathrm{nm})$ [27]. Conversely, the slip length in the direction along the axis of the carbon nanotube (Fig. 1c) is $88\,\mathrm{nm}$ indicating that the slip length is not a material property of the fluid-solid interface, but depends on the particular flow configuration. Work in on the way to derive alternative slip models and will be report at the meeting.

Multiscale simulations of nanoscale flow problems

Direct numerical simulation of nanoscale flows through MD simulations is computationally expensive, and presents a level of detail only required in a specific regions of interest e.g., in the vicinity of the fluid-solid interface. The remaining part of the computational domain may be described by continuum models, here the Navier-Stokes equations, and provides orders of magnitude improvement in the computational efficiency. The implementation of such a multiscale scheme requires the coupling of mass and momentum fluxes across the interfaces between the atomistic (Ω_A) and continuum domains (Ω_C) cf. Fig. 2. A Schwarz alternating procedure is employed to ensure the conservation of the fluxes across the overlap region between the two systems cf. Ref. [28]. The iterations proceed by sampling the atomistic system at the boundary of the continuum system to provides boundary conditions for the continuum solver. The continuum system is solved to steady-state and provides at the boundary to the atomistic system an updated flux of mass and momentum. The mass flux is imposed by introducing or removing atoms in the vicinity of the interface. The insertion of atoms into a dense fluid is non-trivial and achieved using the Usher algorithm cf. [9]. The convective momentum flux is imposed by adjusting the mean velocity of

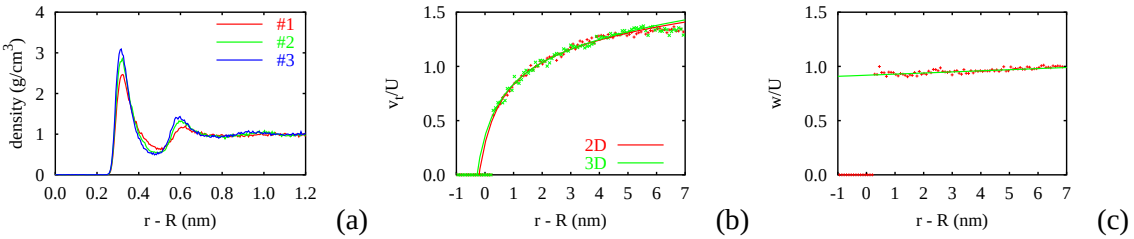

Figure 1: The time averaged radial density profile of water (a) flowing past an array of carbon nanotubes [27]. The diameter of the carbon nanotube is 2.50 nm and the onset flow speed 100 m s^{-1}. The profiles are sampled upstream (- -: section III), at the mid-section (– –: section II), and downstream section (—: section I). The time averaged tangential (b) and axial (c) component of the streaming velocity for the three-dimensional flow past an array of carbon nanotubes. The measured tangential profile (–×– and - -) is sampled from section II and V and compared with a fit to the Stokes veloicity profile for the flow past a circular cylinder [2], and to the corresponding results (–+– and —) from a purely two-dimensional flow. The axial profiles were found to be similar for all the six sections, and a combined average is fitted to the linear profile $w(r) = a + br$.

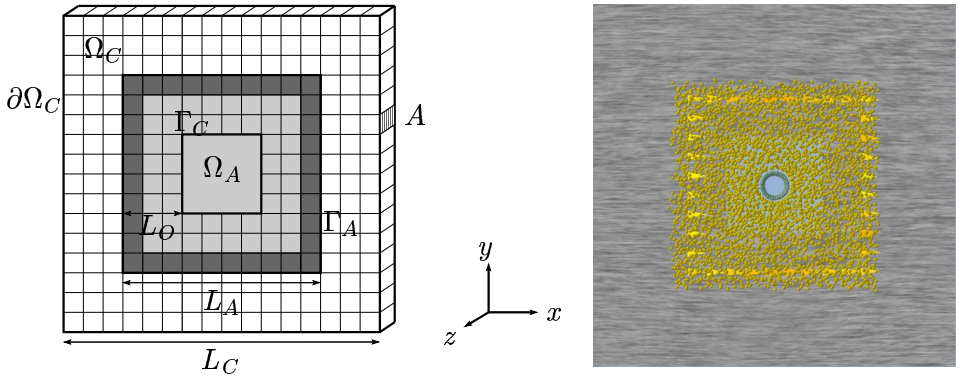

Figure 2: Schematic of a hybrid atomistic/continuum computational domain [28]. L_O denotes the size of the overlap domain between the atomistic domain Ω_A (entire shaded area) with boundary Γ_A (dark shaded area) and the continuum domain Ω_C with outer boundary $\partial\Omega_C$ and inner boundary Γ_C. The fine grid corresponds to the finite volume mesh and A is the area of a cell face. The right picture is a close-up of a hybrid computational domain to study the flow of liquid argon around a carbon nanotube as used in the present work.

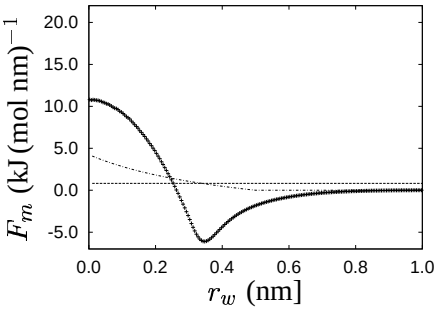

Figure 3: Effective boundary force F_m on a Lennard-Jones particle located at a distance r_w from the boundary of an atomistic system of density $\rho = 1.0\,\mathrm{g\,cm^{-3}}$ and at temperature $T = 215\,\mathrm{K}$. Displayed are the constant force used in Ref. [20] ($--$), a diverging force [19] ($-\cdot-$), and the measured force used in the present study ($+$).

the atoms in the overlap region (Fig. 2) while assuring the desired temperature through a rescaling of the velocity fluctuations. The conservation of the flux of mass and convective momentum therefore secures a proper ideal gas pressure in the atomistic system. The non-ideal virial pressure contribution is imposed through wall potential functions [28] measured in a separate simulation cf. Fig. 3.
Figure 4 compares the results obtained for the flow of argon past a carbon nanotube using a fully atomistic simulations (Fig. 4a,c) with the multiscale algorithm (Fig. 4b,d) [28]. Disregarding the fluctuations inherent of the atomistic system, the agreement of streamlines and flow speeds is excellent. Further details of the method and validations studies may be found in Ref. [28].

Dissipative Particle Dynamics
A continuum, Navier-Stokes description of nanoscale flows lack the fluctuations inherent at this length scale see e.g., Fig. 4, and may in a multiscale algorithm artificially suppress the fluctuations of the atomistic system, hence reducing the fluid temperature [11]. To prevent this we consider modeling the continuum using the method of dissipative particle dynamics (DPD). In this model clusters of atoms and molecules are modeled as a single DPD-particle and are assumed to interact via pair potentials consisting of conservative, stochastic, and dissipative forces cf. [16, 10]. Previous DPD studies have mainly considered fluids in periodic system, and have modeled solid walls by layers of immobile "solid" particles combined with hard walls and reflection schemes to prevent leakage of fluid particles out of the system. The desired behaviour of such a wall model depends on the length scale of the system. Most problems currently addressed by DPD simulations are performed at a length scale where molecular effecs of the wall on the fluid shold be negligible, including the near wall density fluctuations observed in Fig. 1a. However, present DPD wall models do not prevent such fluctuation cf. Fig. 5a. and to minimize these artifacts, we propose to extend the effective wall potential introduced in the previous section [28] to the method of dissipative particle dynamics. The extension involves sampling of the individual force components in both the normal and tangential directions cf. Fig. 6, the latter to ensure satisfaction of the no-slip condition [22, 29, 21].

PPM - A General Purpose Hybrid Parallel-Mesh Library
In an effort to dissiminate particle methods and to improve their computational efficiency we are currently implementing a general purpose hybrid particle-mesh library —the PPM-library cf. [24]. The formalism of particle methods was recently reviewed by Koumoutsakos [17] and amounts to tracking the dynamics of N particles carrying physical properties of the system that is being simulated. The dynamics of the particles are Ordinary Differential Equations (ODEs) that

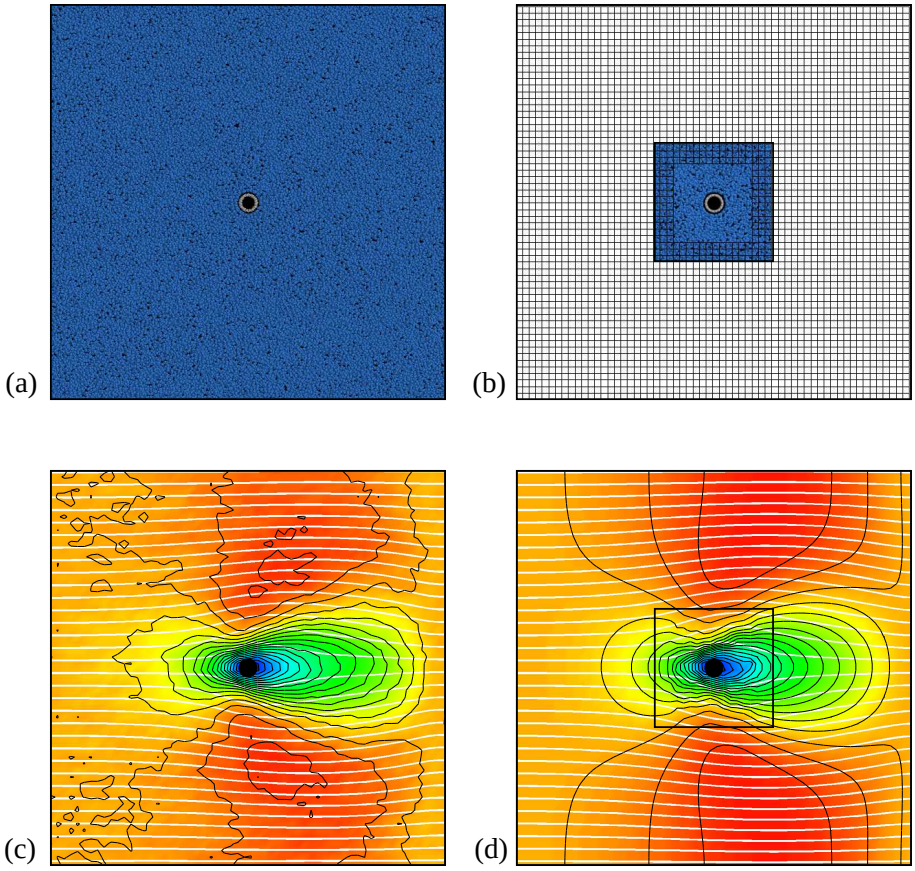

Figure 4: Multiscale simulations of liquid argon flowing part a carbon nanotube [28]. (a) Computational domain for the reference solution of the flow of argon around a carbon nanotube using a purely atomistic description. (b) Hybrid atomistic/continuum computational domain. Both computational domains have an extent of $30 \times 30\,\mathrm{nm}$. (c) Velocity field for the reference solution averaged over 4 ns. The white lines are streamlines, and the black lines are contours of the speed ($|\boldsymbol{u}|$). (d) Velocity field of the hybrid solution after 50 iterations. The black square denotes the location of Γ_A. The solution in Ω_A is averaged over 10 iterations.

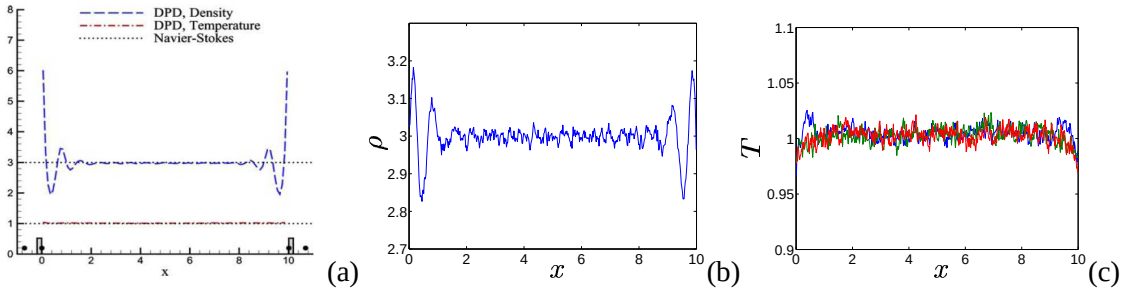

Figure 5: DPD simulations of a fluid at rest and confined between two wall. From left to right is shown (a0 the density profile obtained in Ref. [21], and the present density (b) and temperature profiles (c). The fluctuations observed in the present model is 6 % and 2 % for the temperature and density.

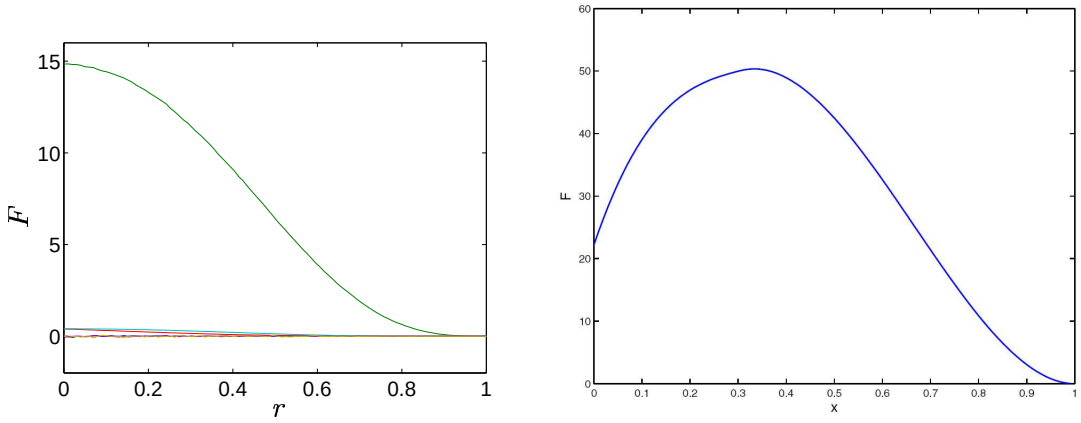

Figure 6: The ensemble average normal and tangential forces acting on DPD at a distance, r from the fictitious wall. The only non-zero components Left: the green curve show the normal component of the conservative force, and on the right the tangential components of the conservative (blue), dissipative (green), and stochastic (light blue) forces. The only non-zero mean forces are the tangential dissipative force (green) and the normal component of the conservative force.

determine the trajectories of the particles p and the evolution of their properties:

$$\frac{d\boldsymbol{x}_p}{dt} = \boldsymbol{u}(\boldsymbol{x}_p, t) = \sum_{q=1}^{N} \boldsymbol{K}(\boldsymbol{x}_p, \boldsymbol{x}_q; \boldsymbol{\omega}_p, \boldsymbol{\omega}_q), \tag{3}$$

$$\frac{d\boldsymbol{\omega}_p}{dt} = \sum_{q=1}^{N} \boldsymbol{F}(\boldsymbol{x}_p, \boldsymbol{x}_q; \boldsymbol{\omega}_p, \boldsymbol{\omega}_q), \tag{4}$$

$$\tag{5}$$

where $\boldsymbol{x}_p$ denotes the position of the p-th particle, $\boldsymbol{u}_p$ its velocity, and $\boldsymbol{\omega}_p$ the vector of properties such as concentration, charge, vorticity, or temperature. The dynamics of the simulated physical system are represented by the functions $\boldsymbol{K}$ and $\boldsymbol{F}$ that represent solutions of the field equations (such as the Poisson equation for velocity-vorticity formulations of the Navier-Stokes equations in VM) or integral representations of diffential operators (such as Laplacian operators in SPH). In Particle-Mesh (PM) methods, the functions $\boldsymbol{K}$ and $\boldsymbol{F}$ are evaluated on a mesh through the corresponding field equation. The hybrid method requires:

- the interpolation of the $\boldsymbol{\omega}_p$ carried by the particles from the irregular particle locations onto the regular mesh points ($\boldsymbol{\omega}_m$)

$$\boldsymbol{\omega}_m \sum_{p=1}^{N} Q(\boldsymbol{x}_m - \boldsymbol{x}_p)\boldsymbol{\omega}_p, \tag{6}$$

  where Q denotes the interpolation function.

- the solution of the field equation:

$$\boldsymbol{D}\boldsymbol{F}_m = \boldsymbol{\omega}_m \tag{7}$$

  where $\boldsymbol{D}$ denotes the diffential operator, and $\boldsymbol{F}_m$ the field quantity on the mesh.

- the interpolation of $\boldsymbol{F}_m$ from the mesh to the particle locations ($\boldsymbol{F}_p$):

$$\boldsymbol{F}_p \sum_{m=1}^{M} Q(\boldsymbol{x}_m - \boldsymbol{x}_p)\boldsymbol{F}_m, \tag{8}$$

  and M is the number of mesh points.

The accuracy of the method depends on the smoothness of $\boldsymbol{K}$ and $\boldsymbol{F}$, on the interpolation function (Q), and on the discretization scheme ($\boldsymbol{D}$) employed for the solution of the field equation.
The parallel implementation of the algorithm is complicated by several factors:

- the simultaneous presence of particles and meshes prohibits a single optimal way of parallelization —the computational cost associated with the interpolation steps and the solution of the field equation are of equal magnitude.
- complex-shaped computational domains and strong particle inhomogeneities require spatially adaptive domain decompositions.
- particle motion may invalidate the domain decomposition and cause rising load imbalance, and inter-particle relations (e.g., chemical bonds in MD) constrain decompositions and data assignment.

The library attains it efficiency using structured, uniform cartesian meshes for the solution of the field equations. As a result, the physical and computational domains are rectangular or cuboidal in two and three dimensions. Complex geometries are handled by immersed boundaries, through the use of source terms in the corresponding field equations, or through boundary element techniques. Adaptive meshing capabilities are possible using AMR concepts as adapted to particle methods [5].
The simultaneous presence of particles and meshes require several different concurrent domain decompositions. These decompostions are assumed to decompose the computational domain into rectangular or cuboidal sub-domains with a sufficient granularity to secure adequate load balance while limiting the number of sub-domains to a minimum. The concurrent presence of different decompositions allows to perform each step of the computational algorithm in its optimal environment with respect to load balance and the computational-to-communicaton ratio. For the actual computations, the individual sub-domains are treated as independent problems and extended with ghost mesh layers and ghost particles to allow for communication between them.
Figure 7 shows a domain decompostion of a cellular compartent (the Endoplasmic Reticulum) using the PPM-library [23]. The decomposition is performed using recursive orthogonal bisection in x and y directions.

Summary

We have presented numerical simulations of fluid fbw at the nano-, meso- and macro-scale. The atomistic description have demonstrated that the classical Navier slip model result in a fbw dependent slip length. We have extended current multiscale algorithms with effective boundary potentials to remove artifacts introduce at the interface between the different nano- and macroscopic description of the fbw. A similar procedure has furthermore been applied to the method of dissipative particle dynamics. Finally, we have outlines elements of a parallel implementation of hybrid particle-mesh algorithms for efficient simulations using particles.

Acknowledgements

The authors gratefully acknowledge the PPM implementation of the DPD method by A. Altenhoff, simulations of slip in atomistic system by A. Kotsalis and T. Werder, and co-developed of the PPM-library by M. Bergdorf, A. Kotsalis, S. Hieber, and I. Sbalzarini. Computer resources were provided by the Swiss National Supercomputer Center (CSCS).

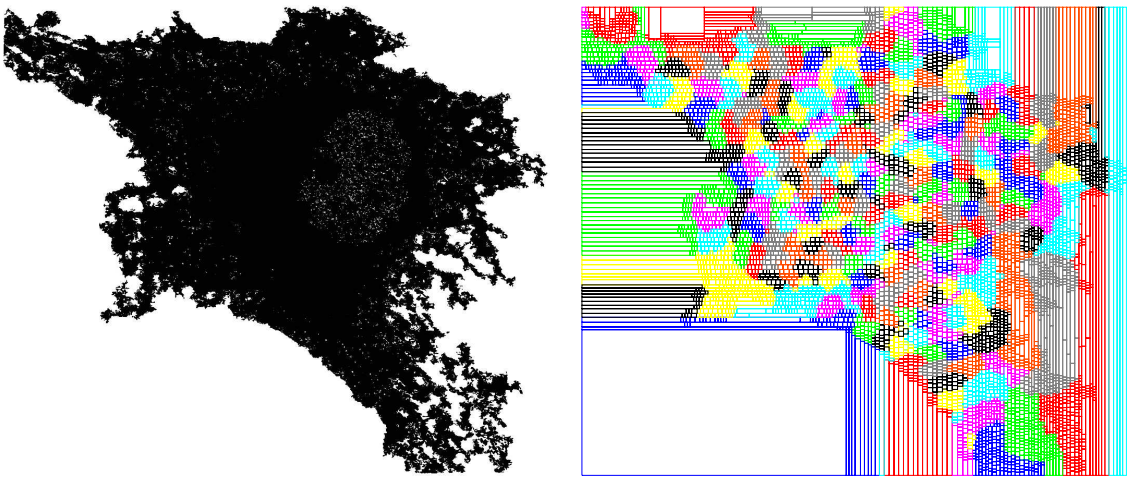

Figure 7: Top view of the computational domain (left panel) used for the study of diffusion in cellular compartments [23]. The resulting PPM domain decomposition (right panel) using recursive orthogonal bisection in x and y directions (z direction fixed) on 242 processors. Rectangles show the 9311 PPM sub-domains, color codes processor affiliation. The peripheral elongated domains are a result of the recursive orthogonal bisection decomposition.

References

[1] J. Barnes and P. Hut. A hierarchical $O(N \log N)$ force-calculation algorithm. *Nature*, 324(4):446–449, 1986.

[2] G. K. Batchelor. *An Introduction To Fluid Dynamics*. Cambridge University Press, 1 edition, 1967.

[3] J. Baudry, E. Charlaix, A. Tonck, and D. Mazuyer. Experimental evidence for a large slip effect at a nonwetting fluid-solid interface. *Langmuir*, 17:5232–5236, 2001.

[4] H. J. C. Berendsen, J. R. Grigera, and T. P. Straatsma. The missing term in effective pair potentials. *J. Phys. Chem.*, 91:6269–6271, 1987.

[5] M. Bergdorf, G.-H. Cottet, and P. Koumoutsakos. Multilevel adaptive particle methods for convection-diffusion equations. *Multiscale Model. Simul.*, 4(1):328–357, 2005.

[6] E. Bonaccurso, M. Kappl, and H.-J. Butt. Hydrodynamic force measurements: Boundary slip of water on hydrophilic surfaces and electrokinetic effects. *Phys. Rev. Lett.*, 88(7):076103, 2002.

[7] N. V. Churaev, V. D. Sobolev, and A. N. Somov. Slippage of liquids over lyophobic solid surfaces. *J. Coll. Interface Sci.*, 97(2):574–581, 1984.

[8] G.-H. Cottet and P. Poncet. Advances in direct numerical simulation of 3D wall-bounded flows by vortex-in-cell methods. *J. Comput. Phys.*, 193:136–158, 2003.

[9] R. Delgado-Buscalioni and P. V. Coveney. USHER: An algorithm for particle insertion in dense fluids. *J. Chem. Phys.*, 119(2):978–987, 2003.

[10] P. Espanol. Hydrodynamics from dissipative particle dynamics. *Phys. Rev. E*, 52(2):1734–1742, 1995.

[11] E. G. Flekkøy, J. Feder, and G. Wagner. Coupling particles and fields in a diffusive hybrid model. *Phys. Rev. E*, 64:066302–1–066302–7, 2001.

[12] L. Greengard and V. Rokhlin. A fast algorithm for particle simulations. *J. Comput. Phys.*, 73:325–348, 1987.

[13] F. H. Harlow. Particle-in-cell computing method for fluid dynamics. *Methods Comput. Phys.*, 3:319–343, 1964.

[14] H. Helmholtz and G. von Piotrowski. Über Reibung tropfbarer Fl¨ussigkeiten. *Sitzungsberichte der Kaiserlich Akademie der Wissenschaften*, 40:607–658, 1860.

[15] R. W. Hockney and J. W. Eastwood. *Computer Simulation Using Particles*. Institute of Physics Publishing, Bristol, PA, USA, 2 edition, 1988.

[16] P. J. Hoogerbrugge and J. M. V. A. Koelman. Simulating microscopic hydrodynamics phenomena with dissipative particle dynamics. *Europhys. Lett.*, 19(3):155–160, 1992.

[17] P. Koumoutsakos. Multiscale flow simulations using particles. *Annu. Rev. Fluid Mech.*, 37:457–487, 2005.

[18] C. L. M. H. Navier. Memoire sur les lois du mouvement des fluides. *Mem. Acad. R. Sci. Inst. Fr.*,

6:389–440, 1827.
[19] X. B. Nie, S. Y. Chen, W. N. E, and M. O. Robbins. A continuum and molecular dynamics hybrid method for micro- and nano-fluid flow. *J. Fluid Mech.*, 500:55–64, 2004.
[20] S. T. O'Connell and P. A. Thompson. Molecular dynamics-continuum hybrid computations: A tool for studying complex fluid flow. *Phys. Rev. E*, 52(6):R5792–R5795, 1995.
[21] I. V. Pivkin and G. E. Karniadakis. A new method to impose no-slip boundary conditions in dissipative particle dynamics. *J. Comput. Phys.*, 207:114–128, 2005.
[22] M. Revenga, I. Zúñiga, and P. Espanol. Boundary models in DPD. *Int. J. Mod. Phy. C*, 9(8):1319–1328, 1998.
[23] I. F. Sbalzarini, A. Mezzacasa, A. Helenius, and P. Koumoutsakos. Organelle shape has an influence on fluorescence recovery results. *Mol. Biol. Cell*, 13:1554, 2002.
[24] I. F. Sbalzarini, J. H. Walther, M. Bergdorf, S. E. Hieber, E. M. Kotsalis, and P. Koumoutsakos. PPM – a highly efficient parallel particle-mesh library for the simulation of continuum systems. *J. Comput. Phys.*, submitted, 2005.
[25] E. Schnell. Slippage of water over nonwettable surfaces. *J. Appl. Phys.*, 27(10):1149–1152, 1956.
[26] O. I. Vinogradova and G. E. Yakubov. Dynamic effects on force measurements. 2. Lubrication and the atomic force microscope. *Langmuir*, 19:1227–1234, 2003.
[27] J. H. Walther, T. Werder, R. L. Jaffe, and P. Koumoutsakos. Hydrodynamic properties of carbon nanotubes. *Phys. Rev. E*, 69:062201, 2004.
[28] T. Werder, J. H. Walther, and P. Koumoutsakos. Hybrid atomistic-continuum method for the simulation of dense fluid flows. *J. Comput. Phys.*, 205:373–390, 2005.
[29] S. M. Willemsen, H. C. J. Hoefsloot, and P. D. Iedema. No-slip boundary conditions in dissipative particle dynamics. *Int. J. Mod. Phy. C*, 11(5):881–890, 2000.

Multiscale Methods for Flow in Porous Media

Knut–Andreas Lie*, Jørg E. Aarnes, Vegard Kippe, and Stein Krogstad
Department Applied Mathematics
SINTEF ICT, Oslo, Norway
e–mail: Knut-Andreas.Lie@sintef.no

Summary We present a hierarchical multiscale method for the numerical solution of two-phase flow in strongly heterogeneous porous media. The method is based upon a mixed finite-element formulation, where basis functions are computed numerically on a coarse grid to correctly and accurately account for subscale permeability variations from an underlying (fine-scale) geomodel.

Introduction

Natural porous rock formations are heterogeneous at all length scales. When modelling fluid flow in porous formations, it is generally not possible to account for all pertinent scales, from the micrometre scale of pore channels to the kilometre scale of the full reservoir. Instead, one has to create models for studying phenomena occurring at a reduced span of length scale, and any modelling attempt should therefore generally be accompanied by appropriate rescaling (up- and downscaling) techniques.

Here we focus on how to incorporate fine-scale features from a detailed geomodel into flow simulations on a reservoir scale. Whereas industry-standard geomodels may contain between 10^6–10^9 grid cells, commercial reservoir simulators are typically capable of simulating models with 10^4–10^6 degrees of freedom. A large activity is therefore devoted to upscaling/downscaling between a detailed reservoir model and a coarser simulation model.

We present an alternative approach based on a multiscale formulation for pressure and flow velocities, where the global flow is computed on a coarse grid and fine-scale heterogeneity is accounted for through a set of generalised, heterogeneous basis functions. The basis functions are computed numerically by solving local flow problems (as is done in many flow-based upscaling methods), and when included in the coarse-grid equations, the basis functions ensure that the global equations are consistent with the local properties of the underlying differential operators. Several different multiscale methods have been proposed, including the multiscale mixed finite-element method (MsMFEM) [2], the multiscale finite-volume method [9], and numerical subgrid upscaling [6]. Common for all three methods is that they produce mass-conservative solutions both on the coarse grid and on the underlying fine grid, and they may thus be used either as very robust upscaling methods or as efficient fine-scale solvers.

Multiscale Mixed Finite Elements

The Two-Phase Flow Model

We consider incompressible flow of two phases (water and oil). For simplicity, we neglect the effects of gravity and capillary forces. The flow equations can then be formulated as an elliptic equation for the pressure p and total velocity v,

$$v = -(\lambda_w + \lambda_o)K\nabla p, \qquad \nabla \cdot v = q. \tag{1}$$

Here q is a source term representing injection and production wells, K is the rock permeability (i.e., the ability to transmit fluids), and $\lambda_\alpha = k^r_\alpha/\mu_\alpha$ is the mobility of phase α, where μ_α is viscosity of phase α and $k^r_\alpha = k^r_\alpha(S)$ is the relative permeability, i.e., the reduced ability of the rock to transmit fluids due to the presence of other phases. The saturation S denotes the volume fraction of water and is described by the transport equation

$$\phi\partial_t S + v \cdot \nabla f(S) = q_s, \tag{2}$$

where ϕ is the rock porosity and $f = \lambda_w/(\lambda_o + \lambda_w)$ is the fractional flow function.

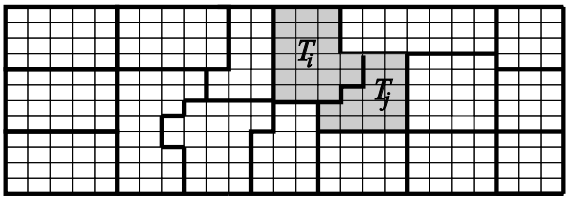

Figure 1: A general coarse grid overlying a uniform fine grid with the grey area giving the support of basis function ψ_{ij}.

Mixed Finite Elements

The mixed finite-element discretisation of the pressure equation (1) in a domain Ω seeks a pair $(v, p) \in U \times V$, where U and V are finite-dimensional subspaces of $H_0^{\text{div}}(\Omega)$ and $L^2(\Omega)$, respectively, such that

$$\int_\Omega v \cdot (\lambda K)^{-1} u \, dx - \int_\Omega p \nabla \cdot u \, dx = 0, \qquad \text{for all } u \in U, \tag{3}$$

$$\int_\Omega l \nabla \cdot v \, dx = \int q l \, dx, \qquad \text{for all } l \in V. \tag{4}$$

Thus letting $\{\psi_i\}$ and $\{\phi_k\}$ be bases for $U \subset H_0^{\text{div}}(\Omega)$ and $V \subset L^2(\Omega)$, we obtain approximations $v = \sum v_i \psi_i$ and $p = \sum p_k \phi_k$, where the coefficients $\mathbf{v} = \{v_i\}$ and $\mathbf{p} = \{p_k\}$ solve a linear system of the form

$$\begin{bmatrix} \mathbf{B} & \mathbf{C} \\ \mathbf{C}^T & \mathbf{O} \end{bmatrix} \begin{bmatrix} \mathbf{v} \\ -\mathbf{p} \end{bmatrix} = \begin{bmatrix} \mathbf{0} \\ \mathbf{q} \end{bmatrix}, \tag{5}$$

where

$$b_{ij} = \int_\Omega \psi_i \cdot (\lambda K)^{-1} \psi_j \, dx, \quad c_{ik} = \int_\Omega \phi_k \nabla \cdot \psi_i \, dx, \quad \text{and} \quad q_k = \int_\Omega \phi_k q \, dx.$$

Multiscale Basis Functions

In a standard discretisation, the spaces U and V typically consist of low-order piecewise polynomials. In the multiscale methods, U and V are given by the solution of local flow problems. Let $\mathcal{K} = \{K_m\}$ be a partitioning of Ω into mutually disjoint grid cells. Furthermore, let $\mathcal{T} = \{T_i\}$ be a coarser partitioning of Ω, in such a way that whenever $K_m \cap T_i \neq 0$ then $K_m \subset T_i$; see Figure 1. Let Γ_{ij} denote the non-degenerate interfaces $\Gamma_{ij} = \partial T_i \cap \partial T_j$. For each Γ_{ij} we assign a basis function $\psi_{ij} \in U_{\text{ms}}$, and for each T_i we assign a basis function $\phi_i \in V$.

The basis function ψ_{ij} is obtained by forcing a unit displacement from cell T_i to T_j; that is, by solving,

$$\psi_{ij} = -\lambda K \nabla \phi_{ij}, \quad \nabla \cdot \psi_{ij} = \begin{cases} w_i(x), & \text{for } x \in T_i, \\ -w_j(x), & \text{for } x \in T_j, \end{cases} \tag{6}$$

with $\psi \cdot \nu = 0$ on $\partial\Omega_{ij}$, where ν is the outward-pointing unit normal to $\partial\Omega_{ij}$ pointing from T_i to T_j. For cells containing a well (i.e., for all T_i for which $\int_{T_i} q \neq 0$), the weight function w_i is given by

$$w_i(x) = \frac{q(x)}{\int_{T_i} q(\xi) \, d\xi}. \tag{7}$$

This choice ensures a conservative approximation of v on the fine grid. For all other cells, we choose $w_i(x) = 1/|T_i|$ or $w_i(x) = \frac{1}{m} \operatorname{trace}_m(K(x))/|T_i|$. The corresponding basis functions can be seen as generalisations of the lowest-order Raviart–Thomas basis functions in a standard mixed method. Figure 2 illustrates the x-velocity basis functions in two different cases.

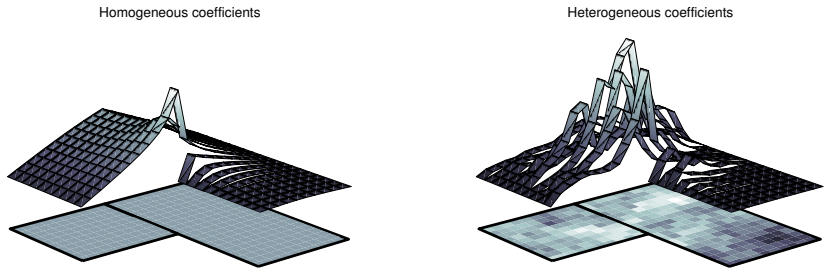

Figure 2: The x component of the velocity basis function associated with an edge between two cells of different size for a homogeneous and a heterogeneous permeability field, respectively.

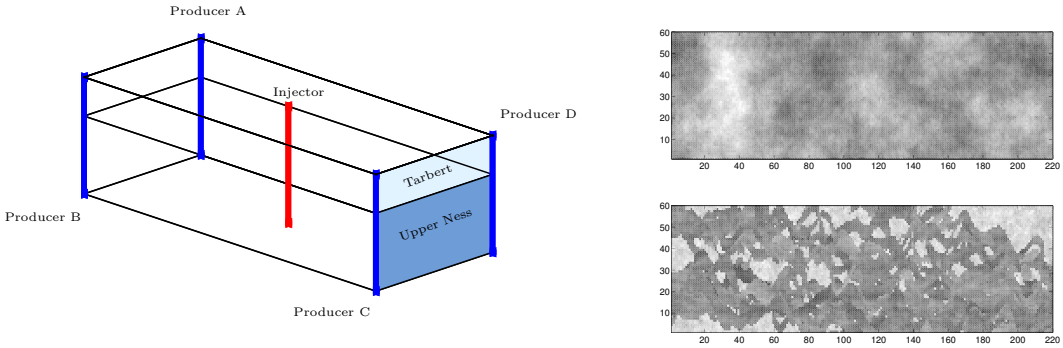

Figure 3: Schematic of the SPE10 reservoir model. The reservoir dimensions are $1200 \times 2200 \times 170$ ft., and the model consists of $60 \times 220 \times 85$ grid cells. The top and bottom plots to the right depict the logarithm of the horizontal permeability in the top layer of the Tarbert formation and the bottom layer of the Upper Ness formation.

Discussion

In this section we show that MsMFEM: (i) is an accurate and robust alternative to upscaling; (ii) is efficient when used as an approximate fine-scale solver for dynamic flow cases; and (iii) is very flexible with respect to the choice of coarse grid cells, given an appropriate fine-grid solver.

Accuracy and Robustness — 10th SPE Comparative Solution Project

Model 2 from SPE10 [7] was designed as a benchmark for various upscaling techniques and consists of two different rock formations; see Figure 3. Both formations are highly heterogeneous, with permeability variations of more than eight orders of magnitude, but are qualitatively different. The shallow-marine Tarbert formation is smooth, and therefore not too hard to upscale. The fluvial Upper Ness formation contains intertwined networks of high-permeability channels and poses severe challenges to any numerical method.

In Figure 4 we compare production curves from a MsMFEM simulation with a reference solution obtained by direct simulation on the full model. For the MsMFEM simulation we used a $5 \times 11 \times 17$ coarse grid and computed the fluid transport on the fine grid using fluxes from the corresponding subscale velocity field. For comparison, we also include results obtained from a upscaling/downscaling approach [8]. The MsMFEM is able to accurately reproduce the flow in the fine-scale channels and therefore matches the reference curves almost exactly. The upscaling/downscaling approach, on the other hand, does not properly account for the coupling between small-scale and large-scale effects and therefore fails to reproduce the production curves of the

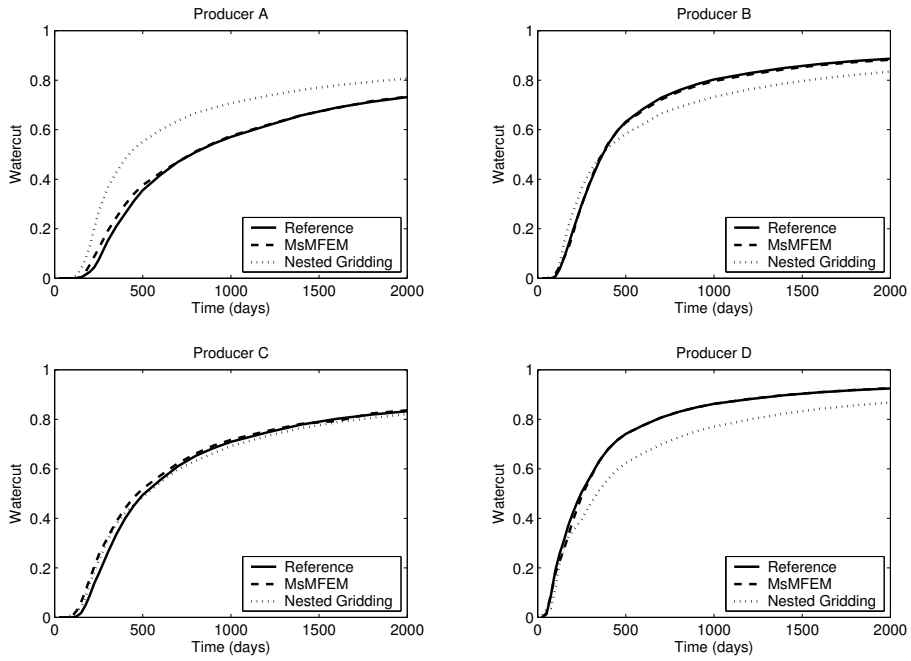

Figure 4: Water-cut curves after 2000 days of production for the SPE10 benchmark.

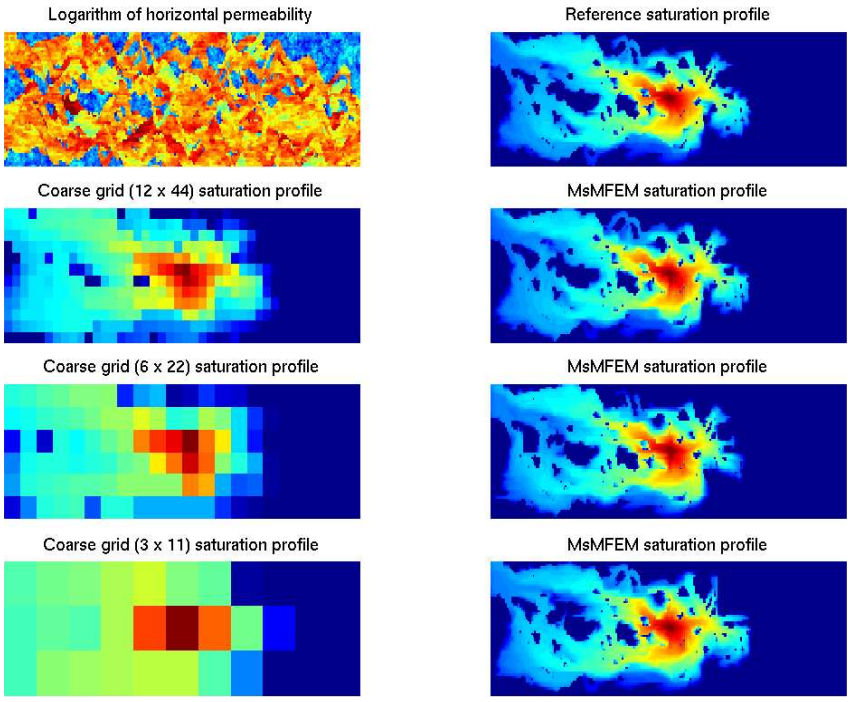

Figure 5: MsMFEM solutions for varying coarse grids on layer 85 from the SPE10 benchmark. In the left column, the coarse-grid fluxes are used to compute fluid transport, and in the right column, the subgrid fluxes are used to compute the transport on the original grid.

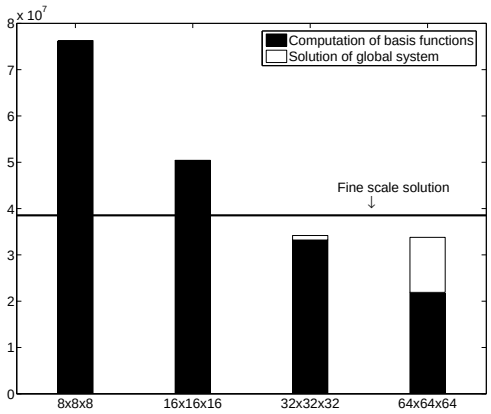

Figure 6: Computational work (idealised) for different coarse grids, assuming a Cartesian $128 \times 128 \times 128$ grid on the fine-scale.

individual wells correctly. See [3] for a more thorough discussion.
Next, we consider flow in the bottom layer computed using three different coarse grids with 12×44 cells, 6×22 cells, and 3×11 cells. Figure 5 compares saturation profiles obtained using the coarse-grid fluxes obtained by MsMFEM, and saturation profiles obtained on the fine 60×220 grid using the subgrid fluxes. The figure shows that the resolution is improved remarkably by utilising the inherent subgrid resolution rather than using MsMFEM as an advanced upscaling method. Moreover, it is evident that MsMFEM is robust with respect to the size of the coarse grid.

Computational Efficiency
Depending on the nonlinearity of the system (1)–(2), the pressure p may need to be recomputed several times throughout a simulation. In fact, the number of pressure solves in a typical flow case of water injection into a oil reservoir is of the order $\mathcal{O}(10^2)$. The key to the computational efficiency of the MsMFEM is the following observation: before the water front has swept through a coarse block T_i, the coefficient $\lambda(S)K(x)$ in (6) is constant (since S is constant), and after the waterfront has left the grid block, $\lambda(S)$ increases slowly. After the initial pressure solve, only a few basis functions ψ_{ij} close to the water front need to be recomputed [2], unless there is an abrupt change in the pressure field due to e.g., changing well configurations.
In Figure 6 we have plotted the computational cost for MsMFEM for different coarse grids compared with the cost of a direct solution on a uniform Cartesian grid with 128^3 grid blocks. The figure shows that the MsMFEM may not necessarily be more efficient than direct fine-scale solution for a single pressure solve, but it is also clear that the work associated with determining basis functions dominates the work associated with solving the global system. Hence, for a full simulation, where a minor fraction of the basis functions need to be updated in each pressure solve, the MsMFEM provides a potentially very large speedup. Moreover, since all basis function can be computed independent of each other, the MsMFEM has an inherent parallelism that can be exploited to speed up the computations.

Flexibility
A major advantage with the multiscale mixed formulation is the flexibility with respect to grids. A bit simplified this can be stated as follows: given an appropriate solver for the fine grid system, the multiscale method can be formulated and basis functions can be computed on (almost) any coarse grid where each grid block consists of an arbitrary collection of connected fine-grid cells. Moreover, numerous numerical tests show that MsMFEM is *not very sensitive* to the shape of the coarse cells and accurate results are obtained for grids containing blocks with pretty 'exotic' shapes [5]. This means that the process of generating a coarse simulation grid from a complex

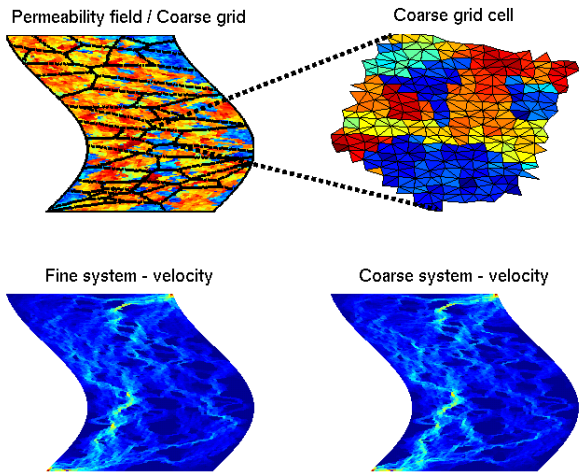

Figure 7: Comparison of flow velocity obtained direct simulation on an unstructured triangular grid and by MsMFEM on an unstructured coarse grid.

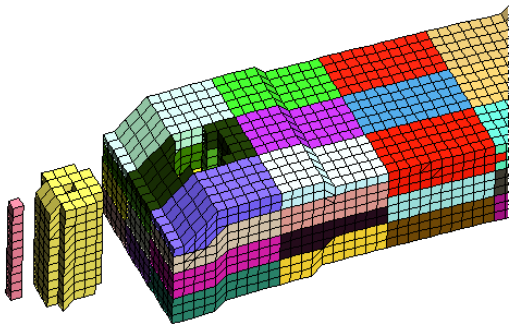

Figure 8: A coarse grid defined on top of a structured corner-point fine grid. The cells in the coarse grid are given by different colours.

geomodel can be greatly simplified, regardless of whether the fine grid is fully unstructured or is a structured corner-point grid with geometrical complications due to faults, throws, and eroded cells.

We end the paper by showing a few grid models to support the claim of the great flexibility inherent in MsMFEM. As the first example we consider an unstructured triangular fine grid in 2D. The coarse grid blocks in Figure 7 are formed as collections of fine-grid cells and can thus have almost arbitrary polygonal shape. The resulting grid contains cells that are (almost) triangular, quadrilateral, pentagonal, and hexagonal. By using unstructured triangular fine grids, it is easy to adapt both the fine grid and the coarse grid to complex external and internal boundaries.

As a next example, Figure 8 shows a vertical well penetrating a structured corner-point grid with eroded layers. On the coarse grid, the well is confined to a single cell consisting of all cells in the fine grid penetrated by the well. Moreover, notice the single neighbouring block shaped like a 'cylinder' with a hole.

Finally, Figure 9 shows a subsection of the SPE10 model, in which we have inserted a few flow barriers with very low permeability. In [5] it was shown that MsMFEM becomes inaccurate if coarse grid cells are cut into two (or more) non-communicating parts by a flow barrier. Fortunately, this can be automatically detected when generating basis functions, and the resolution can

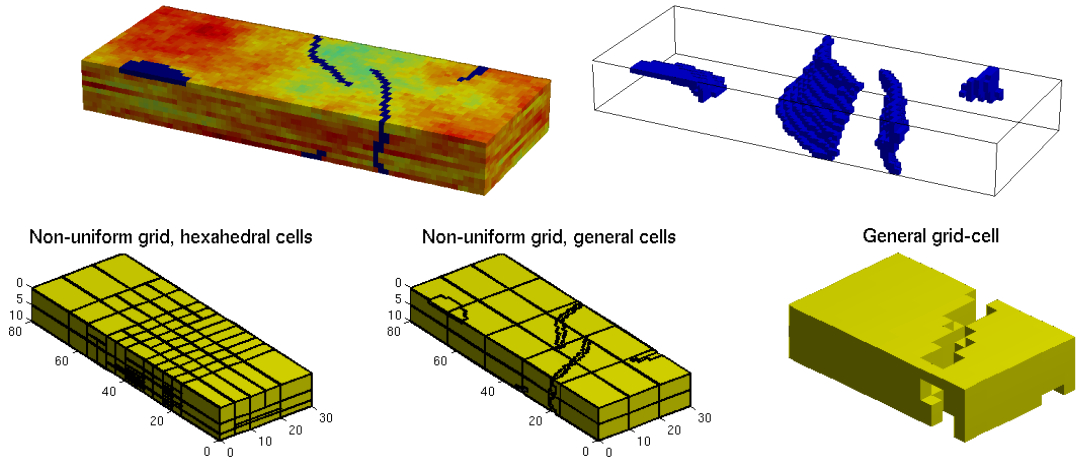

Figure 9: The upper row shows the permeability field (right), and the interior barriers (left). The lower row shows a hierarchically refined grid (left), the barrier grid (middle), and a coarse grid block in the barrier grid (right).

be improved by using some form of grid refinement. The figure shows two different approaches: (i) structured, hierarchical refinement, and (ii) direct incorporation of the flow barriers as extra coarse grid blocks intersecting a uniform $3 \times 5 \times 2$ grid. This results in rather exotic coarse cells, e.g., as shown in the figure, where the original rectangular cell consisting of $10 \times 16 \times 5$ fine cells is almost split in two by the barrier, and the resulting coarse cell is only connected through a single cell in the fine grid. Although the number of grid cells in the barrier grid is five times less than for the hierarchically refined grid, the errors in the production curves are comparable, indicating that MsMFEM is robust with respect to the shape of the coarse cells.

Concluding remarks

The research has been funded by the Research Council of Norway through contracts 158908/I30, 152732/S30, and 162606/V30.

References

[1] Reservoir Simulation on a Geological Scale, `http://www.math.sintef.no/GeoScale/`.

[2] J. E. Aarnes. On the use of a mixed multiscale finite element method for greater flexibility and increased speed or improved accuracy in reservoir simulation. *Multiscale Model. Simul.*, **2(3)**, 421–439, (2004).

[3] J. E. Aarnes, V. Kippe, and K.-A. Lie. Mixed multiscale finite elements and streamline methods for reservoir simulation of large geomodels. *Adv. Water Resources*, **28(3)**, 257–271, (2005).

[4] J. E. Aarnes, V. Kippe, and K.-A. Lie. Multiscale methods and streamline simulation for rapid reservoir performance prediction. In A. Di Bucchianico, R. M. M. Mattheij, and M. A. Peletier, editors, *Progress in Industrial Mathematics at ECMI 2004*, Mathematics in Industry. Springer Verlag (2006).

[5] J. E. Aarnes, S. Krogstad, and K.-A. Lie A hierarchical multiscale method for two-phase flow based upon mixed finite elements and nonuniform coarse grids. *Multiscale Model. Simul.*, submitted.

[6] T. Arbogast. Numerical subgrid upscaling of two-phase flow in porous media. In Z. Chen et al, editors, *Numerical Treatment of Multiphase Flows in Porous Media*, Lecture Notes in Physics, vol. 552, pages 35–49, Springer Verlag, (2000).

[7] M. A. Christie and M. J. Blunt. Tenth SPE comparative solution project: A comparison of upscaling techniques. *SPE Res. Eng. Eval.*, **4**, 308–317, (2001), `http://www.spe.org/csp/`.

[8] Y. Gautier, M. J. Blunt, and M. A. Christie. Nested gridding and streamline-based simulation for fast reservoir performance prediction. *Comp. Geosci.*, **3**, 295–320, (1999).

[9] P. Jenny, S. H. Lee, and H. A. Tchelepi. Multi-scale finite-volume method for elliptic problems in subsurface flow simulation. *J. Comp. Phys.*, **187**, 47–67, (2003).

Inverse Discontinuity Formulation of Fracture

M. Fagerström and R. Larsson*
Department of Applied Mechanics
Chalmers University of Technology, Göteborg, Sweden
e-mail: ragnar@chalmers.se

Summary The focus of this contribution is on dynamic crack propagation modelling, introducing the theoretical continuum mechanical framework and presenting two simple models for crack propagation. Also particular aspects of the numerical implementation is considered.

Introduction

In this contribution, we discuss a finite deformation FE-model for crack propagation based on the concept of *partition of unity*, originally introduced by Melenk and Babuška [1], and the developments by Wells *et al.* [2]. The main concept is to consider the total deformation map as a superposition of two fields, one continuous and one discontinuous, leading to a coupled system of equilibrium equations to be solved using a monolithic approach.

To model the fracture behaviour of the material, we distinguish between two different models. Firstly, a cohesive zone model of damage-plasticity type is formulated in the reference configuration, relating the cohesive Mandel traction to a material 'jump', which in turn is related to the direct (spatial) discontinuity[1]. Secondly, the Material Crack Driving Force (MCDF) model is formulated as a generalised Griffith criterion based on the material crack driving force, identified as a reaction force at the crack tip in the inverse discontinuity problem [4], energy conjugated with the virtual crack extension. Both models are compared and discussed with respect to structural response, efficiency, aspects of implementation etc.

Furthermore, we extend the model to account also for dynamical effects, e.g. rapid transient loading which is of great importance in many manufacturing applications and impact loading situations. The intention is to build a theoretical and numerical foundation for further analyses of important dynamic phenomena such as crack arrest, crack branching and rate dependent cohesive behaviour among others. The introduction of inertia effects also rises interesting questions regarding the numerical treatment in terms of efficient and stable time integration algorithms.

Kinematics

As a basis for the kinematical description, we consider the direct deformation map which maps points in the material reference configuration, $\boldsymbol{X} \in B_0$, onto points in the deformed spatial configuration, $\boldsymbol{x} \in B$ as

$$\boldsymbol{\varphi}\left[\boldsymbol{X},t\right] = \boldsymbol{\varphi}_c\left[\boldsymbol{X},t\right] + H_S\left[S\left[\boldsymbol{X}\right]\right]\boldsymbol{d}\left[\boldsymbol{X},t\right] \text{ with } \boldsymbol{d} = \boldsymbol{x} - \boldsymbol{x}_c \tag{1}$$

[1] The formulation in terms of the Mandel traction and the material jump is made to ensure material frame indifference of the model, cf. [3]

where $H_S\left[S\left[\boldsymbol{X}\right]\right]$ is the Heaviside function centered at the internal (closed) discontinuity boundary, Γ_S, shown in Fig. 1. The argument $S\left[\boldsymbol{X}\right]$ is defined as

$$S\left[\boldsymbol{X}\right]<0\ \boldsymbol{X}\in D_0^-, S\left[\boldsymbol{X}\right]=0\ \boldsymbol{X}\in\Gamma_S, S\left[\boldsymbol{X}\right]>0\ \boldsymbol{X}\in D_0^+ \text{with } \boldsymbol{N}=\frac{\partial S\left[\boldsymbol{X}\right]}{\partial \boldsymbol{X}}\ \boldsymbol{X}\in\Gamma_S, \|\boldsymbol{N}\|=1 \quad (2)$$

where $\boldsymbol{N}$ is the normal vector to Γ_S pointing into the region D_0^+. Note that the discontinuous part, $\boldsymbol{d}$, is defined on a subregion D_0 of B_0 (grey area) with assumed Dirichlet boundary conditions along the boundary $\partial D_0^+ \backslash \Gamma_S$.

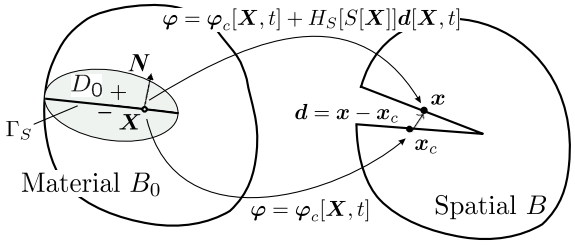

Figure 1: Kinematical representation of the discontinuous direct motion problem.

The pertinent deformation gradient becomes

$$\boldsymbol{F}=\boldsymbol{\varphi}\otimes\boldsymbol{\nabla}_X=\boldsymbol{F}_c+H_S\boldsymbol{F}_d+\delta_S\,\boldsymbol{d}\otimes\boldsymbol{N} \text{ with } \boldsymbol{F}_c=\boldsymbol{\varphi}_c\otimes\boldsymbol{\nabla}_X \text{ and } \boldsymbol{F}_d=\boldsymbol{d}\otimes\boldsymbol{\nabla}_X \quad (3)$$

where $\delta_S[S[\boldsymbol{X}]]$ is the Dirac delta function.

Governing equations and solution strategy

To arrive at the coupled equilibrium equations, we first consider the strong form of the equation of motion

$$\rho_0\ddot{\boldsymbol{u}}-\boldsymbol{\Sigma}_1^t\cdot\boldsymbol{\nabla}_X=\boldsymbol{b}^{\text{mec}} \quad (4)$$

with $\boldsymbol{\Sigma}_1^t$ being the first Piola-Kirchhoff stress tensor and $\boldsymbol{b}^{\text{mec}}$ the (applied) mechanics body forces and where the acceleration $\ddot{\boldsymbol{u}}$ can be subdivided (due to the present kinematical representation) as

$$\ddot{\boldsymbol{u}}=\ddot{\boldsymbol{\varphi}}_c+H_S\ddot{\boldsymbol{d}} \quad (5)$$

From Eq. 4, the standard (continuous) form of the principle of virtual work can easily be established, which in turn may be reformulated to the final coupled continuous/discontinuous form by insertion of the discontinuous kinematical representation in Eqs. 1 and 3:

$$(C):\int_{V_0}\boldsymbol{\Sigma}_1^t:\Delta\boldsymbol{F}_c\,dV=\int_{\Gamma_0}\Delta\boldsymbol{\varphi}_c\cdot\boldsymbol{t}_1 d\Gamma+\int_{V_0}\Delta\boldsymbol{\varphi}_c\cdot\boldsymbol{b}^{\text{mec}}dV-\int_{B_0}\rho_0\Delta\boldsymbol{\varphi}_c\cdot\ddot{\boldsymbol{u}}\,dV \quad (6)$$

$$(D):\int_{D_0}H_S\boldsymbol{\Sigma}_1^t:\Delta\boldsymbol{F}_d\,dV+\int_{\Gamma_S}\Delta\boldsymbol{d}\cdot\boldsymbol{t}_1 d\Gamma=\int_{D_0}H_S\Delta\boldsymbol{d}\cdot\boldsymbol{b}^{\text{mec}}dV-\int_{D_0}H_S\rho_0\Delta\boldsymbol{d}\cdot\ddot{\boldsymbol{u}}\,dV \quad (7)$$

Fracture modelling

We will present and compare two different models, a cohesive zone model and the Material Crack Driving Force model.

Cohesive zone model
To model the stress degradation along the internal interface Γ_S, we formulate a cohesive damage-plasticity model based on previous works [4,5], thus the nominal traction vector is defined in terms of an effective nominal traction $\hat{\boldsymbol{t}}_1$ and a damage variable $0 \leq \alpha \leq 1$ as $\boldsymbol{t}_1 = (1-\alpha)\hat{\boldsymbol{t}}_1$. Furthermore, this effective nominal traction is related to the effective Mandel traction $\hat{\boldsymbol{Q}}$ via $\hat{\boldsymbol{t}}_1 = \boldsymbol{F}_c^{-t} \cdot \hat{\boldsymbol{Q}}$. Finally, $\hat{\boldsymbol{Q}}$ is expressed in terms of a material jump $\boldsymbol{J} = \boldsymbol{F}_c^{-1} \cdot \boldsymbol{d}$ as $\hat{\boldsymbol{Q}} = \boldsymbol{K} \cdot (\boldsymbol{J} - \boldsymbol{J}^p) = \boldsymbol{K} \cdot \boldsymbol{J}^e$ where $\boldsymbol{K}$ is a stiffness parameter for the interface and where $\boldsymbol{J}^p$ and $\boldsymbol{J}^e$ are the plastic and elastic part of the material jump respectively. The evolution laws for $\boldsymbol{J}^p$ an α are then defined such that the resulting relation between $\boldsymbol{t}_1$ and $\boldsymbol{d}$ is according to Fig. 2.

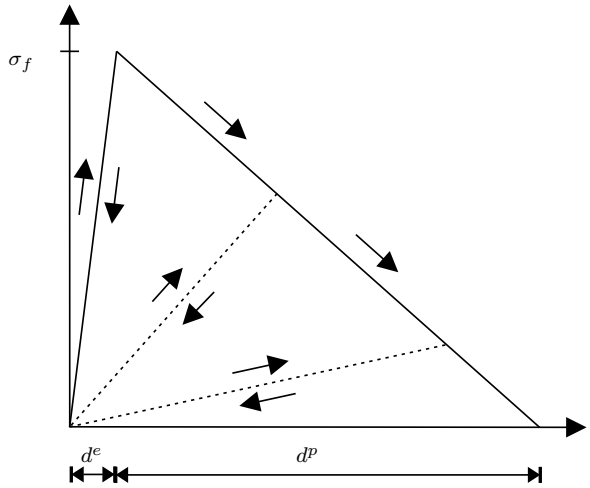

Figure 2: Relation between nominal interface traction and discontinuity.

Material Crack Driving Force model (MCDF)
The second model proposed is based on the MCDF, $\boldsymbol{P}$, identified in the inverse discontinuity problem [4] as a reaction force at the crack tip, energy conjugated with the virtual crack extension. Interesting properties of this force is that the magnitude corresponds to the value of the *J*-integral and that the force is aligned in the direction of maximum energy release. Hence, a fracture criterion may be formulated such that the crack is propagated in the direction of the force when the magnitude exceeds a critical value. The drawback of this model is the large mesh sensitivity. However there are techniques to decrease this dependence, e.g. domain integral methods or equivalent.

Numerical example
To illustrate the capabilities of the proposed model, we study a simple numerical example in terms of a DCB-test with a pre-defined fracture interface (modelled through the finite elements), shown in Fig. 3a, loaded with an increasing loading rate: quasi static (no dynamic effects), $\dot{r} = 5$, 10 and 15 m/s. The coupled continuous/discontinuous problem is discretised using standard finite element approximations for the two fields and solved with an implicit Newmark-β time integration scheme. Moreover, the continuous material response is considered Neo-Hookean with $E = 3.24$ GPa and $\nu = 0.35$ and the fracture process is governed by the proposed cohesive zone model with mode *I* fracture energy $G_f^I = 100$ N/m and failure stress $\sigma_f = 20$ MPa. In Fig. 3b, the damage

distribution along the internal interface at the final load step, corresponding to $r = 0.04$ mm, is presented for the different loading rates.

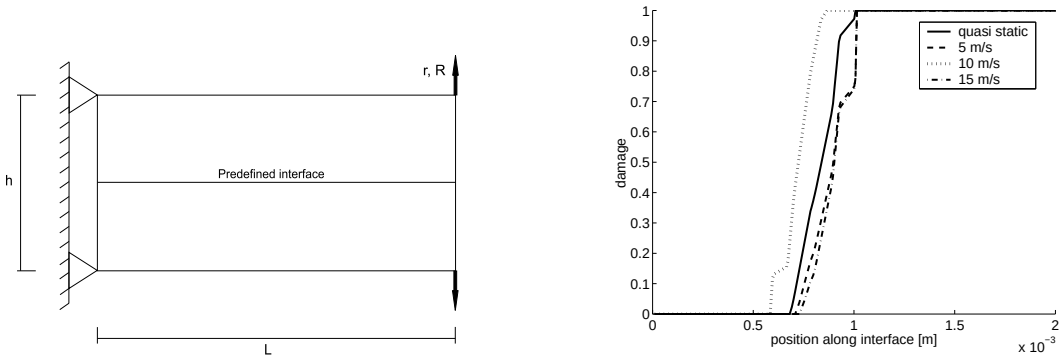

$a)$ $b)$

Figure 3: a) Modelled DCB with h=1mm, L=2mm and a thickness of 1mm. b) Damage distribution along Γ_S for different loading rates

References

[1] J.M. Melenk and I. Babuška. The partition of unity finite element method: Basic theory and applications. *Comp. Meth. Appl. Mech. Engng.*, **139**:289–314, 1996.

[2] G.N. Wells, R. de Borst, and L.J. Sluys. A consistent geometrically non-linear approach for delamination. *Int. J. Num. Meth. Engng.*, **54**:1333–1355, 2002.

[3] M. Fagerström and R. Larsson. Theory and numerics for finite deformation fracture modelling using strong discontinuities. *Int. J. Num. Meth. Engng. Accepted 2005*

[4] R. Larsson and M. Fagerström. A framework for fracture modelling based on the material forces concept with XFEM kinematics. *Int. J. Num. Meth. Engng.*, **62**:1763–1788, 2005.

[5] R. Larsson and N. Jansson. Geometrically non-linear damage interface based on regularized strong discontinuity. *Int. J. Num. Meth. Engng.*, **54**:473–497, 2002.

Lessons in wave theory from the Indian Ocean Tsunami of Millennium and from the Baltic Sea Storm Surge of Century

Tarmo Soomere
Centre for Non-linear Studies, Institute of Cybernetics
Tallinn University of Technology, Akadeemia tee 21, 12618 Tallinn,
e-mail: soomere@cs.ioc.ee

We look at the catastrophic tsunami, at the frightening storm surge and at extreme wind wave conditions from simple linear and weakly nonlinear viewpoints. All the phenomena reflect the possibility of wave propagation on the water surface. Tsunami and storm surge are visually very similar to each other on the open sea, but the properties of their transformation in shallow areas and near coastline differ radically. Although the linear theory in many cases fails to correctly represent quantitative properties of these phenomena, it still allows systematic description of their most important features on the level of elementary mathematics.

The extreme devastation caused by the Indian Ocean Tsunami is mostly caused by a rare character of the underlying earthquake. In particular, specific geometric features of the rupture and the resulting wave pattern well explain why this tsunami was particularly hazardous in Sri Lanka and India, and why it remained compact until the African coast.

Storm surges in many cases can also be considered as simple (linear) superposition of different factors. The extreme storm surge in Estonia and Finland during windstorm Erwin/Gudrun (January 2005) can be mostly explained by an (un)fortunate coincidence of relatively uncommon factors.

Finally, we shortly discuss exceptional wave conditions in the northern Baltic Proper during this windstorm. The measured wave heights were relatively modest—maximum significant wave height 7.2 m—only because the most rough seas occurred remote from the wave sensors. Wave models indicate that the largest waves occurred off the coasts of Saaremaa and Latvia where the significant wave height probably exceeded 10 m. Exceptionally long waves with peak periods up to 12 s also occurred in the central part of the Gulf of Finland owing to a specific combination of forcing factors and the geometry of the Baltic Sea.

Inelastic conical shells with cracks

Jaan Lellep* and Ella Puman
Institute of Applied Mathematics,
University of Tartu, Estonia
e-mail: jaan.lellep@ut.ee; ella.puman@ut.ee

Summary Conical shells of piece wise constant thickness made of a metallic material are considered. The shell wall is welded to a rigid central boss whereas the connection between the shell and the boss is weakened with a stable crack. The designs with the maximal load carrying capacity are established under given material consumption of the shell. Material of the shell wall obeys von Mises yield condition.

Introduction

Thin walled circular conical shells under external pressure are of interest in ocean engineering. Also, circular conical shells welded to a cylindrical upper section are used as superstructures for elevated water tanks. The steel vessel is expected to with stand to the pressure of water. This involves the necessity of limit design.

Limit analysis and design of circular conical shells subjected to the lateral distributed loading and shells loaded by a rigid central boss have been studied by several authors. Various solutions developed under different assumptions regarding to loading conditions and yield surface can be found in monograph books by Hodge [4], Chakrabarty [2] and others.

In the previous paper by authors (Lellep and Puman [6]) problems of optimization of conical shells made of an ideal plastic Tresca material were considered. In the present paper conical shells with part through cracks are studied in the case of Mises material.

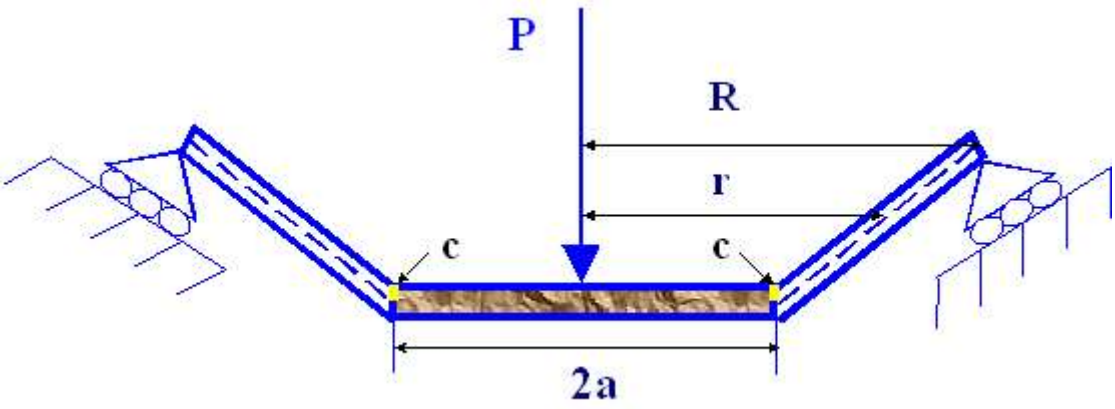

Figure 1: Conical shell with crack loaded by the central boss

Formulation of the problem

Let us consider a conical shell with the rigid central boss of radius a. The shell is simply supported at the outer edge of radius R and clamped at the inner edge (Fig. 1). The shell is loaded through the rigid boss at its vertex by the load P.

It is assumed that the thickness of the shell is piece wise constant, e.g.

$$h = h_j \tag{1}$$

for $r \in (a_j, a_{j+1})$ where $j = 0, \ldots, n$.

It is stated that $a_0 = a$, $a_{n+1} = R$. The number n is assumed to be fixed. However, the parameters a_i $(i = 1,...,n)$ and h_j $(j = 0,...,n)$ are unknown constants which will be defined so that the cost function will attain its minimal value.

Although we consider the internal edge of the shell as a clamped edge the bond between the shell and the boss is not an ideal one. We assume that at $r = a$ a stable crack of constant depth c is located. The circular crack of radius a emanating from the lower part of the connection between the shell and the boss, respectively, is to be classified as a part-through surface crack. Similar cracks of depth c_j are located at $r = a_j$ $(j = 0,...,n)$ as well.

As the perfomance index will be either the limit load or the weight (or, material volume) of the shell. The material volume of the shell corresponding to the thickness distribution (1) is

$$V = \frac{\pi}{\cos\varphi} \sum_{j=0}^{n} h_j \left(a_{j+1}^2 - a_j^2\right) \tag{2}$$

Here φ stands for the angle of inclination of a generator of the shell.

The material of the shell is assumed to be an ideal plastic one. When minimizing the cost function (2) it is expected that the load carrying capacity of the shell is fixed. Alternatively, when maximizing the load carrying capacity the amount of the material, or volume of the material is assumed to be bounded. Material of the shell obeys von Mises yield condition.

Basic equations

The stress components to be incorporated in the study are the membrane forces N_1, N_2 and bending moments M_1, M_2. Corresponding deformation components are ε_1, ε_2 and κ_1, κ_2.

We assume that the metallic material of shells can be modelled as an ideal rigid-plastic material obeying von Mises yield criterion and associated flow law. On the plane of principal stresses σ_1 , σ_2 the ellipse of Mises circumscribes the hexagon of Tresca. Here σ_0 stands for the yield stress of the material. Parametrical equations of the exact yield surface in the space of generalized stresses were derived by A. Iljushin. Due to its complexity the exact yield surface is unsuitable for practical calculations in particular cases.

It was shown by several authors (Robinson [7], Haydl and Sherbourne [3]) that a non-linear approximation of the exact yield surface

$$\frac{1}{N_j^2}\left(N_1^2 - N_1 N_2 + N_2^2\right) + \frac{1}{M_j^2}\left(M_1^2 - M_1 M_2 + M_2^2\right) - 1 = 0 \tag{3}$$

leads to reasonable assessments of the limit load in the lower bound analysis. The approximation (6) will be used in the present study, as well. In (6) M_j and N_j stand for plastic limit moment and limit force for a section with thickness h_j , respectively.

It will be convenient to carry out the optimization procedure in terms of dimensionless quantities defined by

$$\rho = \frac{r}{R}, \quad \alpha_j = \frac{a_j}{R}, \quad \gamma_j = \frac{h_j}{h_*}, \quad w = \frac{W}{R}, \quad u = \frac{U}{R},$$

$$n_{1,2} = \frac{N_{1,2}}{N_*}, \quad m_{1,2} = \frac{M_{1,2}}{M_*}, \quad k = \frac{M_*}{RN_*}\frac{cos^2\varphi}{sin^2\varphi}, \tag{4}$$

$$q = \frac{P}{2\pi RN_* \sin\varphi} - \frac{M_*}{RN_*}\frac{cos^2\varphi}{sin^2\varphi}, \quad v = \frac{V\cos\varphi}{\pi h_* R^2}$$

Here M_* and N_* stand for the yield moment and yield force associated with the reference shell with thickness h_*.

Making use of notations (4) one can present equilibrium equations as

$$\begin{aligned} &(\rho\, n_1)' - n_2 = 0, \\ &k\left[(\rho\, m_1)' - m_2 + 1\right] - \rho\, n_1 + q = 0 \end{aligned} \tag{5}$$

From (3) one can determine making use of (4)

$$m_2 = \frac{m_1}{2} \pm \sqrt{\gamma_j^2 - \frac{3}{4}m_1^2 - n_1^2 - n_2^2 + n_1 n_2} \tag{6}$$

Substituting (6) in (5) yields the set of equations

$$\begin{aligned} &n_1' = -\frac{n_1}{\rho} + \frac{n_2}{\rho}, \\ &m_1' = -\frac{m_1}{2\rho} + \frac{n_1}{k} \pm \frac{1}{\rho}\sqrt{\gamma_j^2 - \frac{3}{4}m_1^2 - n_1^2 - n_2^2 + n_1 n_2} - \frac{1}{\rho}\left(1 + \frac{q}{k}\right), \\ &q' = 0 \end{aligned} \tag{7}$$

The last equation in (7) is a natural consequence of the matter that $q = const.$. Here and henceforth primes denote the differentiation with respect to the dimensionless variable ρ .

The methods of the mathematical theory of optimal control will be used whereas n_1, m_1 and q will be considered as state variables and n_2, m_2 as control variables. The quantities γ_j and α_j are treated as concentrated parameters. Foundations on the control theory can be found in books by Bryson and Ho [1], Hocking [5].

The system of equations (7) is solved numerically. The distribution of bending moments is depicted in Fig. 2.

Concluding remarks

Calculations have been carried out for shells with one or two steps in the thickness. Numerical results revealed the ability of the optimized shell to with stand loads which are much higher in comparison to that of shells of constant thickness. The efficiency of the design depends on the parameter k and the ratio of the internal and external radius, respectively. For instance, if $k = 0,3$ and $\alpha = 0,55$ the redistribution of the material in the framework of designs with a single step gives up to 5% higher limit load. For greater values of the α the efficiency of the design is higher (up to 20% if $\alpha = 0,95$ and $\gamma_0 = 1,2$).

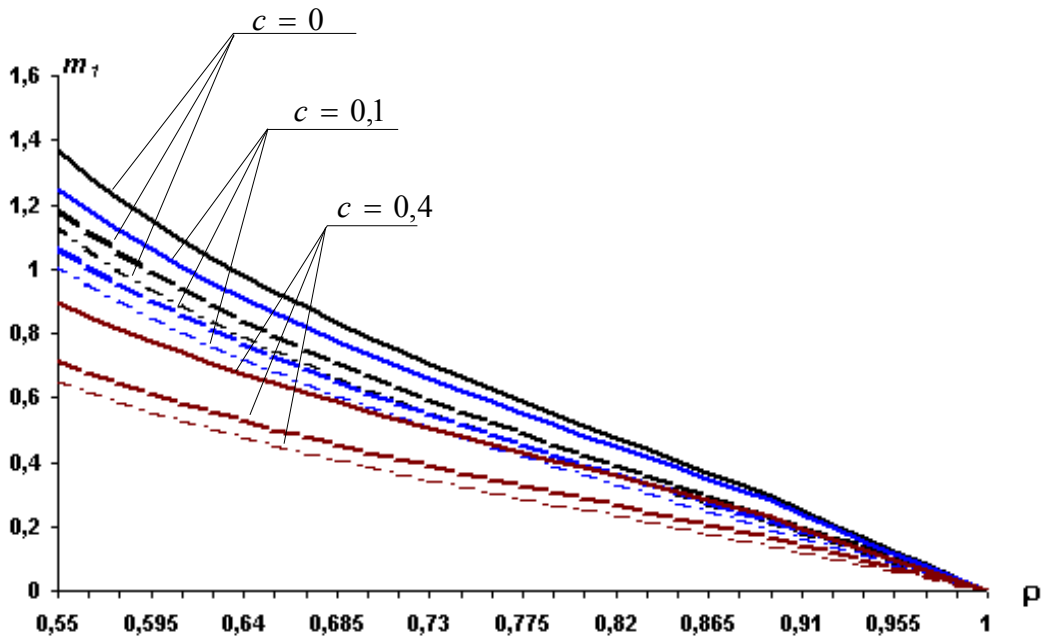

Figure 2: Bending moment distribution for $k = 0,3$ and $\alpha_0 = 0,55$.

Acknowledgements

The support of Estonian Science Foundation through the Grant No 5693 is gratefully acknowledged.

References

[1] A. Bryson and Yu-Chi Ho. *Applied Optimal Control*. New York, Wiley, (1975).

[2] J. Chakrabarty. *Applied Plasticity*. Berlin, New York, Springer, (2000).

[3] H.M. Haydl and A.N. Sherbourne. Some approximations to the Ilyushin yield surface for circular plates and cylindrical shells. ZAMM, **59**, 131-132, (1979).

[4] P.G. Hodge. Limit Analysis of Rotationally Symmetric Plates and Shells. Englewood Cliffs, Prentice Hall, (1963).

[5] L.M. Hocking. Optimal Control. An Introduction to the Theory with Applications. Oxford, Clarendon Press, (2001).

[6] J. Lellep and E. Puman. Optimization of plastic conical shells loaded by a rigid central boss. *Int. J. Solids Struct.,* **37**, 2695-2708, (2000).

[7] M. Robinson. An evaluation of errors in the yield surface for a rotationally symmetric thin shell due to neglecting transverse normal stresses and shell curvature. *Int. J. Mech. Sci*., **42** (6), 1087-1095, (2000).

Simulation of quasi–static crack growth by using the ϑ method

Giovanni Formica
Department of Structural Engineering
University of Roma 3, Roma, Italy
e–mail: formica@unical.it

Stefania Fortino
Laboratory of Structural Mechanics
Helsinki University of Technology, Espoo, Finland
e–mail: stefania.fortino@tkk.fi

Mikko Lyly*
CSC - Scientific Computing Ltd.,
Espoo, Finland
e–mail: mikko.lyly@csc.fi

Summary This work presents an algorithm for the automatic simulation of quasi–static crack growth in linear elastic bodies with existing cracks. The algorithm, based on the so-called ϑ method, provides the load vs. crack extension curves in the case of stable rectilinear crack propagation. Some results for 2D problems of linear elastic fracture (LEFM) are reported.

Introduction

The evaluation of crack growth in brittle and quasibrittle bodies with existing cracks is a fundamental topic when the structural reliability related to a certain crack length has to be studied. In particular, the crack length extension under a certain load increment is an important variable to be analyzed during a given loading process [1]. In this context, the Griffith energy release rate still represent a strong theoretical tool for establishing the onset of crack growth in LEFM. Furthermore, several criteria for determining the direction of crack propagation under various mode loading can be found in the fracture mechanics literature ([2]). Instead, as already observed in [3], a general theoretical model for calculating the increments of crack growth during a loading process does not exist yet. This limit still characterizes the computer codes for simulation of crack propagation in linear elastic fracture (see references in [3]). In the present work we propose a new approach for quasi–static crack growth simulation based on the so–called ϑ method originally introduced by Destuynder and Djaoua in [4].

The basic idea of the ϑ method is to transform the variables of the current configuration in a one-to-one manner to the variables of the perturbed equilibrium problem. All physical quantities of the perturbed configuration are then rewritten in the current. The method introduces an energetic domain parameter known in literature as the $G\theta$ and characterized by a smooth value vector function ϑ defined along a known direction of crack growth in a subdomain of the current configuration (see [4]).

In the present paper, successive $G\vartheta$–based crack growth problems written in the current configuration furnish the increments of crack growth relative to given load increments. Furthermore, at each load step the equilibrium is imposed in the current configuration with updated crack length. For sake of simplicity, the method is defined for cases of stable rectilinear crack growth but it can be extended to curvilinear crack propagation in nonlinear materials. The proposed algorithm is implemented by using the computational tools of the computer code ELMER (CSC - Scientific Computing LTD., Espoo, Finland). Remeshing and a standard FEM discretization are employed. Some results for rectilinear crack growth in case of plane strain are presented.

The ϑ method

In this section we briefly recall the ϑ method by analyzing the rectilinear crack growth of a two–dimensional elastic cracked body of unit thickness subjected to a load process (see Figure 1). The Destuynder ϑ method introduces a linear perturbation from the current configuration Ω to the updated domain $\Omega_{\delta a}$:

$$\mathbf{F}_{\delta a}\mathbf{x} = \mathbf{x} + \delta a\, \boldsymbol{\vartheta}(\mathbf{x})\,, \quad \forall \mathbf{x} \in \Omega \tag{1}$$

where $\boldsymbol{\vartheta}$ represents a smooth vector valued function defined in Ω such that $|\boldsymbol{\vartheta}| = 1$ at the crack tip and $\boldsymbol{\vartheta} = 0$ on $\partial\Omega \backslash S_f$.

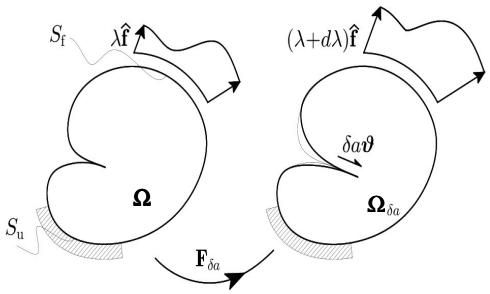

Figure 1: Current (Ω) and perturbed ($\Omega_{\delta a}$) cracked domains; $S_{\rm f}$ = boundary with applied forces; $S_{\rm u}$ = boundary with applied displacements; λ=control parameter; $\hat{\mathbf{f}}$= fixed load; $\delta\lambda\,\hat{\mathbf{f}}$= load increment; $\delta a > 0$ = crack length increment; $\boldsymbol{\vartheta}$ = vector field. Homogeneous material; no traction along the surface of the crack; body forces neglected.

The transformation $\mathbf{F}_{\delta a}$ permits to rewrite each function of the updated domain as an associated function of the current configuration (see details in [4]). By approximating the determinant of the Jacobian of $\mathbf{F}_{\delta a}$ and the inverse of the Jacobian as

$$|\,\mathbf{J}_{\delta a}\,| \approx 1 + \delta a\,(div\boldsymbol{\vartheta}), \quad (\mathbf{J}_{\delta a})^{-T} \approx 1 - \delta a\,(\nabla\boldsymbol{\vartheta})^T \tag{2}$$

the associated solution in the configuration Ω, written in terms of displacements and stresses, is:

$$\mathbf{u}_{\delta a} = \mathbf{u}_0 + \delta\mathbf{u} + R_u, \quad \boldsymbol{\sigma}_{\delta a} = \boldsymbol{\sigma}_0 + \delta\boldsymbol{\sigma} + R_\sigma \tag{3}$$

where $(\mathbf{u}_0, \boldsymbol{\sigma}_0)$ represents the elastic solution of the equilibrium problem in the current configuration and $\delta a^{-1}(||R_{\mathbf{u}}||_{\mathcal{V}} + ||R_{\boldsymbol{\sigma}}||_\Sigma) \to 0$ as $\delta a \to 0$. Furthermore the increments $(\delta\mathbf{u}, \delta\boldsymbol{\sigma})$ are the unique solution in $\mathcal{V} \times \Sigma$ of the following problem (see proof in [4] for the case of null load increments):

$$\left\{ \begin{array}{ll} \int_\Omega \delta\boldsymbol{\sigma} :: \nabla\mathbf{v} - \delta a \int_\Omega \mathbf{s}_0 :: \nabla\mathbf{v} = \delta\lambda \int_{S_f} \hat{f}\cdot\mathbf{v} & \forall \mathbf{v} \in V \\ \int_\Omega \mathbf{C}\,\delta\boldsymbol{\sigma} : \boldsymbol{\tau} - \int_\Omega \boldsymbol{\tau} :: \nabla\delta\mathbf{u} - \delta a \int_\Omega \mathbf{r}_0 : \boldsymbol{\tau} = 0 & \forall \boldsymbol{\tau} \in \Sigma \end{array} \right. \tag{4}$$

where the spaces $\mathcal{V}$ and Σ are, respectively, $\mathcal{V} = \{\mathbf{v} \in (H^1(\Omega))^2,\ \mathbf{v} = 0 \ \text{ on } \ S_u\}$ and $\Sigma = \{\boldsymbol{\tau} \in (L^2(\Omega))^4,\ \boldsymbol{\tau}^T = \boldsymbol{\tau}\}$ while $\mathbf{s}_0 = \boldsymbol{\sigma}_0\nabla\boldsymbol{\vartheta}^T - (div\boldsymbol{\vartheta})\boldsymbol{\sigma}_0$ and $\mathbf{r}_0 = -\frac{1}{2}(\nabla\mathbf{u}_0\nabla\boldsymbol{\vartheta} + (\nabla\mathbf{u}_0\nabla\boldsymbol{\vartheta})^T)$. As a direct result, the method introduces the so called $G\vartheta$ parameter:

$$G\vartheta = \frac{1}{2}\int_\Omega \mathbf{s}_0 :: \nabla\mathbf{u}_0 - \frac{1}{2}\int_\Omega \mathbf{r}_0 : \boldsymbol{\sigma}_0 \tag{5}$$

This parameter has the same meaning as the Griffith energy release rate in LEFM and coincides with the Rice J integral for all subdomains $\Omega_\vartheta \in \Omega$ (see [4]). Then, the choice of $\boldsymbol{\vartheta}$ has the same meaning as that of the path along which the J integral function is integrated.

A $G\vartheta$-based crack growth formulation

From a theoretical point of view, the new idea of this work is to use domain transformation (1) for solving a problem of crack growth during a load process. At this aim, the $G\vartheta(\mathbf{u}, \boldsymbol{\sigma})$ of the perturbed configuration $\Omega_{\delta a}$, taking into account (3), after some manipulations can be written in the current configuration Ω as

$$G\vartheta(\mathbf{u}_0 + \delta\mathbf{u}, \boldsymbol{\sigma}_0 + \delta\boldsymbol{\sigma}) \approx G\vartheta(\mathbf{u}_0, \boldsymbol{\sigma}_0) + \delta G\vartheta \tag{6}$$

where $\delta G\vartheta = \int_\Omega \mathbf{s}_0 : \nabla\delta\mathbf{u} - \int_\Omega \mathbf{r}_0 : \delta\boldsymbol{\sigma}$.
In the case of flat resistance curves and stable quasi–static crack growth, the following conditions must be locally satisfied for each load increment (see [2]):

$$G\vartheta = G_f, \quad \delta G\vartheta = 0 \tag{7}$$

where G_f represents the fracture energy. For sake of simplicity, the unknowns of the incremental problem and of condition $\delta G\vartheta = 0$ are reduced to $(\delta\mathbf{u}, \delta a)$. Then, we have $\delta\boldsymbol{\sigma} = \mathbf{E}[\boldsymbol{\varepsilon}(\delta\mathbf{u}) + \delta a\, \mathbf{r}_0]$ where $\mathbf{E}$ is the elasticity tensor and $\boldsymbol{\varepsilon}$ the strain tensor. Finally, the following system is obtained:

$$\begin{cases} \int_\Omega \mathbf{E}\,\boldsymbol{\varepsilon}(\delta\mathbf{u}) \,:\, \boldsymbol{\varepsilon}(\mathbf{v}) - \delta a \int_\Omega \mathbf{t}_0 : \nabla\mathbf{v} = \delta\lambda \int_{S_f} \hat{\mathbf{f}} \cdot \mathbf{v} \\ - \int_\Omega \mathbf{t}_0 : \nabla\delta\mathbf{u} + \delta a \int_\Omega \mathbf{E}\mathbf{r}_0 : \mathbf{r}_0 = 0 \end{cases} \quad \forall \mathbf{v} \in V; \;\; \delta a > 0 \tag{8}$$

where $\mathbf{t}_0 = \mathbf{s}_0 - \mathbf{E}\mathbf{r}_0$. The system provides the crack length increment δa. In operator form we have:

$$\begin{bmatrix} \mathbf{A} & \mathbf{B}^T \\ \mathbf{B} & C \end{bmatrix} \begin{bmatrix} \delta\mathbf{u} \\ \delta a \end{bmatrix} = d\lambda \begin{bmatrix} \mathbf{F} \\ \mathbf{0} \end{bmatrix} \tag{9}$$

Starting from a state defined by the index $i = 0$, the proposed algorithm for crack growth is characterized by successive analyses consisting of the following steps:

1. Linear elastic analysis for the cracked body of domain Ω_i subjected to the load factor λ_i. In operator form we have:
$$\mathbf{A}_i\mathbf{u}_i = \lambda_i\mathbf{F} \tag{10}$$

2. Evaluation of the crack increment in the updated configuration $\Omega_{\delta a_i}$ trough the equation obtained by solving system (9):
$$\delta a_i = \frac{1}{\mathbf{B}_i^T\mathbf{A}_i^{-1}\mathbf{B}_i - C_i} \frac{d\lambda_i}{\lambda_i} \mathbf{B}_i^T\mathbf{u}_i \tag{11}$$

3. Updating of the new current configuration Ω_{i+1} and remeshing.

4. Updating of the load factor:
$$\lambda_{i+1} := \lambda_i + d\lambda_i \tag{12}$$

Results and concluding remarks

The presented approach is implemented by using the computational tools of the FEM computer code ELMER (CSC - Scientific Computing Ltd., Espoo, Finland). During crack propagation, remeshing is performed. In this section the rectilinear crack propagation in a rectangular cracked plate in plane strain is analyzed (see Figure 2 for the details). The proposed algorithm provides the curve load vs. crack length during crack growth.
In order to directly extend the method to curvilinear crack growth, the simplest way is to represent the curvilinear path by means of a linear piecewise curve. Then, the described algorithm can be

used for determining the crack growth increments along each line of the curve after calculating the direction of crack extension by using one of the methods existing in literature (see [2]). A more rigorous approach should take into account the real shape of the path and define the direction of crack growth like a variable of the problem. A theoretical formulation for differentiating energy functionals with respect to the crack length in case of curvilinear cracks was presented in [5]. Anyway, also in that work the shape of the path had to be known before calculating the derivative of the functionals.
The approach presented in this paper is also very suitable to be extended to elastic–plastic materials as suggested in [6].

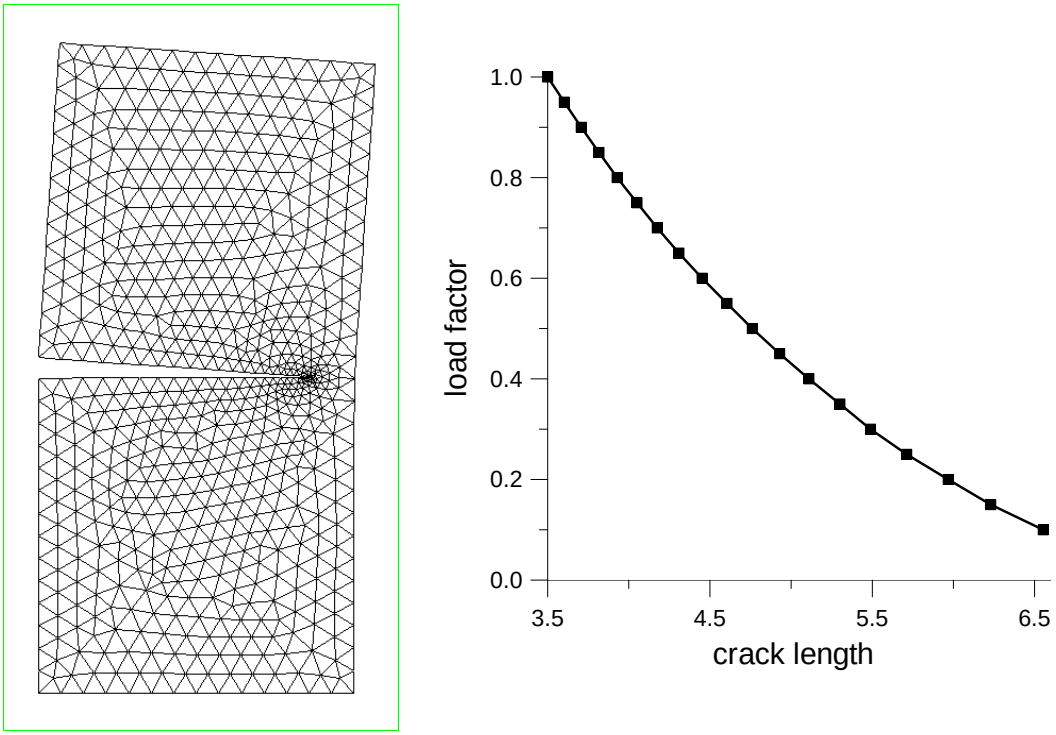

Figure 2: Edge cracked plate clamped on the bottom and loaded by a uniform traction on the top: dimensions = 7×14; E= 30×10^6; ν=0.25; initial traction= 1.0; initial crack length=3.5; final crack length= 6.5. SI units. Plane strain state. Quadratic triangular FE. Displacements and final mesh (left). Curve load vs. crack length (right).

References

[1] Xi Y, Bažant ZP. Random growth of crack with R-curve: Markov process model. Eng. Frac. Mech. 1997;57:593–608.

[2] Bažant ZP, Planas J. Fracture and size effect in Concrete and Other Quasibrittle Materials. CRC Press, 1998.

[3] Fortino S, Bilotta A. Evaluation of the amount of crack growth in 2D LEFM problem. Eng. Frac. Mech., 71, 2004: 1403–1419.

[4] Destuynder P, Djaoua M. Sur une interprétation mathématique de l'intégrale de Rice en Théorie de la Rupture Fragile. Math. Meth. in the Appl. Sci., 3, 1981: 70–87.

[5] Rudoy EM. Differentiation of energy functionals in two-dimensional elasticity theory for solids with curvilinear cracks. Journal of Appl. Mech. and Tech. Phys., 45 (6), 2004: 843–852.

[6] Fortino S, Formica G, Lyly M. A Gϑ-based method for simulating crack growth in ductile materials. Proceedings of the VIII International Conference on Computational Plasticity Fundamentals and Applications (ECCOMAS), Barcelona, Spain, September 5-8, 2005.

Explicit FE-procedure for Numerical Modeling of Rock Fracture under Dynamic Indentation

Timo Saksala
Institute of Applied Mechanics and Optimization
Tampere University of Technology, Tampere, Finland
e-mail: timo.saksala@tut.fi

Summary An explicit FE-procedure for modeling rock failure process under dynamic indentation is presented. The basic ideas, with some modifications, of the recently developed numerical code for simulating the quasi-static rock failure named RFPA are combined here with an explicit time integrator for simulating the dynamic failure. The impact of the indenter is modeled by imposing the contact constraints with the forward increment Lagrange multiplier method. A numerical example is solved.

Introduction

Numerical modeling of the brittle fracture is an important task in rock engineering. Engineers therein are interested in modeling the rock failure process, e.g., during percussive drilling. This paper presents an explicit procedure for FE-modeling of rock failure under dynamic indentation which process is essential in percussive drilling. This work is a continuation of the author's work presented in [1] where an explicit FE-procedure for modeling the stress wave propagation due to impact of a piston in a domain with non-reflecting boundaries was presented. In this work the method presented in [1] is combined with the rock fracture model of a recently developed numerical code RFPA (Rock Failure Process Analysis Code) (Tang [2], Zhu & Tang [3]) resulting in an explicit code where the impact of the indenter is modeled by considering it as a deformable body. The basic ideas of RFPA utilized here are as follows: The heterogeneity of rock is considered by assuming the material parameters to be conformed to the Weibull distribution. Progressive failure and the constitutive law for mesoscopic elements are modeled within the framework of damage mechanics. The Mohr-Coulomb criterion with tensile cut off (Rankine criterion) is used as the crack initiation condition. Cracking is similar to the smeared crack models. In this study the crack model of RFPA is modified at the element level so that the tensile crack is orientated orthogonally to the greatest principal stress.

Statistical modeling of rock heterogeneity

According to Tang [2], the global nonlinear behavior of brittle materials can be simulated by linear finite elements with heterogeneous material properties. In RFPA these properties, including compressive and tensile strengths σ_c, σ_t, Young's modulus E, and Poisson's ratio ν (in this study the density ρ also) are assumed to conform to the Weibull distribution, for which the density and distribution functions are, respectively

$$f(u) = \frac{m}{u_0}\left(\frac{u}{u_0}\right)^{m-1} \exp\left(-\frac{u}{u_0}\right)^m, \quad Q(u) = 1 - \exp\left(-\frac{u}{u_0}\right)^m . \tag{1}$$

Interpretation of the Weibull parameters in this context is that m is a homogeneity index for rock and u_0 is the mean value of, e.g. Young's modulus. In order to generate Weibull distributed properties for a rock sample, a single number ($Q(u)$ in (1)) from uniformly distributed random data between 0 and 1 is assigned to each element of the mesh. This is done separately for each material parameter. Then the corresponding material parameter u is solved from the second equation (1). The element size accepted, based on laboratory experiments, for obtaining good results is 1mm×1mm (in plane) [3].

Constitutive-damage mechanical model for elements

It is assumed that rock behaves like brittle material under loading and, thus, linear damage mechanics can be used for describing the gradual failure process. During the degradation of an element, the Young's modulus (and strength of rock) is defined as [4]

$$E = (1 - D)E_0, \tag{2}$$

where D is the isotropic damage variable and E_0 is the Young's modulus of intact rock. The uniaxial constitutive law for a finite element is illustrated in Fig. 1 (a) [3]

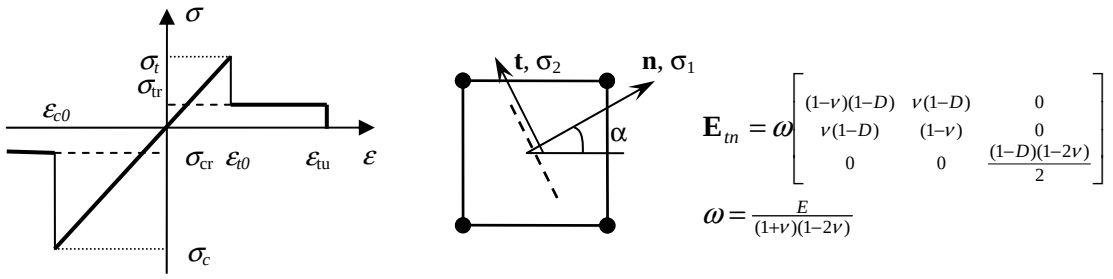

$$\mathbf{E}_{tn} = \omega \begin{bmatrix} (1-\nu)(1-D) & \nu(1-D) & 0 \\ \nu(1-D) & (1-\nu) & 0 \\ 0 & 0 & \frac{(1-D)(1-2\nu)}{2} \end{bmatrix}$$

$$\omega = \frac{E}{(1+\nu)(1-2\nu)}$$

Figure 1: Uniaxial constitutive law of element (a) and aligned crack model with local coordinates (b)

In Fig. 1 (a) σ_t, σ_c denote the compressive and tensile strengths of rock, respectively, and σ_{tr}, σ_{cr} denote the corresponding residual strengths which the element still possess after the brittle failure. The initiation of failure is indicated by the Rankine and Mohr-Coulomb criteria for the tensile and shear modes, respectively, as

$$\sigma_1 \le \sigma_t \text{ (tensile)}, \quad \sigma_3 - k\sigma_1 \ge \sigma_c, \; k = (1 + \sin\varphi)/(1 - \sin\varphi) \text{ (shear)} \tag{3}$$

where σ_1, σ_3 are the greatest and smallest principal stress, respectively, and φ is the friction angle of rock. Criteria (3) are checked at the center of each element. The damage variable is calculated as follows [3]

$$D = \begin{cases} 0, & \varepsilon_{\text{eqv}} < \varepsilon_{t0} \\ 1 - \lambda\dfrac{\varepsilon_{t0}}{\varepsilon_{\text{eqv}}}, & \varepsilon_{t0} \le \varepsilon_{\text{eqv}} < \varepsilon_{\text{tu}} \\ 1, & \varepsilon_{eqv} \ge \varepsilon_{\text{tu}} \end{cases} \text{ (tensile)}, \quad D = \begin{cases} 0, & \varepsilon_3 > \varepsilon_{c0} \\ 1 - \lambda\dfrac{\varepsilon_{c0}}{\varepsilon_3}, & \varepsilon_3 \le \varepsilon_{c0} \end{cases} \text{ (shear)} \tag{4}$$

In (4) λ is a residual strength coefficient defined as $\sigma_t/\sigma_{t0} = \sigma_c/\sigma_{c0} = \lambda$, ε_{tu} is the ultimate tensile strain defined as $\varepsilon_{\text{tu}} = \eta\varepsilon_{t0}$, where ε_{t0} is the elastic limit strain ($=\sigma_t/E_0$) and η is an ultimate strain coefficient [3]. In order to extend the constitutive law described in Fig. 1 (a) to multiaxial stress states, the uniaxial strains in (4) are replaced by ε_3 (maximum compressive strain) [3],

$$\varepsilon_{\text{eqv}} = \sqrt{\sum_{i=1}^{3} <\varepsilon_i>^2} \text{ and } \varepsilon_{c0} = \tfrac{1}{E_0}\left(-\sigma_c + k\sigma_1 - \nu(\sigma_2 + \sigma_1)\right) \tag{5}$$

where McAuley brackets have been used and k is as in (3). Since the damage process is irreversible for materials like rock, the damage variable cannot decrease. Thus, if the strain ε_{eqv}, at some strain states, is smaller than its maximal previously reached value, then D is kept constant. The same applies to the strain ε_3.

In RFPA both the shear and tensile damage causes the degradation of finite elements but the tensile failure is considered as the main cause for the crack initiation. When the equivalent strain reaches the ultimate tensile strain limit, the element loses its ability to transfer stresses (D = 1) and it is treated as an "air element" but it is not removed from the mesh. This is the method, similar to the smeared crack models, how RFPA simulates crack initiation, propagation and

interaction of cracks. In this study the unilateral nature of damage is taken into account similarly as in [4]. The deactivation of damage is done independently for each principal stress as follows.

$$\sigma_i = 2G(1-H(\varepsilon_i)D)\varepsilon_i + 2K\nu(1-H(\varepsilon_V)D)\varepsilon_V, \quad i=1,2 \tag{6}$$

In (6) ε_V is the volumetric strain, G is the shear modulus, $K = E/((1+\nu)(1-2\nu))$, and $H(\bullet)$ is the Heaviside function. This method keeps the mapping between stresses and strains continuous.

In the above described model the macro crack is represented by connecting arrays of fully damaged elements. Thus the model doesn't account for the local orientation of the discontinuity at the (meso)element level. In the present approach the tensile crack is allowed to rotate locally so that it is orthogonal to the greatest principal stress σ_1 as indicated in Fig. 1 (b). When the failure initiates its inclination angle α is kept fixed. This introduces anisotropy to the model which is taken into account by transforming the elasticity matrix written in the local **t**,**n**-coordinate (see Fig. 1) system into the global coordinate system. In addition, the strain ε_{eqv} in (4) is replaced by the strain normal to the crack. Thus, in this modified model the element is able to transfer stresses in the direction normal to the crack only when crack is closing but in the tangential direction, it transfers normal stresses as intact material.

Explicit procedure for solving the dynamic indentation problem

In order to simulate the crack propagation in time domain the explicit modified Euler time integrator is chosen because it is readily compatible with the viscous non-reflecting boundary scheme and the forward increment Lagrange multiplier method which is employed for imposing the contact constraints. Combining these methods leads to the following equations for solving the incremental response of the system [1].

$$\begin{aligned}
&\ddot{\mathbf{u}}^t = \tilde{\ddot{\mathbf{u}}}^t - \mathbf{M}^{-1}\mathbf{G}^{\mathrm{T}}\boldsymbol{\lambda}^t && \tilde{\ddot{\mathbf{u}}}^t = \mathbf{M}^{-1}\left(\mathbf{f}_{\mathrm{qp}}^t + \mathbf{f}_{\mathrm{qs}}^t - \mathbf{f}_{\mathrm{int}}^t\right)\\
&\dot{\mathbf{u}}^{t+\Delta t} = \dot{\mathbf{u}}^t + \Delta t\ddot{\mathbf{u}}^t && \text{, where} \quad \tilde{\mathbf{u}}^{t+\Delta t} = \mathbf{u}^t + \Delta t\dot{\mathbf{u}}^t + \Delta t^2\tilde{\ddot{\mathbf{u}}}^t\\
&\mathbf{u}^{t+\Delta t} = \mathbf{u}^t + \Delta t\dot{\mathbf{u}}^t + \Delta t^2\ddot{\mathbf{u}}^t && \boldsymbol{\lambda}^t = \left(\Delta t^2\mathbf{G}\mathbf{M}^{-1}\mathbf{G}^{\mathrm{T}}\right)^{-1}\left(\mathbf{G}\tilde{\mathbf{u}}^{t+\Delta t} - \mathbf{b}\right)
\end{aligned} \tag{7}$$

In (7), the denotions are: **u** is the nodal displacement vector, **M** is the lumped mass matrix, $\mathbf{f}_{qp}$, $\mathbf{f}_{qs}$ are the nodal force vectors (corresponding to the dilatation and shear waves, respectively) integrated from the viscous type of non-reflecting boundary conditions, $\mathbf{f}_{int}$ is the internal force vector assembled from the element contributions $\mathbf{f}_{\mathrm{int}}^{\,e} = t\int\mathbf{B}^{\mathrm{T}}\mathbf{D}(E(D))\mathbf{B}dA\mathbf{u}$, **G** is the contact constraint matrix, $\boldsymbol{\lambda}$ is the lagrange multiplier vector which has the physical meaning of contact forces in this context, and **b** is the initial distance between the indenter and rock.

Numerical example

The presented procedure is demonstrated by solving the dynamic indentation problem depicted in Fig. 2.

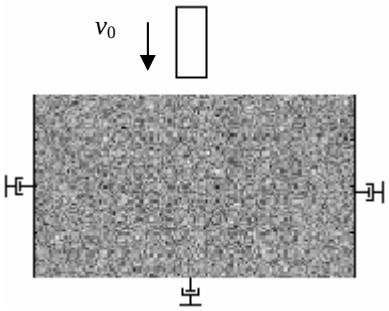

Data for indenter	Data for rock
ρ = 7800 kg/m^3	ρ_0 = 2500 kg/m^3, m_ρ = 100
ν = 0.3	ν_0 = 0.2, m_ν = 100
E = 200 GPa	E_0 = 60 GPa, m_E = 6
v_0 = 6 m/s	σ_{c0} = 100 MPa, m_σ = 6
	$\sigma_t = 0.1\sigma_c$, φ = 30°,
	λ = 0.1, η = 5

Figure 2: Illustration of dynamic indentation problem and initial data

In order to simulate the infinity of rock viscous damper type non-reflecting boundary conditions are imposed on the boundaries of the rock. The plane strain case is assumed, and the bilinear quadrilateral element is used in the generation of a regular mesh consisting of 120×80 elements for the rock and 20×30 for the indenter. The size of each element is 1mm×1mm. The parameters η, λ and m (Fig. 1) are chosen so as to make the rock domain correspond to hard rock, e.g. granite. The tensile strengths of the elements are generated from the compressive strengths of those elements by multiplying the latter values by a factor 0.1. A time step Δt = 8.2E-8s is used in numerical simulations. Fig. 3 shows the crack patterns simulated with the present approach.

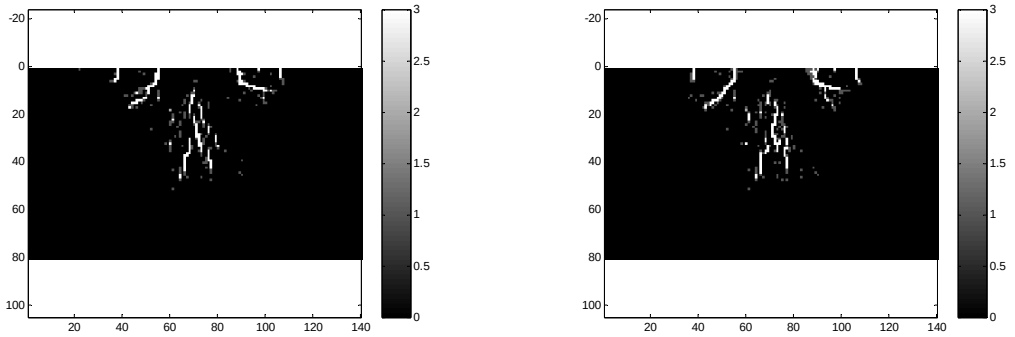

(a) (b)

Figure 3: Simulated crack patterns without (a) and with the oriented crack (b)

In Fig. (3) the black color corresponds to the intact rock, the dark gray (1 in color bar) to partly damaged rock in tensile mode, the light gray (2 in color bar) to rock damaged in shear mode, and the white color to fully damaged rock (in tensile mode). It can be seen that the crack pattern between the two models are very similar. Both of them produce the Herzian cone cracks, typical for right-angled indenters, and the vertical median cracks. Finally it is noted that virtually no shear failures occur which is due to the fact that the compressive strength is 10 times higher than the tensile strength.

Concluding remarks

An explicit FE-code for simulating the dynamic indentation, which occurs e.g. in percussive drilling, is developed in this work. The results of the simulations show that the present model is promising. The explicit approach to the considered problem is computationally cheap, not only because of the lumped mass matrix approach but also because the response of the structure need and can be calculated only within the reach of the propagating stress wave. It is also simple and thus allows easily for the extension of simulating the whole percussive drilling process including the piston, rods, couplings, and even some hydraulics.

References

[1] T. Saksala. Exact and Explicit FE-procedure for Modeling Stress Waves due to Impact in Domain with Non-reflecting Boundary. In: Mathisen, K.M., Kvamsdal, T., Okstad, K.M. (eds.) *Proceedings of 16th Nordic Seminar on Computational Mechanics*, Trondheim, Norway, 159-162 (2003).

[2] C.A. Tang. Numerical Simulation of Progressive Rock Failure and Associated Seismicity. *Int. J. Rock Mech. Min. Sci.*, **34**, 249-261, (1997).

[3] W.C. Zhu and C.A. Tang. Micromechanical Model for Simulating the Fracture Process of Rock. *Rock Mechanics and Rock Engineering*, **37**, 25-56, (2004).

[4] J. Lemaitre. *A Course on Damage Mechanics.* Springer-Verlag, (1992).

[5] S.Q. Kou et al. Rock Fragmentation Mechanisms induced by a Drill Bit. *Int. J. Rock Mech. Min. Sci.*, **41**, Paper 2B11-SINOROCK2004 Symposium, (2004).

Residual Based Approximations of Fine Scales in Variational Multiscale Approximations of Navier-Stokes Equations

M. G. Larson*
Department of Mathematics
Umeå University, S-90187, Umeå, Sweden
e–mail: mats_larson@yahoo.com
R. E. Bensow
Department of Naval Architecture
Chalmers University of Technology, S-41296, Göteborg, Sweden
e–mail: ribe@na.chalmers.se

The Variational Multiscale Method, see Hughes et al [2] provide a general framework for derivation of multiscale methods where the effects of fine (unresolved) scales on coarse (resolved) scale are accounted for through additional terms in the variational formulation. The additional terms involve the fine scale part of the solution, which satisfies an equation driven by the residual of the coarse scale part of the solution. In the simplest case the fine scale part of the solution can be approximated by a suitable scaling of the residual. Some problems require, more refined approaches, where the fine scales are approximated using solutions to localized problems, see Larson and Målqvist [4].

In this talk we present recent results, see [1], on the Navier-Stokes equations where we consider feedback to the coarse scales based on the fine scale velocity gradient. By taking the gradient of the Navier-Stokes equations we obtain an equation for the velocity gradient. We model the fine scale velocity gradient in terms of the residual obtained when inserting the coarse scale velocity gradient into this equation. The method is illustrated in several applications to realistic 3D turbulent flows. In particular, we show examples of the force fields generated by the additional fine scale terms.

The new additional terms are not constructed in such a way that they provide stabilization to the method, on the contrary, they drive certain phenomena in the flow. For instance, the simplest possible term modifies the vorticity vector with a vortex stretching term, which feed energy into the vortex. In fact, we may expect that discretization may introduce more viscosity into the model and thus effects of the fine scales could in some situations be driving instead of stabilizing. This property is in sharp contrast to standard stabilized methods such as the SUPG and GLS. The recent method of Hughes et al display similar properties, see [3].

References

[1] R.E. Bensow and M.G. Larson. Turbulence Models based on the Residual Variational Multiscale Method. *Chalmers Finite Element Center Preprint*, to appear 2005.
[2] T.J.R. Hughes, G.R. Feijóo, L. Mazzei, and J.-B. Quincy. The Variational Multiscale Method—A Paradigm for Computational Mechanics. *Comput. Methods Appl. Mech. Engrg.* **166**, 3–24, (1998).
[3] T.J.R. Hughes, V.M. Calo, and G. Scovazzi. Variational and Multiscale Methods in Turbulence. *ICES Report 04-46*, www.ices.utexas.edu.
[4] M.G. Larson and A. Målqvist. Adaptive Variational Multiscale Methods Based on A Posteriori Error Estimates: Energy Norm Estimates for Elliptic Problems. *Chalmers Finite Element Center Preprint 2004-18*, www.phi.chalmers.se, submitted to SIAM J. Numer. Analysis.

Adaptive simulation of multiphysics problems

M. G. Larson* **and F. Bengzon**
Department of Mathematics
Umeå University, S-90187, Umeå, Sweden
e–mail: mats_larson@yahoo.com

In this talk we outline a basic framework for adaptive simulation of multiphysics problems. We assume that we have access to solvers for the different kinds of physics in the problem. A multiphysics solver can then be obtained by letting these solvers communicate in a network. This situation is typical in industrial and lab environments where efficient solvers with detailed modeling of certain physical phenomena have been developed over the years. These solvers are then combined in multiphysics simulations.

We develop a basic a posteriori error analysis for such networks of solvers. We assume that each solver is adaptive and supports duality based a posteriori estimates for the error in linear functionals of the solution. The error in the functional is basically estimated by terms accounting for the discretization of the problem and the error in data to the problem. The discretization error is controlled using standard adaptive mesh refinement based on the a posteriori error analysis. The data error can account for uncertainty in given data or may depend on another solver. In the latter case the data error can be controlled by sufficient accurate solution of that problem. This dependency between the problems in the network is captured and quantified by solving a specific sequence of dual problems.

The basic theory is illustrated on some examples including solution of the pressure equation together with the transport equation with applications to oil reservoir simulation and the heat equation coupled with linear elasticity with application to stresses caused by heat in gearbox casings.

References

[1] M.G. Larson. A Framework for Adaptive Simulation of Multiphysics Problems. *Chalmers Finite Element Center Preprint 2005*, www.phi.chalmers.se.

[2] M.G. Larson, A. Målqvist and F. Bengzon. Simulation of Oil Reservoirs Using Goal Oriented A Posteriori Error Estimates and the Adaptive Variational Multiscale Method. *Chalmers Finite Element Center Preprint 2005*, www.phi.chalmers.se.

Algorithms for fluid-structure interaction of flow around two or more cylinders with large relative motions

By
Trond Kvamsdal[1], Kjell Herfjord[2], Knut M. Okstad[3] and Karstein Sørli[4]

[1]SINTEF ICT, Dept. of Applied Mathematics, N-7465 Trondheim, Trond.Kvamsdal@sintef.no
Norsk Hydro Research Centre Bergen, P.O. Box 7190, N-5020 Bergen, Kjell.Herfjord@hydro.com
FEDEM Technology AS, Vestre Rosten 78, N-7075 Tiller, Knut.M.Okstad@fedem.com
[4]SINTEF ICT, Dept. of Applied Mathematics, N-7465 Trondheim, Karstein.Sorli@sintef.no

ABSTRACT

We present herein methodology for handling fluid-structure interaction involving hydrodynamical flow around two or more cylinders. Due to vortex induced vibration of the cylinders the relative motions between them may be large and even collision may occur. To handle such cases we have developed tailored algorithms for mesh movement and remeshing that is robust and efficient. The fluid grid is composed of a structured part around the cylinders taking care of the boundary layer and an unstructured part away from the cylinder that makes it possible to do automatic remeshing in a flexible manner. Special care is taken in the remeshing step in order to not perturb the fluid loads on the cylinders due to interpolation between the old and new mesh.

We will focus on the methodology and validate its performance against high quality laboratory tests of two cylinders in a tandem set up. The computed response of the cylinders and the corresponding computed fluid loads will be compared with the physical experiments. These tests are particular relevant for analyzing the possibility for collisions of offshore risers or submerged pipelines which is important unresolved issues for oil exploration on deep water.

Finite Element analysis of jar connections: Modeling considerations

Anders Schmidt Kristensen*
Esbjerg Technical Institute
Aalborg University, Esbjerg, Denmark
e–mail: ask@aaue.dk

Kashif Toor
TRACS Information Systems Aps
Vilslevvej 68, DK-6771 Grestedbro
e–mail: kktoor@spemail.org

Sigurd Solem
TRACS Information Systems Aps
Vilslevvej 68, DK-6771 Grestedbro
e–mail: sigurd@vdstracs.com

A new tool joint system is considered. Traditionally these rotary connections have been designed with only one shoulder geometry. However, in order to increase the torque rating of the tool joint, a new design is introduced using two shoulders. This design allow reduced tool joint dimensions whereby down-hole equipment more easily can be fitted. In order to evaluate the validity of the design, finite element analysis have been performed in ANSYS. The results obtained indicate that the new design is valid and further tests can be performed.

Introduction

In a drill string different components are connected by tool joints. The tool joints are rotary connections with a box member and a pin member. A typical drill string with such tool joints is shown in figure 1(Left) and in figure 2(Top). In order to maintain internal and external pressure in the drill pipe and transmit torque these rotary shouldered connections (RSC) are pre-loaded by a so-called make-up torque. In the conventional connection only one shoulder is defined and the joint is conical with tapered threads as specified by [1], [2], [3], and [7].

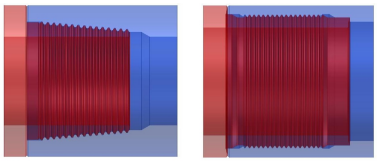

Figure 1: (Left) A conventional rotary single shouldered connection (RSC), i.e. a conical threaded connection with tapered pin and box threads, and sealing shoulders. (Right) A rotary double shouldered connection (RDSC).

The new type of connection, see figure 1(Right) and figure 2(Bottom), is not conical and two shoulders are defined. The new connection is termed a rotary double shouldered connection (RDSC) in the following.

The shoulder in these rotary connections function as a metal to metal seal for maintaining the pressure down-hole. During operation the connection is subjected to various load systems, however, the main load systems are: tensile forces and bending moments acts simultaneously with a high torque, e.g. during directional drilling where the bore hole is deviated.

The rotary connections with given dimensions depicted in 2 are selected for the finite element analysis conducted. Material used for the connections is AISI4145 with a yield limit $Y_m = 124.73 \times 10^3[psi]$ and modulus of elasticity $E = 29.8 \times 10^6[psi]$. The new design RDSC allow a smaller wall thickness, pitch of thread, and root radius, thus, more design space for fitting

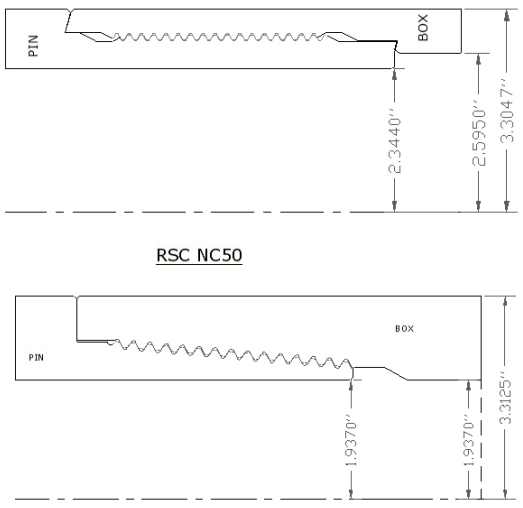

Figure 2: (Top) A RSC NC 50 with dimensions. (Bottom) A comparable RDSC with dimensions.

down hole equipment compared to the load bearing capacity. Comparison with design formulas indicate that care must be taken when evaluating the stresses in a pre-tensioned threaded connection. [8], [4], [6], and [5] suggest different approaches to determine the induced tension in the connection. Depending on how the friction is taken into account the results obtained from the design formulas can vary significantly. Therefore, the objective have been to gain confidence with the RDSC model with respect to the same modeling considerations, i.e. friction at the shoulders, as for the RSC model which should be replaced. The finite element analysis programme ANSYS is used for the numerical analysis.

Analysis

The load configuration considered is determined from [7] and is given as the make-up torque T_m

$$T_m = \frac{SA}{12}\left[\frac{p}{2\pi} + \frac{R_t f}{cos\alpha} + R_z f\right] \tag{1}$$

where the recommended stress level $S = 0.6 \times Y_m = 74838[psi]$, A is the cross-sectional area, $p = 0.25[in]$ is the pitch or lead, $f = 0.08$ is the coefficient of friction between mating surfaces [2], and $\alpha = 60/2 = 30[^\circ]$ is the thread angle or pitch angle.

The friction coefficient R_t taking into account the friction at the thread surfaces is given as

$$R_t = \frac{C + (C - (L - 0.625) \times tpr \times 1/12)}{4} \tag{2}$$

where $C = d_p$, tpr is the taper ratio, and $L = 4.5[in]$ is the length of the thread.

The friction coefficient R_z taking into account the friction between the mating shoulder surfaces is given as $R_z = \dfrac{OD - Q_c}{4}$, where $Q_c = 5.3125[in]$ is the box counter-bore, and the outside diameter $OD = 6.625[in]$.

For the RSC NC 50 $d_p = 6.625[in]$ and $tpr = 2[in/ft]$, i.e. the torque is found to be $T = 21454[ft - lb]$ thus $F_z = 77720.15[lbs]$. Tension induced P due to the applied torque $P =$

$533 \times 10^3[lbs] = F_y$. The forces F_z and F_y are applied as combined loading of the model and solution is run for the static case using axi-symmetry.

For the new connection RDSC $d_p = 5.68[in]$ and $tpr = 0$, $F = 90650[lbs] = F_z$. Tension induced due to the applied torque $P = 487 \times 10^3[lbs] = F_y$.

Results

The resulting shear stress distribution τ_{yz} can seen from figure 3.

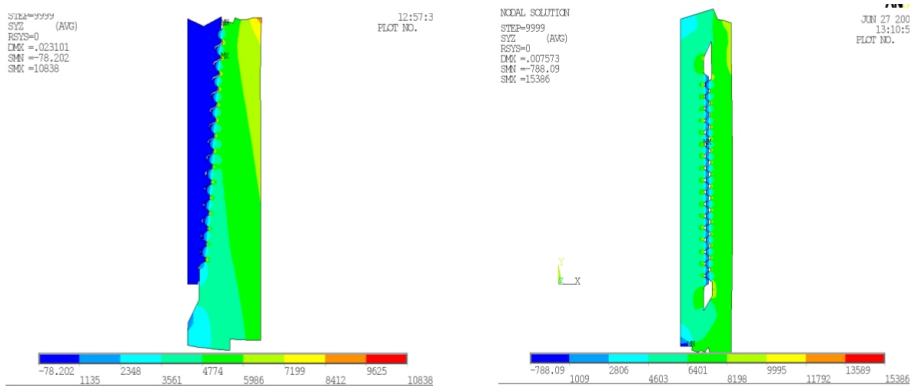

Figure 3: (Left) The shear stress distribution for the RSC NC 50. (Right) The shear stress distribution for the RDSC model.

As RSC NC 50 and the RDSC connection have different thickness, for a good comparison the computational values are taken at the same distance from the centre of the connection. Eight points are selected through the thickness of the connection as depicted in figure 4.

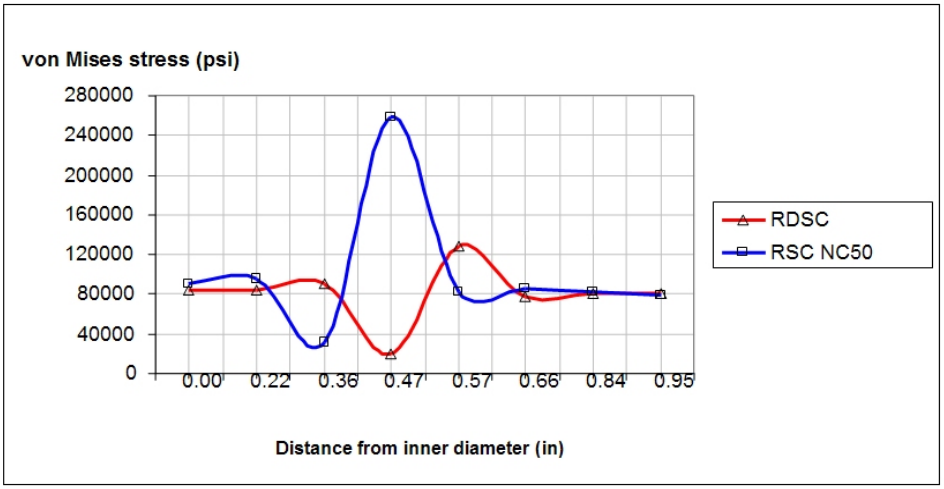

Figure 4: (Left) The through thickness von Mises stress distribution for the RSC NC 50. (Right) The through thickness von Mises stress distribution for the RDSC model.

Although the overall dimensions in the RDSC have been reduced the effect of the double shoulder reduces the maximum stress von Mises.

In order to evaluate the effect of the double shoulder further contact analyses have been performed

with ANSYS applying element types plane82, contact171, contact172, and target169. The resulting stress von Mises distribution is shown in figure 5

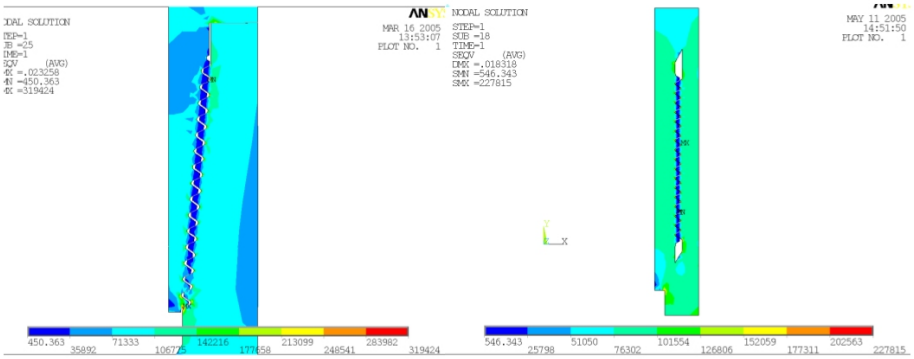

Figure 5: (Left) The von Mises stress distribution for the RSC NC 50 resulting from a contact analysis. (Right) The von Mises stress distribution for the RDSC model resulting from a contact analysis.

The contact analysis also indicates that the stress distribution in the double shouldered connection is more smooth and the maximum stress level has been reduced.

Conclusion

A RSC NC 50 and a RDSC have been compared using axi-symmetric finite element models. The effect of pre-tension is considered using an induced tension combined with a make-up torque. The results indicates that the stresses in the RDSC model are reduced compared to the RSC NC 50, allowing a full-scale prototype of the RDSC model to be tested as the next step.

References

[1] API. Specifications for rotary drill stem elements. *API spec. 7*, 39th ed., 1997.

[2] API. Recommeded practice for drill stem design and operating limits. *API RP 7G*, 16th ed., 1998.

[3] S. Baragetti and A. Baryshnikov. Rotary shouldered thread connections: Working limits under combined static loading. *Transactions of ASME*, vol. 123, 2001.

[4] J. A. Collins. *Mechanical Design of Machine Elements and Machines*. John Wiley & Sons, ISBN:0-471-03307-3, 2003.

[5] R. C. Juvinaal and K. M. Marshek. *Fundmentals of Machine Component Design*. John Wiley & Sons, ISBN: 0-471-24448-1, 3rd edition, 2000.

[6] P. Kempster and M. Dowell. *Guidelines to derivations of bolt torque*. 2002.

[7] Everage S. D. Lee K. McCarthy, J. P. Application of increased make up torque on api rotary shouldered connections: Good man diagram vs strain life model. *IADC/SPE 87190*, 1990.

[8] Joseph E. Shingley and Charles R. Mischke. *Standard Handbook of Machine Design*. MGraw-Hills, ISBN: 0-07-056958-4, 2nd edition, 1996.

Deformation of a Paper Roll Loaded Against a Nip Roller

Kilwa Ärölä*
Laboratory for Mechanics of Materials
Helsinki University of Technology, Espoo, Finland
e–mail: kilwa.arola@tkk.fi

Raimo von Hertzen
Laboratory of Fatigue and Strength
Lappeenranta University of Technology, Lappeenranta, Finland
e–mail: raimo.von.hertzen@lut.fi

Summary An elastoplastic material model accounting for the interlayer slippage of paper layers is used to study the deformation of a paper roll compressed against a rigid nip roller. Calculated load–deformation paths are compared to experimental results. It is found that the interlayer slippage in the nip area plays a key part in the deformation mechanism of the roll.

Introduction

Material constants for paper have been measured and reported by many authors [1], [2], [3]. However, the elastic material parameters obtained from the tests are not directly applicable to a wound roll. A purely elastic continuum model cannot correctly describe the layered structure of a paper roll and account for the slippage of the paper layers during the deformation. This can be a real drawback, since the interlayer slippage can play a key role in the mechanism of deformation [4], [5]. This is especially true in the case of nip[1] loads when high local stress concentrations in the roll can occur.

In this paper, an orthotropic elastoplastic material model, with the interlayer slippage described by plastic shear [6], is used to study the load–deformation paths, permanent deformations and layer–to–layer slippage in a paper roll loaded against a nip roller. It is demonstrated that compression tests of paper rolls against solid nip rollers can be used in determining the material parameters of paper by fitting the corresponding computed and measured results. Using this approach, values for the radial and shear moduli of paper are determined. The model can correctly predict the permanent deformations and hysteresis found in experimental tests.

Constitutive model for layered structure

The detailed mathematical formulation of the model used in this work is given in [6]. The main idea of the model is that the layered structure of the roll is embedded in the constitutive equation defining the material response. Larger elements of this jointed material, each spanning over several hundreds of layers, can then be used in the finite element model of the roll. The description of slippage between the layers in the material is based on the theory of plasticity. Since the layers in a roll are closely spaced compared to the characteristic dimensions of the domain of the model, they can be smeared into a continuum with slip surfaces. The outcome was an elastoplastic jointed material model for orthotropic materials with shear limits based on Coulomb friction. Finally, the model was implemented in ABAQUS/Standard finite element structural analysis software to perform the calculations.

Compression test and FE-model

In the compression test a roll of catalog paper was compressed against a solid nip roller as shown in Fig. 1. Since the initial radial pressure distribution, generated in the roll during winding, can have a significant effect on the slippage of the layers, it had to be taken into account. This pressure distribution was estimated using pull tab measurements. The indentation δ, *i.e.*, the relative

[1] the contact region between the paper roll and nip roller

displacement of the centres of the roll and roller, as well as the nip load P and paper to paper coefficient of friction μ_{pp} were also measured.

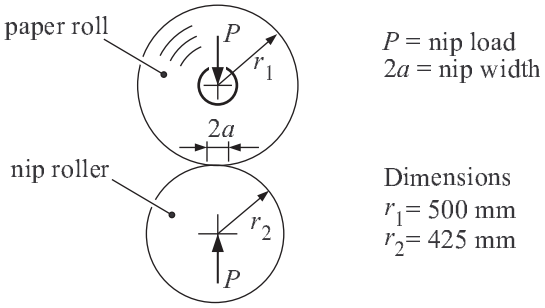

Figure 1: Paper roll compressed against a nip roller. The radii of the roll and roller are r_1 and r_2, respectively.

To model the compression test, a finite element simulation of a hollow cylinder of orthotropic jointed material around a rigid core, representing the paper roll, compressed against a rigid roller was performed. During one load cycle the roller was first compressed against the roll and then withdrawn. A total of two load cycles were simulated. A two dimensional model under plane strain conditions was used. Only one half of the roll had to be modelled when using the appropriate symmetry conditions. Numerical studies indicated that the results were

- practically independent of the Poisson's ratios $\nu_{r\theta}$, ν_{rz}, $\nu_{\theta z}$ and the coefficient of friction between the paper roll and nip roller μ_{pr}. For the Poisson's ratios typical values from [7] were used.
- only slightly dependent on the elastic moduli E_θ and E_z. The modulus E_θ was measured. A value typical for catalog paper was used for E_z.

The values for E_r and $G_{r\theta}$ were determined by fitting the calculated and measured results. It should be noted that values for the shear modulus $G_{r\theta}$ are rarely reported in existing literature, and yet it is an important parameter in modern winding models including the nip action. A summary of the parameter values used in the ultimate calculations are given in Table 1.

Table 1: Values of the parameters used in the calculation. The indices r, θ and z refer to the radial, circumferential and axial directions of the roll, respectively.

Elastic moduli	Poisson's ratios	Shear modulus	Coefficients of friction
$E_r = 10.0\,\mathrm{MPa}$	$\nu_{r\theta} = -0.0055$	$G_{r\theta} = 42.0\,\mathrm{MPa}$	$\mu_{pp} = 0.275$
$E_\theta = 5100\,\mathrm{MPa}$	$\nu_{rz} = -0.0035$		$\mu_{pr} = 0.4$
$E_z = 2600\,\mathrm{MPa}$	$\nu_{\theta z} = 0.37$		

Results

The indentation δ as a function of the nip load P is shown in Fig. 2. A preload of $1\,\mathrm{kN/m}$ was applied to remove the entrained air below the top layers of the paper roll and to set the zero point for the displacement. The calculated results (solid line) are in relatively good agreement with the

experimental results (dotted line). Note that the loading and unloading do not happen along the same path. Instead, a hysteresis cycle can be seen and a permanent indentation of approximately $0.3\,\mathrm{mm}$ remains after the first load cycle. For comparison, the calculation was repeated using a purely elastic, orthotropic model for the paper roll. The result is shown in Fig. 2 (dashed line). Obviously the elastic model cannot produce the hysteresis cycle and, thus, the loading and unloading occur along the same path. The elastic model is also more than 30% stiffer than the elastoplastic model. This can be understood, since in the plastic model layer–to–layer slippage softens the behaviour.

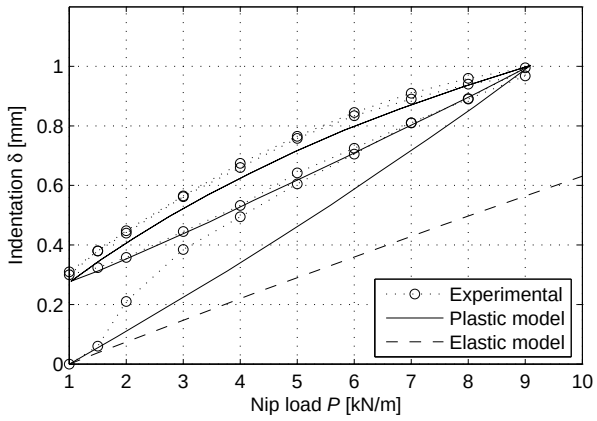

Figure 2: Indentation δ as a function of the nip load P. Experimental results (circles and dotted line) and calculated results obtained using the elastoplastic model (solid line) and elastic model (dashed line).

Regions of interlayer slippage

Since the interlayer slippage contributes significantly to the indentation–load behaviour, it is interesting to see where the slippage occurs. The permanent plastic engineering shearing strain (or permanent interlayer slippage) after two load cycles is shown in Fig. 3.

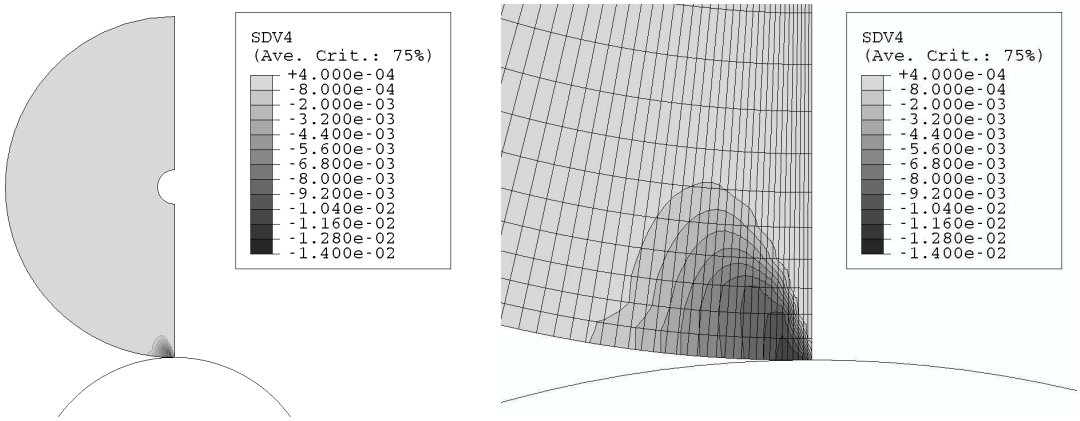

Figure 3: Plastic engineering shearing strain (or interlayer slippage) in the paper roll after two completed load cycles. A close up of the nip region and the finite element mesh are shown on the right. Only the left half of the roll is shown.

The area of high slippage is found on the side of the nip region close to the roll surface, penetrating about $40\,\mathrm{mm}$ into the roll. This can be expected, since this is the region of high shear stresses of cylindrical contact problems where shear stresses overcome the frictional forces and slippage occurs. Note also that in this region the radial compressive stresses are not as high as right below the nip area.

Concluding remarks

An orthotropic elastoplastic jointed material model accounting for the slippage and separation of the paper layers has been used to study the deformation of a paper roll compressed against a nip roller. The calculated results were compared to experimental data and a good correspondence was found. If other parameter values are known, the present model can also be utilized in an indirect method for determining the shear modulus $G_{r\theta}$ of paper from roll compression tests. A direct measurement of $G_{r\theta}$ is difficult due to the thinness of paper. It was also shown that a purely elastic model highly exaggerates the stiffness of the roll. In conclusion, the interlayer slippage plays a key role in the deformation mechanism of a paper roll, and it has to be taken into account in the calculations if accurate results are to be achieved.

References

[1] R.W. Mann, G.A. Baum and C.C. Habeger. Determination of all nine orthotropic elastic constants for machine–made paper. *TAPPI Journal*, **63**, 163–166, (1980).

[2] G.A. Baum, D.C. Brennan and C.C. Habeger. Orthotropic elastic constants of paper. *TAPPI Journal*, **64**, 97–101, (1981).

[3] N. Stenberg, C. Fellers and S. Östlund. Measuring the stress–strain properties of paperboard in the thickness direction. *J. Pulp and Paper Sci.*, **27**, 213–221, (2001).

[4] J.D. McDonald and A. Menard. Layer-to-layer slippage within paper rolls during winding, *J. Pulp. Pap. Sci.*, **25**, 148–153, (1999).

[5] D. McDonald, J. Hamel and A. Menard. Out–of–round paper rolls, In *Proceedings of the 7th Int. Conference on Web Handling*, Oklahoma, (2003).

[6] K. Ärölä and R. von Hertzen. Modelling interlayer slippage in wound rolls. In A. Eriksson, J. Månsson, G. Tibert, editors, *NSCM-17: Proceedings of the 17th Nordic Seminar on Computational Mechanics*, pages 124–127, Stockholm, (2004).

[7] Q. Xia, M. Boyce and D. Parks. A constitutive model for the anisotropic elastic–plastic deformation of paper and paperboard. *Int. J. Solids and Structures*, **39**, 4053–4071, (2002).

Comparison between Approaches to Explicit Filtering in Large Eddy Simulation

Tellervo Brandt
Laboratory of Aerodynamics
Helsinki University of Technology, Espoo, Finland
e-mail: tellervo.brandt@tkk.fi

Summary In this paper, we discuss different approaches to explicit filtering in LES and the choice of the filter function. Explicit filtering of the whole velocity field fails to predict the flow statistics while filtering of the change in the velocity field or only the convection term of the Navier–Stokes equations behave better. Using a filter as close as possible to the spectral cut-off produces the best result. However, using explicit filtering increases the effect of the modelling error on the statistics.

Introduction

In Large Eddy Simulation (LES), the large scales of fluid motion are solved from the Navier–Stokes equations, and a sub-grid scale (SGS) model is applied to describe the effect of the small scales on the large scales. When low-order (i.e. second or fourth order) finite-difference-type methods, where discretization is not performed in the Fourier space, are applied, and the computational grid is let to define the separation between resolved and SGS scales, the numerical error becomes a problem. It can be larger than the effect of the SGS model. Explicit filtering of the resolved flow field has been noticed to improve the situation [1].

Filtering of the whole velocity field in the end of each time step has been the traditional approach, but it has been criticised of leading to multiple filtering of the velocity field from the previous time levels [2], and in *a priori* testing, it has lead to unphysical behaviour of the SGS term [3]. Filtering of the non-linear convection term of the Navier–Stokes equations has been suggested as an alternative approach [2]. The approach has been applied in actual simulations [4], and it has given promising results also in *a priori* tests [3]. However, filtering of only the convection term breaks the Galilean invariance. This can be recovered by using a filter as close as possible to the spectral cut-off filter or by proper SGS modelling.

In this paper, we discuss different approaches to explicit filtering and compare between some explicit filters. As the test case, we have a fully developed turbulent channel flow between two infinite parallel walls. The Reynolds number based on the friction velocity and the channel half-height is $\mathrm{Re}_\tau = 395$. This corresponds approximately to $\mathrm{Re} \approx 6500$ based on the mean velocity.

Governing Equations and Applied Numerical Methods

In LES of an incompressible flow, we solve the filtered Navier–Stokes equations, which are written here in the non-dimensional form as:

$$\frac{\partial \tilde{u}_i}{\partial t} = -\frac{\partial P}{\partial x_i} - \frac{\partial \tilde{p}}{\partial x_i} + \frac{\partial}{\partial x_j}\left(- \tilde{u}_i\tilde{u}_j - \tau_{ij} + \frac{1}{\mathrm{Re}_\tau}\left(\frac{\partial \tilde{u}_i}{\partial x_j} + \frac{\partial \tilde{u}_j}{\partial x_i}\right)\right), \tag{1}$$

where $(x_1, x_2, x_3) = (x, y, z)$ refer to non-dimensional streamwise, wall-normal and spanwise spatial coordinates, respectively, t to time, $(\tilde{u}_1, \tilde{u}_2, \tilde{u}_3) = (u, v, w)$ to resolved velocity vector, ρ to density, P to mean pressure, $\tilde{p}$ to fluctuating resolved pressure, and τ_{ij} is a model for the SGS stress tensor $\widetilde{u_i u_j} - \tilde{u}_i\tilde{u}_j$. Here, the equations are scaled by the channel half-height, $0.5h$, and friction velocity $u_\tau = \sqrt{\tau_{\mathrm{wall}}/\rho}$, and the Reynolds number is thus defined as $\mathrm{Re}_\tau = 0.5hu_\tau\rho/\mu$. The standard Smagorinsky model [5] is applied to model τ_{ij}.

In the present simulations, the second-order central-difference scheme was applied on a staggered grid system for spatial discretization. For time integration, a third-order, three-stage Runge–Kutta method was applied. For details of the methods see Ref. [6]. The applied resolution and the domain size are given in Table 1.

Table 1: Resolution and domain size of the applied LES grid.

	x	z	y
length of the domain (scaled by $0.5h$)	6.0	3.2	2.0
number of grid points	54	54	60
size of the grid cell in wall units (Δ^+)	44	11	min 2, max 27

wall units: $x^+ = \mathrm{Re}_\tau x$, where x is scaled by the channel half-height.

Different Approaches to Explicit Filtering

One step of the applied Runge-Kutta method may be written as:

$$\tilde{u}_i^{n+1} = \tilde{u}_i^n + \Delta t^n \left(c_1 \Delta \tilde{u}^n + c_2 \Delta \tilde{u}^{n-1} \right), \tag{2}$$

where the superscript refers to time levels and c_1 and c_2 are the coefficients of the method. In the first applied approach to explicit filtering, the whole velocity field, $\tilde{u}_i^{n+1}$, is filtered in the end of each step. In this case, the velocity field $\tilde{u}_i^n$ from the previous step will be multiply filtered. This leads to loss of information if a filter other than sharp spectral cut-off is applied [2]. In the second approach, the change in the velocity field, $\Delta\tilde{u}_i^n$, is filtered, and in the third and fourth approaches, only the non-linear convection term, $\tilde{u}_i\tilde{u}_j$, and the sum of non-linear convection term and the SGS term, $\tilde{u}_i\tilde{u}_j + \tau_{ij}$, are filtered, respectively. The second, third and fourth approach avoid the multiple filtering of the velocity field. In the fourth approach, also the possible higher frequencies produced by the SGS model are removed from the resolved field.

Some Discrete Filters

We apply altogether four discrete filters in this paper: the Trapezoidal and Simpson filters and a third and fifth order commutative filters from Ref. [7]. Here, filtering is applied only in the homogeneous directions, and thus the commutation of filtering with differentiation is not required. However, the commutative filters are closer to the spectral cut-off filter than the Trapezoidal and Simpson filters. The applied filters are described in Table 2.

Table 2: Coefficients of the applied discrete filter functions. $\overline{\tilde{u}}_i\left(x_j\right) = \Sigma_{l=-K}^{K} a_l \tilde{u}_i\left(x_{j+l}\right)$.

	a_0	$a_{\pm1}$	$a_{\pm2}$	$a_{\pm3}$	$a_{\pm4}$	$a_{\pm5}$
Trapezoidal	1/2	1/4				
Simpson	2/3	1/6				
3rd order commut.	1/2	9/32	0	-1/32		
5th order commut.	1/2	75/256	0	-25/512	0	3/256

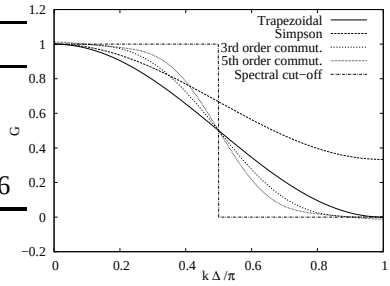

Results

Comparison between the Filtering Approaches

In cases discussed in this subsection, the third-order commutative filter was applied. Filtering of the whole velocity field in the end of each time step spoiled the simulation. The mean velocity and Reynolds stresses were overpredicted by more than 100% and even the total shear stress was incorrectly predicted, and thus the mean momentum balance was not satisfied in the channel. Since the applied filter was not the spectral cut-off, multiple filtering of the velocity field resulted in excessive smoothing of the velocity field.

The mean velocity profile, the deviatoric diagonal streamwise Reynolds stress and the SGS shear stress from the other approaches are plotted in Figure 1. In the mean velocity profile, the slope

is incorrect in all the cases. When $\Delta\tilde{u}_i$ is filtered, the mean velocity is under-predicted and when $\tilde{u}_i\tilde{u}_j$ or $\tilde{u}_i\tilde{u}_j + \tau_{ij}$ are filtered, it is slightly over-predicted. The deviatoric diagonal Reynolds stress is over-predicted in all the cases, and the approach where $\Delta\tilde{u}_i$ in filtered is closest to the DNS results. The peak in the SGS shear stress increases in approaches where $\tilde{u}_i\tilde{u}_j$ or $\tilde{u}_i\tilde{u}_j + \tau_{ij}$ are filtered, but further away from the wall, it decreases in all the cases. Filtering of the SGS term has no effect on the statistics since the Smagorinsky model does not introduce new frequencies in the resolved flow field. The situation would be different if a scale-similarity-type model was applied.

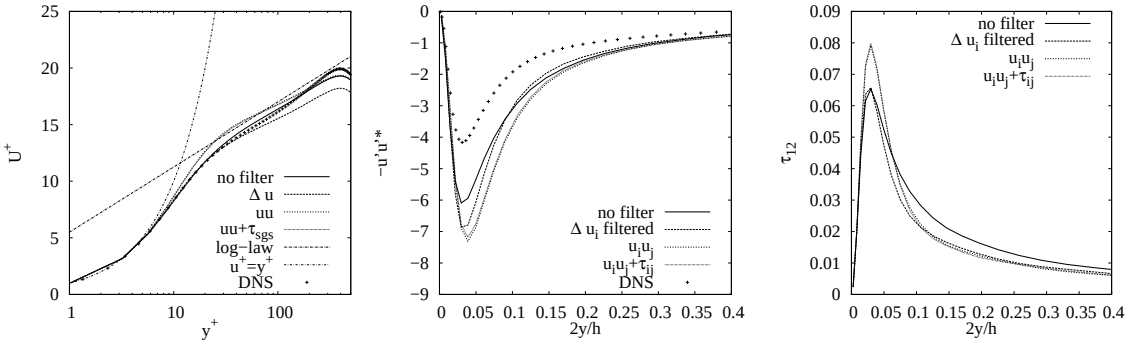

Figure 1: Comparison between the filtering approaches. Left: Mean velocity profile. Middle: Deviatoric diagonal streamwise Reynolds stress $-u'u'^*$. Right: SGS shear stress τ_{12}.

Comparison Between Different Filters

In this subsection, we study the effect of the chosen filter on the flow statistics using the approach where $\tilde{u}_i\tilde{u}_j + \tau_{ij}$ is filtered. The mean velocity profile, the deviatoric streamwise Reynolds stress and the SGS shear stress are plotted in Figure 2. The slope of the mean velocity improves and the over-prediction of the mean velocity and the Reynolds stress decrease as a filter closer to the spectral cut-off is applied. The over-prediction of both quantities is worst when the Trapezoidal filter is applied. The peak in the SGS shear stress decreases as a filter closer to the spectral cut-off is applied.

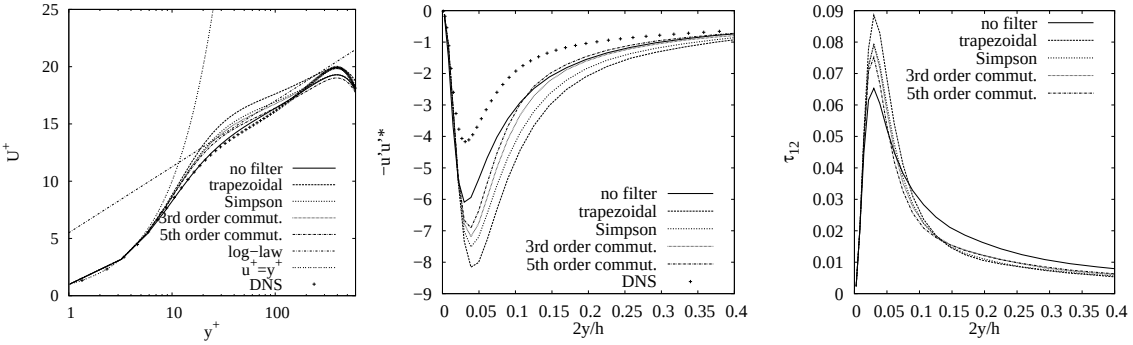

Figure 2: Comparison between filters. Left: Mean velocity profile. Right: Deviatoric diagonal streamwise Reynolds stress $-u'u'^*$. Right: SGS shear stress τ_{12}.

Computational cost

In the present case, taking one step in the time integration method took on average 0.57 CPU seconds. When explicit filtering was applied, this took approximately 1.5 CPU seconds. The

differences in CPU time between the applied filters were at maximum 0.05 CPU seconds per time step.

Conclusions

In this paper, we have discussed two aspects of explicit filtering in LES. Firstly, four approaches were compared and secondly, four filters were tested using one of the approaches. Filtering was applied only in the homogeneous directions, and the standard Smagorinsky model was applied.
Explicit filtering of the whole velocity field seriously damaged the flow statistics, which was due to the multiple filtering of the velocity from the previous time levels. This situation can be avoided only if the spectral cut-off filter is applied.
There were only small differences between the other tested approaches, and all the studied statistics were further away from DNS results than the traditional LES with no filtering. This can be due to counteraction between numerical and modelling errors, which has been noticed to lead to a situation where a decrease in either one can lead to increased total error [8]. Filtering of $\Delta\tilde{u}_i$ produced results closest to the DNS results. However, based on results of Ref. [4], it seems possible that using a mixed model with a scale-similarity term could change the situation.
The effect of the chosen explicit filter was studied using the approach where the resolved and the SGS convection terms are filtered. In this approach, using a filter as close as possible to the spectral cut-off minimises the error due to the broken Galilean invariance and the effect of filtering to the large scales. Here, it was noticed that as the applied filter approached the spectral cut-off filter, the prediction of the slope of the mean-velocity profile and the peak of the Reynolds stress were improved. The peak in the SGS stress decreased as the filter approached the spectral cut-off. The effect of the chosen filter was larger than the effect of the choice of the filtering approach.
As a conclusion, it seems that just applying explicit filtering does not necessarily improve the simulation results. As shown by the present results, one has to pay attention to the choice of the filtering approach and especially to the filter. In addition, since the effect of the model did not increase when the Smagorinsky model was applied, improved SGS modelling has to be considered. Also, the increased computation time is a drawback. However, the clear benefit in explicit filtering is that the effect of the numerical error decreases. As long as it has a major role in the simulation results, the interpretation of for example the behaviour of different SGS models is difficult.

Acknowledgements

This work has been funded by the Finnish CFD Graduate School. The computer capacity was partly provided by CSC. The applied channel-flow code is based on a code written by Dr. Boersma from TU Delft.

References

[1] A. G. Kravchenko and P. Moin. On the effect of numerical errors in large eddy simulations of turbulent flows. *Journal of Computational Physics*, 131:310–322, 1997.

[2] T. S. Lund. On the use of discrete filters for large eddy simulation. *Center for Turbulence Research, Annual Research Briefs*, pages 83–95, 1997. Stanford University.

[3] T. Brandt. Discretization errors in LES using second-order central-difference scheme. In P. Neittaanmäki, T. Rossi, K. Majava, and O. Pironneau, editors, *European Congress on Computational Methods in Applied Sciences and Engineering*, Jyväskylä, Finland, July 2004. ECCOMAS 2004.

[4] J. Gullbrand. Grid-independent large-eddy simulation in turbulent channel flow using three-dimensional explicit filtering. *Center for Turbulence Research, Annual Research Briefs*, pages 167–179, 2002. Stanford University.

[5] J. S. Smagorinsky. General circulation experiments with the primitive equations, part I: The basic experiment. *Monthly Weather Review*, 91:99–152, 1963.

[6] T. Brandt. *Studies on numerical errors in large eddy simulation*. Licentiate's thesis, Helsinki University of Technology, August 2004. ISBN 951-22-7192-3.

[7] O. V. Vasilyev, T. S. Lund, and P. Moin. A general class of commutative filters for LES in complex geometries. *Journal of Computational Physics*, 146(1):82–104, October 1998.

[8] B. Vreman, B. Geurts, and H. Kuerten. Comparison of numerical schemes in large-eddy simulation of the temporal mixing layer. *International Journal for Numerical Methods in Fluids*, 22:297, 1996.

Mathematical Modelling of Biosensors with Perforated and Selective Membranes

Feliksas Ivanauskas*
Institute of Mathematics and Informatics,
Vilnius University, Vilnius, Lithuania
e–mail: feliksas.ivanauskas@maf.vu.lt

Romas Baronas
Faculty of Mathematics and Informatics
Vilnius University, Vilnius, Lithuania
e–mail: romas.baronas@maf.vu.lt

Juozas Kulys
Department of Chemistry and Bioengineering,
Vilnius Gediminas Technical University, Vilnius, Lithuania
e–mail: juozas.kulys@fm.vtu.lt

Summary This paper presents a two-dimensional-in-space mathematical model of amperometric biosensors with perforated and selective membranes acting under internal and external diffusion limitations. The model is based on non-linear reaction-diffusion equations. Using numerical simulation the influence of the geometry of the biosensor as well as of the external diffusion region on the biosensor response was investigated.

Introduction

Biosensors are measuring devices that contain a biological entity [1]. The enzyme in a biosensor recognizes the substrate to be measured and specifically converts it into a product of the biochemical reaction. The amperometric biosensors measure the faradic current that arises on a working indicator electrode by direct electrochemical oxidation or reduction of the product. The amperometric biosensors are known to be reliable, cheap and highly sensitive for environment, clinical and industrial purposes [2].

A practical biosensor contains a multilayer enzyme membrane [3]. The electrode acting as a transducer of the biosensor is covered by selective membrane, following a layer of immobilized enzyme and an outer perforated membrane [4].

The goal of this research was to build a model approaching the practical amperometric biosensor and taking into account the geometry of the membrane perforation. Using computer simulation the influence of the geometry of the biosensor as well as of the external diffusion region on the biosensor response was investigated. The simulation was carried out using the finite difference technique [5].

Mathematical model

The holes in the perforated membrane were modelled by right cylinders. The holes are of uniform diameter and spacing, forming a hexagonal pattern. Fig. 1a presents the biosensor schematically.

The entire biosensor may be divided into equal hexagonal prisms with regular bases. For simplicity, it is reasonable to consider a circle whose area equals to that of the hexagon and

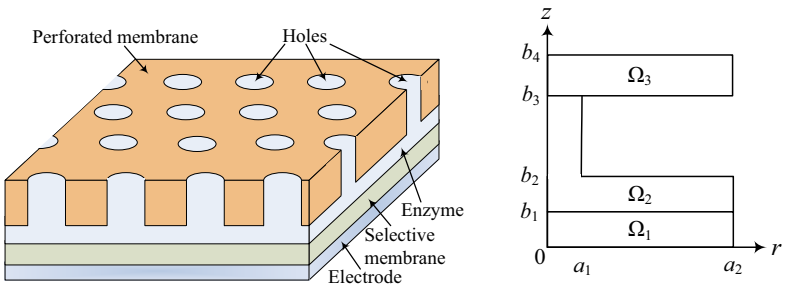

a) b)

Figure 1: A principal structure of the biosensor and the profile of the unit cell at Y-plane.

to regard one of the cylinders as a unit cell of the biosensor. Fig. 1b shows the profile of the unit of the biosensor. b_1, b_2-b_1, b_3-b_2, b_4-b_3 are the thicknesses of the selective membrane, basic enzyme layer, perforated membrane and external diffusion layer, respectively, a_2 is the radius of the base of the unit cell, a_1 is the radius of the holes. We also assume that holes are filled with the enzyme.

Let Ω_1, Ω_2, Ω_3 be open regions corresponding to the selective membrane, enzyme region, diffusion layer, respectively, and Γ_2 - the boundary between of Ω_2 and Ω_3,

$$\begin{aligned} &\Omega_1 = (0,a_2)\times(0,b_1), \quad \Omega_2 = ((0,a_2)\times(b_1,b_2))\cup((0,a_1)\times[b_2,b_3)), \\ &\Omega_3 = (0,a_2)\times(b_3,b_4), \quad \Gamma_2 = [0,a_1]\times b_3. \end{aligned} \tag{1}$$

The biosensor action is described by the reaction - diffusion system ($t>0$)

$$\frac{\partial P_1}{\partial t} = D_1\Delta P_1,\ (r,z)\in\Omega_1, \tag{2}$$

$$\frac{\partial S_2}{\partial t} = D_2\Delta S_2 - \frac{V_{max}S}{K_M+S_2}, \quad \frac{\partial P_2}{\partial t} = D_2\Delta P_2 + \frac{V_{max}S}{K_M+S_2},\ (r,z)\in\Omega_2, \tag{3}$$

$$\frac{\partial S_3}{\partial t} = D_3\Delta S_3, \quad \frac{\partial P_3}{\partial t} = D_3\Delta P_3,\ (r,z)\in\Omega_3, \tag{4}$$

where Δ is the Laplacian in cylindrical coordinates, $S_i(r,z,t)$ is the concentration of the substrate in Ω_i, $i=2,3$, $P_j(r,z,t)$ is the concentration of the reaction product in Ω_j, $j=1,2,3$, V_{max} is the maximal enzymatic rate and K_M is the Michaelis constant.

Let $\overline{\Omega}_i$ be the closure of the corresponding open region Ω_i, $i=1,2,3$. The initial conditions ($t=0$) are as follows:

$$\begin{aligned} &S_2(r,z,0)=0, \quad (r,z)\in\overline{\Omega}_2\setminus\Gamma_2, \quad S_2(r,z,0)=S_0,\ (r,z)\in\Gamma_2, \\ &S_3(r,z,0)=S_0,\ (r,z)\in\overline{\Omega}_3, \\ &P_i(r,z,0)=0, \quad (r,z)\in\overline{\Omega}_i,\ i=1,2,3. \end{aligned} \tag{5}$$

The boundary and matching conditions ($t>0$) are

$$P_1(r,0,t)=0, \quad S_3(r,b_4,t)=S_0, \quad P_3(r,b_4,t)=0, \quad \frac{\partial S_2}{\partial z}\Big|_{z=b_1}=0 \quad r\in[0,a_2], \tag{6}$$

$$\frac{\partial P_1}{\partial r}\Big|_{r=0} = \frac{\partial P_1}{\partial r}\Big|_{r=a_2} = 0, \quad z \in [0, b_1], \tag{7}$$

$$\frac{\partial P_2}{\partial r}\Big|_{r=0} = \frac{\partial S_2}{\partial r}\Big|_{r=0} = \frac{\partial P_2}{\partial r}\Big|_{r=a_2} = \frac{\partial S_2}{\partial r}\Big|_{r=a_2} = 0, \quad z \in [b_1, b_2], \tag{8}$$

$$\frac{\partial P_2}{\partial r}\Big|_{r=0} = \frac{\partial S_2}{\partial r}\Big|_{r=0} = \frac{\partial P_2}{\partial r}\Big|_{r=a_1} = \frac{\partial S_2}{\partial r}\Big|_{r=a_1} = 0, \quad z \in [b_2, b_3], \tag{9}$$

$$\frac{\partial P_3}{\partial r}\Big|_{r=0} = \frac{\partial S_3}{\partial r}\Big|_{r=0} = \frac{\partial P_3}{\partial r}\Big|_{r=a_2} = \frac{\partial S_3}{\partial r}\Big|_{r=a_2} = 0, \quad z \in [b_3, b_4], \tag{10}$$

$$\frac{\partial P_2}{\partial z}\Big|_{z=b_2} = \frac{\partial S_2}{\partial z}\Big|_{z=b_2} = \frac{\partial P_3}{\partial r}\Big|_{z=b_3} = \frac{\partial S_3}{\partial r}\Big|_{z=b_3} = 0, \quad r \in [a_1, a_2], \tag{11}$$

$$D_1 \frac{\partial P_1}{\partial z}\Big|_{z=b_1} = D_2 \frac{\partial P_2}{\partial z}\Big|_{z=b_1}, \quad P_1(r, b_1, t) = P_2(r, b_1, t), \quad r \in [0, a_2], \tag{12}$$

$$D_2 \frac{\partial P_2}{\partial z}\Big|_{z=b_3} = D_3 \frac{\partial P_3}{\partial z}\Big|_{z=b_3}, \quad P_2(r, b_3, t) = P_3(r, b_3, t), \quad r \in [0, a_1], \tag{13}$$

$$D_2 \frac{\partial S_2}{\partial z}\Big|_{z=b_3} = D_3 \frac{\partial S_3}{\partial z}\Big|_{z=b_3}, \quad S_2(r, b_3, t) = S_3(r, b_3, t), \quad r \in [0, a_1]. \tag{14}$$

The measured current depends upon the flux of the reaction product at the electrode surface. The density $i(t)$ of the current at time t can be obtained explicitly from Faraday's and Fick's laws

$$i(t) = n_e F D_1 \frac{1}{\pi a_2^2} \int_0^{2\pi} \int_0^{a_2} \frac{\partial P_1}{\partial z}\Big|_{z=0} r dr d\varphi, \tag{15}$$

where n_e is a number of electrons involved in a charge transfer and F is Faraday constant. We assume, that the system (2)-(14) approaches an equilibrium or steady - state when $t \to \infty$, $i_\infty = \lim\limits_{t\to\infty} i(t)$.

The problem was solved numerically using the finite difference technique [5]. We introduced a non-uniform discrete grid in all three directions: r, z and t. Using the alternating direction method, an implicit finite difference scheme was built. The resulting systems of linear algebraic equations were solved efficiently because of the tridiagonality of their matrices.

Results of calculations

The thickness $\delta = b_4 - b_3$ of the external diffusion layer is inversely proportional to the intensity of solution stirring [6]. To investigate the effect of the external diffusion on the biosensor response we calculated the normalized steady-state current,

$$i_N(\delta) = \frac{i_\infty(\delta)}{i_\infty(0)}, \quad \delta = b_4 - b_3, \ \delta \geq 0, \tag{16}$$

where $i_\infty(\delta)$ is the steady-state biosensor current at given thickness δ of the diffusion layer. Fig. 2 shows the results of calculations.

One can see in Fig. 2, i_N is a monotonous increasing function of the thickness δ of the diffusion layer in the cases of relatively large radius a_1 of the holes of the perforated membrane ($a_1 > 0.2a_2 = 0.2\,\mu$m). Due to the external diffusion the biosensor current can

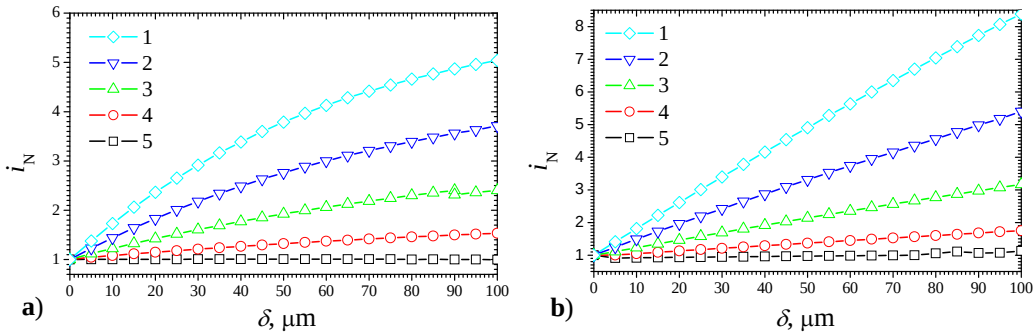

Figure 2: The normalized steady-state current i_N versus the thickness δ of the diffusion layer at different values of the radius a_1 of holes, $a_1 = 1.0$ (1), 0.8 (2), 0.6 (3), 0.4 (4), 0.2 (5) μm, S_0: 100 **(a)**, 1 **(b)** μM, V_{max}: 100 **(a)**, 1 **(b)** μM/s, $a_2 = 1$, $b_1 = 2$, $b_2 = 4$, $b_3 = 14\,\mu$m, $D_1 = 1\,\mu$m^2/s, $D_2 = 300\,\mu$m^2/s, $D_3 = 2D_2$, $K_M = 100\,\mu$M, $n_e = 2$.

vary even in an order of magitude. In the opposite case of relatively small radius a_1 of holes the biosensor response practically does not depend upon the intensity of stirring of analyte (Fig. 2). This property is valid for wide rages of the substrate concentration S_0 and maximal enzymatic rate V_{max}.

Concluding remarks

The mathematical model (2)-(14) of operation of the amperometric biosensors with selective and perforated membrane can be used to investigate pecularities of the biosensor response in stirred and non stirred analytes.

In the case of relatively large radius of holes of the perforated membrane, the steady-state current is a monotonous increasing function of the thickness of the external diffusion layer and that layer should be taken into consideration when modelling the biosensor action (Fig. 2). In the case of relatively small radius of holes the biosensor response practically does not depend upon the intensity of stirring of analyte (Fig. 2), and the external diffusion layer may be neglected to model the operation of biosensors with perforated membrane.

Acknowledgement

This work was partially supported by Lithuanian State Science and Studies Foundation, project No. C-03048.

References

[1] F. Scheller and F. Schubert. *Biosensors*. Elsevier, Amsterdam, (1992).

[2] U. Wollenberger, F. Lisdat and F.W. Scheller. *Frontiers in Biosensorics 2. Practical Applications*. Birkhauser Verlag, Basel, (1997).

[3] A.J. Baeumner, C. Jones, C.Y. Wong and A. Price. A generic sandwich-type biosensor with nanomolar detection limits. *Anal. Bioanal. Chem.*, **387**, 1587 – 1593, (2004).

[4] T. Schulmeister and D. Pfeiffer. Mathematical modelling of amperometric enzyme electrodes with perforated membranes. *Biosens. Bioelectron.*, **8**, 75 – 79, (1993).

[5] A.A. Samarskii. *The Theory of Difference Schemes*. Marcel Dekker, New York-Basel, (2001).

[6] R. Baronas, F. Ivanauskas and J. Kulys. Computer simulation of the response of amperometric biosensors in stirred and non stirred solution. *Nonlinear Analysis: Modelling and Control*, **8**, 3–18, (2003).

Modeling Aircraft Ground Behavior into a Flight Simulation

John Öström*
Laboratory of Aerodynamics
Helsinki University of Technology, Espoo, Finland
e-mail: john.ostrom@hut.fi

Miika Haatio
Finnair Oyj, Finland
e-mail: miika.haatio@finnair.fi

Summary This paper describes an aircraft ground behavior model of a Valmet Vinka –type light aircraft developed for a Matlab/Simulink-based flight simulation software. This simulation could be used in preliminary flight training in the Training Wing of the Finnish Air Force. The model was found out to perform realistically despite simplifications and constants that had to be estimated due to lack of data.

Introduction

Valmet Vinka light aircraft, shown in Fig. 1, is used for flight training in the Finnish Air Force. The Laboratory of Aerodynamics at Helsinki University of Technology is developing a new flight simulation model of the aircraft that could replace the existing outdated analog simulators. The aircraft landing gear and ground behavior form a part of the aircraft model so that taxiing, take-off and landing can be trained as well as up-and-away flying.

Figure 1: Valmet Vinka light trainer aircraft.

The aircraft model is developed into an in-house developed Matlab/Simulink-based flight simulation software HUTFLY2 described in reference [1]. The basic simulation program includes an atmospheric model, non-linear six-degree-of-freedom rigid-body flat-earth equations of motion, determination of forces and moments and other common routines required by the simulation. The simulation can be controlled using a joystick, a throttle and pedals connected to the computer, and it can be run synchronized to real-time clock (“near real-time”). Virtual Reality Modeling Language (VRML) is used extensively in the visualizations. Matlab/Simulink can also be used to control simulator cockpits and motion platforms. Therefore, the present simulation could be used in flight training if an aircraft model is available for the application.

Landing gear and its modeling

Valmet Vinka has a fixed tricycle landing gear with a freely-castoring nose wheel. At low speeds on the ground, the steering is controlled using differential braking. As the speed builds up, the rudder power becomes adequate for aerodynamic steering control. The main landing gear legs are attached to a fuselage frame and the oil/nitrogen-filled shock absorbers to the leg and the center beam of the aircraft. The firewall-attached nose-wheel strut steering angle is limited to ±15º, and a spring is used to keep the strut straight during flight. The strut has an oil/nitrogen-filled shock absorber as well. The landing gear layout and main components are shown in Fig. 2.

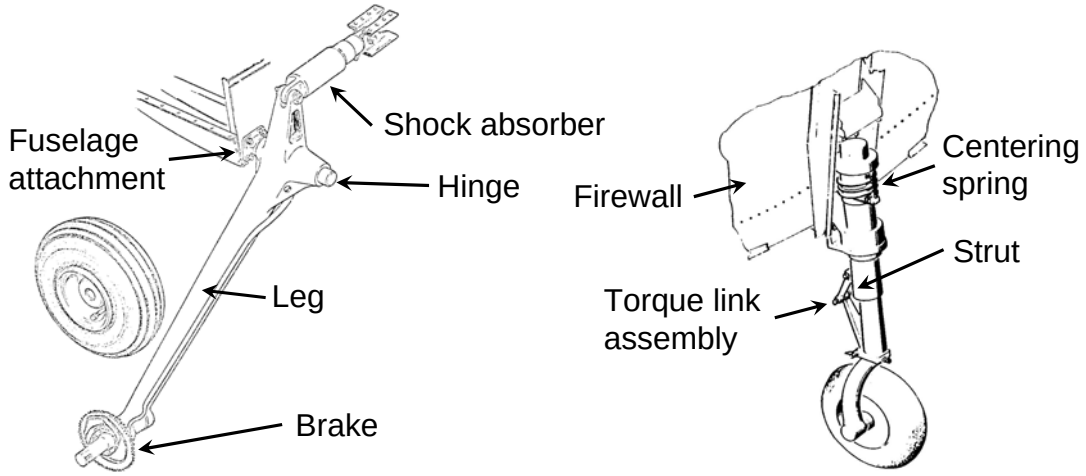

Figure 2: Landing gear components.

The ground behavior model is fully described in reference [2] and can only be discussed very briefly in this context. The principle of the model is to first calculate virtual positions of the three tires corresponding to the fully extended gear flight geometry to be compared to the ground level at each simulation time step. If some of the tires are below ground level, ground contact is detected, and landing gear calculation is carried on further. The next step is to solve the true tire positions, landing gear shock absorber displacements and velocities using the solved gear deflections and their previous values. The damper forces can then be calculated using an ordinary spring-damper-equation with non-linear springs. The damping ratio of the dampers had to be estimated from test simulations at maximum sink rates since only static test data were available.

The non-trivial freely-castoring nose wheel is modeled using equation

$$I_z\ddot{\beta} = M_1(\beta) + M_2(\dot{\beta}) + M_3(\alpha) + M_4(\dot{\beta}/V) \qquad (1)$$

In Eq. 1, the first moment term (M_1) is the straightening spring moment due to steering angle β. The second one (M_2) is the combined damping effect of the strut bearings and the spring. The term M_3 is the moment due to tire deformation. It depends on the straightening moment due to tire sliding angle α and moment due to tire cornering force and caster length of the strut. The tire sliding moment is non-linear and takes the maximum sliding angle into account. After the maximum sliding angle, the moments related to tire deformation are only dependent on the cornering force and caster length. The last term M_4 models the damping of the tire in ground contact and depends on the velocity (V), steering angle, contact surface length and normal force. The inertial moment I_z of the nose landing gear had to be estimated.

The tire velocities are calculated in their own coordinate systems referred to the ground to be used in determining the coefficients of friction in longitudinal and lateral directions. The lateral movement of the main wheels with aircraft vertical displacement is an important factor. Friction is naturally divided into rolling and sliding, but the tires have no forward sliding friction, since due to simplification, they are considered to be only rolling. Therefore, the brakes are also simplified to be anti-locking. A friction circle principle is used to limit the maximum coefficient of friction during hard lateral maneuvering and braking. The coefficients are scaled to zero when velocity is zero to assure zero friction forces at complete rest. The coefficients of friction are chosen for dry pavement, but can be scaled to simulate wet or icy runway conditions.

Finally, the friction forces affecting the tires are calculated and combined with the normal supporting forces. These forces are then transferred into the center of gravity of the aircraft again with a new coordinate transform. Dealing with multiple coordinate systems in six degrees of freedom unavoidably adds complexity into the model. The model has constraints on hard landings with too high rates of descent. The aircraft geometry is also taken into account to stop simulation in situations were other parts of the aircraft than the wheels have contact with ground. The model also provides landing gear parameters into a VRML animation, which was also used in validating the realism of the model.

Simulation results

To demonstrate the ground behavior model, results from a landing simulation are presented in Fig. 3. The landing at groundspeed of 30m/s was performed with a -5° aircraft sideslip angle (nose right with respect to the velocity vector) to show non-symmetric effects.

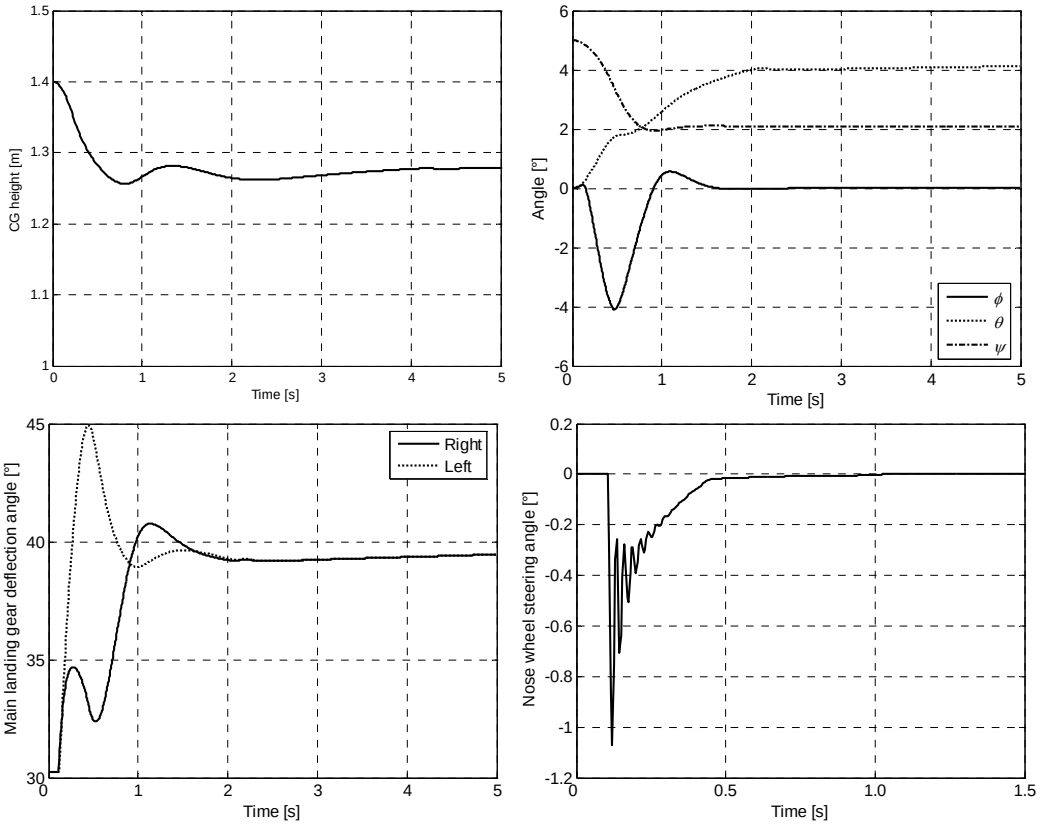

Figure 3: Results from a landing with -5° sideslip angle.

The first two frames of Fig. 3 show the height of the aircraft center of gravity and the Euler angles that represent aircraft attitude. The roll angle Φ is positive right wing down, pitch angle θ positive nose up and azimuth angle ψ positive nose right. The two lower frames show the main landing gear deflection angles and the nose gear steering angle. The main landing gear angle is the angle between the aircraft symmetry plane and the landing gear leg viewed from the nose of the aircraft. This angle is about 30° when the main landing gear is unloaded and about 40° loaded on the ground with an aircraft weight of 1100kg. The nose wheel steering angle is positive right.

The main gear touches down at a center of gravity height of 1.35m and the nose gear a while later as seen from the main landing gear and nose wheel steering angle plots. As the aircraft has negative sideslip, the left shock absorber compresses more than the right one and the aircraft banks left as seen in frame two. The nose gear steers left towards the direction of the velocity vector as it touches the ground, but some oscillations are apparent. The aircraft rotates its nose up and wings level to a ground rest attitude. The azimuth and nose wheel steering angles decrease as the aircraft steers away form the sideslip condition. The attitude angles settle nicely after about 2 seconds of ground roll. The main landing gear angles settle to values slightly less than at rest since there is still aerodynamic lift present.

Concluding remarks

A series of simulations was performed with the landing gear model to verify its performance. It was observed that the model simulates the ground behavior of the aircraft realistically despite the fact that certain numeric values used in the model had to be estimated. The model is now implemented to the HUTFLY2 flight simulation as part of the Valmet Vinka aircraft model.

References

[1] J. Öström. Developing a Low-Cost Flight Simulation to Support Fatigue Analysis. *AIAA Modeling and Simulation Technologies Conference*. AIAA 2004-5161, (2004).

[2] M. Haatio. Modeling of aircraft ground behavior into a flight simulation program. Master's thesis. Espoo, Finland. Teknillinen korkeakoulu, (2004), (in Finnish).

A benchmark study: MITC4-S and boundary layer-type deformations

Antti Niemi*, Juhani Pitkäranta and Harri Hakula
Institute of Mathematics
Helsinki University of Technology, Espoo, Finland
e–mail: antti.h.niemi@tkk.fi

Summary We study one of the open problems in the finite element modelling of shell deformations, the approximation of boundary and interior layers. We consider here a special finite element construction named MITC4-S in the context of a simplified shallow shell model. The element is closely related to engineering practice and is certainly one of the best bilinear elements aimed for general shell analysis.

Introduction

The phenomena of *membrane and shear locking* are known to impair various elements in the bending-dominated deformation of a thin shell. The problem results from the inability of the standard finite element subspace to satisfy the conditions of vanishing shear and membrane strains. To reduce the effects of the consraints, the variational formulation is often modified by applying reduction operators to the strains. The reductions must be designed very carefully to avoid the loss of stability in other (more common) deformation states where the membrane and shear strains play a more dominant role. It is often argued that a finite element scheme that performs well in both bending-dominated and membrane-dominated deformations would also perform well in the so called *intermediate* cases where boundary layer-type deformations typically dominate. However, already in the Reissner-Mindlin plate model, there are algorithms that are free of locking when the solution is smooth but cause error growth at a free boundary where the layer is known to be strong [3]. This "plate layer", which has a very short range, is found also in shells, but as a result of curvature effects the shell layers may have significantly wider ranges [2]. Therefore it seems to be necessary to isolate the layers and study them as a separate problem.

To investigate the numerical effects that arise in the FEM approximation of shell layers, we have presented a model problem with a concentrated point load [1]. The problem setup is such that reference solutions of arbitrary precision are computable using Fourier techniques. We focus here in particular to the approximation of a point layer in an elliptic shell but also line layers generated by the characteristic lines of a parabolic or a hyperbolic shell midsurface are studied.

Our approach is based on a simplified shallow shell model and an interpretation of the bilinear MITC4 shell element in this context. The simplified formulation, named here MITC4-S, has turned out to be very handy as it preserves the essential features of the original (degenerated) 3D approach while making mathematical error analysis possible to some extent, at least. In the present study we observe experimentally that the numerical modifications of MITC4-S unlock the standard bilinear element also when approximating layers although some traces of other side effects are found in the case of a point layer.

The Reissner-Naghdi shallow shell model

The deformation of the shell is described in terms of a displacement field $\boldsymbol{u} = (u, v, w, \theta, \psi)$ defined on the shell midsurface ω. In addition to the tangential displacements u, v and the transverse displacement w, the vector field $\boldsymbol{u}$ consists of the dimensionless rotations θ, ψ related to the transverse shear deformations. In our model the scaled strain energy of the shell with a constant thickness t may be expressed as

$$\mathcal{A}(\boldsymbol{u}, \boldsymbol{u}) \;=\; \mathcal{A}_m(\boldsymbol{u}, \boldsymbol{u}) + \mathcal{A}_s(\boldsymbol{u}, \boldsymbol{u}) + \mathcal{A}_b(\boldsymbol{u}, \boldsymbol{u}), \tag{1}$$

where the different bilinear forms represent the portions of energy stored in membrane, transverse shear and bending deformations. They are defined as

$$\begin{aligned}
\mathcal{A}_m(\boldsymbol{u},\boldsymbol{u}) &= \int_\omega \left\{\nu(\beta_{11}+\beta_{22})^2 + (1 \quad \nu)(\beta_{11}^2+2\beta_{12}^2+\beta_{22}^2)\right\}\, d\omega, \\
\mathcal{A}_s(\boldsymbol{u},\boldsymbol{u}) &= \frac{1 \quad \nu}{2}\int_\omega \left\{ \ {}^2_1 + \ {}^2_2\right\}\, d\omega, \\
\mathcal{A}_b(\boldsymbol{u},\boldsymbol{u}) &= \frac{t^2}{12}\int_\omega \left\{\nu(\kappa_{11}+\kappa_{22})^2 + (1 \quad \nu)(\kappa_{11}^2+2\kappa_{12}^2+\kappa_{22}^2)\right\}\, d\omega,
\end{aligned} \tag{2}$$

where β_{ij}, $\ _i$, and κ_{ij} are the membrane, transverse shear, and bending strains, respectively.
In the following we assume that ω is a rectangular domain expressed in the coordinates x, y. We also assume that the curvature tensor $\{b_{ij}\}$ of the midsurface is constant and write $a = b_{11}$, $b = b_{22}$, and $c = b_{12} = b_{21}$. The shell is then called elliptic when $ab \quad c^2 > 0$, parabolic when $ab \quad c^2 = 0$, and hyperbolic when $ab \quad c^2 < 0$. The above assumptions are valid for example when the shell is shallow, i.e. the midsurface differs only slightly from a plane. In general the strain fields in Eqs. (2) depend on the geometry of the shell. In the simplest case one may set $d\omega = dxdy$ and write the relation between the strain and the displacement fields as

$$\begin{aligned}
\beta_{11} &= \frac{\partial u}{\partial x} + aw, \quad \beta_{22} = \frac{\partial v}{\partial y} + bw, \quad \beta_{12} = \frac{1}{2}\left(\frac{\partial u}{\partial y} + \frac{\partial v}{\partial x}\right) + cw, \\
{}_1 &= \theta \quad \frac{\partial w}{\partial x}, \qquad {}_2 = \psi \quad \frac{\partial w}{\partial y}, \\
\kappa_{11} &= \frac{\partial \theta}{\partial x}, \qquad \kappa_{22} = \frac{\partial \psi}{\partial y}, \qquad \kappa_{12} = \frac{1}{2}\left(\frac{\partial \theta}{\partial y} + \frac{\partial \psi}{\partial x}\right).
\end{aligned} \tag{3}$$

If $\mathcal{L}$ is a linear functional corresponding to the potential energy of the external load, then the deformation of the shell is obtained by minimizing the total energy

$$\mathcal{F}(\boldsymbol{u}) = \frac{1}{2}\mathcal{A}(\boldsymbol{u},\boldsymbol{u}) \quad \mathcal{L}(\boldsymbol{u}) \tag{4}$$

over the kinematically admissible displacements $\boldsymbol{u} \in \mathcal{U}$.

The model problem
We consider a model problem such that the shell is loaded in the transverse direction with a periodic and self-balancing point load of the form

$$f = \quad F\sum_{i,j}(\ \ 1)^{i+j}\delta(x \quad 2i)\delta(y \quad 2j), \tag{5}$$

where the load amplitude $F > 0$ is a constant (Fig. 1). The corresponding linear functional is then given by

$$\mathcal{L}(\boldsymbol{u}) = \quad F\sum_{i,j}(\ \ 1)^{i+j} w(2i, 2j). \tag{6}$$

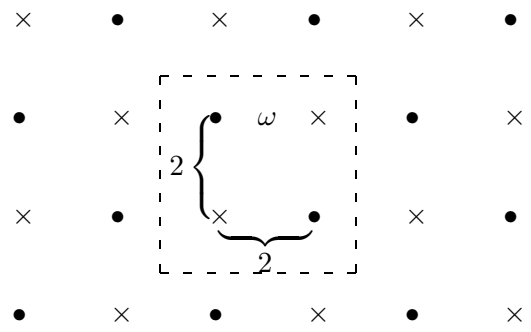

Figure 1: Periodic point loading: $\bullet \mathrel{\widehat{-}}$ 'upwards', $\times \mathrel{\widehat{-}}$ 'downwards'.

The proposed problem may be regarded as a generalization of the classical pinched cylinder benchmark test where two normal and equal point loads are applied centrally at the opposite sides of a cylindrical surface. The quality of approximate solutions is often measured by only comparing the transverse displacement under the point load to some reference value. We would like to point out that this can be misleading since the exact value of the transverse deflection is infinite at the load application points if Reissner-Mindlin type kinematic assumption is made in the underlying shell model.
Taking into account the strain expressions (3) and the specific nature of the load potential (6), we conclude that in general the displacement field is of the form

$$\begin{cases} u(x,y) &= \displaystyle\sum_{m,n} \left\{ U^A_{mn} \sin\frac{m\pi x}{2} \cos\frac{n\pi y}{2} + U^B_{mn} \cos\frac{m\pi x}{2} \sin\frac{n\pi y}{2} \right\}, \\ v(x,y) &= \displaystyle\sum_{m,n} \left\{ V^A_{mn} \cos\frac{m\pi x}{2} \sin\frac{n\pi y}{2} + V^B_{mn} \sin\frac{m\pi x}{2} \cos\frac{n\pi y}{2} \right\}, \\ w(x,y) &= \displaystyle\sum_{m,n} W_{mn} \cos\frac{m\pi x}{2} \cos\frac{n\pi y}{2}, \\ \theta(x,y) &= \displaystyle\sum_{m,n} \Theta_{mn} \sin\frac{m\pi x}{2} \cos\frac{n\pi y}{2}, \\ \psi(x,y) &= \displaystyle\sum_{m,n} \Psi_{mn} \cos\frac{m\pi x}{2} \sin\frac{n\pi y}{2}. \end{cases} \tag{7}$$

We also observe that the load is not able to excite Fourier modes with m or n even. Consequently, we have to sum over odd indices only in the above expressions.
To determine the unknown coefficients, we substitute the Ansatz (7) directly into the expression (4) for the total energy and integrate the strain energy density over one period ω as indicated by the dash line in Fig. 1. The solution is then obtained by choosing

$$\boldsymbol{z}_{mn} = \begin{pmatrix} U^A_{mn} & V^A_{mn} & U^B_{mn} & V^B_{mn} & W_{mn} & \Theta_{mn} & \Psi_{mn} \end{pmatrix} \tag{8}$$

to make

$$\mathcal{F}(u,v,w,\theta,\psi) \;=\; \frac{1}{2} \sum_{m,n} \boldsymbol{z}^T_{mn} \boldsymbol{A}_{mn} \boldsymbol{z}_{mn} \quad \sum_{m,n} \boldsymbol{z}^T_{mn} \boldsymbol{b} \;=\; \min! \tag{9}$$

The symmetric matrix $\boldsymbol{A}_{mn}$ is also positive definite and the load vector $\boldsymbol{b}$ is defined as

$$\boldsymbol{b} = \quad 4F\,(0 \quad 0 \quad 0 \quad 0 \quad 1 \quad 0 \quad 0)\,. \tag{10}$$

We evaluated by symbolic computation the entries of the matrix $\boldsymbol{A}_{mn}$ as functions of the indices m, n and the parameters ν, t, a, b, c. Symbolic expansion of the solution $\boldsymbol{z}_{mn}$ is also in the realms of possibility but the expressions become so complicated that their applicability is questionable. However, the numerical values of the Fourier coefficients are easily obtained by giving some values to the parameters and choosing suitable stopping indices for m, n.
As an example we show in Fig. 2 the strain field $e_{12} = \beta_{12} \quad \frac{t}{2}\kappa_{12}$ in an elliptic shell ($a = b = 1$, $c = 0$) and compare it to the one calculated by the MITC4-S algorithm.

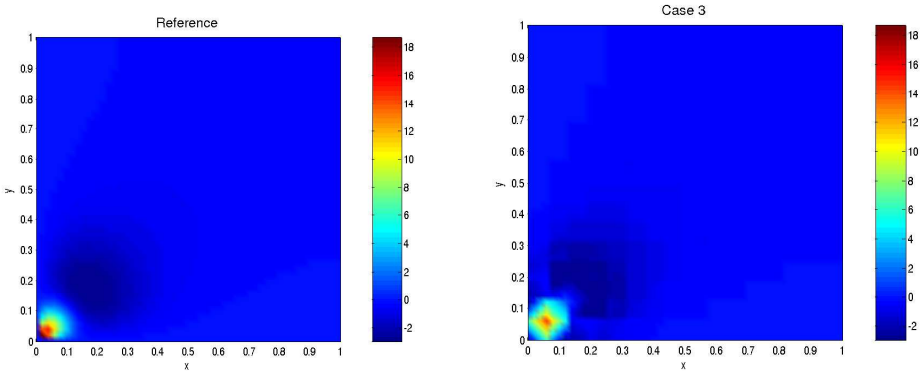

Figure 2: The tangential shear strain e_{12} in an elliptic shell as given by the MITC4-S algorithm (right) and Fourier analysis (left).

References

[1] A. Niemi, J. Pitkäranta, H. Hakula Benchmark computations on point-loaded shallow shells: Fourier vs. FEM *Preprint submitted to Comput. Methods Appl. Mech. Engrg.* 2005;

[2] J. Pitkäranta, A.-M. Matache, C. Schwab Fourier mode analysis of layers in shallow shell deformations *Comput. Methods Appl. Mech. Engrg.* 2001; **190**:2943–2975.

[3] J. Pitkäranta, M. Suri Upper and lower error bounds for plate-bending finite elements *Numerische Mathematik* 2000; **84**:611–648.

Computational results for the superconvergence and postprocessing of MITC plate elements

Mikko Lyly
CSC
Scientific Computing Ltd., Espoo, Finland
e–mail: mikko.lyly@csc.fi

Jarkko Niiranen* **and Rolf Stenberg**
Institute of Mathematics
Helsinki University of Technology, Espoo, Finland
e–mail: jarkko.niiranen@tkk.fi, rolf.stenberg@tkk.fi

Summary We summarize the main parts of the theoretical results introduced and analyzed in [5] for the MITC plate elements [2], [4]. We also illustrate and verify the superconvergence properties and the post-processing method with various numerical computations.

Introduction

The deflection approximation of the MITC plate elements [2], [4] is shown to be superconvergent with respect to a special interpolation operator [5]. This property holds in the H^1-norm and the interpolation operator is closely related to the reduction operator used in the MITC methods. A part of the superconvergence result is, roughly speaking, that the vertex values obtained with the MITC methods are superconvergent. This may be an explanation why these methods have become so popular.

By utilizing the superconvergence property a postprocessing method has been introduced in [5] — to improve the accuracy of the deflection approximation. The new approximation for the deflection is constructed element by element which implies low computational costs. The new approximation is a piecewise polynomial of one degree higher than the original one.

Here we first summarize the main parts of the theoretical results. Then we show various computational results illustrating the superconvergence properties of the original approximation and confirming the improved accuracy of the postprocessed approximation. In the numerical tests both uniform and non-uniform meshes are used and cases with different kinds of boundary conditions are studied.

MITC finite elements for Reissner-Mindlin plates

We consider a linearly elastic and isotropic plate with the shear modulus G and the Poisson ratio ν. The midsurface of the undeformed plate is $\Omega \subset \mathbb{R}^2$ and the plate thickness t is constant. The boundary of the plate we divide into hard clamped, hard simply supported and free parts: $\partial\Omega = \Gamma_{\rm C} \cup \Gamma_{\rm SS} \cup \Gamma_{\rm F}$. The spaces of kinematically admissible deflections and rotations are then

$$W = \{v \in H^1(\Omega) \ \mid \ v_{|\Gamma_{\rm C}} = 0,\ v_{|\Gamma_{\rm SS}} = 0\}, \tag{1}$$

$$\boldsymbol{V} = \{\boldsymbol{\eta} \in [H^1(\Omega)]^2 \ \mid \ \boldsymbol{\eta}_{|\Gamma_{\rm C}} = \boldsymbol{0},\ (\boldsymbol{\eta}\cdot\boldsymbol{\tau})_{|\Gamma_{\rm SS}} = 0\}, \tag{2}$$

where $\boldsymbol{\tau}$ is the unit tangent to the boundary. For the analysis the problem is written in mixed form in which the shear force $\boldsymbol{q} = t^{-2}(\nabla w - \boldsymbol{\beta})$ is taken as an independent unknown in the space $\boldsymbol{Q} = [L^2(\Omega)]^2$ [4], [5]. For the bilinear form we define the bending part and the linear strain

tensor:

$$a(\boldsymbol{\phi},\boldsymbol{\eta}) = \frac{1}{6}\{(\boldsymbol{\varepsilon}(\boldsymbol{\phi}),\boldsymbol{\varepsilon}(\boldsymbol{\eta})) + \frac{\nu}{1-\nu}(\operatorname{div}\boldsymbol{\phi},\operatorname{div}\boldsymbol{\eta})\}, \tag{3}$$

$$\boldsymbol{\varepsilon}(\boldsymbol{\eta}) = \frac{1}{2}(\nabla\boldsymbol{\eta} + (\nabla\boldsymbol{\eta})^T). \tag{4}$$

We consider the triangular family but we emphasize that all the results are valid for quadrilateral families as well. By $\mathcal{C}_h$ we denote the triangulation of $\overline{\Omega}$. As usual, we denote $h = \max_{K\in\mathcal{C}_h} h_K$, where h_K is the diameter of K. The space of polynomials of degree k on K is denoted by $P_k(K)$. By C we denote positive constants independent of the thickness t and the mesh size h.
In the MITC methods [2], [4] the finite element subspaces $W_h \subset W$ and $\boldsymbol{V}_h \subset \boldsymbol{V}$ are defined for the polynomial degree $k \geq 2$ as

$$W_h = \{w \in W \ \mid \ w_{|K} \in P_k(K) \ \ \forall K \in \mathcal{C}_h\}, \tag{5}$$

$$\boldsymbol{V}_h = \{\boldsymbol{\eta} \in \boldsymbol{V} \ \mid \ \boldsymbol{\eta}_{|K} \in [P_k(K)]^2 \oplus [B_{k+1}(K)]^2 \ \ \forall K \in \mathcal{C}_h\}, \tag{6}$$

with the "bubble space"

$$B_{k+1}(K) = \{b = b_3 p \ \mid \ p \in \tilde{P}_{k-2}(K),\ b_3 \in P_3(K),\ b_{3|E} = 0 \ \ \forall E \subset \partial K\}, \tag{7}$$

where $\widetilde{P}_{k-2}(K)$ is the space of homogeneous polynomials of degree $k-2$ on the element K. The discrete shear space is the rotated Raviart-Thomas space of order $k-1$,

$$\boldsymbol{Q}_h = \{\, \boldsymbol{r} \in \boldsymbol{H}(\mathrm{rot};\Omega) \ \mid \ \boldsymbol{r}_{|K} \in [P_{k-1}(K)]^2 \oplus (y,-x)\tilde{P}_{k-1}(K) \ \forall K \in \mathcal{C}_h \,\}. \tag{8}$$

The reduction operator $\boldsymbol{R}_h : \boldsymbol{H}(\mathrm{rot};\Omega) \to \boldsymbol{Q}_h$ is defined locally, with $\boldsymbol{R}_K = \boldsymbol{R}_{h|K}$, through the conditions

$$\langle(\boldsymbol{R}_K\boldsymbol{\eta} - \boldsymbol{\eta})\cdot\boldsymbol{\tau}_E, p\rangle_E = 0 \ \ \forall p \in P_{k-1}(E) \ \ \forall E \subset \partial K, \tag{9}$$

$$(\boldsymbol{R}_K\boldsymbol{\eta} - \boldsymbol{\eta}, \boldsymbol{p})_K = 0 \ \ \forall \boldsymbol{p} \in [P_{k-2}(K)]^2, \tag{10}$$

where E denotes an edge to K and $\boldsymbol{\tau}_E$ is the unit tangent to E. $(\cdot,\cdot)_K$ and $\langle\cdot,\cdot\rangle_E$ are the L^2-inner products.
With these assumptions and notation the MITC finite element method for the Reissner-Mindlin plate model, under the transverse loading $g \in H^{-1}(\Omega)$, can be written in the following form [4], [5]: *Find the deflection $w_h \in W_h$ and the rotation $\boldsymbol{\beta}_h \in \boldsymbol{V}_h$ such that*

$$a(\boldsymbol{\beta}_h,\boldsymbol{\eta}) + \frac{1}{t^2}(\boldsymbol{R}_h(\nabla w_h - \boldsymbol{\beta}_h), \boldsymbol{R}_h(\nabla v - \boldsymbol{\eta})) = (g, v) \ \ \forall (v,\boldsymbol{\eta}) \in W_h \times \boldsymbol{V}_h. \tag{11}$$

The discrete shear force is $\boldsymbol{q}_h = t^{-2}\boldsymbol{R}_h(\nabla w_h - \boldsymbol{\beta}_h) \in \boldsymbol{Q}_h$.

Superconvergence and postprocessing
For the superconvergence result we need the classical quasi-optimal interpolation operator $I_h : H^s(\Omega) \to W_h$, $s > 1$, [5]: *With a vertex a and an edge E of the triangle K, we define*

$$(v - I_K v)(a) = 0 \ \ \forall a \in K, \tag{12}$$

$$\langle v - I_K v, p\rangle_E = 0 \ \ \forall p \in P_{k-2}(E) \ \ \forall E \subset K, \tag{13}$$

$$(v - I_K v, p)_K = 0 \ \ \forall p \in P_{k-3}(K), \tag{14}$$

with $I_K = I_{h|K} \ \ \forall K \in \mathcal{C}_h$. The key property for the proof of the superconvergence is the close connection between the interpolation and reduction operators [5, Lemma 4.5]:

$$\boldsymbol{R}_h\nabla v = \nabla I_h v \ \ \forall v \in H^s(\Omega),\ s \geq 2. \tag{15}$$

Then the following superconvergence result holds [5, Theorem 4.1]:

Theorem 1. *There is a positive constant C such that*

$$\|\nabla(I_h w - w_h)\|_{0,K} \le C h_K \|\boldsymbol{\beta}-\boldsymbol{\beta}_h\|_{1,K} + \|\boldsymbol{\beta}-\boldsymbol{\beta}_h\|_{0,K} + t^2\|\boldsymbol{q}-\boldsymbol{q}_h\|_{0,K} + t^2\|\boldsymbol{q}-\boldsymbol{R}_h\boldsymbol{q}\|_{0,K}. \quad (16)$$

For one element this gives a local improvement of order $h_K + t$ when comparing the convergence rate for $\|w_h - I_h w\|_1$ to the rates for both $\|w - w_h\|_1$ and $\|w - I_h w\|_1$ [5, Theorem 3.2, Lemma 4.2]. Since $I_h w$ interpolates w at the vertices (see Eq. (12)) this also gives an indication that the vertex values of w_h converge with an improved speed.
In the postprocessing we construct an improved approximation for the deflection in the space

$$W_h^* = \{v \in W \ \mid \ v_{|K} \in P_{k+1}(K) \ \ \forall K \in \mathcal{C}_h\}. \quad (17)$$

For the postprocessing we first introduce the interpolation operator $I_h^* : H^s(\Omega) \to W_h^*$, $s > 1$, by the equations (12)—(14) with $k+1$ in place of k. Thus, the interpolation operators I_h^* and I_h are hierarchical, and the local spaces for the additional degrees of freedom are defined as

$$\widehat{W}(K) = \{v \in P_{k+1}(K) \ \mid \ I_K v = 0, \ (v,p)_K = 0 \ \ \forall p \in \tilde{P}_{k-2}(K)\}, \quad (18)$$

$$\overline{W}(K) = \{v \in P_{k+1}(K) \ \mid \ I_K v = 0, \ \langle v,p\rangle_E = 0 \ \ \forall p \in \tilde{P}_{k-1}(E) \ \ \forall E \subset K\}. \quad (19)$$

Furthermore, the space $\boldsymbol{Q}_h^*$ follows the definition (8) and the operator $\boldsymbol{R}_h^*$ the definitions (9) and (10), with $k+1$ in place of k. Now the method is defined as follows [5]:

Postprocessing scheme. *For all the triangles $K \in \mathcal{C}_h$ find the local postprocessed finite element deflection $w_{h|K}^* \in P_{k+1}(K) = P_k(K) \oplus \widehat{W}(K) \oplus \overline{W}(K)$ such that*

$$I_h w_{h|K}^* = w_{h|K}, \quad (20)$$

$$\langle \nabla w_h^* \cdot \boldsymbol{\tau}_E, \nabla \hat{v} \cdot \boldsymbol{\tau}_E\rangle_E = \langle (\boldsymbol{\beta}_h + t^2\boldsymbol{q}_h)\cdot\boldsymbol{\tau}_E, \nabla\hat{v}\cdot\boldsymbol{\tau}_E\rangle_E \ \ \forall E \subset \partial K, \quad \forall \hat{v} \in \widehat{W}(K), \quad (21)$$

$$(\nabla w_h^*, \nabla \bar{v})_K = (\boldsymbol{\beta}_h + t^2\boldsymbol{q}_h, \nabla\bar{v})_K \ \ \forall \bar{v} \in \overline{W}(K). \quad (22)$$

We note that the postprocessed deflection is conforming since $(\boldsymbol{\beta}_h + t^2\boldsymbol{q}_h)\cdot\boldsymbol{\tau}$ is continuous along inter element boundaries. For the method we have the following error estimate [5, Theorem 5.1]:

Theorem 2. *There is a positive constant C such that*

$$\begin{aligned}
&\|\nabla(w - w_h^*)\|_{0,K} \\
&\quad \le C\big(h_K\|\boldsymbol{\beta}-\boldsymbol{\beta}_h\|_{1,K} + \|\boldsymbol{\beta}-\boldsymbol{\beta}_h\|_{0,K} + t^2\|\boldsymbol{q}-\boldsymbol{q}_h\|_{0,K} \\
&\qquad + \|\nabla(w - I_h^* w)\|_{0,K} + \|\boldsymbol{\beta} - \boldsymbol{R}_h^*\boldsymbol{\beta}\|_{0,K} + t^2\|\boldsymbol{q}-\boldsymbol{R}_h^*\boldsymbol{q}\|_{0,K} + t^2\|\boldsymbol{q}-\boldsymbol{R}_h\boldsymbol{q}\|_{0,K}\big).
\end{aligned} \quad (23)$$

Also this result is local and it is made up of two parts: The first part is related to the error of the original method and the second part consists of interpolation estimates — both parts giving an improvement by the factor $h_K + t$ compared to the original approximation.

Selected computational results

Our numerical computations are performed for a test problem for which an analytical solution has been obtained in [1]. The domain is the semi-infinite region $\Omega = \{(x,y) \in \mathbb{R}^2 \ \mid \ y > 0\}$ and the loading is $g = \frac{1}{G}\cos x$. The Poisson ratio is $\nu = 0.3$, the shear modulus is $G = 1/(2(1+\nu))$, the shear corrector factor is $\kappa = 1$ and the thickness is $t = 0.01$. The boundary $\Gamma = \{(x,y) \in \mathbb{R}^2 \ \mid \ y = 0\}$ is either hard simply supported or free. We have used both uniform and non-uniform meshes with quadratic ($k = 2$) and cubic ($k = 3$) elements.

The numerical results are clearly in accordance with the theory: In the interior of the plate the convergence rate of the original finite element deflection in the H^1-norm is $r \approx k$, and the convergence rate of the postprocessed finite element deflection is $r^* \approx k+1 \approx r+1$, as seen in Fig. 1 (left). The behavior in the L^2-norm looks very similar, although to rigorously prove the improvement in that case seems to be difficult. In the boundary region of the free edge case the rate of convergence rapidly slows down for both the original and the postprocessed deflection, as proved in [6], [3]. But still, a significant accuracy improvement is obtained, especially for coarse meshes and lower order elements. Furthermore, the superaccuracy of the vertex values is obvious, as seen in Fig. 1 (right).

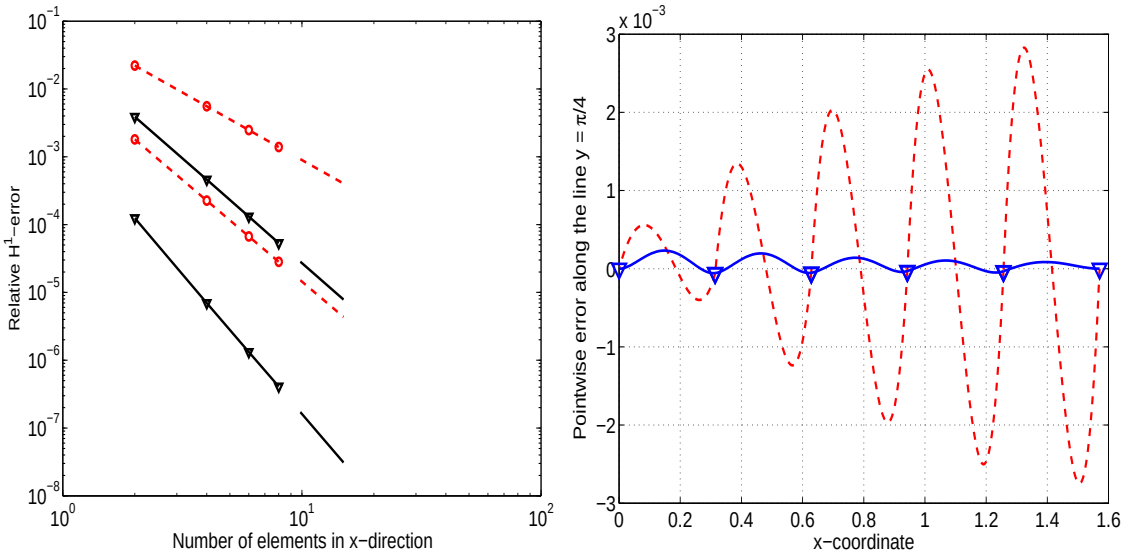

Figure 1: *Left:* Simply supported edge; Interior region; Uniform mesh; H^1- error with $k = 2, 3$ (dashed line for the original, solid line for the postprocessed deflection).
Right: Free edge; Boundary region; Non-uniform mesh; Pointwise error along the line $y = \pi/4$ with $k = 2$ (dashed line for the original, solid line for the postprocessed deflection, triangles for the vertex values).

References

[1] D. N. Arnold and R. S. Falk. Edge effects in the Reissner-Mindlin plate theory. In A. K. Noor, T. Belytschko and J. C. Simo, editors, *Analytic and Computational Models of Shells*, pages 71—90, New York. ASME (1989).

[2] K.-J. Bathe, F. Brezzi and M. Fortin. Mixed-interpolated elements for Reissner-Mindlin plates. *Int. J. Num. Meths. Eng.*, **28**, 1787—1801 (1989).

[3] L. Beirão da Veiga. Finite element methods for a modifi ed Reissner-Mindlin free plate model. *SIAM J. Num. Anal.*, **42**, 1572—1591 (2004).

[4] F. Brezzi, M. Fortin and R. Stenberg. Error analysis of mixed-interpolated elements for Reissner-Mindlin plates. *Math. Mod. Meth. Appl. Sci.*, **1**, 125—151 (1991).

[5] M. Lyly, J. Niiranen and R. Stenberg. Superconvergence and postprocessing of MITC plate elements. Research Reports A 474, Helsinki University of Technology, Institute of Mathematics, January 2005. `http://math.tkk.fi/reports`.

[6] J. Pitkäranta and M. Suri. Design principles and error analysis for reduced-shear plate-bending fi nite elements. *Numer. Math.*, **75**, 223—266 (1996).

Locking-Free Plate Elements at Free Boundary

Juhani Pitkäranta
Insitute of Mathematics
Helsinki University of Technology, Espoo, Finland
e–mail: juhani.pitkaranta@tkk.fi

Summary We study here a special problem that arises in some locking-free finite elements for the Reissner-Mindlin plate model when part of the boundary of the plate is free. We demonstrate unexpected (though predicted by theory) local error growth when the mesh is coarse as compared with the thickness of the plate.

Introduction

In plate bending problems based on the Reissner-Mindlin model, standard finite elements are known to suffer from shear locking at the limit of zero plate thickness. To avoid the effect, various special finite element formuations have been proposed. The generic idea in these so called *locking-free* formulations is to impose some numerical *shear reduction* within the otherwise usual energy principle. The reduction is done by modifying the shear energy term elementwise, e.g. by local projections, selective underintegration, mixed interpolation, numerical dampening factors, etc. In this paper we demonstrate that some of these locking-free formulations suffer from unexpected error growth at a free boundary where the boundary layer is relatively strong. Being absent in the standard FEM, the effect may be viewed as a backlash caused by shear reduction. It appears on relatively coarse meshes where the mesh spacing is large compared with the thickness of the plate. It even appears (and is particularly unexpected) at the limit of zero thickness where the exact solution has no layer.

The benchmark problem

We consider a square plate occupying the domain $\Omega = [0,1] \times [0,1] \times [\ \ t/2,\, t/2]$ ($t =$ dimensionless thickness) and the Reissner-Mindlin plate bending model where the energy of the plate is given by

$$\begin{aligned} \mathcal{F}(\theta,\psi,w) \;=\; & \frac{1}{2}\int_0^1\int_0^1 [\,\nu(\kappa_{11}+\kappa_{22})^2 + (1 \quad \nu)(\kappa_{11}^2+2\kappa_{12}^2+\kappa_{22}^2)]\,dxdy \\ & + \frac{3(1 \quad \nu)}{t^2}\int_0^1\int_0^1 (\ {}_1^2 + \ {}_2^2)\,dxdy \qquad \int_0^1\int_0^1 fw\,dxdy. \end{aligned} \tag{1}$$

Here ν is the Poisson ratio and κ_{ij} and $\ _i$ stand for the bending and transverse shear strains, respectively. The strains have their usual expressions in terms of θ, ψ (rotations) and w (transverse deflection). The transverse load f is chosen to be of the simple form

$$f(x,y) = F\cos ky, \quad k = 2\pi. \tag{2}$$

The boundary conditions are set as follows:

$$\begin{aligned} x = 0: &\qquad \text{free} \\ x = 1: &\qquad \text{clamped} \\ y = 0,1: &\qquad \text{periodic} \end{aligned}$$

With these assumptions the problem reduses to one dimension and is solvable exactly. The solution $\mathbf{u} = (\theta,\psi,w)$ is of the form

$$\mathbf{u} = \mathbf{u}_l + \mathbf{u}_s, \tag{3}$$

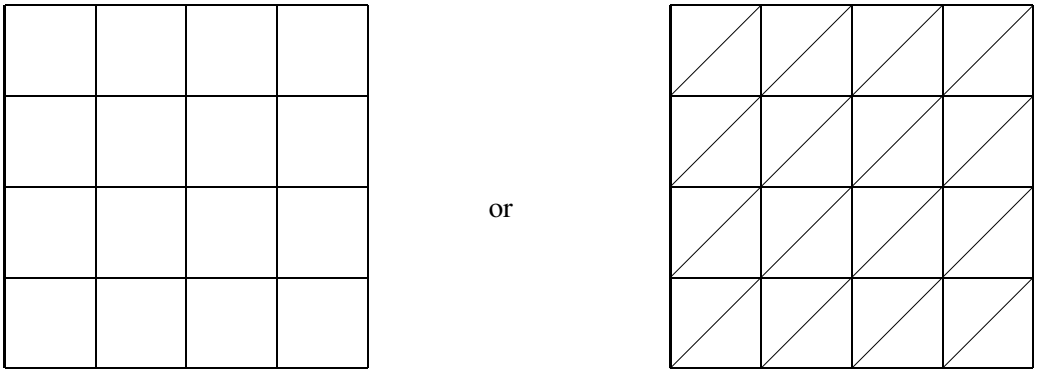

Figure 1: The finite element meshes

where $\mathbf{u}_s$ is smooth uniformly in t, apart from a weak layer at $x = 1$, and $\mathbf{u}_l$ is the dominant layer at the free boundary as given by

$$\mathbf{u}_l = G\,(kt^2 \sin ky,\; at \cos ky,\; 0)\, e^{\;ax/t}, \tag{4}$$

where G is proportional to F and $a = \sqrt{12 + k^2 t^2}$.

The finite element models
We ssume either a uniform rectangular mesh with mesh spacing h or a triangular mesh obtained by subdividing the rectangels into two triangles, see Fig. 1. We consider three locking-free plate elements of lowest order:

E1 The bilinear MITC4/QUAD4 element — one of the classics of finite element engineering. The shear reduction is imposed either by mixed interpolation or (equivalently) by anisotropic underintegration, see [1, 2]. For the error analysis, see [3] and the references therein.

E2 A modification of the previous element. In addition to shear reduction one imposes here numerical *shear dampening* by factor $t^2/(h^2 + t^2)$ — an idea that dates back to [4]. The combination of the two modifications is suggested by mathematical error analysis, see [5] for the analysis in a slightly different context.

E3 A triangular element proposed in [6]. In this formulation, which also originates from mathematical error analysis, the usual linear element is enriched by cubic bubble functions for the rotations and is used as nonconforming element (with the dgrees of freedom at the midpoints of the sides) for the transverse deflection.

Error bounds
We decompose the finite element solution in the benchmark problem in analogy with Eq. (3) as

$$\mathbf{u}_h = \mathbf{u}_{lh} + \mathbf{u}_{sh}\,,$$

where $\mathbf{u}_{lh}$ and $\mathbf{u}_{sh}$ stand for the finite element projections of $\mathbf{u}_s$ and $\mathbf{u}_l$, respectively. Since $\mathbf{u}_s$ is smooth uniformly in t and since the finite elements considered are all locking-free, the elements behave optimally when approximating $\mathbf{u}_s$. Quantitatively this means that the error $\mathbf{u}_s \quad \mathbf{u}_{sh}$, when measured in the energy norm, is of order $\mathcal{O}(h)$ uniformly in t for all the three elements [3, 7, 8].

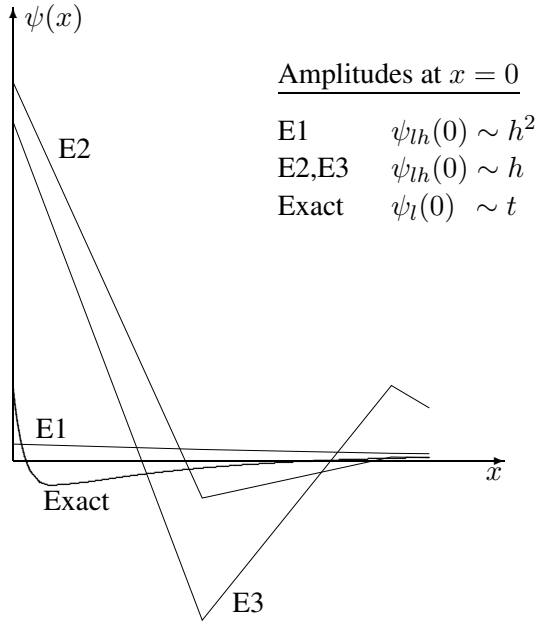

Figure 2: Finite element layer modes

For the layer error term, the analysis in [7, 8] gives the following bounds in the energy norm:

$$h < t: \quad \mathbf{u}_l \quad \mathbf{u}_{lh} = \mathcal{O}(h/\sqrt{t}) \qquad \text{(E1,E2,E3)} \tag{5}$$

$$h \geq t: \quad \mathbf{u}_l \quad \mathbf{u}_{lh} = \begin{cases} \mathcal{O}(h + \sqrt{t}) & \text{(E1)} \\ \mathcal{O}(\sqrt{h}) & \text{(E2,E3)} \end{cases} \tag{6}$$

Here the bound (5) indicates that on sufficiently fine meshes ($h < t$), all the three elements behave optimally (as compared with interpolation accuracy) even when approximating the layer. On coarser meshes, especially when $t \ll h$, the finte element models considered obviously fail to capture the layer. The best one can then hope for is that the layer in the numerical model is more or less absent. That being the case, the layer error should be of the same order as the layer itself, i.e., of order $\mathcal{O}(\sqrt{t})$. As shown by the second bound (6), this is essentially how the element E1 behaves (modulo an additional term of order $\mathcal{O}(h)$). Instead the elements E2 and E3 behave differently: The layer approximation error is of order $\mathcal{O}(h^{1/2})$ uniformly in the range $0 \leq t \leq h$, a result confirmed by a *lower* error bound in [8]. Thus there arises numerical *layer amplification* on coarse meshes with elements E2,E3. According to the error analysis this is not a locking effect but rather a consistency (or equilibrium) error caused by the shear reductions [8]. The phenomenon is particularly interesting at $t = 0$, where the exact solution is the Kirchhoff solution with no layer.

Benchmark solutions

We solve the benchmark problem by the three finite elements methods, choosing $\nu = 0$, $t = 0.01$ and $h = 0.05 = 5t$. We focus on the layer mode $\mathbf{u}_{lh}$ in each case. In Fig. 2 the horizontal profiles of the numerical layer modes are shown for the vertical rotation ψ. For comparison, the exact layer mode is also shown. We observe that the E1 aproximation of the layer mode has a small amplitude and gives little indication of the presence of the layer as expected. In the E2 and E3 approximationsis, a numerical boundary layer appears. The amplitude and the length scale of decay of this layer are both of order $\mathcal{O}(h)$, so the strength in the energy norm is of order $\mathcal{O}(h^{1/2})$. The slow rate of convergence when $t \ll h$ is thus explained.

Conclusions

We have demonstrated by benchmark solutions that in some of the locking-free plate element formulations proposed in the literature there arises numerical layer amplification at free boundary. In the MITC4/QUAD4 formulation this effect does not appear, so some shear modifications are better than others in this respect. In general, when designing locking-free finite element formulations for plates or shells, one should take into account that numerical modifications focusing on one solution component may cause unwanted error growth on other components.

References

[1] R.H. MacNeal. A simple quadrilateral shell element. *Computers & Structures*, **8**, 175–183, (1978).

[2] K.J. Bathe and E.N: Dvorkin. A four-node plate bending element based on Mindlin/Reissner plate theory and mixed interpolation. *Int. J. Num. Meth. Eng.*, **21**, 367–383, (1985).

[3] J. Pitkäranta. Mathematical and historical reflections on the lowest-order finite element models for thin structures. *Computers & Structures*, **81**, 895–909, (2003).

[4] I. Fried and S.K. Yang. Triangular, nine-degrees-of-freedom, C^0 plate bending element of quadratic accuracy. *Quart. Appl. Math.*, **31**, 303–312, (1973).

[5] D. Chapelle and R. Stenberg. An optimal low-order locking-free finite element method for Reissner-Mindlin plates. *Math. Models Methods Appl. Sci.*, **8**, 407–430, (1998).

[6] D.N. Arnold and R.S. Falk. A uniformly accurate finite element method for the Reissner-Mindlin plate. *SIAM J. Numer. Anal.*, **26**, 1276–1290, (1989).

[7] J. Pitkäranta and M. Suri. Design principles and error analysis for reduced-shear plate-beding finite elements. *Numer. Math.*, **75**, 223–266, (1996).

[8] J. Pitkäranta and M. Suri. Upper and lower error bounds for plate-bending finite elements. *Numer. Math.*, **84**, 611–648, (2000).

Finding the most efficient rotation-free triangular shell element

Mattias Gärdsback and A. Gunnar Tibert*
Department of Mechanics
Royal Institute of Technology, Stockholm, Sweden
e–mail: gunnart@mech.kth.se

Summary To simulate the deployment of lightweight structures, efficient shell elements are required. Triangular rotation-free shell elements, where the out-of-plane rotation around each edge is approximated from the main element and the adjacent element, represent a group of such elements. Various formulations for the plate bending part have been published. Simple elements, such as the CST and the LST, have then been used for the membrane part. In this article, the aim has been to find the best possible superposition of a rotation-free plate part and membrane part.

Introduction

For most thin-film structures, i.e. airbags, the bending stiffness may be neglected in the simulation. Contrary, for space inflatables, the vanishingly small bending stiffness may have non-negligible effects on the deployment behaviour. In the micro-gravity environment of space, the strain energy, induced by the folding of the structure, may be sufficient to cause premature deployment for certain structures, e.g. crease-pattern folded tubes [1]. Wrinkling is also an important issue in many applications. Therefore, it is crucial to take into account the bending stiffness.

Due to the singularity of the unstressed folded configuration, explicit time integration schemes should be used in a dynamic deployment simulation. Since a time-consuming explicit integration scheme is required, at least during the initial phase of the deployment, simple and rapidly computed elements are desirable. Triangular elements are usually the preferred choice as they can be adapted to arbitrary geometries and because of efficient triangle mesh generators. In this respect, the triangular shell elements without rotational DOF are particularly interesting since the bending stiffness can be included without increasing the size of the problem. This paper reviews the various formulations available for these elements in an attempt to find a simple, yet accurate, one for deployment simulations of inflatable structures.

Summary of rotation-free elements

The shell elements without rotational DOF, i.e. *rotation-free* (RF) elements are composed of a plate bending part, which uses the out-of-plane displacements of the three adjacent elements to approximate the curvatures, and a common membrane element, using the in-plane displacements to compute the in-plane strains.

Plate bending

Hamphire et al. [2], Phaal and Calladine [3] [4], Oñate et al. [5] [6] [7], Brunet and Sabourin [8] and Guo et al. [9] have all developed RF plate elements. The derivations differ, but the main assumptions are almost the same. They are all based on Kirchoffs plate bending theory and assumes constant curvatures for simplicity, i.e the basic assumptions are the same as used by Morley [10]. In the RF elements the rotations used by Morley are approximated using the out-of-plane displacements.

The elements are derived differently, but the resulting stiffness matrices are almost the same for all the RF elements listed above, except the one by Phaal and Calladine [3] [4]. The reason is that the same important steps and the same important assumptions are used. The hinges around each edge of the main element can be described by the two elements sharing the edge. The first step is to determine the deflection angles (α), i.e. the angles that each of the two elements indivdually forms relative to the common edge due to the displacements in the nodes. All but Phaal and

Calladine [3] [4] then relates α to the rotations, and then the rotations to the (constant) curvatures. The only difference is how the contribution from the two deflection angles are weighted. Oñate et al. used the average in their first BST element [5] [6], then updated it to use second degree polynomial shape functions in their EBST element [7]. Brunet and Sabourin [8] and Guo et al. [9] used weights proportional to the inverse of the heights of the triangles perpendicular to the edge.

Phaal and Calladine [3] [4] use a different approach. The displacements are expressed as polynomials of second degree, where the coefficients of the quadratic terms are proportional to the curvatures. The curvatures (κ) are then determined to best fit with the the coordinates and displacements of the nodes. A small disadvantage is that the inverse of a 3 times 3 matrix relating κ and α is required, which makes the handling of boundary conditions slightly more complicated.

Membrane part

In most of the rotation-free shell elements, the constant strain triangle (CST) is used to represent the membrane stiffness. The CST element has been the preferred choice because of its simplicity, having only the in-plane translations in the three corner nodes as degrees of freedom.

The second most simple choice would be to use a linear strain triangle (LST) approach. Recently, Oñate and Flores [7] suggested to use the six nodes in the same patch of elements as for the plate bending part to compute an isoparametric LST triangle. This approach has primarily two disadvantages because of the overlapping: it is nonconforming and it becomes unnecessarily computationally expensive. This nonconformity may cause problems especially for unstructured grids.

Here, we also suggest that isoparametric LST elements are used because of the superior accuracy compared to CST elements. The LST elements are computed as usual by using the same nodes as for the plate bending part, but one fourth of the elements compared to the LST approach by Oñate and Flores [7].

The advantages are that the accuracy is better than for the CST element, and the nonconformity, overlapping and cumbersome boundary conditions associated with the approach by Oñate and Flores [7] are avoided. The main disadvantage with this approach would be that some additional work is necessary when all nodes are not in the same plane. If the difference is small, which it usually will be, the projections can simply be used. If the difference is large then distances normal to the surface should be used. Another problem may be the same as for LST elements in general, shear-locking may occur if more than one point is used in the reduced integration.

References

[1] Tsunoda H, Senbokuya Y, Watanabe M. Deployment method of space inflatable structures using folding crease patterns. In *Proceedings of the 44th AIAA/ASME/ASCE/AHS/ASC Structures, Structural Dynamics, and Materials Conference and Exhibit*, Norfolk, VA, USA, April 7–10, 2003. AIAA 2003-1979.

[2] Hampshire JK, Topping BHV, Chan HC. Three node triangular bending elements with one degree of freedom per node. *Engineering Computations* 1992; **9**:49-62.

[3] Phaal R, Calladine R. A simple class of finite elements for plate and shell problems. I: Elements for beams and thin flat plates. *International Journal for Numerical Methods in Engineering* 1992; **35**:955-977.

[4] Phaal R, Calladine R. A simple class of finite elements for plate and shell problems. II: An element for thin shells, with only translational degrees of freedom. *International Journal for Numerical Methods in Engineering* 1992; **35**:979-996.

[5] Oñate E, Cervera M. Derivation of thin plate bending elements with one degree of freedom per node: A simple three node triangle. *Engineering Computations* 1993; **10**:543-561.

[6] Oñate E, Zárate F. Rotation-free triangular plate and shell elements. *International Journal for Numerical Methods in Engineering* 2000; **47**:557-603.

[7] Oñate E, Flores GF. Improvements in the membrane behaviour of the three node rotation-free BST shell triangle using an assumed strain approach. *Computer Methods in Applied Mechanics and Engineering* 2005; **194**:907-932.

[8] Brunet M, Sabourin F. A simplified triangular shell element with a necking criterion for 3-D sheet-forming analysis. *Journal of Materials Processing Technology* 1995. **50**:238-251.
[9] Guo YQ, Gati W, Naceur H, Batoz JL. An efficient DKT rotation free shell element for springback simulation in sheet metal forming. *Computers and Structures* 2002. **80**:2299-2312.
[10] Morley LSD. The constant-moment plate-bending element. *Journal of Strain Analysis* 1971; **6**:20-24.

A Posteriori Error Estimates in Linear Elastic Fracture Mechanics based on Different FE-Solution Spaces for the Primal and the Dual Problem

Marcus Rüter*, **Sergey Korotov and Christian Steenbock**
Institute of Mathematics
Helsinki University of Technology, P.O. Box 1100, 02015 TKK, Finland
e–mail: Marcus.Ruter@hut.fi

Summary The objective of the present paper is to derive goal-oriented a posteriori error estimators for the error obtained while approximately evaluating the nonlinear J-integral as a fracture criterion in linear elastic fracture mechanics (LEFM) using the finite element method. Such error estimators are based on the well-established strategy of solving an auxiliary dual problem. In a straightforward fashion, the solution to the dual problem is sought in the same FE-space as the solution to the primal problem, i.e. on the same mesh, although it merely acts as a weight of the discretization error only. In this paper, we follow the strategy recently proposed by Korotov [6] and derive goal-oriented error estimators of the averaging type, where the dual solution is computed on a different—usually coarser—mesh than the primal solution.

Introduction

In (macroscopic) continuum mechanics of elastic deformations, the failure of structures can generally be analyzed within the framework of fracture mechanics as one possible approach. In this paper, we restrict our considerations to the special case of linear elastic fracture mechanics as used in analyzing the fracture behavior of materials denoted as "brittle". A fundamental step was the introduction of the J-integral concept by Cherepanov [3] and Rice [7] as an appropriate criterion for crack propagation, which can be interpreted within the framework of Eshelbian mechanics as the absolute value of the material force acting on the crack tip, see e.g. Steinmann [11].
In a finite element setting, the a posteriori estimation of the error of the J-integral requires a special approach widely known as *goal-oriented* error estimation as introduced by Eriksson et al. [4] and developed further by Becker and Rannacher [2] and others. A key feature in this context is the construction of the dual data. Since the J-integral is nonlinear by definition, a suitable linearization is required to pose and to solve the dual problem.
In recent years, goal-oriented adaptive finite element methods in fracture mechanics have been established, see Rüter et al. [8, 10, 9] and Heintz et al. [5]. Remarkably, the first steps in this direction have already been taken in 1984 by Babuška and Miller [1].
The paper is organized as follows: first, the boundary value problem of linearized elasticity is introduced and the J-integral is presented. Subsequently, we discuss the construction of the dual data. Finally, we focus on averaging-based error estimation techniques for the error of the J-integral based on the solution of the dual problem and present an illustrative numerical example.

Linear elastic fracture mechanics

The linearized elasticity problem

In this section, we briefly present the linearized elasticity problem. To begin with, let us introduce the elastic body which is given by the closure of a bounded open set $\Omega \subset \mathbb{R}^3$ with a piecewise smooth, polyhedral and Lipschitz continuous boundary Γ such that $\Gamma = \bar{\Gamma}_D \cup \bar{\Gamma}_N$ and $\Gamma_D \cap \Gamma_N = \emptyset$, where Γ_D and Γ_N are the portions of the boundary Γ where Dirichlet and Neumann boundary conditions are imposed, respectively. Assuming, for the sake of simplicity, homogeneous Dirichlet boundary conditions, all admissible displacements $\boldsymbol{u} : \bar{\Omega} \to \mathbb{R}$ of the elastic body $\bar{\Omega}$ are elements of the Hilbert space $\mathscr{V} = \{\boldsymbol{v} \in [H^1(\Omega)]^3 \ ; \ \boldsymbol{v}|_{\Gamma_D} = \boldsymbol{0}\}$.
The weak formulation of the linearized elasticity problem then reads: find $\boldsymbol{u} \in \mathscr{V}$ such that

$$a(\boldsymbol{u}, \boldsymbol{v}) = F(\boldsymbol{v}) \quad \forall \boldsymbol{v} \in \mathscr{V} \tag{1}$$

with the continuous, symmetric and $\mathscr{V}$-elliptic bilinear form $a : \mathscr{V} \times \mathscr{V} \to \mathbb{R}$ and the continuous linear form $F : \mathscr{V} \to \mathbb{R}$ defined by

$$a(\boldsymbol{u}, \boldsymbol{v}) = \int_{\Omega} \boldsymbol{\sigma}(\boldsymbol{u}) : \boldsymbol{\varepsilon}(\boldsymbol{v}) \, \mathrm{d}V \quad \text{and} \quad F(\boldsymbol{v}) = \int_{\Gamma_N} \bar{\boldsymbol{t}} \cdot \boldsymbol{v} \, \mathrm{d}A, \tag{2}$$

respectively. Here, $\boldsymbol{\sigma} = \mathbb{C}_{\sigma} : \boldsymbol{\varepsilon}$ denotes the stress tensor given in terms of the fourth-order elasticity tensor $\mathbb{C}_{\sigma}$ and the strain tensor $\boldsymbol{\varepsilon}$ defined as the symmetric gradient of $\boldsymbol{u}$. Furthermore, $\bar{\boldsymbol{t}} \in [L_2(\Gamma_N)]^3$ are prescribed tractions imposed on the Neumann boundary Γ_N. For the sake of simplicity, body forces are omitted in our formulation.
The discrete counterpart of the variational problem (1) consists in seeking a solution $\boldsymbol{u}_{1h}$ in a finite-dimensional subspace $\mathscr{V}_{1h} \subseteq \mathscr{V}$ satisfying

$$a(\boldsymbol{u}_{1h}, \boldsymbol{v}_{1h}) = F(\boldsymbol{v}_{1h}) \quad \forall \boldsymbol{v}_{1h} \in \mathscr{V}_{1h}. \tag{3}$$

The J-integral as a crack propagation criterion
In the classical theory of LEFM, three principally different but equivalent strategies have been developed in the last century, namely the *energy release rate concept*, the *stress intensity approach* and the *J-integral concept*, as originally proposed by Cherepanov [3] and Rice [7].
In this paper, we deal in particular with the widely-used J-integral concept. The J-integral, which is a nonlinear functional $J : \mathscr{V} \to \mathbb{R}$, can be conveniently derived by a straightforward application of the concept of material forces, since J is the projection of the material force $\boldsymbol{F}_{\text{mat}}$ acting on the crack tip into the direction of crack propagation (given in terms of the unit vector $\boldsymbol{e}_{||}$), i.e.

$$J(\boldsymbol{u}) = \int_{\Gamma_J} \boldsymbol{e}_{||} \cdot \tilde{\boldsymbol{\Sigma}}(\boldsymbol{u}) \cdot \boldsymbol{n} \, \mathrm{d}A, \tag{4}$$

where Γ_J is an arbitrary contour around the crack tip and $\tilde{\boldsymbol{\Sigma}}$ denotes the so-called Newton-Eshelby stress tensor given by $\tilde{\boldsymbol{\Sigma}} = W_s \boldsymbol{I} - \boldsymbol{H}^T \cdot \boldsymbol{\sigma}$ with specific strain-energy function W_s, identity tensor $\boldsymbol{I}$ and displacement gradient $\boldsymbol{H}$. Hence, the material force acting on the crack tip can be evaluated in terms of the (material) tractions $\tilde{\boldsymbol{\Sigma}} \cdot \boldsymbol{n}$ at the contour Γ_J. Notice the analogy to a physical force which can be determined by the (physical) tractions $\boldsymbol{\sigma} \cdot \boldsymbol{n}$.
A pre-existing crack then starts to grow if J reaches the material dependent threshold J_c.
From a computational point of view, however, it proves convenient to compute the J-integral by means of the equivalent domain expression

$$J(\boldsymbol{u}) = -\int_{\Omega_J} \boldsymbol{H}(q\boldsymbol{e}_{||}) : \tilde{\boldsymbol{\Sigma}}(\boldsymbol{u}) \, \mathrm{d}V \tag{5}$$

rather than by the contour expression (4). In the above, $q = q(x, y)$ (or $q = q(x, y, z)$ in three dimensions) represents an arbitrary, continuously differentiable weighting function with $q = 1$ at the crack tip and $q = 0$ on the contour (or surface) Γ_J that bounds the area (or volume) Ω_J.

A posteriori error estimation

The error of the J-integral
Our main objective in this paper is to estimate the nonlinear error measure $J(\boldsymbol{u}) - J(\boldsymbol{u}_{1h})$. Since J is nonlinear by definition, we first derive its exact linearization $J_S : \mathscr{V} \to \mathbb{R}$ such that $J(\boldsymbol{u}) - J(\boldsymbol{u}_{1h}) = J_S(\boldsymbol{u}, \boldsymbol{u}_{1h}; \boldsymbol{e})$ with discretization error $\boldsymbol{e} = \boldsymbol{u} - \boldsymbol{u}_{1h}$. Upon applying the fundamental theorem of calculus on J, the so-called secant linear form J_S takes on the form

$$J_S(\boldsymbol{u}, \boldsymbol{u}_{1h}; \boldsymbol{e}) = -\int_0^1 \int_{\Omega_J} \boldsymbol{H}(q\boldsymbol{e}_{||}) : \mathbb{C}_{\Sigma}(\boldsymbol{\xi}(s)) : \boldsymbol{H}(\boldsymbol{e}) \, \mathrm{d}V \, \mathrm{d}s, \tag{6}$$

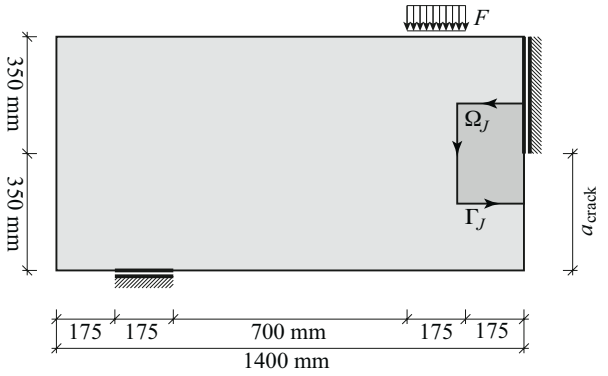

Figure 1: Parallel-edge-cracked borosilicate glass plate, primal loading and area Ω_J.

see Rüter and Stein [9], with $\boldsymbol{\xi}(s) = \boldsymbol{u}_{1h} + s\boldsymbol{e}$, $s \in [0,1]$ and fourth-order tensor of elastic tangent moduli associated with the Newton-Eshelby stress tensor $\mathbb{C}_\Sigma$, cf. Heintz et al. [5], defined as

$$\mathbb{C}_\Sigma = \frac{\partial \tilde{\boldsymbol{\Sigma}}}{\partial \boldsymbol{H}} = \boldsymbol{I} \otimes \boldsymbol{\sigma} - \boldsymbol{I} \underline{\otimes} \boldsymbol{\sigma} - \lambda \boldsymbol{H}^T \otimes \boldsymbol{I} - \mu \left(\boldsymbol{H}^T \underline{\otimes} \boldsymbol{1} + \boldsymbol{H}^T \overline{\otimes} \boldsymbol{1} \right), \tag{7}$$

where λ and μ are Lamé parameters.

Duality techniques
In order to estimate the error of the J-integral, we follow the general strategy of solving an auxiliary dual problem which reads: find a solution $\overset{*}{\boldsymbol{u}} \in \mathscr{V}$ that satisfies

$$a(\overset{*}{\boldsymbol{u}}, \boldsymbol{v}) = J_S(\boldsymbol{u}, \boldsymbol{u}_{1h}; \boldsymbol{v}) \quad \forall \boldsymbol{v} \in \mathscr{V}. \tag{8}$$

An *exact* error representation formula for the error measure $J_S(\boldsymbol{u}, \boldsymbol{u}_{1h}; \boldsymbol{e})$ in terms of the solution of the dual problem (8) is now simply obtained by substituting $\boldsymbol{v} = \boldsymbol{e}$ into (8) and reads

$$J_S(\boldsymbol{u}, \boldsymbol{u}_{1h}; \boldsymbol{e}) = a(\boldsymbol{e}, \overset{*}{\boldsymbol{u}} - \pi \overset{*}{\boldsymbol{u}}_{2h}) + a(\boldsymbol{e}, \pi \overset{*}{\boldsymbol{u}}_{2h}) \qquad \forall \pi \overset{*}{\boldsymbol{u}}_{2h} \in \mathscr{V}_{2h} \tag{9a}$$

$$= a(\boldsymbol{e}, \overset{*}{\boldsymbol{u}} - \pi \overset{*}{\boldsymbol{u}}_{2h}) + R(\boldsymbol{u}_{1h}; \pi \overset{*}{\boldsymbol{u}}_{2h}) \quad \forall \pi \overset{*}{\boldsymbol{u}}_{2h} \in \mathscr{V}_{2h} \tag{9b}$$

with residual functional of the primal problem $R : \mathscr{V} \to \mathbb{R}$ defined as

$$R(\boldsymbol{u}_{1h}; \pi \overset{*}{\boldsymbol{u}}_{2h}) = F(\pi \overset{*}{\boldsymbol{u}}_{2h}) - a(\boldsymbol{u}_{1h}, \pi \overset{*}{\boldsymbol{u}}_{2h}), \tag{10}$$

where the finite-dimensional subspace $\mathscr{V}_{2h} \subseteq \mathscr{V}$ is generally different from $\mathscr{V}_{1h}$. Note that in the special case where $\mathscr{V}_{2h} \subseteq \mathscr{V}_{1h}$, the residual R clearly vanishes due to the Galerkin orthogonality. In computational practice, we choose $\pi \overset{*}{\boldsymbol{u}}_{2h}$ as the finite element solution of the discretized dual problem (8). In this case, the secant form $J_S(\boldsymbol{u}, \boldsymbol{u}_{1h}; \boldsymbol{e})$ is approximated by its tangent $J_T(\boldsymbol{e}) = J_S(\boldsymbol{u}_{1h}, \boldsymbol{u}_{1h}; \boldsymbol{e})$. The goal-oriented a posteriori error estimator is then simply obtained by averaging the gradients that appear in the bilinear form a (on the element level) as described in Korotov [6], see also the references therein. In this fashion, however, no error bounds can be obtained. Finally, it should be emphasized that only the bilinear form a needs to be approximated for the computation of the error estimator, since the residual functional R can be computed exactly.

Numerical Example
The system considered in this numerical example is a parallel-edge-cracked borosilicate glass plate in plane-stress state subjected to 4-point bending, as depicted in Figure 1. For the chosen

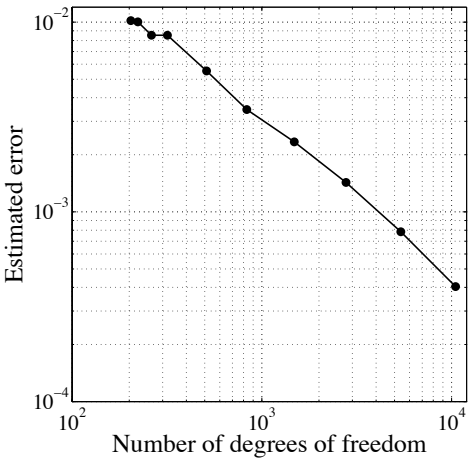

Figure 2: Estimated error $J(\boldsymbol{u}) - J(\boldsymbol{u}_{1h})$.

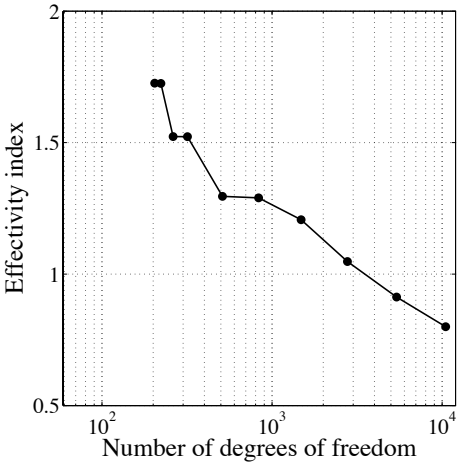

Figure 3: Effectivity index.

borosilicate glass, the following material data are assumed: $E = 64\,000$ N/mm^2, $\nu = 0.2$ and $J_c = 0.015$ kJ/m^2. The chosen load in this example is $F = 0.6$ N/mm^2. Due to symmetry considerations, only one half of the specimen is modeled using triangular P_1-elements.
The estimated error of the J-integral is plotted in Figure 2. Here, an optimal error convergence can be observed, although—within the adaptive mesh refinement process—the dual finite element solution is solved only once on a coarse mesh (758 degrees of freedom). The associated effectivity index is visualized in Figure 3 and also shows a good result around the desired value of "1".

Acknowledgments
Marcus Rüter is supported by the DFG under the grant no. RU1213/1-1. Sergey Korotov is supported by the Academy Research Fellowship no. 208628 from the Academy of Finland. Christian Steenbock is supported by the project no. 211512 from the Academy of Finland.

References

[1] I. Babuška and A. Miller The post-processing approach in the finite element method. Part 3: A posteriori error estimates and adaptive mesh selection. *Int. J. Numer. Meth. Engng,* **20**, 2311–2324, (1984).
[2] R. Becker and R. Rannacher A feed-back approach to error control in finite element methods: Basic analysis and examples. *East-West J. Numer. Math.,* **4**, 237–264, (1996).
[3] G. Cherepanov Crack propagation in continuous media. *J. Appl. Math. Mech.,* **31**, 503–512, (1967).
[4] K. Eriksson, D. Estep, P. Hansbo and C. Johnson Introduction to adaptive methods for differential equations. *Acta Numer.*, 106–158, (1995).
[5] P. Heintz, F. Larsson, P. Hansbo and K. Runesson Adaptive strategies and error control for computing material forces in fracture mechanics. *Int. J. Numer. Meth. Engng,* **60**, 1287–1299, (2004).
[6] S. Korotov New technologies for control of local errors in engineering computations by FEM. *Proceedings of the 18th Nordic Seminar on Computational Mechanics*, Helsinki, Finland, (2005).
[7] J. Rice A path independent integral and the approximate analysis of strain concentration by notches and cracks. *J. Appl. Mech.,* **35**, 379–386, (1968).
[8] M. Rüter, P. Heintz, F. Larsson, P. Hansbo, K. Runesson and E. Stein Strategies for goal-oriented a posteriori error estimation in elastic fracture mechanics. In E. Lund et al., editors, *Proceedings of the 15th Nordic Seminar on Computational Mechanics* pages 43–46, Aalborg, Denmark, (2002).
[9] M. Rüter and E. Stein Goal-oriented a posteriori error estimates in linear elastic fracture mechanics. *Comput. Methods Appl. Mech. Engrg.,* in press, (2005).
[10] E. Stein, M. Rüter and S. Ohnimus Adaptive finite element analysis and modelling of solids and structures. Findings, problems and trends. *Int. J. Numer. Meth. Engng,* **60**, 103–138, (2004).
[11] P. Steinmann, D. Ackermann and F.J. Barth Application of material forces to hyperelastostatic fracture mechanics. II. Computational setting. *Int. J. Solids Structures,* **38**, 5509–5526, (2001).

FPK-equation solutions for stochastic structural response

Pentti Varpasuo
Fortum Nuclear Services Ltd,
Helsinki, Finland, e-mail:
pentti.varpasuo@kolumbus.fi

Summary Brownian motion studies enabled the modeling of the stochastic structural response with the aid of multi-dimensional Markov processes. The state transition probability function for a Markov process is the solution of a partial differential equation, known as the Fokker Planck Kolmogorov (FPK) equation, or forward diffusion equation. The FPK- equation governs the diffusion of probability mass in state space. It is analogical in form to the diffusion equations for heat and mass transfer in thermo-hydraulic problems. The drift and diffusion coefficients in the FPK-equation can be related to the parameters in the dynamic equations of motion. The finite element formulation using standard software for diffusion problems forms an effective approach for solving non-linear random vibration problems with the aid of FPK -equation.

Introduction

The Brownian motion studies were the basis for the modeling of the response of dynamic systems to random excitation in terms of multi-dimensional Markov processes (Soong, 1973), (Roberts & Spanos, 1990), (Soong & Grigoriu, 1993), (Lin & Cai, 1995), (Soize, 1998). The state transition probability function for a Markov process can be exoressed in the form of the solution of partial differential equation, known as the Fokker Planck Kolmogorov (FPK) equation.

The Fokker Planck Kolmogorov equation that determines the diffusion of probability mass in state space, is analogical to the diffusion equations of heat or mass transfer in thermo-hydraulic problems. The drift coefficients and the diffusion matrix in the FPK equation are related to the parameters in equations of motion of the vibration systems.

The solution of FPK –equation offers an approach for solving non-linear random vibration problems.

The finite element solution follows the references (Yi, Spencer & Bergman, 1997), (Wojtkiewicz & Bergman, 2001a) and (Wojtkiewicz & Bergman, 2001b).

Literature survey

Soong (1973) gives the FPK-equation formulation and solution for a single-degree of freedom oscillator excited with white noise W(t):

$$X''(t) + 2\beta X'(t) + k(X) = W(t) \tag{1}$$

With X(t) = X1(t), X'(t) = X2(t) and with the vector X(t) = [X1(t), X2(t)]T Equation (1) can be presented in Ito equation form as follows:

$$dX(t)=[X_2(t),-k(X_1(t))-2\beta X_2(t)]^T dt+[0,dB(t)]^T \tag{2}$$

where

$$E\{dB(t)\} = 0,\ E\{[dB(t)]^2\} = 2Ddt \tag{3}$$

The Fokker-Planck-Kolmogorov equation can then be written

$$\partial f(x,t|x_0,t_0)/\partial t = -\partial/\partial x_1(x_2 f) + \partial/\partial x_2\{[k(x_1) +2\beta x_2]f\} +\partial^2/\partial x_2{}^2(Df) \tag{4}$$

The solution for the stationary density function $f_s(x_1,x_2)$ can then be written

$$f_s(x_1,x_2) = c\ \exp\{-2\beta/D[\int_0^{x1} k(x)dx + x_2^2/2]\} \quad (5)$$

Soong&Grigoriu, 1993, give the solution of Duffing – equation with the aid of FPK- equation as follows. The oscillator has the unit mass, the damping parameter is c, and the restoring force is given by the function U'(x). The oscillator is subjected to zero-mean Gaussian white-noise excitation W(t) with one-sided power spectral density G_0. The displacement X(t) of the oscillator satisfies the differential equation

$$X''(t) + cX'(t) + U'(X(t)) = W(t) \quad (6)$$

an alternative Ito form of this equation is

$$dX_1(t) = H_{,2}[\underline{X}(t)]dt; \quad (7)$$
$$dX_2(t) = -\{H_{,1}[\underline{X}(t)] + cH_{,2}[\underline{X}(t)]\}dt + (\pi G_0)^{1/2}dB(t)$$

In Equation (7) $X_1(t) = X(t)$; $X_2(t) = X'(t)$; $H(\underline{\mathbf{X}}) = U(X) + X^2/2$ denotes the total mechanical energy; $H_{,k} = \partial H/\partial x_k$; and B(t) is the standard Wiener process with independent increments dB(t) of zero means and variances dt. The vector process $\underline{\mathbf{X}}(t)$ having components X_1 (t) and X_2 (t) is of the diffusion type. The stationary Fokker-Planck equation for the transition probability density $f(\underline{\mathbf{x}},t|\underline{\mathbf{x}}_0,t_0)$ is

$$-\partial/\partial x_1(H_{,2}f) - \partial/\partial x_2[(-H_{,1} - cH_{,2})f] + \pi G_0/2\partial^2 f/\partial x_2^2 \quad (8)$$

Suppose $U'(X) = \omega_0^2 X(1 + \varepsilon X^2)$. The system with this restoring function is called the Duffing oscillator. The stationary probability density of $\underline{\mathbf{X}}(t)$ is

$$f(x_1,x_2) = \{(2\pi)^{1/2}\sigma_0' q \exp[-1/(2\sigma_0^2)(x_1^2 + \varepsilon/2x_1^4)]\}\ \{1/(2\pi\sigma_0')^{1/2}\exp(-x_2^2/(2\sigma_0^{2'})\} \quad (9)$$

where $\sigma_0^2 = \pi G_0/(2c\omega_0^2)$ and $\sigma_0^{2'} = \omega_0^2\sigma_0^2$ represent stationary variances of X(t) and X'(t) for linear oscillator when $\varepsilon=0$. The normalization constant q is given by

$$q-1 = \pi(G_0/(2c\varepsilon))^{1/2}\exp\ [1/(8\varepsilon\sigma_0^2 K_{1/4}(1/(8\varepsilon\sigma_0^2))] \quad (10)$$

where $K_{1/4}$ is the modified Bessel function of order ¼. The stationary variance of the displacement is

$$\sigma_X^2 = (\pi\varepsilon/2)^{1/2}(2\sigma_0^2/\varepsilon)^{3/4}\ D_{-3/2}(1(2\varepsilon\sigma_0^2)^{1/2})/K_{1/4}(1/(8\varepsilon\sigma_0^2)) \quad (11)$$

where $D_{-3/2}(\ )$ is the parabolic cylinder function. Lin&Cai, 1995, consider the nonlinearly damped SDOF- system under multiplicative and additive white noise excitation. The nonlinear system governed by

$$X'' + (\alpha + \beta X^2)X' + \omega_0^2[1 + W_1(t)]\,X = W_2(t) \quad (12)$$

where $W_1(t)$ and $W_2(t)$ are independent Gaussian white noises with spectral densities K_{11} and K_{22}, respectively. Equation (12) is replaced by the following Ito equations:

$$dX_1 = X_2 dt \quad (13)$$

$$dX_2 = -[(\alpha + \beta X_1^2)X_2 + \omega_0^2 X_1]dt + [2\pi(\omega_0^4 K_{11}X_1^2 + K_{22})]^{1/2}dB(t) \quad (14)$$

The reduced Fokker-Planck equation, corresponding to (13) and (14), is given by

$$x_2\partial p/\partial x_1 - \partial/\partial x_2\{[(\alpha+\beta x_1^2)x_2 + \omega_0^2 x_1]p\} + \pi(\omega_0^4 K_{11}x_1^2 + K_{22})\partial^2 p/\partial x_2^2 = 0 \quad (15)$$

The solution for the stationary probability density function in Equation (15) is given by

$$p(x_1,x_2)=C\exp[-\alpha/(2\pi K_{22})(\omega_0^2 x_1^2+x_2^2)] \quad (16)$$

Equation (16) shows that the displacement $X(t) = X_1(t)$ and the velocity $X'(t) = X_2(t)$ at the same t are jointly Gaussian distributed. The same Gaussian distribution is obtained if we set $\beta = 0$ and $W_1(t) = 0$, that is, if the system is linear and under only the additive white noise excitation. This means that under a suitable combination of additive and multiplicative Gaussian random excitations, the stationary response of a nonlinear system can also be Gaussian. Different stochastic systems can sometimes share a common probability distribution.

Soize, 1998, gives extensive formulations for the use FPK-equation in different types of random vibration problems. For numerical solution example of the stochastic differential equation, the Monte Carlo numerical simulation is used. The random vibration problem is formulated with the aid of the first order Ito equation and a Crank-Nicholson numerical time integration scheme is used for the solution. The Ito equation can be written as

$$d(Q(t),P(t)^T = b(Q(t),P(t))dt + [A]\, dW \quad (17)$$

In equation (17) Q(t) are the generalized coordinates and P(t) are the generalized momentums. **b** is the drift vector and [A] is the diffusion matrix and W is normalized Wiener process. To make the solution of the equation (17) suitable for the use a Crank-Nicholson method the following identity is introduced

$$[M(q)]^{-1} = [M_o]^{-1} + ([M(q)]^{-1} - [M_o]^{-1}) \quad (18)$$

With the aid of Equation (18) Equation (17) can be written as

$$dX = [\underline{A}]Xdt + V(X)dt + [A]dW \quad (19)$$

where $[A] = [\,[0], g_0[S_0]]^T$ and $X = (Q,P)$ and matrix $\underline{A}$ and vector V(X) are defined by

$$\underline{A}_{11} = [0],\ \underline{A}_{12} = [M_0]^{-1},\ \underline{A}_{21} = [K_0],\ \underline{A}_{22} = -[B_0][M_0]^{-1} \quad (20)$$

$$V(X) = [\,U(Q,P),\ R(Q,P) - [B_0]U(Q,P)\,]^T \quad (21)$$

In Equation (21) $[B_0]$ is the damping matrix, $U(Q,P) = ([M(Q)]^{-1} - [M_0]^{-1})P$ and R(Q,P) is a vector whose components $R_j(Q,P)$ are given by the inner vector product

$$Rj(Q,P) = 1/2 \langle [D^j(Q)][M(Q)]^{-1}P, [M(Q)]^{-1}P \rangle \quad (22)$$

$$[D^j(Q)] = \partial/\partial Q_j [M(Q)] \quad (23)$$

With these the Crank-Nicholson time integration scheme yields

$$X_{n+1}-X_n = 1/2\Delta t\,[A\,](X_{n+1}+X_n) + 1/2\Delta t\,\{V(X_{n+1})+V(X_n)\} + [A\,]\,\Delta W_{n+1} \quad (24)$$

Equation (24) can be written as

$$X_{n+1} = [K]\,N(X_{n+1}) + G_{n+1} \quad (25)$$

where G_{n+1} is independent from X_{n+1}, but depends on X_n and ΔW_{n+1}, and [K] is a constant matrix. Each time step, X_{n+1} in Equation (25) is solved by the iterative algorithm $X^{(j+1)}{}_{n+1} = [K\,]\,V(X^{(j)}{}_{n+1} + G_{n+1}$, for $j > 0$ with initial value $X^{(0)}{}_{n+1} = X_n$

Finite element formulation of numerical solution

Two dimensional form of FPK - equation can be written as

$$\partial f/\partial t = -\Sigma\partial/\partial x_i(z_i f) + \tfrac{1}{2}\,\Sigma\Sigma\,\partial^2/\partial x_i\partial x_j(H_{ij}f) \quad (26)$$

Indices i and j in the sums of Equation (26) go from 1 to 2. Vector z_i in Equation (26) is called the drift vector and matrix H_{ij} the diffusion matrix. With f=0 on boundary of the investigated domain and with initial condition $f_{x0}(x_0,0) = f_{x0.}$ Equation (26) is amenable to solution with the aid of finite element method. Approximating the transition probability density function f by the following expression

$$f_x(x,t) = \Sigma N_j(x) f_j^e(t) \quad (27)$$

where the functions N_j are shape functions expressing the unknown transition probability density function inside one finite element using its nodal values.
The solution of Equation (26) is obtained by weighted residual formulation using the Bubnov–Galerkin method (Wedig&von Wagner, 1999). First the residual of Equation (26) is defined by substituting into equation the approximation of Equation (27). The weighted residual is then formed by multiplying the residual with weighting functions and the weighted residual is integrated over the investigated domain and the result is set to zero. This means that the residual is required to be orthogonal to the space, where the base vectors are the weighting functions. The special feature of the Bubnov–Galerkin method is that weighting functions are the same as the shape functions in Equation (27) i. e. $W_i = N_i$. In this study four node quadrilateral elements are used and shape and weighting functions in local system of coordinates are as follows

$$N_1 = \tfrac{1}{4}(1-\xi)(1-\eta) \quad (28)$$
$$N_2 = \tfrac{1}{4}(1+\xi)(1-\eta) \quad (29)$$
$$N_3 = \tfrac{1}{4}(1+\xi)(1+\eta) \quad (30)$$
$$N_4 = \tfrac{1}{4}(1-\xi)(1+\eta)\S \quad (31)$$

In Equations (28) – (31) ξ and η are coordinates in the local elemental system of coordinates and their values vary from -1 up to +1. By implementing the procedure described above the governing matrix equation of problem is obtained as

$$K_{ij}=\Sigma\int\{N_j\partial N_i/\partial x_2\partial H_{22}/\partial x_2+ H_{22}\partial N_i/\partial x_2\partial N_j/\partial x_2+N_i\,\Sigma z_r\partial N_j\partial x_{\,r}- N_iN_j\Sigma\partial z_r/\partial x_r\}d\underline{x} \quad (32)$$
$$C_{ij} = \Sigma\int N_iN_jd\underline{x} \quad (33)$$

In Equations (33) and (34) the indices in first sums go from 1 to N_e, where N_e is the number of elements in the model, and the indices in sums inside the brackets go from 1 to 2. The underline in $\underline{x}$ means that $\underline{x}$ is a vector of two components. The integrations in (33) and (34) go over the volume of the element. In order to clarify the meanings of drift vector {z} and diffusion matrix [H] we look into the case of Duffing oscillator, which has the following governing equation

$$y'' + 2\beta y' + \omega^2 y^3 = W(t); \quad (34)$$

where the autocorrelation function for W(t) is $E[W(t)W(t+\tau)] = 2\pi S_0\delta(t)$ and $\tau = t_2 - t_1$ and $\delta(t)$ is Dirac's delta function. In this case the drift vector and the diffusion matrix of the FPK- equation are as follows

$$z_1 = y' \quad (35)$$

where y' is the velocity of the Duffing oscillator.

$$z_2 = -2\beta y' - \omega^2 y^{3\,\S} \quad (36)$$

where y is the displacement of the Duffing oscillator. The diffusion matrix is given by only one element as follows

$$H_{22} = 2\pi \underline{S_0} \tag{37}$$

where S_0 is constant power spectral density of white noise process.

Conclusion

The paper shows how the well established finite element apparatus and the standard linear finite element codes can be used to solve nonlinear random vibration problems

References

[1] Soong T.T., Random Differential Equations in Science and Engineering, Academic Press, New York and London, 1973.

[2] Roberts J.B., Spanos P.D., Random Vibration and Statistical Linearization. John Wiley & Sons, Chicester, England, 1990.

[3] Soong T. T. Grigoriu Mircea, Random Vibration of Mechanical and Structtural Systems, Prentice –Hall, Englewood Cliffs, New Jersey, 1993.

[4] Y.K.Lin, G. Q. Cai, Probabilistic Structural Dynamics, McGraw-Hill, Inc., New York, 1995.

[5] Soize C., The Fokker-Planck Equation For Stochastic Dynamic Systems and its explicit steady state solutions, World Scientific, New Jersey, 1998

[6] Yi W., Spencer B. F., Bergman L. A., Solution of Fokker – Planck equations in higher dimensions

The Effect of Delamination on the Natural Frequencies of the Composite Beams on Two-Parameter Foundation

Helle Hein
Institute of Computer Science
University of Tartu, Liivi 2, 50409 Tartu, Estonia
e-mail: helle.hein@ut.ee

Summary A general analytical solution for the delaminated composite beam on a two-parameter elastic foundation is derived. The solution is not restricted to a particular range of magnitudes of the foundation parameters. The effect of size and location of the delamination on the frequencies and mode shapes are investigated.

1. Introduction

Delamination in composite laminates may develop from small cracks due to imperfect fabrication processes or impact loading during service. The presence of delamination is known to cause strength and stiffness degradation as well as changes to the vibration characteristics of the structure. The vibrations of delaminated beams have been studied in many papers [1]-[8]. On the other hand, beams resting on elastic foundations are very common technical problems in structural and geotechnical engineering. The influences of elastic foundation stiffness on the free vibration of beams and plates have been examined in [9]-[12]. Various types of foundation models have been developed. The simplest model is the Winkler model in the case of which the foundation medium is taken into account as a system of infinitely close linear springs. Another model proposed by Pasternak acquires shear interaction between springs.

In the present study, the free vibration analysis of delaminated layered composite beams resting on elastic foundation is considered. The elastic foundation is modeled with the aid of two parameters [11], [12].

Formulation of the problem

In this section, the analytical solution to the free vibration of a delaminated composite beam resting on the elastic foundation is formulated. For the sake of simplicity the case with one delamination region is considered. The geometry of the asymmetrically delaminated beam with width b is shown in Figure 1. The delaminated beam can be viewed as a combination of four beams, each beam having thickness H_i and length L_i ($i = 1, \ldots, 4$), connected at the delamination boundaries $x = x_2$, $x = x_3$. Each of the beams is treated as a classical Euler-Bernoulli beam. The following assumptions are considered:

1. The delaminated layers are assumed to be in touch along their whole length all the time, but are allowed to slide over each other.
2. The cross-sections near the delamination fronts remain perpendicular to the deformed midplane of the beam and thus take full account of the differential stretching between the two delaminated layers of the beam.

The governing equations of the free vibrations of the i-th ($i = 1;4$) beam segment for the transverse displacement are:

$$D_i \frac{d^4 w_i}{dx^4} - k_2 \frac{d^2 w_i}{dx^2} + (k_1 - \rho_i A_i \omega^2) w_i = 0, \qquad (1)$$

where D_i is the bending stiffness, ρ_i is the mass density, w_i is the mode shape and A_i is the cross sectional area of the i-th beam. The quantity ω denotes the frequency, the quantities k_1 and k_2 denote the Winkler and Pasternak parameters, respectively.

The mechanical properties of the composite beams can be determined using the classical laminate theory [13]:

$$D_i = D_{11}^i - \frac{\left(B_{11}^i\right)^2}{A_{11}^i}, \tag{2}$$

where

$$D_{11}^i = \frac{b}{3}\sum_{k=1}^{n_i}\hat{Q}_{11}^k(z_k^3 - z_{k-1}^3), \quad A_{11}^i = b\sum_{k=1}^{n_i}\hat{Q}_{11}^k(z_k - z_{k-1}), \quad B_{11}^i = \frac{b}{2}\sum_{k=1}^{n_i}\hat{Q}_{11}^k(z_k^2 - z_{k-1}^2), \tag{3}$$

$$\hat{Q}_{11}^k = Q_{11}^k\cos^4\theta + Q_{22}^k\sin^4\theta + 2\cos^2\theta\sin^2\theta(Q_{11}^k + 2Q_{66}^k),\ Q_{11} = \frac{E_{11}}{1-\nu_{12}\nu_{21}},$$

$$Q_{22} = \frac{E_{22}}{1-\nu_{12}\nu_{21}}, \quad Q_{66} = G_{12},\ \nu_{21} = \frac{\nu_{12}E_{22}}{E_{11}}.$$

In (2) and (3) D_{11}^i denotes the bending stiffness, A_{11}^i is the extensional stiffness and B_{11}^i is coupling bending/extensional stiffness of the beam section. The quantity $\hat{Q}_{11}^k$ is the coefficient stiffness of the k-s lamina of the beam section and can be calculated with the aid of lamina parameters. In (3) E_{11}, E_{22} and ν_{12}, ν_{21} stand for the longitudinal and transverse Young's modules and Poisson's ratio of a single lamina, respectively; θ is the lamina orientation angle; z_k and z_{k-1} are the locations of the k-th lamina with respect to the mid-plane of the beam section (Fig. 1 b). The second term in (2) takes into account the reduction of stiffness due to the bending-extension coupling [14].

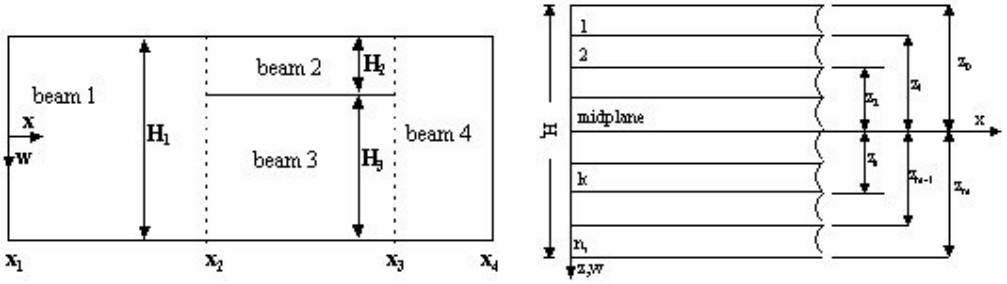

Figure 1: The geometry of the composite beam: (a) model of the beam with one delamination; (b) the i-th beam laminate

The following quantities are introduced:

$$\lambda_i = \sqrt[4]{\frac{k_1 - \rho_i A_i\omega^2}{4D_1^i}},\ \delta_i = \frac{k_2}{4D_i},\ \alpha_i = \sqrt{\lambda_i^2 + \delta_i} \tag{4}$$

Taking (4) into account the solution of (1) can be expressed as

$$w_i = \sum_{k=1}^{4} C_k^i F_k^i(x) \tag{5}$$

where the functions $F_k^i(x)$ can be presented as following:

$$\begin{Bmatrix} F_1^i(x) \\ F_2^i(x) \\ F_3^i(x) \\ F_4^i(x) \end{Bmatrix} = \begin{Bmatrix} \cos\beta_i x \cosh\alpha_i x \\ \cos\beta_i x \sinh\alpha_i x \\ \sin\beta_i x \cosh\alpha_i x \\ \sin\beta_i x \sinh\alpha_i x \end{Bmatrix}, \ if \ \ \delta_i < \lambda_i^2, \tag{6}$$

$$\begin{Bmatrix} F_1^i(x) \\ F_2^i(x) \\ F_3^i(x) \\ F_4^i(x) \end{Bmatrix} = \begin{Bmatrix} e^{\sqrt{2}\lambda_i x} \\ xe^{\sqrt{2}\lambda_i x} \\ e^{-\sqrt{2}\lambda_i x} \\ xe^{-\sqrt{2}\lambda_i x} \end{Bmatrix}, \ if \ \ \delta_i = \lambda_i^2, \tag{7}$$

$$\begin{Bmatrix} F_1^i(x) \\ F_2^i(x) \\ F_3^i(x) \\ F_4^i(x) \end{Bmatrix} = \begin{Bmatrix} \cosh\beta_i x \cosh\alpha_i x \\ \cosh\beta_i x \sinh\alpha_i x \\ \sinh\beta_i x \cosh\alpha_i x \\ \sinh\beta_i x \sinh\alpha_i x \end{Bmatrix}, \ if \ \ \delta_i > \lambda_i^2. \tag{8}$$

The quantity β_i is defined as

$$\beta_i = \begin{cases} \sqrt{\lambda_i^2 - \delta_i} & in\ eq.\ (6), \\ \sqrt{\delta_i - \lambda_i^2} & in\ eq.\ (7). \end{cases} \tag{9}$$

The governing equation for beam segments 2 and 3 is

$$(D_2 + D_3)\frac{d^4 w_2}{dx^4} - 2k_2 \frac{d^2 w_2}{dx^2} + \left[2k_1 - (\rho_2 A_2 + \rho_3 A_3)\omega^2\right] w_2 = 0. \tag{10}$$

The solution can be found similarly as in the previous case. The unknown coefficients C_k^i can be determined by four boundary conditions and 8 continuity conditions.

The continuity conditions for deflection, slope, shear force and bending moments at $x = x_2$ are:

$$\begin{aligned} &w_1 = w_2, \qquad w_1' = w_2', \\ &D_1 w_1''' = (D_2 + D_3) w_2''', \\ &D_1 w_1'' = (D_2 + D_3) w_1'' - P_d \frac{H_1}{2}, \end{aligned} \tag{11}$$

where the load P_d depends upon the extent of differential stretching of the delaminated layers. The load P_d can be obtained from the axial equilibrium and compatibility conditions between shortening/stretching of the delaminated layers [2]. Similar conditions can be established at $x = x_3$. The boundary conditions and the continuity conditions provide 12 homogeneous equations for 12 unknown coefficients C_k^i. A non-trivial solution for the coefficients exists only when the determinant of the coefficient matrix vanishes.

Numerical results

The calculations is performed on a T300/934 graphite/epoxy cantilever beam with a $[0^0/90^0]_{2s}$ stacking sequence, which was studied by Shen and Grady [4]. The dimensions of the 8-ply beam are 127x12.7x1.016 mm^3. The material properties for the lamina are: E_{11} = 134 GPa, E_{22} = 10.3 GPa, G_{12} = 5 GPa, ν_{12} = 0.33 and ρ = 1.48e3kg/m^3. All delaminations are at the

midspan and the delaminations sizes are 0.0 (intact beam), 25.4, 50.8, 76.2 and 101.6 mm. The results of the calculations are presented in Table 1.

Table 1
The primary frequencies of symmetrically delaminated cantilever beam (Hz)

Delamination length	Present $k_1=k_2=0$	FEM [4] $k_1=k_2=0$	Analytical[6] $k_1=k_2=0$	Present $k_1=400$, $k_2=0$
Intact	82.01	82.04	81.88	84.31
25.4	80.73	80.13	80.47	83.30
50.8	75.83	75.29	75.36	78.87
76.2	66.73	66.94	66.14	70.70
101.6	56.24	57.24	55.67	61.60

Acknowledgement

Financial support from the Estonian Science Foundation under Grant ETF-5240 is gratefully acknowledged.

References

[1] J.T.S. Wang, Y.Y. Liu and J.A. Gibby. Vibrations of split beams. *J. Sound Vib.*, **84**, 491–502, (1982) .

[2] P.M. Mujumdar and S. Suryanarayan. Flexural vibrations of beams with delaminations. *J. Sound Vib.*, **125**, 441-461, (1988).

[3] J.J. Tracy and G.C. Pardoen. Effect of delamination on the natural frequencies of composite laminates. *J. Compos. Mater.,* **23**, 1200-1215, (1989).

[4] M.H.H. Shen and J.E. Grady. Free vibrations of delaminated beams. *AIAA J.,* **30**, 1361-1370, (1992).

[5] D. Shu. Vibration of sandwich beams with double delaminations. *Compos. Sci. Technol.,* **54**, 101-109, (1995).

[6] D. Shu and C.N. Della. Vibrations of multiple delaminated beams. *Compos. Struct.,* **64**, 467-477, (2004).

[7] J. Lee. Free vibration analysis of delaminated composite beams. *Comput. Struct.,* **74**, 121-129, (2000).

[8] Y. Zou, L. Tong and G.P. Steven. Vibration-based model-dependent damage (delamination) identification and health monitoring for composite structures - a review. *J. Sound Vib.*, **230**, 357-378, 2000).

[9] O. Barton. The natural frequency of rectangular symmetric angle/ply laminates resting on an elastic foundation. *J. Sound Vib.*, **206**, 126-132, (1997).

[10] I. Coskun and H. Engin. Non-linear vibrations of a beam on an elastic foundation. *J. Sound Vib.*, **223**, 335-354, (1999).

[11] M. Eisenberger. Vibration frequencies for beams on variable one- and two- parameter elastic foundations. *J. Sound Vib.*, **176**, 577-584, (1994).

[12] B.N. Alemdar and P. Gülkan. Beams on generalized foundations: supplementary element matrices. *Eng. Struct.* **19**, 910-920, (1997).

[13] J.N. Reddy and A. Miravete. *Practical analysis of composite laminates.* CRC, Boca Raton, (1995).

[14] R.M. Jones Mechanics of composite materials. Philadelphia, Taylor and Francis Inc, (1999).

Fatigue life prediction of polymer covered roll

R. Karjalainen* and S-G. Sjölind
Department of Mechanical Engineering
University of Oulu, Oulu, Finland
e-mail:reetta.karjalainen@me.oulu.fi

Summary The main object in this study is to apply failure criteria to the fatigue life prediction of FRP covered rolls running in paper machines. This abstract reflects the theory of failure criterion for the model under development.

Introduction

In a calender paper is running through the contact area between two rolls, where the loading rates are quite high. The calender composite covers run for long times in paper machines and can reach respectable ages in number of loadings received, and thus the effect of the repeated compressive loadings on the cover durability is interesting.

Fatigue analysis of composite materials is difficult due to several concurrent failure modes and their mechanisms. Especially for compression failure, the mechanisms that lead to failure are not fully understood yet.

Several theories have been proposed for predicting the failure of composites. After a thorough review of various composite failure theories [1, 2], a criterion for matrix failure in compression called LaRC03 [3], was selected as the best candidate. LaRC03 criterion predicts matrix failure without requiring curve-fitting parameters and it has been shown accurate and physically consistence [4].

LaRC03 criterion for matrix failure in compression

LaRC03 is based on Hashin's criteria and Puck's action plane concept. However, for matrix compression Hashin was not able to calculate the angle for the fracture plane. The Mohr-Coulomb (M-C) criterion is commonly used in applications where fracture under tension loading is different from fracture under compression loading and now in LaRC03 criterion it is applied to calculate the angle of fracture. Boehler, while studying the failure of chopped glassfiber/epoxy mat laminates under confining pressures, formulated a shearing criterion based on the M-C criterion and found it to fit his experimental measurements well.

The matrix failure under compression loading is assumed to result from a quadratic interaction between the effective shear stresses τ_{eff}^{T} and τ_{eff}^{L} acting on the faces of a fracture plane. The effective stress τ_{eff} is related to the stresses τ^{T} and σ_n (see Fig. 1) by the expression $\tau_{eff} = \tau^{T} + \eta\sigma_n$. In the literature, $\tan^{-1}(\eta)$ is called the angle of internal friction and it is assumed to be a material constant. In general, the effective stresses must be defined in both directions as shown in Eq. 1.

$$\begin{aligned} \tau_{eff}^{T} &= \left\langle \left|\tau^{T}\right| + \eta^{T}\sigma_n \right\rangle \\ \tau_{eff}^{L} &= \left\langle \left|\tau^{L}\right| + \eta^{L}\sigma_n \right\rangle \end{aligned} \tag{1}$$

where terms η^T and η^L are referred to as coefficients of transverse and longitudinal influence, respectively, and the operand $\langle x \rangle = x$ if $x \geq 0$; otherwise $\langle x \rangle = 0$. The matrix failure index (FI_M) is written as

$$FI_M = \left(\frac{\tau_{eff}^T}{S^T} \right)^2 + \left(\frac{\tau_{eff}^L}{S^L} \right)^2, \tag{2}$$

where S^T and S^L are the transverse and in-plane shear strengths, respectively.

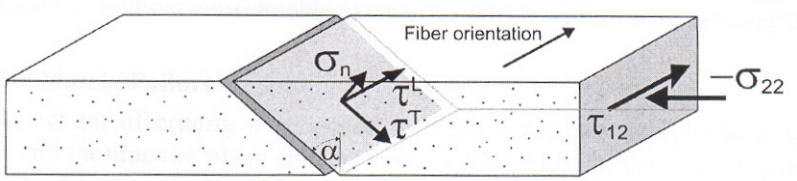

Figure 1. Fracture of a unidirectional lamina subjected to transverse compression and in-plane stress.

The stress components can be expressed in terms of the in-plane stresses σ_{22} and τ_{12} and the angle of the fracture plane α, and thus the effective stresses can be defined as

$$\begin{aligned} \tau_{eff}^T &= \left\langle -\sigma_{22} \cos\alpha \left(\sin\alpha - \eta^T \cos\alpha \right) \right\rangle \\ \tau_{eff}^L &= \left\langle \cos\alpha \left(|\tau_{12}| + \eta^L \sigma_{22} \cos\alpha \right) \right\rangle \end{aligned}, \tag{3}$$

The angle of the fracture plane α is the one that maximizes the failure index (FI_M) and it depends on the applied transverse stress σ_{22} as shown in Fig. 2.

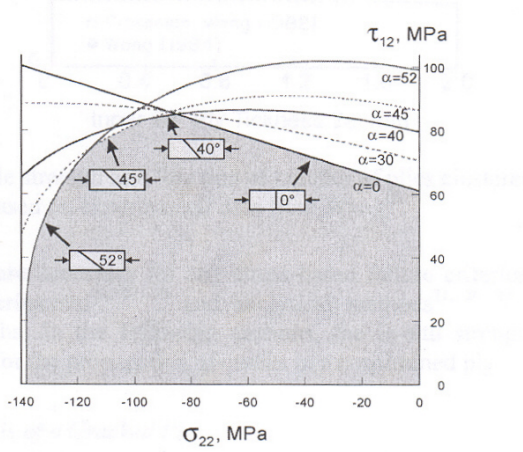

Figure 2: Matrix failure envelopes for a typical unidirectional E-glass lamina subjected to in-plane compression and shear loading.

The coefficient of transverse influence η^T is

$$\eta^T = \frac{-1}{\tan 2\alpha_0}. \tag{4}$$

The angle of fracture plane $\alpha_0=53^o\pm2^o$ is a typical for composites. Therefore, the coefficient of transverse influence is in the range $0.21 \le \eta^T \le 0.36$.

The coefficient of longitudinal influence η^L can be determined by shear tests, but in absence of test data, it can be estimated as

$$\eta^L = -\frac{S^L \cos 2\alpha_0}{Y^C \cos^2 \alpha_0}. \tag{5}$$

The transverse shear strength S^T is difficult to measure experimentally, but it can be determined from

$$S^T = Y^C \cos\alpha_0 \left(\sin\alpha_0 + \frac{\cos\alpha_0}{\tan 2\alpha_0} \right). \tag{6}$$

For a typical fracture angle of 53° $S^T = 0.378\ Y^C$.

The stiffnesses and strengths used in LaRC03 curve are shown in Fig. 3, in which there are also the envelopes for other criteria.

E_{11}	E_{22}	G_{12}	ν_{12}	Y^T	Y^C	S^L
53,480	17,700	5,830	0.278	36	138	61

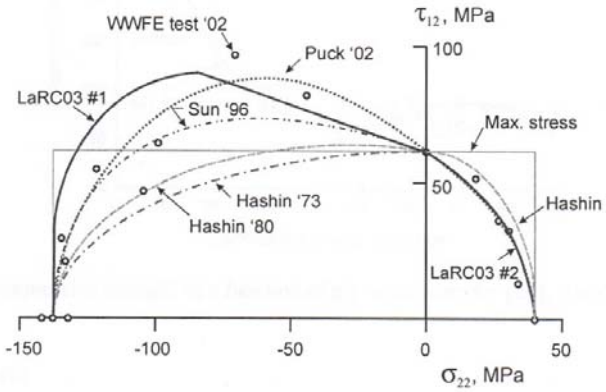

Figure 3. Failure envelopes and WWFE test data for unidirectional composite E-Glass/LY556.

Modelling

A 2-D FE-modelling of the polymer covered roll is to be performed using the commercial finite element software ABAQUS. The model geometry and the boundary conditions take advantage of the symmetry conditions. The contact area between rolls will be modelled by specifying a contact between them, and the load is to be created by forced displacement of the contrary roll. The criterion will be programmed as subroutine and implemented into ABAQUS.

Concluding remarks

This study presents a criterion, which seems to be promising in predicting the fatigue failure in compression. In the future there is the possibility to verify the computed results with the test results.

Acknowledgements

The funding of this research from the Metso Paper, Inc. is gratefully acknowledged.

References

[1] F. París. A study of failure criteria of fibrous composite materials. NASA/CR-2001-210661, (2001).

[2] M.J. Hinton, A.S. Kaddour and P.D. Soden. A comparison of the predictive capabilities of current failure theories for composite laminates, judged against experimental evidence. *Composite Science and Technology*, 62, 1725-1797, (2002)

[3] C.G. Dávila and P.P. Camanho. Failure criteria for FRP laminates in plane stress. NASA/TM-2003-212663, (2003).

[4] S. Ragionieri and D. Weinberg. Finite element implementation of advanced failure criteria for composites. *The NAFEMS World Congress*, (2005).

Extension of ASME regulatory for validation of dynamical calculation when deviations in as-buildt

Lic engrg Lena Strömberg
LTech, Fredrlg 38, Se-38237 Nybro
(previously Dep of Solid Mechanics, Royal Instititute of Techn, KTH)
e-mail: lest0400@student.miun.se

Summary At construction based on design plan, there are often deviation in support positions, bends, welds and mass distributions. For a pipe model to be valid, certain rules regarding deviation from model based on drawings, are convenient. In the present context, a method to validate a dynamical calculation is proposed. New eigen frequencies for the as-buildt system are calculated from a modal analysis, and compared to design frequencies. If the deviation is within a certain range, it is assumed that other properties are also limited, and that, the results from the original complete model are valid.

Introduction

A piping system attached to the reactor tank and the main steam line was calculated for dynamical loads, static loads and thermal expansion. The purpose of the pipe is to ensure that the level of water in the tank(vessel) is known, by leading exhaust gases from the facility of measurment at the top of the pipe. Due to the close vicinity of the reactor, the piping system is Class 1, according to ASME[1], however since the diameter of pipes are small, the rules for Class 2 are sufficient to validate the system. Thus, thermal transients leading to low cycle fatigue, need not be considered.

The dynamical loads that are present, in various combinations with static loads, are e.g. water hammer due to closure of inner or outer valves, water hammer due to opening of safety walves for steam pipe, oscillations from wet-well, floor respons spektra for earthquake, occuring for different levels of operation, such us normal operation, start and shut-down, safety shut-down. Load input are present as time history as well as spectral amplitudes.

Combination of loads are done according to rules given by the owner in a document specified for the system.

Loads due to weight, pressure and thermal expansion are always combined with superposition. In some cases, dynamical loads could be combined with SRSS. This is less conservative causing the larger load to give the main contribution.
Since the valve opening causes the 'chugging', it emanates from the same source, and it is most likely that the effects are not superposed as maximum contributions, but are in different phases.

Model

For small pipes, there is a regulatory [2], that admits installation without a calculation. This contains rules for distance between supports, types of support and a restriction on the lowest eigen frequency (approx 33Hz, in this case). For the exhaustion pipe, the expansion loop at the attachment to steam pipe, gives lower eigen frequencies (approx 8Hz), cf. Figure 1. Hereby, a full dynamic analysis was performed.

The pipe was calculated in the program Pipe Stress [3].

To achieve a model with correct, known boundary condition, parts of attached pipes needed to be invoked. The rigid ends of the model was the tank, the inside wall of the reactor containment, and the floor above wet-well.

Results for design configuration

Pipe orientations and support positions were adjusted in order to achieve sufficiently low stresses for load combinations at all levels. Based on these results, corresponding loads on supports were deduced, and components were designed to withstand the loads.

Since the model contained both the large steam pipes and the exhaust pipe, the entries of the stiffness matrix where different in magnitude. Such conditions, could be known to introduce some sensitivity to the system, however that is handled in the program. It was observed however, that (minor) changes of support positions, and piping, caused over-stresses for dynamical loads. This was mostly due to the fact, that there were small margins from the beginning.

Adaption to as-buildt configuration

After construction, there were some deviation in support positions, change in pipe lengths, bends, welds and mass distributions. Distributed mass consists of pipe and heat isolation, whereas valves often are modeled as point masses.

Within the code, there are some possibility to tune parameters, such as stiffness of valves and direction of supports. Within these ramifications, it may have been possible, however time consuming, to verify the system by calculation.

Extension of ASME nonmandatory appendix 11, for validation of dynamical calculation when deviations in as-buildt

For a pipe model to be valid, certain rules regarding deviation from model based on drawings, are convenient. Suggestions on admissable alterations in as-buildt compared to design, are given in ASME appendices. In this context, the rules are extended to dynamical variations.

Admissable alteration for mass distribution is according to ASME appendix, 20%. This may be expressed in alteration of eigen frequencies for oscillation of bending degrees of freedom at a beam with given boundary conditions, free ends/supported ends, and is 9%. (The alteration is independent of boundary conditions.) A suggestion on code development is that every change is permitted, that results in a change in eigen frequencies less than this value.

Since the analysis for the dynamical loads requires significant calculation effort, and the result is highly dependant of eigen frequencies that are obtained through a quite simple modal analysis, this proposal is a significant improvement, and a great part of the calculations done before hardware construction, will be valid also for as-buildt.

This code development is valid for dynamical loads, when as-buildt differs from used calculation profound (input data). The static load cases eigenweight (DW), operating pressure (PO) and thermal expansion (TO), are not enveloped. These are verified with the static mandatory rules.

The shift in eigen frequency could be allowed to be the sum (or SRSS or max) of the shift in eigen frequencies, for all admissable changes. An investigation, and evaluation of validity should be done, for some chosen systems.

$\Delta\omega(\text{allowed})=F(\Delta\omega(\text{ch in mass distr}), \Delta\omega(\text{ch in supp pos}), \Delta\omega(\text{ch in point masses}))$

$F(x,y)=x+y$, or $F(x,y)=(x^2+y^2)^{1/2}$, or $F(x,y)=\max(x,y)$

Conclusion
A new method to verify a calculation analysis, compared with revised drawings and input data was proposed. Instead of the calculation of new actual loads on the system, a comparison between eigen frequencies, for as-buildt, and previously analysed system, is made. If changes are within a certain tolerance, a full analysis is not required.

Advantages of the method

- New input data for dynamical loads are not necessary. (When support positions are moved, the dynamical loads may change, and new files for load basis have to be deduced, which implies significant work load.
- Only modal analysis required.
- New calculation of support loads is not required
- Highlights the present approach to dynamical effects, in terms of load combination and calculation profound for input data

Remarks
In order to actually reduce dynamical loads, damping facilities need to be installed.
Oscillation of the building could be damped by a liquid in communicating vessel at top of the building, as is done in buildings subjected to ground motions, eg earthquakes. This will reduce the loads from the floor response. Vibrations in the system are reduced by installing a rubber spring facility, with the unwanted eigen frequency, near the oscillating area.

In nuclear application, vibrations of the system with the circulation pump, where eliminated by installing a so called damping weight. The name is somewhat misleading, since it changes the eigen frequency, but does not introduce energy consuming damping.

Since the system response close to resonance is exponenential, it should be discussed whether there are some cases that should be excepted from the rule extension, 9%.

Acknowledgements
The author acknowledge Erik Adolfsson, ÅF, for valuable help on the subject.

References

[1] ASME Code for pressurized equipment in e.g. nuclear application, www.asme.org. Results are valid for other dynamic evaluations

[2] ’Dragning och stagning av klenrör’.

[3] Pipe Stress. Finite element program, based on ASME Code.

Forces Between Joined Discrete Particles in Discrete Element Method

Jani Paavilainen* **and Jukka Tuhkuri**
Laboratory for Mechanics of Materials, Department of Mechanical Engineering
Helsinki University of Technology, Espoo, Finland
e–mail: Jani.Paavilainen@tkk.fi, Jukka.Tuhkuri@tkk.fi

Summary Determination of the forces between joined rectangular discrete particles (elements) is presented. A two-dimensional discrete element program is developed further to handle these forces. A vibrating beam is simulated to benchmark the calculation of the forces between particles joined together.

Introduction

Discrete element method (DEM) is a numerical tool used to simulate the nonlinear dynamics of a system of particles. In DEM, individual material particles (discrete elements) are considered to be separate, but the elements can interact with each other through particle–particle contacts [1] [2]. Thus DEM has been applied especially to studies of granular materials in, for example, rock and ice mechanics.

However, DEM is also usefull in analyses of fragmentation of solids as well as structural failure and collapse [3] [4] [5]. In such studies, in addition to modelling fracture, also the behavior of the structure before fracture must be modelled with DEM. As an example, when simulating the failure of a floating sea ice sheet against a structure, the dynamics of the ice sheet before failure must also be modelled. In a discrete element simulation, the ice sheet, or beam in 2D, is composed of discrete elements which are joined or "glued" together. In this work, the joining of discrete elements together and calculation of forces between joined discrete elements is presented and implementation into a DEM code is verified through simulations of a vibrating beam.

Equations of motion

In this context all the particles (discrete elements) are rigid and uniform rectangles. In discrete element method, the motion of each rigid particle, position $\mathbf{r}$, velocity $\mathbf{v}$, orientation $\boldsymbol{\theta}$ and angular velocity $\boldsymbol{\omega}$, has to be determined in some frame of reference. According to Newton's second law of motion, the motion of a rigid particle is described by the following differential equations

$$m_i \frac{d^2\mathbf{r}_i}{dt^2} = \mathbf{F}_i \quad \text{and} \quad I_i \frac{d^2\boldsymbol{\theta}_i}{dt^2} = \mathbf{T}_i \tag{1}$$

for each particle i. In Equation (1) m_i, $\mathbf{F}_i$, I_i and $\mathbf{T}_i$ are the mass, force, moment of inertia and torque respectively.

The forces $\mathbf{F}_i$ and torques $\mathbf{T}_i$ contain both the internal and external forces acting on the particle i. To distinguish the internal and external forces from one another we introduce a group of discrete particles: A group of particles is a collection of particles that are joined together in such a manner that the group can support both tensile and compressive forces. Now, the internal forces are due to relative movement between two adjacent particles in a same group of particles and the external forces are due to other sources such as collisions between particle groups, gravity and bouyancy of individual particles etc. It follows from these definitions and the fact that the particles are rigid, that one particle alone can not have any internal forces. In the rest of this work only internal forces are considered.

Forces between joined particles

Forces between joined particles in discrete element method is covered by e.g. Hopkins [6]. Since, with our definitions, there are no internal forces defined between different particle groups or in one particle, we next consider two adjacent particles in a same group, see Fig. 1(a). The particles have an adjacent edge by which they are joined together. The joint is considered viscous-elastic. In DEM, the forces between joined particles are due to relative movement of the particles. In Fig. 1(b) two adjacent particles, which have moved with respect to one another, are shown. The local frame of particle 1 and the frame on edge of the particle 1, with normal and tangential directions, are also shown in Fig. 1(b). The distance between the corresponding points on the adjacent edges of particles 1 and 2 is denoted by δ and will be called a stretch. The stretch is a function of t, the tangential direction of the edge, i.e. $\delta(t)$.

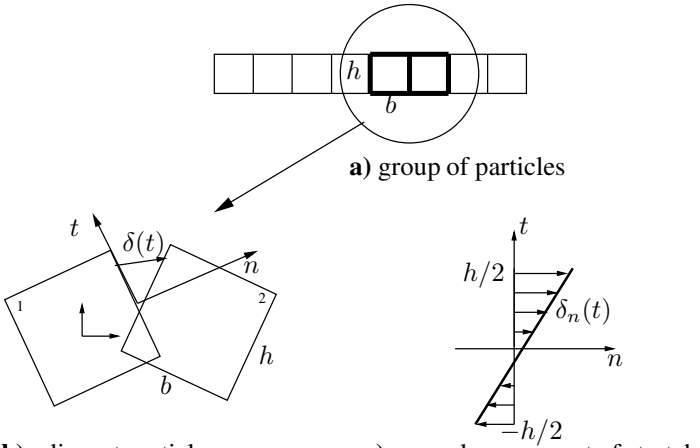

Figure 1: a) A group of particles with two adjacent particles highlighted. b) Two adjacent particles which have moved with respect one another. c) Normal component of the stretch $\delta_n(t)$.

In Fig. 1(c) the normal component of the stretch is shown. Following [6], the normal component of the elastic and dissipative forces exerted on particle 1 is integrated over the length of the joint as follows

$$F_n = F_{ne} + F_{nd} = \frac{E}{b}\int_{-h/2}^{h/2} \delta_n(t)\mathrm{d}t + c_n \int_{-h/2}^{h/2} \dot{\delta}_n(t)\mathrm{d}t, \tag{2}$$

where E is Young's modulus, b is the width and h is the height of the particle and c_n is the normal damping constant. The tangential component of the force, the shear force, is derived analogously by using the shear modulus G and the tangential component of the stretch $\delta_t(t)$

$$F_t = F_{te} + F_{td} = \frac{G}{b}\int_{-h/2}^{h/2} \delta_t(t)\mathrm{d}t + c_t \int_{-h/2}^{h/2} \dot{\delta}_t(t)\mathrm{d}t, \tag{3}$$

where c_t is the tangential damping constant. The torque from the elastic and dissipative normal forces in the local frame of particle 1 is

$$T_n = T_{ne} + T_{nd} = -\frac{E}{b}\int_{-h/2}^{h/2} t\delta_n(t)\mathrm{d}t - c_n\int_{-h/2}^{h/2} t\dot{\delta}_n(t)\mathrm{d}t. \tag{4}$$

The torque exerted by shear forces to the local frame of particle 1 is

$$T_s = \frac{b}{2}(F_{te} + F_{td}). \tag{5}$$

Solving the equations of motion

After all the forces and torques have been calculated for each particle by using (2), (3), (4) and (5), the equations of motions (1) are solved using explicit time integration. The following central difference method is used:

$$\begin{aligned} \mathbf{r}^{i+1} &= \mathbf{r}^i + \mathbf{v}^i\Delta t + \frac{(\Delta t)^2}{2}\frac{F^i}{m} \\ \mathbf{v}^{i+1} &= \mathbf{v}^i + \frac{\Delta t}{2}(\frac{F^i}{m} + \frac{F^{i+1}}{m}), \end{aligned} \tag{6}$$

for each time step $i = 1, 2, \ldots$ The orientation $\boldsymbol{\theta}$ and angular velocity $\boldsymbol{\omega}$ of each particle are also determined by the same method.

Vibration of a beam

As a simple test case for the calcutation of the forces between joined particles, a vibrating beam was modeled with different boundary conditions. Both the longitudinal and transverse vibrations were studied. Figure 2a) shows the displacement of the midpoint of the beam in case of longitudinal vibration and Figure 2b) shows the displacement of the midpoint of the beam in transverse vibration.

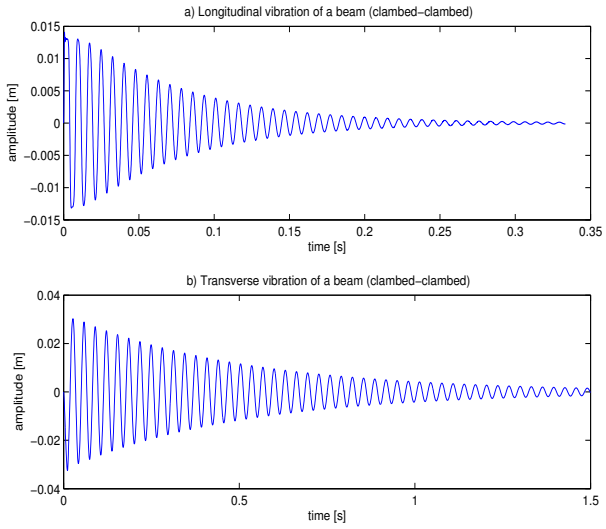

Figure 2: a) Longitudinal vibration of a beam. b) Transverse vibration of a beam.

The natural frequences of the beam with different boundary conditions were calculated and compared to the analytical solutions presented in [7]. Young's modulus $E = 1.0 \cdot 10^9$ MPa, density $\rho = 920$ kg/m^3 and the height of the beam $h = 0.5$ m were the same for all the test cases. Other used properties and results are shown in table 1.

Table 1: Natural frequences of the beam.

boundary conditions	vibration	length of the beam [m]	Δt [s]	number of elements	ω [1/s] ([7])	ω [1/s] (DEM)
clambed–clambed	longitudinal	3.96	$5.0 \cdot 10^{-7}$	19	827.1	826.7
clambed–clambed	transverse	4.0	$5.0 \cdot 10^{-5}$	9	210.4	209.4
clambed–free	transverse	4.25	$5.0 \cdot 10^{-5}$	9	29.3	29.2

Concluding remarks

The calculation of the forces between joined rectangular particles in discrete element method was presented and implemented to a DEM program. Vibrating beam was simulated with the program and the natural frequences obtained were compared to ones given by analytical solutions. No significant differences between the solutions could be found.

Acknowledgement

This work was supported by the Finnish Cultural Foundation and Heikki and Hilma Honkanen Foundation which are gratefully acknowledged.

References

[1] P.A. Cundall and O.D.L.Strack. A discrete numerical model for granular assemblies. *Géotechnique*, **29**, 47–65, (1979).

[2] O.R. Walton and R.L. Braun. Viscosity, Granular–Temperature, and Stress Calculations for Shearing Assemblies of Inelastic, Frictional Disks. *Journal of Rheology*, **30**, 949–980, (1986).

[3] D.R.J. Owen et al. The modelling of multi-fracturing solids and particulate media. *Int.J. for Numerical Methods in Engineering*, **60**, 317–339, (2004).

[4] M.A. Hopkins, J. Tuhkuri and M. Lensu. Rafting and ridging of thin ice sheets. *Journal of Geophysical Research*, **104**, 13,605–13,613, (1999).

[5] A. Munjiza. *The Combined Finite-Discrete Element Method*. Wiley, (2004).

[6] M.A. Hopkins. A Particle Beam Simulation. *Mechanics Computing in 1990s and Beyond Proceedings*, 1274–1278,(1991).

[7] D.J. Inman. *Engineering Vibration*. Prentice-Hall, New Jersey, Second edition, (2001).

A Finite Element Method for General Boundary Condition

Mika Juntunen* **and Rolf Stenberg**
Institute of Mathematics
Helsinki University of Technology, Espoo, Finland
e–mail: mika.juntunen@tkk.fi

Summary In this note we introduce a method for handling general boundary conditions based on an approach suggested by Nitsche (1971) for the approximation of Dirichlet boundary conditions. We use Poisson's equations as a model problem and present the a priori and the a posteriori error estimates. Also, we show that conventional error estimates for Dirichlet and Neumann boundary conditions are a special case of the proposed error estimates.

Introduction

Enforcing perturbed Dirichlet boundary condition i.e. the Robin boundary condition with small coefficient in the derivative term leads to a high condition number in the system matrix. Perturbed boundary condition also plagues the adaptive mesh refinement based on the a posteriori error estimate since the straight forward formulation of the problem leads to a posteriori estimate that induces a too dense mesh on the boundary. A numerical scheme has to take these facts into account in order to produce an efficient and numerically stable method.

Perturbed boundary conditions arise for example in linear elasticity where a solid is on a very stiff but elastic support. Also, enforcing normal Dirichlet boundary condition with the penalty method is equivalent to solving a problem with perturbed Dirichlet boundary conditions since the penalty method is not consistent.

We show a method based on the Nitsche method [1] [2] [3] to circumvent the high condition number of the system matrix in the case of the perturbed boundary condition. The method is proposed in a way that it is possible to move continuously between the Neumann and the Dirichlet boundary conditions. We show the a priori error estimate that has the optimal rate of convergence. Under the saturation assumption we also show the a posteriori error estimate.

Deriving The Nitsche Method

We use the Poisson problem as a model problem.

$$\begin{aligned} -\Delta u &= f && \text{in } \Omega \\ \frac{\partial u}{\partial n} &= \frac{1}{\epsilon}(g-u)+q && \text{on } \Gamma \\ u &= 0 && \text{on } \partial\Omega \setminus \Gamma \end{aligned} \tag{1}$$

where Ω is a bounded domain in space with polygonal boundary, $f \in L^2(\Omega)$, $g, q \in L^2(\Gamma)$ and $\epsilon \in \mathbb{R}$, $\epsilon > 0$.

Remark 1. *The value of the parameter ϵ allows to move between the Dirichlet and Neumann problems continuously i.e.*

$$\begin{aligned} \epsilon \to 0 \;&\Rightarrow\; u = g && \textit{on } \Gamma \\ \epsilon \to \infty \;&\Rightarrow\; \frac{\partial u}{\partial n} = q && \textit{on } \Gamma \;. \end{aligned} \tag{2}$$

We suppose that we have shape regular finite element partitions $\mathcal{T}_h$ of the domain $\Omega \in \mathbb{R}^N$, $N = 2, 3$. By $K \in \mathcal{T}_h$ we denote an element of the mesh and by E we denote an edge of the element. The mesh induces a partitioning also to the boundary of the domain $\partial\Omega$ and we denote

$$\mathcal{G}_h = \{E \,:\, K \cap \Gamma,\; K \in \mathcal{T}_h\} \,.$$

(The Nitsche Method). *Find $u_h \in V_h$ such that*

$$\mathcal{B}_h(u_h, v) = \mathcal{F}_h(v) \quad \forall v \in V_h \tag{3}$$

where

$$\begin{aligned}\mathcal{B}_h(u,v) = \big(\nabla u, \nabla v\big)_\Omega + \sum_{E\in\mathcal{G}_h} \Bigg\{ &- \frac{\gamma h_E}{\epsilon+\gamma h_E}\Big[\big\langle \frac{\partial u}{\partial n}, v\big\rangle_E + \big\langle u, \frac{\partial v}{\partial n}\big\rangle_E\Big] \\ &+ \frac{1}{\epsilon+\gamma h_E}\big\langle u, v\big\rangle_E - \frac{\epsilon\gamma h_E}{\epsilon+\gamma h_E}\big\langle \frac{\partial u}{\partial n}, \frac{\partial v}{\partial n}\big\rangle_E \Bigg\}\end{aligned} \tag{4}$$

and

$$\begin{aligned}\mathcal{F}_h(v) = \big(f, v\big)_\Omega + \sum_{E\in\mathcal{G}_h} \Bigg\{ &\frac{1}{\epsilon+\gamma h_E}\big\langle g, v\big\rangle_E - \frac{\gamma h_E}{\epsilon+\gamma h_E}\big\langle g, \frac{\partial v}{\partial n}\big\rangle_E \\ &+ \frac{\epsilon}{\epsilon+\gamma h_E}\big\langle q, v\big\rangle_E - \frac{\epsilon\gamma h_E}{\epsilon+\gamma h_E}\big\langle q, \frac{\partial v}{\partial n}\big\rangle_E \Bigg\}.\end{aligned} \tag{5}$$

Remark 2. *Setting $\gamma = 0$ in equation* (3) *yields the conventional variational formulation of the model problem* (1)*. Due to the inconsistency of the penalty method this variational form can also be seen as the variational form induced by the application of the penalty method with penalty parameter ϵ to the problem*

$$\begin{aligned} -\Delta u &= f && \text{in } \Omega \\ u &= g + \epsilon q && \text{on } \Gamma\,. \end{aligned}$$

Remark 3. *Setting $\epsilon = 0$ in equation* (3) *yields the variational form of the Nitsche method applied to problem [2]*

$$\begin{aligned} -\Delta u &= f && \text{in } \Omega \\ u &= g && \text{on } \Gamma\,. \end{aligned}$$

Remark 4. *Letting $\epsilon \to \infty$ in equation* (3) *yields the variational form of the Neumann problem*

$$\begin{aligned} -\Delta u &= f && \text{in } \Omega \\ \frac{\partial u}{\partial n} &= q && \text{on } \Gamma\,. \end{aligned}$$

Lemma 1 states that the proposed method is indeed consistent.

Lemma 1. *The solution u of the equations* (1) *satisfies*

$$\mathcal{B}_h(u, v) = \mathcal{F}_h(v) \quad \forall v \in V\,. \tag{6}$$

A priori error estimate

For the analysis of the method we define the following mesh-dependent norm

$$\|v\|_h^2 := \|\nabla v\|^2_{L^2(\Omega)} + \sum_{E\in\mathcal{G}_h} \frac{1}{\epsilon + h_E}\|v\|^2_{L^2(E)}\,. \tag{7}$$

Lemma 2. *There is a positive constant C_I such that [3]*

$$\sum_{E\in\mathcal{G}_h} h_E \left\| \frac{\partial v}{\partial n} \right\|^2_{L^2(E)} \leq C_I \|\nabla v\|^2_{L^2(\Omega)} \quad \forall v \in V_h \,. \tag{8}$$

Since it is possible to compute a value to the coefficient C_I of Lemma 2, it follows from Lemma 3 that the proposed method is always stable.

Lemma 3. *Suppose that $\gamma < 1/C_I$. Then there exists a positive constant C such that*

$$\mathcal{B}_h(v,v) \geq C\|v\|^2_h \quad \forall v \in V_h \,. \tag{9}$$

Following interpolation estimate holds [3].

Lemma 4. *Suppose that $u \in H^s(\Omega)$, with $3/2 < s \leq p+1$. Then it holds*

$$\inf_{v\in V_h} \|u - v\|_h \leq Ch^{s-1}\|u\|_{H^s(\Omega)} \,. \tag{10}$$

Now we can formulate the a priori error estimate in the mesh dependent norm.

Theorem 1. *Suppose that $\gamma < 1/C_I$. Then it holds*

$$\|u - u_h\|_h \leq C \inf_{v\in V_h} \|u - v\|_h \tag{11}$$

and if $u \in H^s(\Omega)$ and $3/2 < s < p+1$, then

$$\|u - u_h\|_h \leq Ch^{s-1}\|u\|_{H^s(\Omega)} \,. \tag{12}$$

A posteriori error estimate

The a posteriori error estimate of the Nitsche method is based on the saturation assumption [4]. The assumption is that refining the mesh produces better solution in the mesh dependent energy norm.

Assumption 1. *Assume there exists $\beta < 1$ such that*

$$\|u - u_h\|_h \leq \beta \|u - u_{2h}\|_h \,, \tag{13}$$

where u_{2h} is a solution on a mesh size $2h$.

Theorem 2. *Suppose the saturation Assumption 1 holds and that $\gamma < 1/C_I$. Then it holds*

$$\|u - u_h\|_h \leq C\Big(\sum_{K\in\mathcal{T}_h} E^2_K(u_h) \Big)^{1/2} , \tag{14}$$

where

$$\begin{aligned} E^2_K(u) = h^2_K \|\Delta u + f\|^2_{L^2(K)} + h_E \left\| \left[\!\left[\frac{\partial u}{\partial n} \right]\!\right] \right\|^2_{L^2(\partial K \cap \mathcal{I})} \\ + \frac{h_E}{(\epsilon + \gamma h_E)^2} \left\| \epsilon\big(\frac{\partial u}{\partial n} - q\big) + u - g \right\|^2_{L^2(\partial K \cap \Gamma)} \,, \end{aligned} \tag{15}$$

where $\mathcal{I}$ is the internal boundaries of the mesh.

Remark 5. *Setting $\epsilon = 0$ yields*

$$E_K^2(u) = h_K^2 \|\Delta u + f\|_{L^2(K)}^2 + h_E \left\| \left[\!\left[\frac{\partial u}{\partial n} \right]\!\right] \right\|_{L^2(\partial K \cap \mathcal{I})}^2 + \frac{1}{h_E} \|u - g\|_{L^2(\partial K \cap \Gamma)}^2 \ , \tag{16}$$

which is the a posteriori estimate of the Nitsche method for the non-perturbed problem.

Remark 6. *Setting $\gamma = 0$ yields*

$$E_K^2(u) = h_K^2 \|\Delta u + f\|_{L^2(K)}^2 + h_E \left\| \left[\!\left[\frac{\partial u}{\partial n} \right]\!\right] \right\|_{L^2(\partial K \cap \mathcal{I})}^2 + h_E \left\| \frac{\partial u}{\partial n} - q + \frac{1}{\epsilon}(u - g) \right\|_{L^2(\partial K \cap \Gamma)}^2 \ , \tag{17}$$

which is the a posteriori estimate of the penalty method or the conventional approach to the perturbed problem.

Remark 7. *Letting $\epsilon \to \infty$ yields*

$$E_K^2(u) = h_K^2 \|\Delta u + f\|_{L^2(K)}^2 + h_E \left\| \left[\!\left[\frac{\partial u}{\partial n} \right]\!\right] \right\|_{L^2(\partial K \cap \mathcal{I})}^2 + h_E \left\| \frac{\partial u}{\partial n} - q \right\|_{L^2(\partial K \cap \Gamma)}^2 \ , \tag{18}$$

which is the a posteriori estimate of the Neumann problem.

These remarks show that the a posteriori estimate holds for all values of ϵ, even the limit values of ϵ yield the correct a posteriori estimate. In addition, setting $\gamma = 0$ yields the conventional approach or the penalty method, depending on the problem.
For the proofs of the error estimates check [5].

References

[1] J.A. Nitsche. Über ein Variationsprinzip zur Lösung von Dirichlet-Problemen bei Verwendung von Teilräumen, die keinen Randbedingungen unterworfen sind. *Abhandlungen aus dem Mathematischen Seminar der Universität Hamburg* **36**, 9–15, (1970/71)

[2] R. Stenberg. Mortaring by a method of J.A. Nitsche. Computational Mechanics; New Trends and Applications S. Idelsohn, E. Oate and E. Dvorkin (Eds.) *@CIMNE, Barcelona, Spain, 1998*

[3] R. Becker, P. Hansbo, and R. Stenberg. A finite element methods for domain decomposition with non-matching grids. *Mathematical Modelling and Numerical Analysis* **37**, 209–225, (2003)

[4] D. Braess and R. Verfürth A posteriori error estimator for the Raviart-Thomas element. *SIAM J. Numer. Anal* **33**, 2431–2444, (1996)

[5] M. Juntunen and R. Stenberg. The Nitsche method for general boundary condition. *In preparation.*

New Technologies for Control of Local Errors in Engineering Computations by FEM

Sergey Korotov
Institute of Mathematics
Helsinki University of Technology, Espoo, Finland
e–mail: sergey.korotov@hut.fi

Summary We show that popular gradient averaging techniques can be successfully used for reliable control of local errors appearing in finite element computations for linear elliptic type boundary value problems. Error control in terms of linear functionals with local supports and also in terms of local integral norms is considered. General schemes for construction of easily computable estimates for both types of control are described and effectivity of the proposed estimates is demonstrated in numerical tests.

Introduction

The paper is devoted to a recent trend in a posteriori error estimation which is based on the concept of control of local computational errors. Error estimates of such type control are strongly motivated by practical needs, in which analysts are often interested not only in the classical error in global energy norms, i.e., over the whole solution domain, but also in information about local errors over certain parts of it. One way for obtaining such an information is to introduce a linear functional ℓ associated with a subdomain of special interest and to construct a posteriori computable estimate for $\ell(u-\bar{u})$, where u is the exact solution and $\bar{u}$ is the approximate one. We show that popular and computationally cheap gradient averaging procedures can be effectively used for such a purpose if $\bar{u}$ is computed by the finite element method. Moreover, we show that also an error measured in local integral norms can be effectively estimated via estimates of the error in terms of suitably constructed linear functionals. The effectivity of proposed estimates is demonstrated in numerical tests.

Control of error by linear functionals

Model elliptic problem. Let Ω be a bounded and connected domain in $\mathbb{R}^d$ ($d = 1, 2, ...$) with a Lipschitz continuous boundary $\partial\Omega$, we consider the problem: Find u such that

$$-\mathrm{div}(\mathrm{A}\nabla u) = f \quad \text{in} \quad \Omega, \quad u = 0 \quad \text{on} \quad \partial\Omega, \tag{1}$$

where $f \in L_2(\Omega)$, matrix $\mathrm{A} = \{a_{ij}(x)\}_{i,j=1}^d$ is symmetric and is such that

$$a_{ij}(x) \in L_\infty(\Omega), \quad \mathrm{A}(x)\xi\cdot\xi \geq c\,\|\xi\|^2 \quad \forall \xi \in \mathbb{R}^d \quad \forall x \in \overline{\Omega}. \tag{2}$$

To find an approximation for problem (1) by the finite element method we employ the so-called *weak formulation* of (1): Find $u \in H_0^1(\Omega)$ such that

$$\int_\Omega \mathrm{A}\nabla u\cdot\nabla w\,dx = \int_\Omega fw\,dx \quad \forall w \in H_0^1(\Omega). \tag{3}$$

Let $u_h \in H_0^1(\Omega)$ be a continuous piecewise polynomial finite element approximation of u computed on the *primal mesh* $\mathcal{T}_h$. The question is in which sense to measure the *error* $e := u - u_h$. One way to do that is via linear functional ℓ_φ (e.g., with a local support $\omega \subseteq \Omega$), i.e., to estimate the value, for example, of

$$\ell_\varphi(e) = \ell_\varphi(u-u_h) := \int_\Omega \varphi(u-u_h)\,dx, \quad \text{where} \quad \mathrm{supp}\,\varphi = \omega. \tag{4}$$

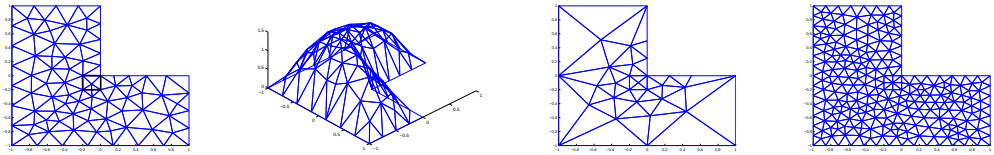

Figure 1: Ω, ω, $\mathcal{T}_h$ (88 nodes), u_h, and typical $\mathcal{T}_\tau$ (31 and 247 nodes).

It is clear that the estimates for the above value can also be used to estimate the value of $\ell_\varphi(u) = \int\limits_\omega \varphi u \, dx$, called often as the *quantity of interest*.

Error decomposition. In order to estimate (4), one usually introduces the so-called *adjoint problem:* Find $v \in H_0^1(\Omega)$ such that (cf. (3))

$$\int\limits_\Omega \mathrm{A}\nabla v \cdot \nabla w \, dx \;=\; \int\limits_\Omega \varphi w \, dx \quad \Big(= \ell_\varphi(w)\Big) \quad \forall w \in H_0^1(\Omega). \tag{5}$$

If function $\varphi \in L_2(\Omega)$, then problem (5) has a unique solution. Usually, one cannot solve (5) exactly and only the finite element approximation v_τ, obtained on *adjoint mesh* $\mathcal{T}_\tau$ (not necesarily coinciding with $\mathcal{T}_h$), is available. Then we can represent error (4) as follows

$$\int\limits_\Omega \varphi(u-u_h)dx = \int\limits_\Omega \mathrm{A}\nabla v\cdot\nabla(u-u_h)dx = \int\limits_\Omega \mathrm{A}\nabla(v-v_\tau)\cdot\nabla(u-u_h)dx + \int\limits_\Omega \mathrm{A}\nabla v_\tau\cdot\nabla(u-u_h)dx =$$

$$= \int\limits_\Omega f v_\tau dx - \int\limits_\Omega \mathrm{A}\nabla v_\tau\cdot\nabla u_h dx + \int\limits_\Omega \mathrm{A}\nabla(v-v_\tau)\cdot\nabla(u-u_h)dx = E_0(u_h,v_\tau) + E_1(u_h,v_\tau). \tag{6}$$

Construction of estimator. It is well known that averaged gradients of finite element approximations for linear elliptic problems usually demonstrate so-called *superconvergence effect* (see, e.g., [1]). This suggests to use averaged gradients instead of unknown gradients in (6) and estimate (4) by the following *a posteriori computable* value (called *estimator*) $\tilde{E}(u_h,v_\tau) = E_0(u_h,v_\tau) + \tilde{E}_1(u_h,v_\tau)$, where

$$\tilde{E}_1(u_h,v_\tau) = \int\limits_\Omega \mathrm{A}(G_\tau(\nabla v_\tau) - \nabla v_\tau)\cdot(G_h(\nabla u_h) - \nabla u_h)\, dx, \tag{7}$$

and G_h and G_τ are suitable gradient averaging operators.

Numerical test. Let Ω be a L-shaped domain with reentrant corner at $(0,0)$ obtained from a square $(-1,1)\times(-1,1)$, $\omega := (-0.2,0)\times(-0.2,0)$ (see Fig. 1 (left)), let $\varphi \equiv 1$ in ω (and vanish outside of ω), A be the unit matrix, $f \equiv 10$ in Ω. The continuous piecewise linear finite element solution u_h is calculated on $\mathcal{T}_h$ with 88 nodes, then $\ell(u-u_h) = 0.005346$. The performance of the estimator for various choices of adjoint meshes (having 31, 42, ..., 2077 nodes) is presented in Fig. 2. The *effectivity index* $I_{eff} := \tilde{E}(u_h,v_\tau)/\ell(u-u_h)$. We clearly observe that: a) estimator gives reasonably good results ($0.72 \le I_{eff} \le 0.93$) for adjoint meshes which are considerably coarser than the primal meshes; b) estimator is asymptotically ($\tau \to 0$) correct. Very similar results are reported in [2, 3, 4, 5] for the problem (1) with mixed boundary conditions and also for problems in linear elasticity.

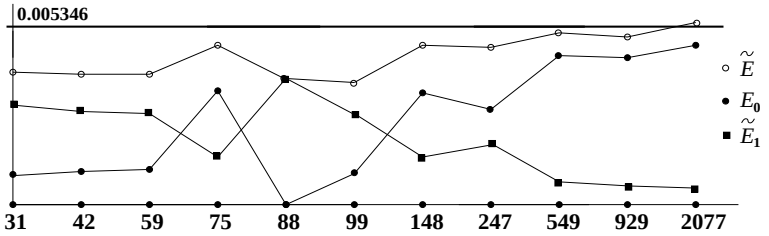

Figure 2: Behaviour of estimator $\tilde{E}$ and its parts, E_0 and $\tilde{E}_1$, for various adjoint meshes.

Mesh adaptivity. The estimator $\tilde{E}(u_h, v_\tau) = \sum_{T \in \mathcal{T}_h^{(i)}} I_T$, where each contribution I_T is a value of the integral taken over a particular element T of the current primal mesh $\mathcal{T}_h^{(i)}$. This suggests to construct the next primal mesh $\mathcal{T}_h^{(i+1)}$ in order to decrease the error (4) as follows. First, we find the maximum among all modulus $|I_T|$'s and, secondly, mark up those elements T's which have their contributions larger than the "user-given threshold" θ ($\theta \in [0, 1]$) times that maximum value. Refining the marked elements and making the mesh conforming, we get $\mathcal{T}_h^{(i+1)}$. The high effectivity of this adaptive procedure has been demonstrated in [2, 3, 5].

Control of error in local integral norms

Estimates for the error measured in terms of specially constructed functionals can be used also for evaluating local integral norms of the error. Let us consider, for example,

$$\|e\|_{2,\omega}^2 = \|u - u_h\|_{2,\omega}^2 = \int_\omega |u(x) - u_h(x)|^2 \, dx. \tag{8}$$

It is obvious that $\|u - u_h\|_{2,\omega} = \sup_{\eta \in L_2(\omega)} \frac{\int_\omega \eta(u-u_h)dx}{\|\eta\|_{2,\omega}}$, where supremum is attained at $\eta = u - u_h$. If a priori known that $u - u_h \in \Xi(\omega) \subset L_2(\omega)$, then

$$\|u - u_h\|_{2,\omega} = \sup_{\eta \in \Xi(\omega)} \frac{\int_\omega \eta(u - u_h)dx}{\|\eta\|_{2,\omega}} =: |u - \bar{u}|_\Xi. \tag{9}$$

However, $|u - u_h|_\Xi$ is only *seminorm* and equality in (9) is normally replaced by inequality. Nevertheless, $|\cdot|_\Xi$ may give adequate presentation on norm $\|\cdot\|_{2,\omega}$ provided Ξ contains sufficiently large amount of trial functions. Let $\Xi := \{\varphi_1, \varphi_2, \ldots, \varphi_n\}$, where φ_i are given. In [4] it is first proved that

$$|u - u_h|_\Xi = (\mathbf{B}^{-1}\mathbf{l} \cdot \mathbf{l})^{\frac{1}{2}}, \tag{10}$$

where

$$\mathbf{l} = (\ell_{\varphi_1}, \ell_{\varphi_2}, \ldots, \ell_{\varphi_n})^T, \quad \ell_{\varphi_i}(u - u_h) = \int_\omega \varphi_i(u - u_h)dx, \quad \mathbf{B} = \Big(\int_\omega \varphi_i\varphi_j \, dx\Big)_{i,j=1}^n. \tag{11}$$

Further, it is proved that $\Big||u - u_h|_\Xi - \|u - u_h\|_{2,\omega}\Big| = \mathcal{O}(\mathrm{diam}(\omega)^k)$, where k depends on regularity of u and number of trial functions used in definition of $|\cdot|_\Xi$, see [4]. Thus, estimates from Section 2 can be efectively used to estimate the error (8) by (10)–(11) with ℓ_{φ_i}, $i = 1, \ldots, n$, replaced by corresponding estimates.

Numerical test. Consider the test problem from Section 2, for which $\|u-u_h\|_{2,\omega} = 0.028703$. To estimate this local norm of the error we can use e.g. estimates via 4 functionals, $\ell_{\varphi_1}, \ldots, \ell_{\varphi_4}$, with $\varphi_1, \ldots, \varphi_4$ being bilinear over ω and constructed so that they are equal to 1 at one node and 0's at the other. If the error in terms of functionals can be computed exactly then $|u-u_h|_\Xi = 0.028182$, which gives a very good estimation of (8) as predicted theoretically in [4]. However, in practice we only have estimators' values, which estimate the error by the value 0.019795 if the adjoint mesh with 42 nodes is used, and by the value 0.026881 - for the case of the adjoint mesh with 549 nodes.

Comments

1. The approach proposed in Section 2 is different from the others available in the literature, where it is always assumed that primal and adjoint problems are solved on the same mesh. Using our technique one can obtain reliable estimates also for the case when the number of nodes in adjoint mesh is considerably smaller than the number of nodes in primal mesh.
2. The effectivity of the estimator $\tilde{E}$ strongly increases when one is interested not in a single solution of the primal problem for a concrete data, but analyzes a series of approximate solutions for a certain set of boundary conditions and various right-hand sides (which is typical in the engineering design when it is necessary to model the behavior of a construction for various working regimes). In this case, the adjoint problem can be solved *only once* (for each ω and ℓ_φ), and this solution can be further used in testing the accuracy of approximate solutions of various primal problems.
3. In the above we considered problem (1) with a homogeneous Dirichlet boundary condition only for simplicity. A more general problem with nonhomogeneous mixed boundary conditions can be treated in the same way (see [2]). Similar estimates can be straightforwardly constructed (using the ideas described above) for the other elliptic models, e.g., in linear elasticity (see [3, 5]), etc. The same ideology can be also applied to approximations obtained by hp-version of FEM.

Acknowledgement

The author was supported by the Academy Research Fellowship no. 208628 from the Academy of Finland.

References

[1] I. Hlaváček, M. Křížek. On a superconvergent finite element scheme for elliptic systems. I. Dirichlet boundary conditions. *Apl. Mat.* 32, 131–154, 1987.
[2] S. Korotov. A posteriori error estimation of goal-oriented quantities for elliptic type BVPs. *J. Comput. Appl. Math.* (in press).
[3] S. Korotov. Error control in terms of linear functionals based on gradient averaging techniques. *Computing Letters* (submitted).
[4] S. Korotov, P. Neittaanmäki, S. Repin. A posteriori error estimation of goal-oriented quantities by the superconvergence patch recovery. *J. Numer. Math.* 11, 33–59, 2003.
[5] M. Rüter, S. Korotov, Ch. Steenbock. A posteriori error estimates in linear elastic fracture mechanics based on different FE-solution spaces for the primal and the dual problem. In *Proc. of the 18-th Nordic Seminar of Comput. Mech. (NSCM18), Helsinki-Stockholm* 2005.

Solution of the Helmholtz equation with controllability and spectral element methods

Erkki Heikkola
VTT Processes, Jyväskylä, Finland

Sanna Mönkölä*, Anssi Pennanen, Tuomo Rossi
Department of Mathematical Information Technology,
University of Jyväskylä, Jyväskylä, Finland
*e–mail: sanna.monkola@it.jyu.fi

Summary We formulate the Helmholtz problem as an exact controllability problem for the time-dependent wave equation. The problem is discretized in space domain with spectral elements leading to high accuracy and diagonal mass matrices. After discretization, exact controllability problem is reformulated as a least squares problem, which is solved by conjugate gradient method. We illustrate the method with some numerical experiments on an acoustic scattering simulation.

Introduction

We consider a controllability method for the numerical solution of the two-dimensional Helmholtz equation with an absorbing boundary condition describing the scattering of a time-harmonic incident wave by a sound-soft obstacle:

$$-\frac{\kappa(\mathbf{x})^2}{\rho(\mathbf{x})}U - \nabla\cdot\Big(\frac{1}{\rho(\mathbf{x})}\nabla U\Big) = 0, \qquad \text{in } \Omega, \tag{1}$$

$$U = 0, \qquad \text{on } \Gamma_0, \tag{2}$$

$$-i\kappa(\mathbf{x})U + \frac{\partial U}{\partial \mathbf{n}} = G_{\text{ext}}, \qquad \text{on } \Gamma_{\text{ext}}, \tag{3}$$

where $U(\mathbf{x})$ denotes the total acoustic pressure consisting of the scattered wave $U_{\text{scat}}(\mathbf{x})$ and the incident wave $U_{\text{inc}}(\mathbf{x}) = \exp(i\vec{\omega}\cdot\mathbf{x})$, where i is the imaginary unit and the vector $\vec{\omega}$ gives the propagation direction. The function G_{ext} depends on the incident wave. The domain Ω is bounded by the surface of the obstacle Γ_0 and an absorbing boundary Γ_{ext}. Vector $\mathbf{n}$ is the outward normal vector to domain Ω. The wavenumber and density of the material are denoted by $\kappa(\mathbf{x})$ and $\rho(\mathbf{x})$, respectively, and they are varying with respect to $\mathbf{x}$. The wavenumber is related to the angular frequency $\omega = \|\vec{\omega}\|_2$ and to the speed of sound $c(\mathbf{x})$ by the formula $\kappa(\mathbf{x}) = \frac{\omega}{c(\mathbf{x})}$. The corresponding wavelength is given by $\lambda(\mathbf{x}) = \frac{2\pi}{\kappa(\mathbf{x})}$.

Numerous solution methods exist directly for the time-harmonic equation above. For example, various fictitious domain and domain decomposition methods have been applied to the corresponding finite element problems. A common quality of these methods is that they lead to large-scale indefinite linear systems, which are solved iteratively. It is difficult to develop efficient preconditioners for the iterative solution, especially when the material coefficients are varying. Another difficulty in the finite element solution of the Helmholtz equation is the pollution effect, which deteriorates accuracy when wave number increases even if discretization resolution is kept fixed (see, e.g., [6]). Many techniques have been developed to reduce the pollution effect and during recent years various methods using plane waves as basis functions have turned out to be succesful (see, e.g., [3], [5]). In this work, we adhere to a polynomial basis, but increase the order of the basis functions to reduce the pollution effect.

Exact controllability formulation

An alternative approach to solving the time-harmonic equation is to return to the corresponding time-dependent equation and look for time-periodic solution. Direct time-integration of the wave equation can be used to reach the time-periodic case, but convergence is usually too slow to be useful in practice. We use the idea of Bristeau, Glowinski and Périaux to speed up the convergence by control techniques [1]. The original time-harmonic equation is reformulated as exact controllability problem for the wave equation: Find initial conditions e_0 and e_1 such that:

$$\frac{1}{\rho(\mathbf{x})c(\mathbf{x})^2}\frac{\partial^2 u}{\partial t^2} - \nabla\cdot\left(\frac{1}{\rho(\mathbf{x})}\nabla u\right) = 0, \qquad \text{in } Q = \Omega\times[0,T], \tag{4}$$

$$u = 0, \qquad \text{on } \gamma_0 = \Gamma_0\times[0,T], \tag{5}$$

$$\frac{1}{c(\mathbf{x})}\frac{\partial u}{\partial t} + \frac{\partial u}{\partial \mathbf{n}} = g_{\text{ext}}, \qquad \text{on } \gamma_{\text{ext}} = \Gamma_{\text{ext}}\times[0,T], \tag{6}$$

$$u(\mathbf{x},0) = e_0, \quad \frac{\partial u}{\partial t}(\mathbf{x},0) = e_1 \qquad \text{in } \Omega, \tag{7}$$

$$u(\mathbf{x},T) = e_0, \quad \frac{\partial u}{\partial t}(\mathbf{x},T) = e_1 \qquad \text{in } \Omega. \tag{8}$$

Spectral element discretization

For the spatial discretization of the wave equation (4)-(7), we use spectral element method, which combines the geometric flexibility of classical finite elements with the high accuracy of spectral methods. The computational domain is divided into quadrilateral elements, and in each element a local higher-order polynomial basis is introduced. The degrees of freedom corresponding to the basis functions are located at the Gauss-Lobatto integration points of the elements. This method is especially useful for the solution of time-dependent wave equations, because it leads to a diagonal mass matrix also with a higher-order basis [2] (see also [8]). This fact is very beneficial for the time-dependent simulation with explicit schemes. After spatial discretization we have the semi-discrete equation

$$\mathcal{M}\frac{\partial^2\mathbf{u}}{\partial t^2} + \mathcal{S}\frac{\partial\mathbf{u}}{\partial t} + \mathcal{K}\mathbf{u} = \mathcal{F}, \tag{9}$$

where vector $\mathbf{u}(t)$ contains the nodal values of the function $u(\mathbf{x},t)$ at time t, and satisfies the initial condition (7) at time $t = 0$. Because mass matrices $\mathcal{M}$ and $\mathcal{S}$ are diagonal, explicit time stepping with central finite differences requires only matrix-vector multiplications. Stiffness matrix is denoted by $\mathcal{K}$, and $\mathcal{F}$ is the vector due to the function g_{ext}.

Least-squares problem

The exact controllability problem for computing $T-$periodic solution for the wave equation involves finding such initial conditions e_0 and e_1 that the solution u and its time derivative $\frac{\partial u}{\partial t}$ at time T would coincide with the initial conditions. For the numerical solution, the exact controllability problem is replaced by a least-squares optimization problem with the functional J, which is, on the discrete level, of the form:

$$J(e_0,e_1,\mathbf{u}) = \frac{1}{2}\left((\mathbf{u}(t)-e_0)^T\mathcal{K}(\mathbf{u}(t)-e_0) + \left(\frac{\partial\mathbf{u}(t)}{\partial t}-e_1\right)^T\mathcal{M}\left(\frac{\partial\mathbf{u}(t)}{\partial t}-e_1\right)\right). \tag{10}$$

The purpose is to minimize functional J, which depends on the initial conditions both directly and indirectly through the solution of the wave equation.

Conjugate gradient method
Since vector $\mathbf{u}$ depends linearly on the initial conditions e_0 and e_1, J is a quadratic function, and (10) can be minimized by solving the linear system $\nabla J(e_0, e_1) = 0$ with a preconditioned conjugate gradient (CG) method. The transition procedure to compute the initial approximation of e_0 and e_1 for the CG algorithm as well as the block-diagonal preconditioner,

$$\mathcal{L} = \begin{pmatrix} \mathcal{K} & 0 \\ 0 & \mathcal{M} \end{pmatrix}, \tag{11}$$

are the same as the ones used in [1].

Each CG iteration step requires computation of the gradient ∇J, which involves the solution of the wave equation (4)-(8) and its adjoint equation. Also solution of one linear system with matrix $\mathcal{L}$ and some matrix-vector operations are needed. In [1], formulas for the gradient corespond to the continuous function, while we compute the gradient of the discretized function (10). Thus, the formulas are slightly different, but the basic operations are the same.

Solution of a linear system with the preconditioner requires the solution of two systems with the stiffness matrix $\mathcal{K}$ and the diagonal mass matrix $\mathcal{M}$. Efficient solution of linear systems with the matrix $\mathcal{K}$ is critical for the overall efficiency of the control method. We apply the algebraic multigrid (AMG) by Kickinger [7] at this stage. The use of AMG methods for spectral elements has recently been studied in [4].

Numerical examples
We illustrate the performance of the controllability method with scattering in domain $\Omega = [0, 5] \times [0, 4]$, where we have two coated non-convex semi-open cavities as reflectors. Internal width and height of cavities are 0.75 and 1.25. Thickness of both the wall and the coating material is 0.25, and distance between cavities is 1.0 (see Fig. 1). To guarantee accuracy demands also for higher orders, the time interval $[0.0, 1.0]$ is divided into 300 timesteps of equal size. Computations have been carried out on a HP 9000/785/J5600 workstation at 552 MHz PA-RISC 8600 CPU.

The absorbing boundary condition is presented such that $g_{\text{ext}} = \frac{\partial u_{\text{inc}}}{\partial \mathbf{n}} + \frac{\partial u_{\text{inc}}}{\partial t}$ with the incidence plane wave of the form $u_{\text{inc}}(\mathbf{x}, t) = \cos(\vec{\omega} \cdot \mathbf{x}) \cos(\omega t) + \sin(\vec{\omega} \cdot \mathbf{x}) \sin(\omega t)$, whit angular frequency $\omega = 4\pi$ and propagation direction $\vec{\omega} = \frac{\omega}{2}(-\sqrt{2}, \sqrt{2})$. Density is assumed to be constant $\rho(\mathbf{x}) = 1.0$. In the first test, the speed of sound $c(\mathbf{x})$ is varying such that it is equal to one outside the obstacle and 0.5 in the coating, implying that outside the obstacle wavelength $\lambda(\mathbf{x}) = 0.5$ and in the coating $\lambda(\mathbf{x}) = 0.25$. Absorbing boundary is located at a distance of 1.5λ from the obstacle. Since rectangular mesh with element width $h = 0.0625$ is used, there are 8 elements per wavelength outside the obstacle and 4 in the coating. In the second test case, parameters are the same, expect $c(\mathbf{x}) = 0.25$ in the coating of the right hand obstacle.

Both test examples are solved by increasing the order of the spectral element basis. Contour lines representing the total field u in (4)-(8) are plotted in Fig. 1 and Fig. 2 with order of the spectral element basis equal to 4. The number of CG iterations needed to solve the control problem are given in Tbl. 1, which also shows the number of degrees of freedom (DOF) in the spectral element mesh. CPU time in seconds is depicted in Fig. 3, where DOF increases as the order of the spectral element basis increases from 1 to 5. Spectral order equal to one corresponds to bilinear finite elements.

Concluding remarks
Simulation results in Tbl. 1 show that, if the spatial discretization is accurate enough, the number of iterations remains nearly constant while the number of optimization variables (i.e. two times

DOF) increases. In addition, the computational effort of the method seems to depend linearly on DOF (see Fig. 3).

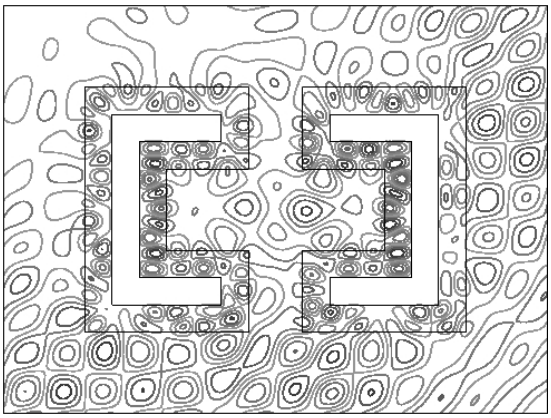

Figure 1: Solution of the first test problem.

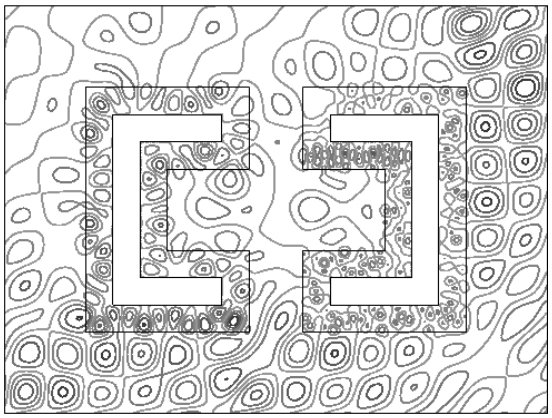

Figure 2: Solution of the second test problem.

order	DOF	number of iterations test 1	test 2
1	4635	372	579
2	18039	289	695
3	40211	292	594
4	71151	292	596

Table 1: Number of iterations which is needed to reduce the relative euclidean norm of the gradient of the functional J below 10^{-4}.

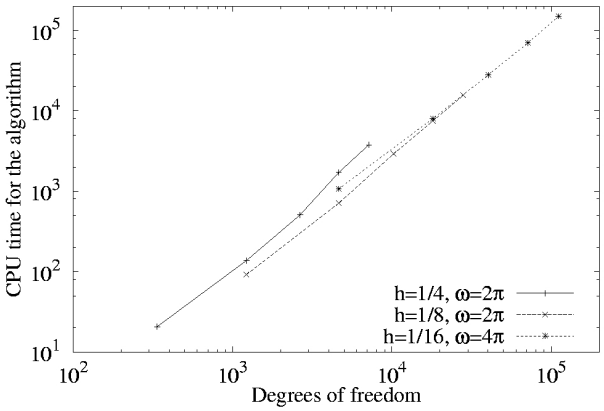

Figure 3: CPU time in seconds with respect to degrees of freedom, when $c(\mathbf{x})$ is 0.5 in both coatings and 1.0 outside the obstacles.

References

[1] M. O. Bristeau, R. Glowinski, and J. Périaux. Controllability methods for the computation of time-periodic solutions; application to scattering. *Journal of Computational Physics*, 147(2):265–292, 1998.

[2] G. Cohen. *Higher-Order Numerical Methods for Transient Wave Equations*. Springer Verlag, 2001.

[3] C. Farhat, P. Wiedemann-Goiran, and R. Tezaur. A discontinuous Galerkin method with plane waves and Lagrange multipliers for the solution of short wave exterior Helmholtz problems on unstructured meshes. *Wave Motion*, 39(4):307–317, 2004.

[4] J.J. Heys, T.A. Manteuffel, S.F. McCormick, and L.N. Olson. Algebraic multigrid for higher-order finite elements. *Journal of Computational Physics*, 204(2):520–532, 2005.

[5] T. Huttunen, J. P. Kaipio, and P. Monk. The perfectly matched layer for the ultra weak variational formulation of the 3D Helmholtz equation. *International Journal for Numerical Methods in Engineering*, 61(7):1072–1092, 2004.

[6] F. Ihlenburg. *Finite Element Analysis of Acoustic Scattering*. Springer Verlag, 1998.

[7] F. Kickinger. Algebraic multi-grid for discrete elliptic second-order problems. In *Multigrid methods V (Stuttgart, 1996)*, pages 157–172. Springer, Berlin, 1998.

[8] O. Z. Mehdizadeh and Paraschivoiu M. Investigation of a two-dimensional spectral element method for Helmholtz's equation. *Journal of Computational Physics*, 189:111–129, 2003.

Vectors and tensors with matrix manipulations

J. Freund*
Laboratory for Mechanics of Materials
Helsinki University of Technology, Espoo, Finland
e–mail: jouni.freund@tkk.fi

J. Paavola and E.-M. Salonen
Laboratory of Structural Mechanics,
Helsinki University of Technology, Espoo, Finland
e–mail: juha.paavola@tkk.fi and eero-matti.salonen@tkk.fi

Summary A matrix-based manipulation to deal with invariant expressions in arbitrary coordinates is described. It can be considered as a simplified tensor analysis formulation for first and second order tensors. The skills demanded from the student to be able to apply the formulation are modest: basic matrix algebra and few rules concerning open products in dyads. Use of the method is demonstrated in connection with polar coordinates and momentum balance equation of mechanics.

Introduction

Tensor analysis formalism is undoubtedly the most elegant way to describe physics and especially mechanics in arbitrary coordinate systems. In basic engineering courses, however, there is usually no possibility to sacrifice time for preparing the students to master the necessary concepts of, say, summation convention, covariant differentiation, Christoffel symbols, etc. [1]. Then, a matrix-based formalism, can be employed with profit as this mathematical tool should be familiar from the elementary courses of linear algebra.

Notation

Two sets of base vectors will be considered simultaneously, of which one is the Cartesian "reference system" and the other one general. These are denoted here by the symbols $\vec{i}, \vec{j}$ and $\vec{e}_\alpha, \vec{e}_\beta$, respectively. The relationship between the systems is written as

$$\begin{Bmatrix} \vec{e}_\alpha \\ \vec{e}_\beta \end{Bmatrix} = [F] \begin{Bmatrix} \vec{i} \\ \vec{j} \end{Bmatrix}, \tag{1}$$

where $[F]$ is a 2×2 matrix having an inverse. As above and in what follows, a square matrix will be represented by square brackets and a column matrix by braces. Inverting or/and transposing (1) and using rules of matrix algebra gives obvious equivalent alternative representations.

Employing these base vectors, a vector $\vec{a}$ can be expressed e.g. in forms

$$\vec{a} = \begin{Bmatrix} a_x & a_y \end{Bmatrix} \begin{Bmatrix} \vec{i} \\ \vec{j} \end{Bmatrix} = \begin{Bmatrix} \vec{i} & \vec{j} \end{Bmatrix} \begin{Bmatrix} a_x \\ a_y \end{Bmatrix} = \begin{Bmatrix} a_\alpha & a_\beta \end{Bmatrix} \begin{Bmatrix} \vec{e}_\alpha \\ \vec{e}_\beta \end{Bmatrix} = \begin{Bmatrix} \vec{e}_\alpha & \vec{e}_\beta \end{Bmatrix} \begin{Bmatrix} a_\alpha \\ a_\beta \end{Bmatrix} \tag{2}$$

and a dyad $\vec{\vec{a}}$ for example as

$$\vec{\vec{a}} = \begin{Bmatrix} \vec{i} & \vec{j} \end{Bmatrix} \begin{bmatrix} a_{xx} & a_{xy} \\ a_{yx} & a_{yy} \end{bmatrix} \begin{Bmatrix} \vec{i} \\ \vec{j} \end{Bmatrix} = \begin{Bmatrix} \vec{e}_\alpha & \vec{e}_\beta \end{Bmatrix} \begin{bmatrix} a_{\alpha\alpha} & a_{\alpha\beta} \\ a_{\beta\alpha} & a_{\beta\beta} \end{bmatrix} \begin{Bmatrix} \vec{e}_\alpha \\ \vec{e}_\beta \end{Bmatrix} = \begin{Bmatrix} \vec{i} & \vec{j} \end{Bmatrix} \begin{bmatrix} a_{x\alpha} & a_{x\beta} \\ a_{y\alpha} & a_{y\beta} \end{bmatrix} \begin{Bmatrix} \vec{e}_\alpha \\ \vec{e}_\beta \end{Bmatrix}. \tag{3}$$

From the matrix algebra point of view, representations of (3) are 1×1-matrices. In ordinary matrix algebra, transposing a 1×1-matrix (often called a scalar) does not change its value. However, here with dyads, transposing any of the right-hand sides of (3) using the ordinary matrix algebra rules produces the conjugate dyad $\vec{\vec{a}}_c$. For example,

$$\vec{\vec{a}}_c = \begin{Bmatrix} \vec{i} & \vec{j} \end{Bmatrix} \begin{bmatrix} a_{xx} & a_{xy} \\ a_{yx} & a_{yy} \end{bmatrix}^T \begin{Bmatrix} \vec{i} \\ \vec{j} \end{Bmatrix} = \begin{Bmatrix} \vec{e}_\alpha & \vec{e}_\beta \end{Bmatrix} \begin{bmatrix} a_{\alpha\alpha} & a_{\alpha\beta} \\ a_{\beta\alpha} & a_{\beta\beta} \end{bmatrix}^T \begin{Bmatrix} \vec{e}_\alpha \\ \vec{e}_\beta \end{Bmatrix} \tag{4}$$

This follows from the non-commutative property of the open products of the base vectors in the dyads. Connections between the components of the invariant quantities $\vec{a}$ and $\vec{a}$ in (2) and (3) in different bases can be easily obtained with the help of relation (1).

Basic tools

The connection indicated above between two sets of base vectors can be employed without necessarily considering the sets associated with two separate coordinate systems. From this on, however, we consider in particular a mapping between the familiar rectangular Cartesian system with coordinates *x* and *y* and another possibly curvilinear one with coordinates α and β

$$\vec{r} = \begin{Bmatrix} x & y \end{Bmatrix} \begin{Bmatrix} \vec{i} \\ \vec{j} \end{Bmatrix} = \begin{Bmatrix} x(\alpha,\beta) & y(\alpha,\beta) \end{Bmatrix} \begin{Bmatrix} \vec{i} \\ \vec{j} \end{Bmatrix}. \tag{5}$$

The conventional obvious way to associate base vectors with the coordinate systems is as follows:

$$\begin{Bmatrix} \vec{e}_x \\ \vec{e}_y \end{Bmatrix} = \begin{Bmatrix} \partial\vec{r}/\partial x \\ \partial\vec{r}/\partial y \end{Bmatrix} = \begin{Bmatrix} \vec{i} \\ \vec{j} \end{Bmatrix} \tag{6}$$

and

$$\begin{Bmatrix} \vec{e}_\alpha \\ \vec{e}_\beta \end{Bmatrix} = \begin{Bmatrix} \partial\vec{r}/\partial\alpha \\ \partial\vec{r}/\partial\beta \end{Bmatrix} = \begin{bmatrix} \partial x/\partial\alpha & \partial y/\partial\alpha \\ \partial x/\partial\beta & \partial y/\partial\beta \end{bmatrix} \begin{Bmatrix} \vec{i} \\ \vec{j} \end{Bmatrix} \tag{7}$$

In tensor analysis literature, base vectors defined as (6) and (7) are said to form a natural basis for the systems or they are called covariant base vectors. As seen, base vectors (6) are here unit vectors whereas base vectors (7) are usually not of unit length. The corresponding unit vectors can be obtained by normalizing. However, formulas remain usually much simpler if the derivations proceed with base vectors (7). If desired, the normalization to unit vectors can be performed at the very end.

Comparison with (1) shows that here the matrix

$$[F] = \begin{bmatrix} \partial x/\partial\alpha & \partial y/\partial\alpha \\ \partial x/\partial\beta & \partial y/\partial\beta \end{bmatrix}. \tag{8}$$

One useful result is obtained as follows:

$$\begin{Bmatrix} \vec{e}_\alpha \\ \vec{e}_\beta \end{Bmatrix} \cdot \begin{Bmatrix} \vec{e}_\alpha & \vec{e}_\beta \end{Bmatrix} = [F] \begin{Bmatrix} \vec{i} \\ \vec{j} \end{Bmatrix} \cdot \begin{Bmatrix} \vec{i} & \vec{j} \end{Bmatrix} [F]^{\mathrm{T}} = [F][F]^{\mathrm{T}} = [G] \tag{9}$$

The interpretation of the manipulations above, and its generalization to other types of products, combining vector and matrix algebra should be rather obvious. The symmetric matrix [*G*] of (9) is the matrix counterpart of the covariant metric tensor. It has a very important role in continuum mechanics and therefore introducing the shorthand notation for it is justified.

The derivatives of the general base vectors with respect to the curvilinear coordinates and given in the same basis are needed in many cases. We find from (1) (as base vectors of the Cartesian system are constants):

$$\frac{\partial}{\partial\alpha} \begin{Bmatrix} \vec{e}_\alpha \\ \vec{e}_\beta \end{Bmatrix} = \frac{\partial}{\partial\alpha}[F] \begin{Bmatrix} \vec{i} \\ \vec{j} \end{Bmatrix} = \left(\frac{\partial}{\partial\alpha}[F] \right) [F]^{-1} \begin{Bmatrix} \vec{e}_\alpha \\ \vec{e}_\beta \end{Bmatrix}, \tag{10}$$

$$\frac{\partial}{\partial\beta} \begin{Bmatrix} \vec{e}_\alpha \\ \vec{e}_\beta \end{Bmatrix} = \frac{\partial}{\partial\beta}[F] \begin{Bmatrix} \vec{i} \\ \vec{j} \end{Bmatrix} = \left(\frac{\partial}{\partial\beta}[F] \right) [F]^{-1} \begin{Bmatrix} \vec{e}_\alpha \\ \vec{e}_\beta \end{Bmatrix}. \tag{11}$$

Comparing these with tensor analysis literature, it is seen that the matrix products multiplying the column matrix of base vectors on the right-hand sides of (10) and (11) are the matrix counterparts of the Christoffel symbols of the second kind.

Applying chain differentiation gives

$$\begin{Bmatrix} \partial/\partial x \\ \partial/\partial y \end{Bmatrix} = \begin{bmatrix} \partial\alpha/\partial x & \partial\beta/\partial x \\ \partial\alpha/\partial y & \partial\beta/\partial y \end{bmatrix} \begin{Bmatrix} \partial/\partial\alpha \\ \partial/\partial\beta \end{Bmatrix} = [F]^{-1} \begin{Bmatrix} \partial/\partial\alpha \\ \partial/\partial\beta \end{Bmatrix}, \tag{12}$$

where the last form is seen to be valid by inverting relation (8). The formula is useful for instance when the nabla operator is employed. Starting with the well-known expression in the rectangular Cartesian case, we obtain

$$\vec{\nabla} = \begin{Bmatrix} \vec{i} & \vec{j} \end{Bmatrix} \begin{Bmatrix} \partial/\partial x \\ \partial/\partial y \end{Bmatrix} = \begin{Bmatrix} \vec{e}_\alpha & \vec{e}_\beta \end{Bmatrix} \left([F][F]^{\mathrm{T}} \right)^{-1} \begin{Bmatrix} \partial/\partial\alpha \\ \partial/\partial\beta \end{Bmatrix} = \begin{Bmatrix} \vec{e}_\alpha & \vec{e}_\beta \end{Bmatrix} [G]^{-1} \begin{Bmatrix} \partial/\partial\alpha \\ \partial/\partial\beta \end{Bmatrix}. \tag{13}$$

These are the tools necessary for applications. We continue with some illustrative examples. The idea is to start from an invariant quantity expressed in a familiar form in a rectangular Cartesian coordinate system and by suitable matrix manipulations express it finally in variables of the other system [2].

Gradient in polar coordinates

We consider first the polar coordinate system with $\alpha \sim r$ and $\beta \sim \theta$ and derive the expression of the gradient operator. The mapping between the Cartesian system and the polar coordinate system of type (5) is given by

$$\vec{r} = \begin{Bmatrix} x & y \end{Bmatrix} \begin{Bmatrix} \vec{i} \\ \vec{j} \end{Bmatrix} = \begin{Bmatrix} r\cos\theta & r\sin\theta \end{Bmatrix} \begin{Bmatrix} \vec{i} \\ \vec{j} \end{Bmatrix}. \tag{14}$$

From this we get

$$[F] = \begin{bmatrix} \cos\theta & \sin\theta \\ -r\sin\theta & r\cos\theta \end{bmatrix}, \quad [G] = [F][F]^{\mathrm{T}} = \begin{bmatrix} 1 & 0 \\ 0 & r^2 \end{bmatrix}, \tag{15}$$

and from (13)

$$\vec{\nabla} = \vec{i}\,\frac{\partial}{\partial x} + \vec{j}\,\frac{\partial}{\partial y} = \begin{Bmatrix} \vec{e}_r & \vec{e}_\theta \end{Bmatrix} [G]^{-1} \begin{Bmatrix} \partial/\partial r \\ \partial/\partial\theta \end{Bmatrix} = \vec{e}_r\,\frac{\partial}{\partial r} + \vec{e}_\theta\,\frac{1}{r^2}\frac{\partial}{\partial\theta}. \tag{16}$$

Let us note that here $|\vec{e}_\theta| = r$ and if the base vectors were normalized one would obtain the usual expression containing just one r in the denominator of the second term of (16). The base vectors of the polar coordinate system are clearly orthogonal as the off-diagonal terms of $[G]$ are zeros.

Momentum balance in continuum mechanics

As a second example, we consider equation describing the momentum balance of continuum. Writing component forms of this –innocent looking– equation may easily turn to disaster. In our opinion, explicit use of base vectors makes the reasoning concerning the various selections and steps leading to the component forms rather easy to follow even in case of large displacements and curvilinear material coordinate system.

To be specific, we aim at writing the component forms of differential equation (actually in two-dimensions)

$$\vec{\nabla} \cdot \vec{\vec{\sigma}} + \vec{f} = 0 \quad \text{in} \quad V \subset \mathbb{R}^3, \tag{17}$$

in which $\vec{\vec{\sigma}}$ is the Cauchy stress and $\vec{f}$ is the given body force so that practical calculations are possible. As the equation describes the momentum balance of a material volume V depending on the solution, the first thing is to rewrite (17) in a coordinate system in which the solution domain is constant V°. For this purpose, one assumes that the position vectors of material particles of the initial and final domains V° and V, respectively, are related with mapping

$$\vec{r} = \vec{r}^{\,\circ} + \vec{u}(\vec{r}^{\,\circ}) = \begin{Bmatrix} x + u_x(x,y) & y + u_y(x,y) \end{Bmatrix} \begin{Bmatrix} \vec{i} \\ \vec{j} \end{Bmatrix} = \begin{Bmatrix} r + u_r(r,\theta) & u_\theta(r,\theta) \end{Bmatrix} \begin{Bmatrix} \vec{e}_r \\ \vec{e}_\theta \end{Bmatrix} \tag{18}$$

of type (5),in which $\vec{r}^{\,\circ}$ identifies a material particle and $\vec{u}(\vec{r}^{\,\circ})$ is its displacement. As vector quantities, these can be expressed in any convenient coordinate system as indicated by the

second form for the Cartesian system and the third form for the polar system. The remaining is just an exercise of the themes discussed.

As a dyad, Cauchy stress is invariant and can be expressed in any coordinate system. When substituted there, the gradient and Cauchy stress in system give representation

$$\nabla\cdot\vec{\vec{\sigma}} = \left\{\vec{e}_\alpha \quad \vec{e}_\beta\right\}[G]^{-1}\begin{Bmatrix}\partial/\partial\alpha\\ \partial/\partial\beta\end{Bmatrix}\cdot(\left\{\vec{e}_\alpha \quad \vec{e}_\beta\right\}\begin{bmatrix}\sigma_{\alpha\alpha} & \sigma_{\alpha\beta}\\ \sigma_{\beta\alpha} & \sigma_{\beta\beta}\end{bmatrix}\begin{Bmatrix}\vec{e}_\alpha\\ \vec{e}_\beta\end{Bmatrix}) \tag{19}$$

for the first term on the left hand side of (17). Assuming e.g. that the components of the body force are given in the Cartesian system, the second terms becomes

$$\vec{f} = \left\{f_x \quad f_y\right\}\begin{Bmatrix}\vec{i}\\ \vec{j}\end{Bmatrix} = \left\{f_x \quad f_y\right\}[F]^{-1}\begin{Bmatrix}\vec{e}_\alpha\\ \vec{e}_\beta\end{Bmatrix} \tag{20}$$

When substituted in (17), expressions (19) and (20) give the component forms. Usually the basic unknowns are the displacement components so that mapping (18) is not known 'a priori', but it rather follows as the part of the solution. Then, naturally an additional (constitutive) equation relating somehow the stress dyad and displacement vector is needed.

The relationship between the base vectors of the material coordinate system $\vec{e}_\alpha, \vec{e}_\beta$, the polar coordinate system $\vec{e}_r, \vec{e}_\theta$ and the reference coordinate system $\vec{i}$, $\vec{j}$ is given by

$$\begin{Bmatrix}\vec{e}_\alpha\\ \vec{e}_\beta\end{Bmatrix} = \begin{bmatrix}1+\dfrac{\partial u}{\partial r} & \dfrac{v}{r}+\dfrac{\partial v}{\partial r}\\ \dfrac{\partial u}{\partial\theta}-vr & 1+\dfrac{u}{r}+\dfrac{\partial u}{\partial\theta}\end{bmatrix}\begin{Bmatrix}\vec{e}_r\\ \vec{e}_\theta\end{Bmatrix} = \begin{bmatrix}1+\dfrac{\partial u}{\partial r} & \dfrac{v}{r}+\dfrac{\partial v}{\partial r}\\ \dfrac{\partial u}{\partial\theta}-vr & 1+\dfrac{u}{r}+\dfrac{\partial u}{\partial\theta}\end{bmatrix}\begin{bmatrix}\cos\theta & \sin\theta\\ -r\sin\theta & r\cos\theta\end{bmatrix}\begin{Bmatrix}\vec{i}\\ \vec{j}\end{Bmatrix} \tag{21}$$

Above we have used the shorthand notations $u = u_r$ and $v = u_\theta$. The last form, written in terms the base vectors of the reference coordinate system, is needed as the base vectors of the reference system were assumed to be constants e.g. in derivation of (13) and those for the polar system do not satisfy this. Matrix $[F]$, appearing in the basic formulas, is obvious from (21) and

$$[G] = [F][F]^{\mathrm{T}} = \begin{bmatrix}1+\dfrac{\partial u}{\partial r} & \dfrac{v}{r}+\dfrac{\partial v}{\partial r}\\ \dfrac{\partial u}{\partial\theta}-vr & 1+\dfrac{u}{r}+\dfrac{\partial v}{\partial\theta}\end{bmatrix}\begin{bmatrix}1 & 0\\ 0 & 1/r^2\end{bmatrix}\begin{bmatrix}1+\dfrac{\partial u}{\partial r} & \dfrac{\partial u}{\partial\theta}-vr\\ \dfrac{v}{r}+\dfrac{\partial v}{\partial r} & 1+\dfrac{u}{r}+\dfrac{\partial v}{\partial\theta}\end{bmatrix}. \tag{22}$$

With these expressions, the component forms of the equations (19) become rather lengthy although the derivation is straightforward. The setting simplifies considerably under the small displacement assumption as then only the middle terms of the right hand side of (22) is retained.

Concluding remarks

We have presented a matrix manipulation formulation for vectors and dyads. To apply it, the skills demanded from the student are modest: basic matrix algebra and few rules concerning open products in dyads. As the number of new concepts beyond those of ordinary is not large, the formulation may be useful alternative in some courses in mechanical engineering education.

The presentation was restricted to two dimensions, but the formulas in the three-dimensional case are obtained by increasing the sizes of the relevant matrices just by one. In the discussed form, the presentation does not go beyond second order tensors (this is, however, often enough in mechanics). If index notation and summation convention are introduced, the matrix formulation above can be transformed to a much more compact form. However, this demands a new step of assimilation from the student and if this is worth the effort depends again on the depth of applications in a course.

References

[1] W. Flügge, *Tensor Analysis and Continuum Mechanics*, Springer-Verlag, New York, (1972).

[2] J. Paavola and E.-M. Salonen, Coping with curvilinear coordinates in solid mechanics, *Int.J.Mech.Enging.Educ.* **32**, 1-10, (2004).

Virtual Work, Lagrange's Equations and Finite Elements

J. Freund
Department of Mechanical Engineering
Helsinki University of Technology
e-mail: jouni.freund@tkk.fi

J. Paavola* and E.-M. Salonen
Department of Civil and Environmental Engineering
Helsinki University of Technology
e-mail: juha.paavola@tkk.fi

Summary It is suggested that the connections between Lagrange's equations and system equations in displacement based finite element method should be emphasized in teaching of mechanics. The only actual difference between them lies in the way the generalized forces due to inertia are traditionally calculated. A simple example shows two ways to evaluate generalized forces due to inertia.

Introduction

It is a common experience that students cannot often form a comprehensive view of a subject especially if the knowledge comes from different courses given by different lecturers using maybe varying terminology and notation. In mechanics, computational procedures, for example, have introduced apparently new concepts into teaching and the students may have difficulties to see any connections with the older analytical methods. Every effort should be made to emphasize the unifying concepts in different courses to help the students to assimilate a solid ground based on the actually few basic principles of mechanics. One of these is the principle of virtual work and the present article deals with two apparently different applications of it showing their close connection.

The importance of the principle of virtual work in applications and in teaching of mechanics cannot be overestimated. Lagrange's equations of motion and system equations in displacement based finite element method are powerful examples of procedures obtained directly from the principle of virtual work. Students of engineering meet Lagrange's equations and finite elements probably in separate courses and probably in the above order.

Equations of motion

Let us recall shortly how classical Lagrange's equations of motion are derived using a particle system as an example case. Let the equation of motion for a particle be written as

$$\mathbf{F}_i + \mathbf{f}_i - m_i \mathbf{a}_i = \mathbf{0}. \tag{1}$$

Here, $\mathbf{F}_i$ is the resultant of the external forces acting on the particle, $\mathbf{f}_i$ is the resultant of the internal forces acting on the particle, m_i is the mass of the particle and $\mathbf{a}_i$ the acceleration of the particle. Multiplying (dot product) both sides of (1) by a virtual displacement $\delta\mathbf{r}_i$ and summing the equations over the particles of the system produces the virtual work equation

$$\delta W \equiv \delta W^{\text{ext}} + \delta W^{\text{int}} + \delta W^{\text{inert}} \equiv \sum_i \mathbf{F}_i \bullet \delta\mathbf{r}_i + \sum_i \mathbf{f}_i \bullet \delta\mathbf{r}_i - \sum_i m_i \mathbf{a}_i \bullet \delta\mathbf{r}_i = 0 \tag{2}$$

The meaning of the additional notation introduced should be obvious. The position vector of particle *i* depends on the generalized coordinates $q_1, q_2, \cdots, q_n$ and possibly also explicitly on time *t*:

$$\mathbf{r}_i = \mathbf{r}_i\left(q_1, q_2, \cdots, q_n, t\right). \tag{3}$$

The virtual displacement is obtained as

$$\delta\mathbf{r}_i = \sum_j \frac{\partial \mathbf{r}_i}{\partial q_j}\delta q_j\,. \tag{4}$$

When this is substituted in (2) and it is demanded that the equation is valid for any selection of the variations of the generalized coordinates, there follows the equations of motion

$$Q_j \equiv Q_j^{\text{ext}} + Q_j^{\text{int}} + Q_j^{\text{inert}} = 0, \quad j = 1, 2, \cdots, n \tag{5}$$

where the generalized forces are evaluated by

$$Q_j^{\text{ext}} = \sum_i \mathbf{F}_i \bullet \frac{\partial \mathbf{r}_i}{\partial q_j}, \tag{6}$$

$$Q_j^{\text{int}} = \sum_i \mathbf{f}_i \bullet \frac{\partial \mathbf{r}_i}{\partial q_j}, \tag{7}$$

$$Q_j^{\text{inert}} = -\sum_i m_i \mathbf{a}_i \bullet \frac{\partial \mathbf{r}_i}{\partial q_j}. \tag{8}$$

Students of engineering meet these equations usually for the first time in courses of classical mechanics. However, in this connection the generalized forces due to inertia are first additionally transformed by a rather involved mathematical manipulation into the forms

$$Q_j^{\text{inert}} = -\left(\frac{\mathrm{d}}{\mathrm{d}t}\frac{\partial T}{\partial \dot{q}_j} - \frac{\partial T}{\partial q_j}\right) \tag{9}$$

where T is the kinetic energy of the system. Thus, finally, the equations of motion become

$$\frac{\mathrm{d}}{\mathrm{d}t}\frac{\partial T}{\partial \dot{q}_j} - \frac{\partial T}{\partial q_j} = Q_j^{\text{ext}} + Q_j^{\text{int}}, \quad j = 1, 2, \cdots, n. \tag{10}$$

These are the famous Lagrange's equations of motion. In conservative cases the generalized forces from external and internal forces can further be represented by derivatives of certain potentials.

We might call expression (9) as the indirect way and expression (8) as the direct way to evaluate the generalized forces due to inertia. Of course, they both give identical results but the efforts demanded to perform the calculations may differ considerably. It seems that in textbooks on classical mechanics the direct way is given hardly any notice.

Later, engineering students usually attend courses on the finite element method in the displacement formulation especially in connection with structural mechanics or strengths of materials. The terminology there is traditionally such that the students cannot easily detect any connections with Lagrange's equations. However, the system equations in the finite element method are exactly according to (5), and the transformation into (9) is not usually performed. Now, it is important for the teacher to emphasize to the students that the nodal displacements (changing the continuum to a finite degree of freedom system) are in fact special kind of generalized coordinates. Then a curious student can start to see some connections but he/she may still wonder why the left-hand side of (10) never appears. The obvious reason is that in the finite element method it is quite straightforward to use the direct way to evaluate the generalized

forces (there often called nodal forces) due to inertia. This is because normally the displacements (and thus positions) are linear in the nodal displacements and therefore the accelerations are also linear in the nodal accelerations. This makes the expressions in the direct formulation simple.

An example

We demonstrate the two alternative ways to evaluate generalized forces due to inertia with an extremely simple example of classical mechanics: a pinned frictionless slender homogeneous rod in plane motion under gravity (Fig. 1).

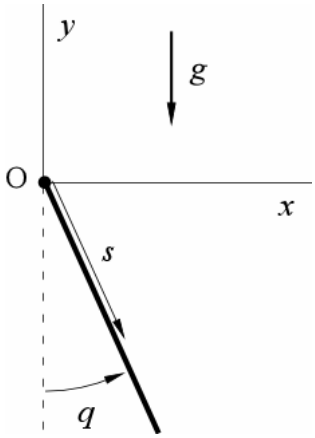

Figure 1: A rod with mass m and length l in plane rotational motion about point O.

Let the inclination angle q (Fig. 1) be the generalized coordinate and let coordinate s along the rod fix generic point on the rod. The position vector is given by

$$\mathbf{r} = s\sin q\,\mathbf{i} - s\cos q\,\mathbf{j} \tag{11}$$

where **i** and **j** are unit vectors along the axes and differentiation gives the velocity

$$\mathbf{v} = s\cos q\,\dot{q}\,\mathbf{i} + s\sin q\,\dot{q}\,\mathbf{j} \tag{12}$$

and acceleration

$$\mathbf{a} = \left(-s\sin q\,\dot{q}^2 + s\cos q\,\ddot{q}\right)\mathbf{i} + \left(s\cos q\,\dot{q}^2 + s\sin q\,\ddot{q}\right)\mathbf{j}. \tag{13}$$

The derivative

$$\frac{\partial \mathbf{r}}{\partial q} = \frac{\mathrm{d}\mathbf{r}}{\mathrm{d}q} = s\cos q\,\mathbf{i} + s\sin q\,\mathbf{j}. \tag{14}$$

The system here is the rod. The generalized force from internal forces is zero. We evaluate the generalized force from external forces (gravity) for simplicity without integrations by reducing the gravity forces to the center of mass to the resultant force

$$\mathbf{F} = -mg\,\mathbf{j}. \tag{15}$$

Thus, according to (6),

$$Q^{\text{ext}} = \mathbf{F}\bullet\frac{\partial \mathbf{r}}{\partial q}\Big|_{s=l/2} = -mg\,\mathbf{j}\bullet\left(\frac{l}{2}\cos q\,\mathbf{i} + \frac{l}{2}\sin q\,\mathbf{j}\right) = -\frac{mgl}{2}\sin q. \tag{16}$$

The indirect way to evaluate the generalized force due to inertia is here very convenient. The kinetic energy of the rod is

$$T = \frac{1}{2} I_0 \dot{q}^2 = \frac{ml^2}{6} \dot{q}^2 \tag{17}$$

and thus from (9):

$$Q_j^{\text{inert}} = -\left(\frac{\mathrm{d}}{\mathrm{d}t} \frac{\partial T}{\partial \dot{q}_j} - \frac{\partial T}{\partial q_j} \right) = -\frac{\mathrm{d}}{\mathrm{d}t} \frac{\partial T}{\partial \dot{q}_j} = -\frac{\mathrm{d}}{\mathrm{d}t} \frac{ml^2}{3} \dot{q} = -\frac{ml^2}{3} \ddot{q}. \tag{18}$$

In the direct way, we obtain using (8) first

$$Q_j^{\text{inert}} = -\int \mathbf{a} \bullet \frac{\partial \mathbf{r}}{\partial q} \mathrm{d}m$$

$$= -\frac{m}{l} \int_0^l \left[\left(-s \sin q \, \dot{q}^2 + s \cos q \, \ddot{q} \right) \mathbf{i} + \left(s \cos q \, \dot{q}^2 + s \sin q \, \ddot{q} \right) \mathbf{j} \right] \bullet \left(s \cos q \, \mathbf{i} + s \sin q \, \mathbf{j} \right) \mathrm{d}s. \tag{19}$$

The integrand becomes

$$\left(-s \sin q \, \dot{q}^2 + s \cos q \, \ddot{q} \right) \left(s \cos q \right) + \left(s \cos q \, \dot{q}^2 + s \sin q \, \ddot{q} \right) \left(s \sin q \right)$$

$$= s^2 \cos^2 q \, \ddot{q} + s^2 \sin^2 q \, \ddot{q} = s^2 \ddot{q}. \tag{20}$$

Thus, finally again,

$$Q_j^{\text{inert}} = -\frac{m}{l} \int_0^l s^2 \ddot{q} \, \mathrm{d}s = -\frac{m}{l} \ddot{q} \int_0^l s^2 \mathrm{d}s = -\frac{m}{l} \ddot{q} \frac{l^3}{3} = -\frac{ml^2}{3} \ddot{q}. \tag{21}$$

The equation of motion becomes

$$Q^{\text{ext}} + Q_j^{\text{inert}} = -\frac{mgl}{2} \sin q - \frac{ml^2}{3} \ddot{q} = 0 \tag{22}$$

or after simplification

$$\ddot{q} + \frac{3g}{2l} \sin q = 0. \tag{23}$$

In the classical textbook applications of Lagrange's equations the systems usually consist of some rigid body and pointmass assemblages. As for these bodies well-known formulas give ready expressions (obtained also originally by integrations) for the kinetic energy, it is easy to see that the indirect way to evaluate generalized forces due to inertia is to be preferred. In the finite element method the situation is different.

Conclusions

Our suggestions based on the above considerations are the following. When Lagrange's equations are lectured on, the teacher should inform the students that later, when they meet the finite element method, the system equations there are in fact "almost" Lagrange's equations, the only difference being the way the generalized forces due to inertia are evaluated. Further, the teacher might present an example like the one above to show in detail the steps needed in obtaining the generalized forces by the two ways. Similarly, when the finite element method is lectured on, the teacher should remind the students about the connections to Lagrange's equations. If a student can see and remember such connections, it leads to a unification of concepts and represents clearly a kind of economy of thought.

Inertia and related topics of education in Mechanics

Lic engrg Lena Strömberg
LTech, Fredrlg 38, Se-38237 Nybro
(previously Dept of Solid Mechanics, Royal Instititute of Techn, KTH)
e-mail: lena_str@hotmail.com

Summary Useful examples in mechanics are given. The merry-go-round walk, as an illustration of kinematics is refered to. An example of Coriolis effect, is revisited and illustrated. Properties of the intertia tensor is highlighted, eg. principal axis, free motion, angle 120-symmetry.

Introduction

It is convenient to introduce properties with their formal three-dimensional definition. Then it is possible to use the tools, already known, from mathematics, eg. trippel vector product and matrix algebra.

Statics

Define: Sum of forces, **F**. Sum of Moment of forces in a point 0, $\mathbf{M}_0$.
Characterize the force-system by the two properties **F**, $\mathbf{M}_0$.
Derive the formula for 'byte av momentpunkt', (change of point for Moment).
Then, it is easy to cathegorize the force-system as either: Nollsystem, Momentsystem, Resultantsystem or Kraftskruv.

Dynamics

In the kinematical formula of acceleration, the different contributions could be exemplified from the 'merry-go-round walk' as in [1].

An interesting observable occurence of the Coriolis effect compared with centripetal acceleration is to be found in river banks, [2][3]. This is illustrated and concluded] [3], cf. Figure 1.

The three dimensional definition of inertia tensor is very useful. With the methods of mathematics, properties of principal axis, symmetries etc, is easily given [1]. As an illustration of free motion around principal axis, a box is thrown in rotation, which is stable or unstable.

From invariance, it could be shown that a 3-'propeller', have two equal principal values, and thus have the same inertia properties as an in-plane circular disc [1].

Conclusion

Some concepts of inertia in classical mechanics were exemplified. Use of modern matrix algebra in conjunction with inertia for rigid bodies, is a challenging combination of abstract formalism and actual moving constructions.

References

[1] Uhlhorn U. Mekanik I och II.
[2] Arnold VI. Mathematical methods of classical mechanics, *Springer*.
[3] Strömberg L. Inertia effects in river flows, *Ltech*, (2003).

Inertia effects in river flows.

Consider an amount of water in motion at a river on earth.
The water fulfils the equation of motion

$m\mathbf{a}=\mathbf{F}$

$\mathbf{a}=\mathbf{a}_{sys}+\mathbf{a}_{rel}$

The system's acceleration $\mathbf{a}_{sys}$ is composed by coriolis-acceleration and centripetal-acceleration.

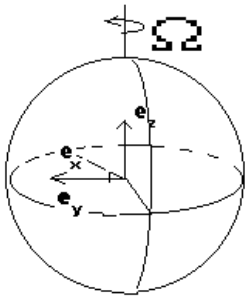

The coriolis-acceleration reads $2\Omega x\mathbf{v}_{rel}$, where Ω is the angular velocity of earth $\Omega=\Omega\mathbf{e}_z$, and $\mathbf{v}_{rel}$ is the velocity of the water relative to the earth.

For river heading west-to-east, the direction of this part regarded as an inertia force is
$-2m\Omega v_{rel}\,\mathbf{e}_z x(-\mathbf{e}_y)= 2m\Omega v_{rel}\,(-\mathbf{e}_x)$.

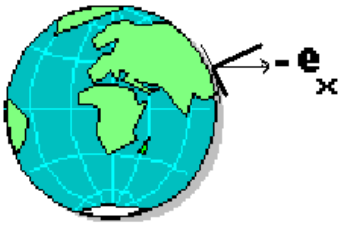

As seen in the figure, on the Northern hemisphere ($-\mathbf{e}_x$) has a component directed towards the equator, south.

In rivers, this could be notified as erodation of the river bank. The effect is largest for straight rivers, where the velocity is directed west-east for a while, (cf. Arnold).

For rivers with sharp bends, the centrifugal force is the dominating. This reads $\omega x(\omega x\mathbf{r})$, where $\omega=v_{rel}/r$, and r is the bending radius.

Hereby, the outer river bank in every bend is affected/erodated, independent of location at earth.

Part of Volga, where the Coriolis-effect is manifested.

The coriolis-effect also cause water eddies to have opposite directions south and north of the equator respectively.

L Strömberg, Fredrikslundsg 38, Se-38237 Nybro
Phone: 0046706275753, lena_str@hotmail.com, www.algonet.se/~lsdata

Stress evaluation in sandwich structures near tri-material wedge

Anders Lyckegaard
Insitute of Mechanical Engineering, Aalborg University,
Pontoppidanstræde 101, DK-9220 Aalborg SØ, Denmark
e–mail: al@ime.aau.dk

Summary It is often necessary to combine different core materials in a sandwich structure. In this case a tri-material wedge is found were the two core materials meet the face sheets. This configuration is known to lead to singular stress state. The evaluation of stresses in this vicinity is not trivial using commercially available analysis software. Here an approach is developed based on the eigenfunction expansion solution used in conjunction with the finite element solution for the whole structure.

Introduction

Sandwich structures consist of two stiff and strong face sheets separated by a thick and compliant core material. This combination results in a structures which is both light weight and has high bending stiffness and strength in addition to high buckling resistance. Sandwich structures often form the basis for extremely light weight application. However, it is often necessary to insert stiff core insert into a sandwich structure, because the main core material is neither strong or stiff enough to support concentrated loads, see Fig. 1(a).
Now a new situation emerges, because at the intersection between the main core and the core insert there is a so-called tri-material wedge. This configuration may lead to singular stresses within the framework of linear elasticity, and this state of stress may seriously affect the strength of the structure – particularity the fatigue strength, see e.g. Bozhevolnaya and Thomsen [1, 2]. It is therefore important to evaluated the strength and magnitude of the singularity.

Assumed solution

The problem is posed a linear elastic solution in two dimensions by assuming plane strain. This may be expressed using Airy's stress function. The solution to Airy stress function is assumed to be (Eq. (1)) expressed in terms of the complex potentials for each of the material domains $z \in \Omega_k$ ($k = \{1, 2, 3\}$) as:

$$\begin{aligned} \varphi_k(z) &= a_{1k} z^{\lambda} + a_{2k} z^{\overline{\lambda}} \\ \psi_k(z) &= b_{1k} z^{\lambda} + b_{2k} z^{\overline{\lambda}} \end{aligned} \tag{1}$$

where z is the coordinate represented as a complex number $z = x + i \cdot y$, λ is an unknown constant that has to be determined, along with the coefficients a_{ik} and b_{ik}, and $\overline{(\dots)}$ denotes the complex conjugated, see e.g. Theocaris [3] or Pageau et al. [4].
This solution may also be determined by using either a separation of variables principle or using the Mellin transform of Airy's stress function, but it leads to the exact same solution.
In the present case a the geometrical configuration is given in Fig. 1, although it is generally possible to vary all angles.

Eigenvalue problem

The next step in the solution procedure is to ensure that tractions (stress) and displacements are continues across the radial material interfaces. This leads to a set of eight nonlinear homogeneous equations. These may be written in matrix form as:

$$C(\lambda) \cdot x = 0 \tag{2}$$

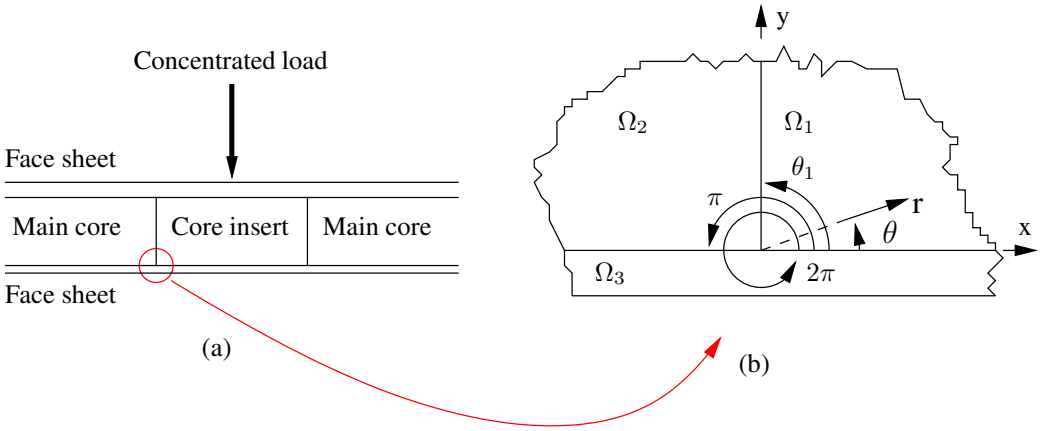

Figure 1: A sandwich structure subjected to a concentrated load fitted with a core insert (a), where a tri-material corner is found at the interface between the core insert and the main core (b).

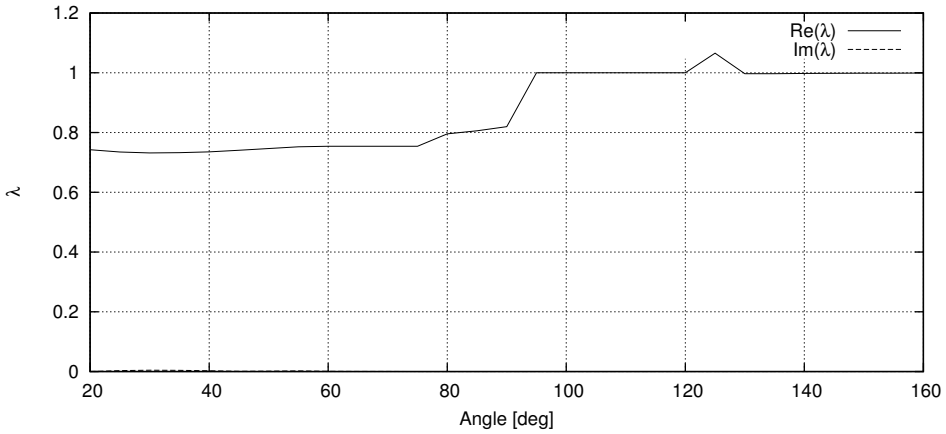

Figure 2: The eigenvalue (λ) as a function of the angle θ_1.

where $C(\lambda)$ is the coefficient matrix, x is a vector of constants (a_{1k}, a_{2k}, b_{1k} and b_{2k}). This system of equations give a non-trivial solution when the determinant of $C(\lambda)$ vanishes. An analytical solution to this equation is not known, but a number of numerically determined roots are shown in Fig. 2 for the materials system given in Table 1. The material properties given in the table are quite common for sandwich structures with in this case represent a sandwich of Divinycell PVC foam core materials [5] and Aluminium face sheets.
The knowledge of the eigenvalues will all ready give some information about the structure of the solution. The stress field is given as:

$$\sigma_{ij} \propto r^{\lambda_r - 1} \cos(\omega \ln(r)) f_k(\theta) \tag{3}$$

Material	Young's modules	Poisson's ratio
Ω_1 (Divinycell H60)	60 MPa	0.32
Ω_2 (Divinycell H200)	310 MPa	0.32
Ω_3 (Aluminium)	70 GPa	1/3

Table 1: The material data used for the determination of the eigenvalue λ.

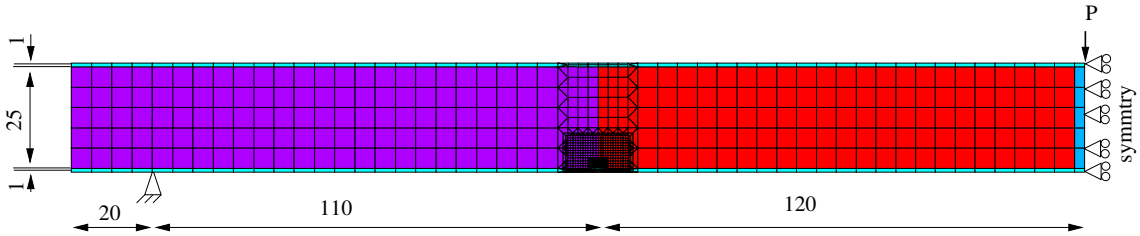

Figure 3: Finite element model of three point bending of a sandwich beam.

where λ_r and ω are the real ($\Re(\lambda)$) and imaginary ($\Im(\lambda)$) parts of the eigenvalue, respectively. It is readily seen that if $\lambda_r < 1$ then the expression will lead to singular stresses. Furthermore, it is seen that if the imaginary part of the eigenvalue $\omega \neq 0$ then the stresses exhibit an oscillating behaviour, with increasing frequency as $r \to 0$. In fact $\ln(r)$ tends to infinity as $r \to 0$, thus the oscillations increase towards the apex of the wedge.
The eigenvalues in Fig. 2 are not unique for any given configuration. It is possible to determine infinitely many eigenvalues and corresponding eigenfunctions (Eq. 3). The sandwich configuration is, however, not suitable for an series expansion based on the eigenfunctions due to thin face sheets. Instead the analytical solution will be used in conjunction with a finite element model.

Finite element model
A finite element model has been developed for general stress analysis of the sandwich specimen, see Fig. 3. It is difficult to determine the stresses near the singularity with standard displacement based elements, however. It is also difficult to get an idea about the convergence properties of any given solution.
Instead it will be assumed that the stress field near the tri-material wedge can be described in the form Eq. (1), where the λ has been determined from Eq. (2). The stress field defined by Eq. (1) will be fitted to the stress field from the finite element solution using the coefficients a_{ik} and b_{ik}, such that it is possible to extrapolate the solution arbitrarily close to the apex of the wedge. Furthermore, it is possible to quantify the convergence of the finite element solution by the correlation with the analytical solution inspired by the approach of Zienkiewicz and Zhu [6, 7]. As a simple test the stresses σ_{xx} along the radial line $\theta = 0$ will be fitted to the analytical solution given as:

$$\sigma_{xx} = c_0 + c_1 r^{\lambda_r - 1} \tag{4}$$

where c_0 and c_1 are to be determined, and $\lambda_r = 0.8194305330$ for the materials given in Table 1. The imaginary part of the eigenvalue has been neglected ($\omega = 0.18 \cdot 10^{-9}$) due to its small magnitude. In Fig. 4 the stresses are plotted in a radial line from the wedge based on the raw finite element data and the fitted function. The function was fitted using the nonlinear least-squares (NLLS) Marquardt-Levenberg algorithm implemented in Gnuplot [8]. As it may be observed in Fig. 4 the fit between the finite element solution and the eigenfunction is very good for $r > 0.5\,mm$, and this corresponds nicely to the element size in this area, where the edge length of elements is approximately $l_e = 0.6\,mm$.
The fitted function may be extended to cover all three domains $\Omega_k = \{\Omega_1, \Omega_2, \Omega_3\}$ if the eigenvalues of Eq. 2 were known, although this has not yet been implemented. In this manner it will be possible to fit the first few terms of the eigenfunction expansion based on Eq. (1) to the finite element solution, such that the stress state near the apex of the tri-material wedge, and in addition obtain an estimate of the accuracy of the finite element solution in this area.

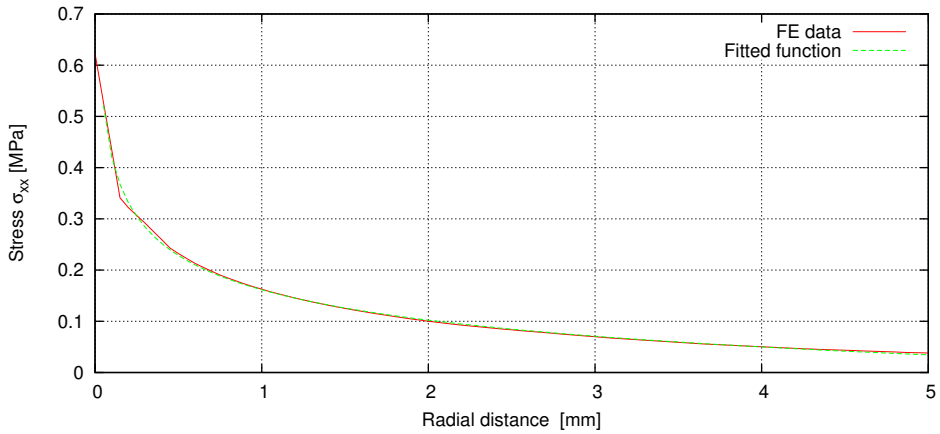

Figure 4: The fit of finite element data for σ_{xx} and the analytical solution for the stress given by Eq. (4).

Concluding remarks

The singular stress state in a tri-material corner is evaluated by fitting the eigenfunction expansion to a finite element solution. In this manner it is possible to extrapolate the stresses from the finite element solution closer to the singularity. It is also possible to set up a measure of the convergence of the finite element solution based on the eigenfunction solution.
This approach will be developed further in the future such that the eigenvectors will be included in the eigenfunction expansion.

References

[1] E. Bozhevolnaya, O. Thomsen, Structurally graded core junctions in sandwich panels: Quasi static loading conditions, Composite Structures .
[2] E. Bozhevolnaya, O. Thomsen, Structurally graded core junctions in sandwich panels: Fatigue loading conditions, Composite Structures .
[3] P. Theocaris, The order of singularity at a multi-wedge corner of a composite plate, International Journal of Engineering Science 12 (1974) 107–20.
[4] S. Pageau, P. Joseph, S. Biggers, Jr, The order of stress singularities for bonded and disbonded three-material junctions, International Journal of Solids and Structures 31 (21) (1994) 2979–2997.
[5] DIAB Group International, Divinycell Data Sheet H Grade.
[6] O. Zienkiewicz, J. Zhu, The superconvergent patch recovery and a posteriori error estimates. part 1: The recovery technique, International Journal for Numerical Methods in Engineering 33 (1992) 1331–1364.
[7] O. Zienkiewicz, J. Zhu, The superconvergent patch recovery and a posteriori error estimates. part 2: Error estimates and adaptivity, International Journal for Numerical Methods in Engineering 33 (1992) 1365–1382.
[8] T. Williams, C. Kelley, gnuplot: An Interactive Plotting Program.

Identification of Material Parameters of a Polymer

Tuomas Peräkylä* and Raimo von Hertzen
Laboratory of Structures and Strength
Lappeenranta University of Technology, Lappeenranta, Finland
e-mail: perakyla@lut.fi , raimo.von.hertzen@lut.fi

Marko Jorkama
Metso Paper, Inc.
Wärtsilänkatu 100, 04400 Järvenpää, Finland
e-mail: marko.jorkama@metso.com

Summary A system identification procedure for the estimation of material parameters associated with a block of polymer is presented. The polymer is modelled as a linear viscoelastic material, whose constitutive law can be expressed by an exponential hereditary relaxation kernel. The identification is based on a nonlinear least squares fit of the model solution to the measured compression data. As a result, the relevant stiffness and viscosity parameters of the material are obtained. The uniqueness of the solution in terms of the number of modelling parameters is discussed.

Introduction

Polymers are widely used engineering materials due to their unique properties such as high durability and good mechanical behaviour. While in many materials (metals or glass, for example) deviations from perfect elasticity are small, in polymeric systems, by contrast, the mechanical behaviour is dominated by viscoelastic phenomena which may be truly spectacular. In the deformation of hard solids, atoms are displaced from their equilibrium positions only locally. In polymers, on the other hand, the flexible threadlike molecules are rearranged on a local as well as long-range scale, giving rise to rapid as well as slow responses, respectively. This leads to viscoelastic behaviour and to a wide range of time scales under external stress [1]. When polymers are used in dynamic systems as components, it is necessary to know the structural parameters, such as stiffnesses and relaxation times, related to the polymers. These parameters can be estimated by an identification technique that utilizes the response of the system to a properly selected external excitation. In this work, the external excitation was provided by a simple compression test. The convolution integral type stress-strain history, expressed in a closed form in terms of the system parameters, was fitted to the corresponding measured values using the nonlinear least squares fit algorithm. As a result, values for the material stiffnesses and time constants were obtained.

Mechanical Model of Viscoelastic Behaviour

The material models of viscoelasticity usually utilize a hereditary approach where stress is a function of the current strain as well as the past history of the strain in the material. For small displacements, a linear model may be assumed. The most popular constitutive models based on mechanical models consisting of springs and dashpots are the well-known Voigt, Maxwell, Kelvin, and Wiechart models [1], [2]. According to the generalized Maxwell model (see Fig. 1), the viscoelastic constitutive law under uniaxial loading is [3], [4]

$$\sigma(t) = E\,\varepsilon(t) - \sum_{i=1}^{n} E_i \left[\varepsilon_i(0)\, e^{-\frac{t}{\tau_i}} + \frac{1}{\tau_i} \int_0^t \varepsilon(\tau)\, e^{\frac{\tau - t}{\tau_i}}\, d\tau \right] \tag{1}$$

where σ and ε are the stress and strain in the material element, respectively, E_∞ and E_i are the elastic moduli, τ_i the relaxation times and $\varepsilon_i(0)$ the initial values of the internal strains of the single Maxwell elements $(i = 1,...,n)$, $E = E_\infty + E_1 + \cdots + E_n$ and t is time.

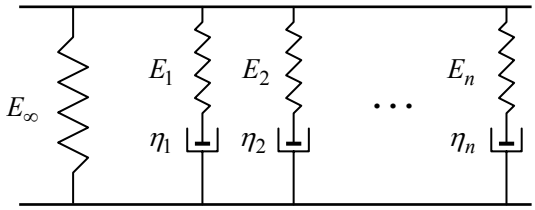

Figure 1: Generalized Maxwell model describing a material element.

The relaxation time τ_i can be expressed in terms of the elastic modulus E_i and dashpot viscosity η_i as

$$\tau_i = \frac{\eta_i}{E_i} \quad , \quad i = 1, \dots , n \tag{2}$$

If the compression of the material element is started from an equilibrium position, the initial values $\varepsilon_i(0)$ vanish. In the uniaxial compression test the measurements were done at times

$$t_j = (j-1)\Delta t \quad , \quad j = 1, \dots , m \tag{3}$$

The corresponding values of stress and strain are denoted by $\hat{\sigma}_j$ and $\hat{\varepsilon}_j$. By defining the integral

$$I_{ij} = \frac{1}{\tau_i} \int_0^{t_j} \varepsilon(\tau) e^{\frac{\tau - t_j}{\tau_i}} d\tau \tag{4}$$

the calculated stresses $\sigma_j = \sigma(t_j)$ can be expressed as

$$\sigma_j = E\,\varepsilon_j - \sum_{i=1}^{n} E_i I_{ij} \quad , \quad j = 1, \dots , m \tag{5}$$

By using the trapezoidal integration rule it is easy to see that the integrals I_{ij} can be calculated recursively as

$$I_{ij} \simeq e^{-\frac{\Delta t}{\tau_i}} I_{i(j-1)} + \frac{\Delta t}{2\tau_i} (\varepsilon_{j-1} e^{-\frac{\Delta t}{\tau_i}} + \varepsilon_j) \quad , \quad I_{i1} = 0 \tag{6}$$

Eqs. 5 and 6 establish the relation between the values of stress and strain in terms of the viscoelastic parameters E, E_i and τ_i $(i = 1, \dots , n)$.

Parameter Estimation

The parameters of a system can be identified by the response of the system to external stimuli. The nature of the model and availability of suitable material tests act as a guide for a proper identification method. The method should be robust enough to give accurate estimates for the

desired system parameters even in the presence of external perturbations and measurement errors. In this work, nonlinear curve fitting in the sense of least squares was utilized. The least squares algorithm is known to be relatively robust due to its low-pass filtering properties. It consists of finding the system parameters so that the squared 2-norm of the residual is minimized, that is

$$\min_{\mathbf{x}} \sum_{j=1}^{m} \left[\sigma_j(\hat{\boldsymbol{\varepsilon}}) - \hat{\sigma}_j \right]^2 \tag{7}$$

where $\mathbf{x} = (E_\infty, E_1, \tau_1, ..., E_n, \tau_n)^T$ is the vector of system parameters, $\hat{\sigma}_j$ and $\hat{\boldsymbol{\varepsilon}} = \{\hat{\varepsilon}_j\}$ are the measured values of stress and strain, respectively, and $\sigma_j(\hat{\boldsymbol{\varepsilon}})$ the stress calculated from Eqs. 5 and 6 for the measured strains $\hat{\varepsilon}_k$ $(k = 1, ..., j)$. The *Matlab*-routine *lsqcurvefit* with large-scale optimization and lower and upper bounds was used. This algorithm is a subspace trust region method and is based on the interior-reflective Newton method and preconditioned conjugate gradients.

An example of the measured stress and strain during the interval 0 - 1 s is shown in Fig. 2a and the stress-strain relation in Fig. 2b. The target value of strain was set to 0.95 %. During the first 0.02 s the compressive stress was increased from zero in such a way that the target value of strain was approximately achieved. After that the force control system regulated the compressive stress so that the target value was sustained. As can be seen from Fig. 2a, the strain remains quite close to the target value. There are, however, small fluctuations around this value due to external disturbances and, possibly, due to small oscillations in the feedback control system. There are also fluctuations in the stress, although not as much as in the strain.

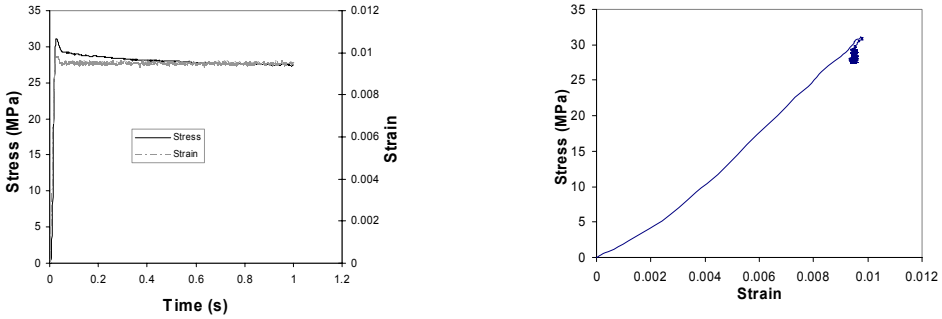

Figure 2: (a) Measured stress and strain as a function of time, and (b) measured stress-strain relation of the compression test.

The model was fitted to the data of Fig. 2b as explained above for one, two and three spring-dashpot pairs in the generalized Maxwell model. The results are shown in Table 1.

Table 1. Results of the parameter estimation.

n	E_∞	E_1	E_2	E_3	τ_1	τ_2	τ_3	r
		(GPa)				(s)		
1	2.438	0.726			0.166			0.7286
2	2.362	1.198	0.518		0.015	0.374		0.0459
3	1.906	1.262	0.337	0.733	0.011	0.137	2.299	0.0325

In addition to the system parameters, the normalized residual of the fit at the solution is shown. This value acts as a good indicator of the goodness of the fit. The measured and calculated stress histories are shown in Fig. 3a. It can be seen that the fit is good with an average error of 0.2 MPa (0.7 %) per measured value.

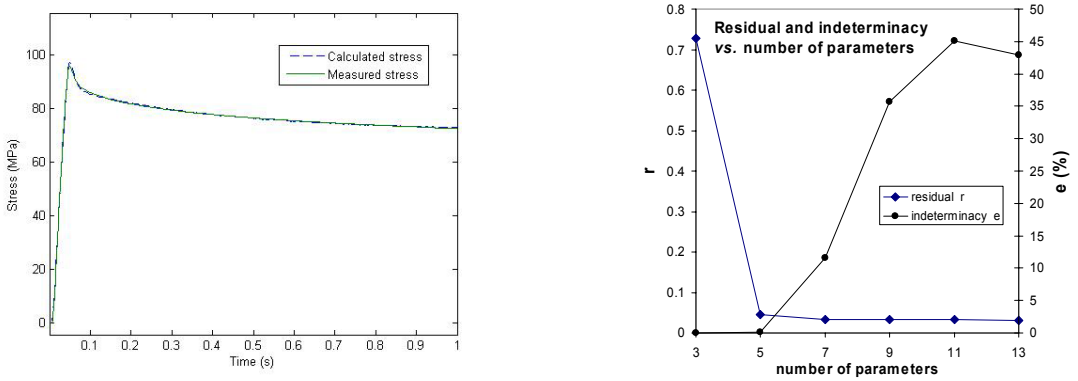

Figure 3: (a) Measured and calculated stress histories, and (b) residual of the fit and the indeterminacy of the solution as a function of system parameters.

To study the uniqueness of the solution, the least squares minimization search was launched from several initial points of the parameter space. The spread of the resulting solutions was considered by the quantity

$$e = \frac{1}{2n+1}\left\{\frac{\Delta E_\infty}{E_{\infty,ave}} + \sum_{i=1}^{n}\left[\frac{\Delta E_i}{E_{i,ave}} + \frac{\Delta \tau_i}{\tau_{i,ave}}\right]\right\} \tag{8}$$

which is a measure of the indeterminacy of the solution. Here $\Delta E_\infty = (E_\infty)_{\max} - (E_\infty)_{\min}$ is the spread and $E_{\infty,ave}$ the average of E_∞ corresponding to the different initial points, and similarly for the other parameters. The residual r of the fit and the indeterminacy e as a function of system parameters is shown in Fig. 3b. It can be seen that the optimal value of system parameters is five ($n = 2$). Above that the fit does not improve but the uniqueness of the resulting system parameters is lost.

Concluding remarks

A system identification procedure for the evaluation of the material parameters of a viscoelastic block of polymer was presented. The numerical evidence of the present work suggests that the uniqueness of the solution is lost when the number of parameters becomes *redundant*, that is, the residual of the fit does not decrease with an increasing number of system parameters.

References

[1] J.D. Ferry. *Viscoelastic Properties of Polymers*. John Wiley & Sons, New York, (1980).

[2] R. Singh, P. Davies and A.K. Bajaj. Estimation of the dynamical properties of polyurethane foam through use of Prony series. *Journal of Sound and Vibration*, **264**, 1005-1043, (2003).

[3] W. Flügge. *Viscoelasticity*. Blaisdell, Waltham, MA, (1967).

[4] C. Carrot and V. Verney. Determination of a discrete relaxation spectrum from dynamic experimental data using the Padé-Laplace method. *European Polymer Journal*, **32**, 69-77, (1996).

Non-local plasticity model for fibre reinforced concrete

Lic engrg Lena Strömberg
LTech, Fredrlg 38, Se-38237 Nybro
(previously Dept of Solid Mechanics, Royal Instititute of Techn, KTH)
e-mail: lena_str@hotmail.com

Summary Topics of fibre reinforced concrete are covered. A non-local plasticity model is used to simulate the failure modes of blocks subjected to vertical displacement. FE-model results display cracking in bands over the specimen, as also visible in experiments. To model the adhesion properties when used in lining, the corresponding gradient plasticity equations, in conjunction with the thin-film formulation are discussed. The maximum plastic strain is located at a distance from the interconnect, depending on length scales.

Introduction
Fibre reinforced concrete is used in a variety of applications, cf. SFC (1985). Nowadays, the main application is known to be lining. The concrete and metal fibres makes a material suitable for covers of rock due to combined desired adhesion properties and ductility.

In general the cracking of a composite may consist of many features cf. Jonsson (2000). Recent modelling have been non-local damage plasticity, Geers et al (1999). Here, we shall focus on macroscopic formation of a shear band, and layer effects, which may be modeled by non-local plasticity.

Recent experiments for various random fibre reinforced concrete mixtures has been performed inlab, Ay (2000). The specimens were blocks of different sizes, and loading was applied as displacement on top. The failure modes were found to be shear band(s), at an angle, which is the typical behaviour of a von Mises material.

Model for blocks
The model is taken from Strömberg and Ristinmaa (1996), and the results display the formation of shear band and global softening. A weaker element is randomly initiated and at softening, ‘cracking’ is present at two slip lines.

Thin film
The nonlocal model could be expanded to a gradient model, cf [7]. The gradient formulation will be used to model adhesion of fibre reinforced concrete when used in lining, and as cover. The geometry and loading is of a thin film of thickness t, subjected to biaxial inplane strain, cf. Gudmundson (2004). In the present formulation, the consistency condition will be a second order differential equation for plastic strain.

Results
For negative plastic modulus (i.e local softening), the solution are the hyperbolic functions.
To achieve size effects, stress is assumed to be a decreasing function, and minimum is located outside the film. Physically, this corresponds to that largest plastic strain delocalizes from the interconnect. The gradient part will contribute with hardening in the stress strain relation, and acts as a stiffener. To calculate an average elastic plastic modulus, the stress is integrated over the film, and divided by thickness. It is found that although the matrix is softening, the overall behaviour may be hardening. The hardening is inversely proportional to film thickness, i.e. the configuration display so called size effect ’the thinner, the harder’.
For positive plastic modulus, the consistency condition is elliptic.

Attention to boundary effects

Preliminaries: The consistency condition in one dim is a Fredholm equation that reads

$$\sigma\text{-}\sigma_y = h\{\lambda\} \tag{1}$$

where σ denotes stress, σ_y constant yield stress, h are hardening/softening, $\lambda=\lambda(x)$, x is the coordinate of film thickness ($0<x<t$) and $\{\lambda\} = \int \exp(x-\xi)^2 / l^2 \ \lambda(\xi)\, \mathrm{d}\xi$, where the integration ranges over plastic part of material body. To get gradient plasticity, a series expansion of $\lambda(\xi)$ is integrated, to achieve spatial derivatives.

The integration of the series expansion in [7] is not exact close to boundaries, since symmetry is not provided. Therefore, a more exact expression to $\{\lambda\}$ will be deduced. Instead of achieving a constant value interpretated as a constant material length parameter, certain fields will appear.

Also, the anti-symmetry, cause the presence of a non-vanishing gradient term.

Thus, the general expression close to plastic boundary may be written

$$\{\lambda\} = \lambda(x) + g(x)\lambda'(x) + l(x)\lambda''(x) + ..$$

where g and l are fields with the dimension of length and square lengths respectively.

Here, we will consider the case when the gradient-term is omitted, motivated by the expression in the interior. (In constitutive modeling (Truesdell), a gradient term introduces direction in a scalar expression if the gradient is not squared, and is therefore not included in first order theories.)

The consistency condition then reads

$$B\varepsilon - \sigma_y = (B+h)\lambda(x) + hl(x)\lambda''(x)$$

where ε is the constant input biaxial strain (load parameter), B is biaxial film modulus, h is hardening/softening.

With the assumption that $\lambda(x)$ is a function of $l(x)$, the equation admits a polynomial solution

$\lambda(x) = \Delta\varepsilon\, B/(B+h) + ax^2 + bx + c$, a,b,c being arbitrary constants, $\Delta\varepsilon = \varepsilon - \varepsilon_y$.

The solution is *arbitrary*. It could be noticed that there are conditions on the parameters depending on sign of h, for the plastic field and the length field l(x) to be positive functions. The function may be normalized such that the constant part is the local, classical solution, i.e. c=0.

At first, the two requirement above will not be pursued, and we will consider a general polynomial solution. To determine the parameters, it is assumed that there is a layer of stress close to the boundary, and that stress decreases at distance. This phenomenon may appear since the hard aggregates acts as stiffener, that are able to produce high stresses. Since the interconnect repel the fibres/aggregates, cf Trouchu (2001), the layer will appear a distance from the interconnect, however in the solution, it will be arbitrary close to the interconnect.

It is assumed that the polynomial solution holds at the region $0 < x < x_b$. From x_b to the surface, $x_b < x < t$, the solution will be constant. The stress field in the film will be approximated to be a decreasing function in $0 < x < x_b$ (according to figure). Adaptation of the polynomial to this case gives

$$\lambda(x) = \varepsilon - \sigma(x)/B = ax^2 + b$$

With the boundary conditions $\lambda(0)= 0$ and $\lambda(x_b) = \Delta\varepsilon$, the most simple solution is found.

To achieve an average modulus, stress is integrated over thickness, and divided by t, from whereas $\sigma_a = \Delta\varepsilon\, B(2/3)\, x_b/t + \sigma_y$

The size effect, the thinner the harder, is displayed, and, due to the assumptions, no dependency of hardening parameter, *h*. Since stress varies, bending is present in the film.
We note that the λ-distribution do not meet the above requirement of a 'softening' layer (h<0). An approach for a 'softening' layer (h>0), would be the field

$$\lambda(x) = \varepsilon - \sigma(x)/B = \varepsilon(2x/x_b - x^2/x_b^2),$$

giving the average stress $\sigma_a = \Delta\varepsilon\ B(1/3)\ x_b/t + \sigma_y$

Assuming other boundary conditions, the constant stress at the film surface may be positive. For large negative values, the overall response may be softening, that is the average modulus is negative. To achieve further dependence on parameter *h*, we assume the boundary condition

$$\lambda(x_b) = \Delta\varepsilon\ B/(B+h) \tag{2}$$

This correspond to local plasticity in $x_b < x < t$. The average modulus M_a reads

$$M_a = (2/3)\ B^2/(B+h)(x_b/t) + Bh/(B+h) \tag{3}$$

for $h << B$; $M_a = ((2/3)B - h)(x_b/t) + h$

We note that the modulus

- decreases with increasing abs(*h*) if h negative
- increases with increasing h if h positive
- the first term is always positive
- there may be softening if abs(*h*) is large enough
- a small x_b corresponds to localisation and promotes softening

Evolution of plastic layer zone, stability and uniqueness of solution
Iteration formula for location of boundary
Consider that the location for layer boundary x_b, may change. Physically, the freedom in location, could be due to material structure, inhomogeneties or a (micro-) cracking process.
Prop: A new location of layer zone x_{new} is assumed, such that $x_n = x_{\text{new}}/x_b$, where x_{n} is given by fix point(s) to the iteration formula.

$$x_{n+1} = f(x_n) = A\ x_n(1 - (2/3)x_n) \tag{4}$$

This was first studied by Fatou (1903), and applied to evolution theory, by May (1970).
When the formula converges *r* = *f*(*r*), and *r* is known as a fix point. Here, the formula is scaled such that $x_{\text{new}} = x_b$ at the last stable fix point (when *A*=3).

At fix point $x_{new}^2 = x_b^2(3/2(1-1/A))^2 = B\Delta\varepsilon/(B+h)/a(3/2(1-1/A))^2$, modifies boundary condition (2).

Remarks
If, at layer boundary, λ' is assumed to depend of a canonical coordinate $Ax_n - x_n + 1$, then (4) corresponds to a mixed Dirichlet-Neumann condition, [4];
$(4/3)A/x_b\lambda(x_n) = \lambda'(Ax_n - x_{n+1})$.
The format could also be seen as a non-local condition, where value in a point depend on values at surrounding points, however these may coincide.
There are also similarities with Newton's law used at boundary condition for heat conduction.
$\lambda'(x_n) = (4/3)/x_b(\lambda(x_n) - \lambda(x_{n+1}))$ and $\lambda'(x_{n+1}) = -A(4/3)/x_b(\lambda(x_{n+1}) - \lambda_0)$.
Note the opposite sign of gradient dependence, giving that contributions to gradient is achieved

at both boundaries. Summation of conditions and λ_0=0, gives the above format, since λ' is linear. For other functions, the format may be given by a series expansion.

Location of boundary layer
Assume that A is an increasing function of $\Delta\varepsilon$. Then, upon loading, the iteration formula (4) display stability, instability and chaos, with qualitative and quantitative results from May (1970) [9].
Conditions for convergence, in terms of material parameters will be 1<A<3, and the corresponding values $0 < (x_{\text{new}} / x_b) < 1$.
For A=3.2, f alters between two values 0.51 and 0.76, which correspond to non-uniqueness of layer location, at constant strain level $\Delta\varepsilon$, A($\Delta\varepsilon$)=3.2, and $x_{\text{new}}/x_{\text{b}}$=0.77 and 1.14.
In the formula of May(1970), convergence of the formula is considered for different A. The inverse could however also be considered: As is seen above, the value 0.51 also corresponds to a value of A less than 3, which means that in a situation where we control f, the parameter A may achieve any of these values.

Localization and softening
As an illustration, we shall apply the effects from the evolutiong zone concept on a specimen subjected to increased loading (strain controlled). Assume that strain localises and the layer appears. Fix point format is assumed active for A>3. As strain increases $A(\Delta\varepsilon)$>3 and the zone width admits two solutions, one wider and one smaller. For the smaller, the average modulus decreases, and softening may appear.
Further, in turn, the smaller may correspond to a lower strain state, thus for this bifurcation branch, we may have snap back. To achieve this at instability, the inverse behaviour at bifurcation need to be considered.
When strain is further increased, the zone width admits 4 solutions, (one of which smaller than at lower strain rate), to be chaotic when $A(\Delta\varepsilon)$>3.57 where it is possible to have (x_{new}/x_b)=0.

Rate sensitivity
Assuming evoluting layer zone is governed by diffusion-like processes or dislocation movement, it could be expected that there is a threshold for loading rate above which the effect is not observable, since the micro structural velocities are lower. This corresponds to a ductile-brittle transition.
For faster deformation rates, it is likely that the self evoluting effect is less, and therefore average hardening behaviour is dominating. Note, however, that either localization or wider zone are possible (or a pending between the two, in a 2^ncyclic solution) at bifurcations.

Conclusion
A nonlocal plasticity model for fibre reinforced concrete was proposed. Numerical simulations of failure in shear, showed good agreement with experimental results.

The adhesion property is due to the fact that for low dense reinforced mixtures, the surface repels the fibres, Trochu (2001). This is reflected by the solution to the layer problem within gradient plasticity, and corresponds to that the surface repels dislocation as notified in Fleck and Hutchinson (1997). The result presented here, give that the maximum plastic strain is located at a distance from the bimaterial boundary, that is not at the interconnect of wall and concrete. The nonuniform strain distribution will cause hardening of the coating.

With attention to behaviour near elastic-plastic boundaries, a new differential equation for effective plastic strain were deduced. A polynomial solution were exploited. It was found that an iterative format of boundary condition gives possibilities of an evoluting layer location. The

resulting format display different properties of stability, multiple solutions and chaos.
Since the strong non-local formulation with integral do not contain explicit boundary condition, it is not equivalent with gradient plasticity (weakly non-local formulation). The non-similar solutions above, show that comparisons with different approaches, are of great importance.

Acknowledgements
The author acknowledge Nils Petersons, Swetech, for valuable discussions, and the Swedish Research Council (TFR) for facilitating the research.

References
[1] Ay, Lutfi, Dept of structural mechanics, KTH. personal communication
[2] Fleck, N.A. and Hutchinson, J.W. Strain gradient Plasticity, *Advances in Applied Mechanics*, **33**, 295-361. (1997).
[3] Geers MGD, de Borst R, Peijs T. *Compos Sci Techn 59*, **10**, 1569-1578. (1999).
[4] Gudmundson P. A unified treatment of strain gradient plasticity, *J. of the Mech and Phys of Solids*, **52**, 1379-1406. (2004).
[5] Jonsson M, *Lic Thesis*. (2000).
[6] Steel fibre concrete. US-Sweden joint seminar (NSF-STU), Stockholm, June 3-5, Editors Surendra P Shah, Ake Skarendahl, (1985).
[7] Strömberg L and Ristinmaa M.FE-formulation of a nonlocal plasticity theory, *Computer Methods in Applied Mechanics and Engineering*, **136**, 127-144, (1996).
[8] Trouchu F. *Proceedings to the 4th int esaform conference on material forming*, Liege, Belgium, (2001).
[9] Robert B Israel, Calculus the Maple Way, 2nd Ed. p 59-63. *Addison Wesley*, (2000).

Time-Temperature Superposition Method for Polyester Resin

Antti-Jussi Vuotikka* and Stig-Göran Sjölind
Department of Mechanical Engineering
University of Oulu, Oulu, Finland
Email: Antti-Jussi.Vuotikka@oulu.fi

Summary The aim of this study was to investigate a time-temperature superposition method for a polyester resin. The principles of thermorheologically simple materials and thermorheologically complex materials are presented, and the method of time-temperature superposition is applied.

Introduction

Possibilities to use polymer matrix composites are versatile. The composite materials can be used for example in railway wagons and road transport vehicles. In this kind of use the polymer matrix composites increase payloads of the transportation vehicles due to their high strength to weight ratio.

Although the use of the polymer matrix composites gives some benefits, they also cause some problems. The polymer resins in composites do not act as time-independent material such as steel. It is possible that its mechanical behaviour changes considerably in process of time. Thereby, it is important to develop methods, which can foresee the long-term behaviour of the polymer matrix composites. The test methods used should also be time saving and easy, because a huge variety of polymer materials exists.

Thermorheologically simple materials

There is a special type of temperature dependence of material properties concerning most polymer materials. They are referred as thermorheologically simple materials (TSM) and their behaviour can be analytically described by time-temperature superposition (TTS). The creep function at arbitrary base temperature $T = T_0$ is $J(t)$, where t is time. When temperature field changes uniformly, it is possible to designate a corresponding creep function $\hat{J}(t, T)$, where T denotes absolute temperature. Then

$$\hat{J}\left(t, T_0\right) = J\left(t\right) = L\left(\log t\right), \tag{1}$$

where the independent variable is changed in $J(t)$. The next relationship is the basic postulate of TSM

$$\hat{J}\left(t, T\right) = L\left[\log t + \varphi\left(T\right)\right], \tag{2}$$

where the shift function $\varphi(T)$ obeys the relations as follows

$$\varphi\left(T_0\right) = 0\,,\ \frac{d\varphi\left(T\right)}{dT} \succ 0\,. \tag{3}$$

The meaning of equation (2) can be physically explained such that the change of temperature shifts the creep function in the horizontal direction when plotted against $\log t$. A change of variable in the shift function is introduced by setting

$$\varphi\left(T\right) = \log a\left(T\right). \tag{4}$$

The conditions of the first shift function in Eq. (3) now imply that

$$a\left(T_0\right) = 1\,,\ \frac{da\left(T\right)}{dT} \succ 0\,. \tag{5}$$

Now, by using equations (1) and (4), equation (2) can be written as

$$\hat{J}(t,T) = L\left[\log ta(T)\right] = J(\xi), \tag{6}$$

where

$$\xi = ta(T). \tag{7}$$

It is referred as reduced time. Thus, the creep function $\hat{J}(t, T)$ at any temperature can directly be obtained from the creep function $J(t)$ at base temperature T_0 by replacing time t with the reduced time ξ. It can be written in the integral presentation for the reduced time when temperature is allowed to change arbitrarily.

$$\xi = \int_0^t a\left(T\left(x_i,\tau\right)\right)d\tau, \tag{8}$$

where x_i are coordinates and τ is time. The shift function $a(T)$ is a basic property of the material and it has to be determined from material tests [1]. The equation (6) represents time-temperature reduction without any vertical shifting. However, it has been observed that the vertical shift can be required to reduce the data [2].

Thermorheologically complex materials

The phenomenon of thermorheological complexity can be applied to the materials, which do not form a smooth master creep curve by simple horizontal sifting. All elastic material parameters are independent of temperature and all time constants should have the same temperature dependence in the TSM, whereas material parameters of thermorheologically complex materials (TCM) are not restricted [3]. If material exhibits different degradation mechanisms, then it will not be thermorheologically simple [4].

TCM can be divided into two classes, namely TCM-1 and TCM-2. The first class includes materials, which are composed of two or more TSM. This class consists also the composite materials. The second class includes other materials [5]. For TCM-2 cases, equation (6) can be modified such that the vertical shifting is taken into account.

$$\hat{J}(t,T) = b(T)J(\xi), \tag{9}$$

where $b(T)$ is a temperature dependent vertical shift factor [4].

In the effective time theory, the strain response is related to the stress σ and the reference complianse curve J by the equation [6]

$$\varepsilon(t) = \int_0^t J\left(\xi - \xi'\right)\frac{d\sigma}{d\tau}d\tau. \tag{10}$$

The shift factor functions

The shift factors between the reference curve and other creep curves can now be calculated by equations (6) or (9), when the relation between the real and reduced time has been obtained experimentally from the creep tests. Another method is to use semi empirical expressions as the WLF equation [4]

$$\log a_T = \frac{-C_1\left(T - T_0\right)}{C_2 + T - T_0}, \tag{11}$$

where C_1 and C_2 are material constants, which can be obtained by material tests. T_0 is usually chosen to be the glass transition temperature T_g. WLF is normally used above T_g.

At temperatures below T_g the Arrhenius equation can be used [7].

$$\log a_T = \frac{AF_c}{k_b}\left(\frac{1}{T}-\frac{1}{T_0}\right), \tag{12}$$

where A is a constant, k_b is Bolzmann constant and F_c is free energy, which is a constant below the glass transition temperature [2].

Mathematical models for the creep compliance

The creep compliance can be illustrated by many different mathematical functions, from which the most commonly used functions are Kohlrausch function and generalized Voigt model which is also known as Prony series. The Kohlrausch function has the form

$$J(t) = J_0 \exp\left(\frac{t}{\tau}\right)^{\beta}, \tag{13}$$

where J_0 is the initial creep compliance and β is a shape parameter. This is usually used to describe the short-term creep compliance. The Prony series is expressed as

$$J(t) = J_0 + \sum_{k=1}^{K-1} S_k \left[1-\exp\left(-\frac{t}{\tau}\right)\right], \tag{14}$$

where K is the number of significant decaying exponent terms and S_k are the Prony coefficients. The Prony series represents the long-term creep compliance in general. [8]

Creep tests

The testing material was a medium reactive ortophthalic or polyester resin. One panel was cast by using this material and specimens were cut from this panel. Dimensions of the specimens were: length 120mm, width 15mm and thickness 5mm. There were three constant testing temperatures: 40°C, 60°C and 75°C. In each temperature four specimens were tested. The stress was approximately 3.3MPa and the duration of creep test was 48 hours for one specimen. The creep compliance curves can be seen in Fig. 1 (Left).

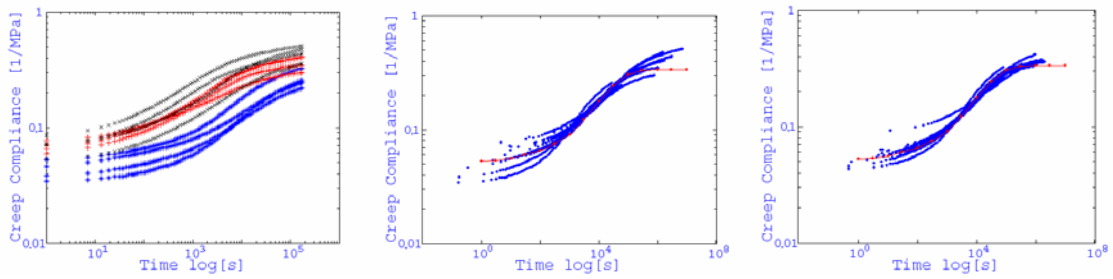

Fig 1. Left: The creep compliance curves from three different constant temperatures. Mid: The curves are shifted in horizontal direction. Right: The curves are shifted in horizontal and vertical directions. Dotted solid line in the mid and right figure is the reference curve.

Reference curves and shift factors

It can be seen that it is not possible to fit Kohlrausch function to the creep compliance curves (Fig. 1. Left) and, thus, only the Prony series is used. One creep compliance curve, which was tested at 40°C, was chosen to be the reference curve. The Prony series were fitted to this curve. After this, other curves were shifted in the horizontal direction at first by using the method of root mean square to obtain the best possible result. The vertical shift factor was forced to be $b_T = 1$. The shifted curves can be seen in Fig.1 (mid) and the shift factors in Fig 2. (left). Thereafter, the vertical shift factor was allowed to vary freely. The horizontal and vertical shift

factors can be again obtained by using the RMS method and they are shown in Fig.2 (mid and right), the shifted curves are in Fig.1 (right).

$$RMS\% = 100\sqrt{\sum_{i=1}^{N}\left[\frac{b_T f\left(a_T x_i\right) - y_i}{y_i}\right]^2}, \qquad (15)$$

where N is the number of measured points in the creep curve, $f()$ is the reference curve, a_T and b_T are the shift factors and (x_i, y_i) are measured points in the creep curve.

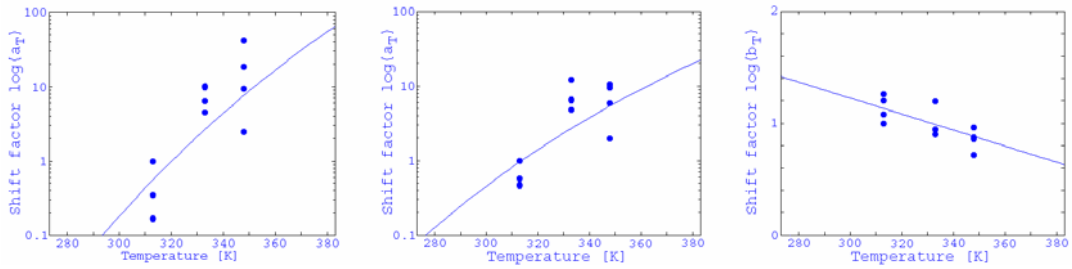

Fig 2. Left: The horizontal shift factors from the first case. Mid and Right: The horizontal and vertical shift factors from the second case. The solid line represents the Arrhenius type shift factor function in the left and middle figure. In the right figure, the shift factor function is a straight line.

Concluding remarks

It can be seen in Fig. 1 (mid) that the horizontal shifting only is not adequate. The creep compliance curves do not smoothly overlap the reference curve. Thus, the vertical shifting is needed and the testing material is clearly thermorheologically complex.

The Arrhenius type shift factor function does not fit to the horizontal shift factors well. The curves obtained at 75°C do not need shifting as much as the curves at 60°C. One reason for this could be that the physical aging, which increases the material stiffness, affects the creep compliance curves at the highest testing temperature.

Acknowledgements

The author would like to recognize Foundation of Technology in Finland (TES) and Tauno Tönning-foundation for sponsorship of this work, and Fibrocom Oy for providing the specimens, which were used in the testing reported.

References

[1] Christensen R.M.. Theory of viscoelasticity: An Introduction. New York. Academic Press. 1971.

[2] O'Connell P.A., McKenna G.B.. Arrhenius-type temperature dependence of the segmental relaxation below T_g. J. Chem. Phy. 110 (1999) 11054-11060.

[3] Heymans, N.. Constitutive equation for polymer viscoelasticity derived from hierarchical models in cases of failure of time-temperature superposition. Signal Procecessing 83 (2003) 2345-2357.

[4] Oliveira B.F., Creus G.J.. An analytical-numerical framework for the study of ageing in fibre reinforced polymer composites. Comp. Struct. 65 (2004) 443-457.

[5] Haddad Y.M.. Viscoelasticity of engineering materials. London. Chapman&Hall. 1995.

[6] Bradshaw R.D., Brinson L.C.. Recovering Nonisothermal Physical Aging Shift Factors Via Continuous Test Data: Theory and Experimental Results. J. Eng.Mat.Tech. 119 (1997) 233-241.

[7] Li, R..Time-temperature superposition method for glass transition temperature of plastic materials. Mat. Sci.&Eng. A278 (2000) 36-45.

[8] Bradshaw R.D., Brinson L.C.. A Continuous Test Data Method to Determine a Reference Curve and Shift Rate for Isothermal Physical Aging. Polym. Eng. Sci., 39 (1999) 211-235.

Slope safety calculation with a non-linear Mohr criterion using finite element method

Johan Clausen* **and Lars Damkilde**
Esbjerg Department of Engineering
Aalborg University Esbjerg, Esbjerg, Denmark
*Email: jc@aaue.dk

Summary Safety factors for soil slopes are calculated using a non-linear Mohr envelope. The often used linear Mohr-Coulomb envelope tends to overestimate the safety as the material parameters are usually determined at much higher stress levels, than those present at slope failure. Experimental data indicates that this leads to overestimation of the soil strength at low stress levels. The calculations are performed with the finite element method, and the plastic integration is carried out in principal stress space which simplifies the computations considerably.

Introduction

Traditionally slope stability calculations are carried out using limit state analysis. If this is to be done analytically the soil must be considered as a Mohr-Coulomb material. The material parameters of the Mohr-Coulomb model, friction angle, φ, and cohesion, c, are often determined by the triaxial test. A substantial amount of experimental data indicates that the linear Mohr-Coulomb envelope does not describe the strength of the soil to a satisfactory degree, see e.g. Baker [1]. This is especially pronounced at low values of the hydrostatic pressure, compared to the chamber pressure of the triaxial test. In slope stability calculations the pressure in yield zones are smaller than the pressure in the standard triaxial test at which the Mohr-Coulomb parameters were determined. This can cause an overestimation of the safety of the slope. A solution to this problem can be obtained by expressing the soil strength as a non-linear Mohr-envelope, see fig. 1. Several such criteria have been proposed in the literature, e.g. Jiang et al. [2] and Yang and Yin [3]. These references then calculates the safety factor by the upper bound method using an approximation of the slip surface. In the present paper a full non-linear finite element analysis will be carried out. This has the advantage that no approximation of the slip surface has to be made.

Nonlinear yield criterion

Baker [1] suggests the following version of a nonlinear Mohr envelope to capture the nonlinear dependence of the failure shear stress on the normal stress on the slip plane:

$$\tau = P_a A \left(T - \frac{\sigma}{P_a} \right)^h \tag{1}$$

Here the parameters τ and σ are the shear and normal stress on the slip surface, respectively, P_a is the atmospheric pressure, T is a nondimensional tensile strength parameter, A is a scaling parameter and h controls the curvature of the envelope. It can be seen on figure 1 that the envelope fits test results quite well.

Yield criterion in principal stresses

The non-linear Mohr envelope of Eq. (1) is expressed with respect to the stresses on a given slip section of the failing soil. i.e. at a certain orientation. In order to apply a yield criterion in a general

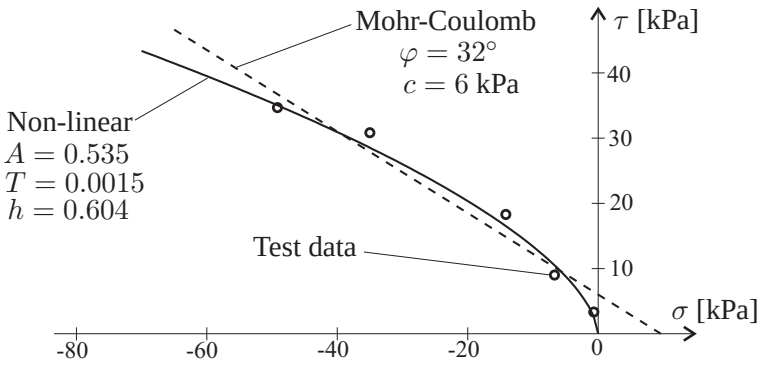

Figure 1: Mohr-Coulomb and non-linear envelope, Eq. (1), fitted to test results. The envelopes are fitted by Baker [1] and the test results are by Perry [5].

framework an isotropic criterion should be formulated in invariants. An explicit translation of Eq. (1) into principal stresses is not possible, but a similar expression is a modified version of the Hoek-Brown criterion given in [4]:

$$f = \sigma_1 - \sigma_3 - \sigma_c \left(1 - \frac{m\sigma_1}{\sigma_c}\right)^n \tag{2}$$

Here σ_1 and σ_3 are the major and minor principal stress, respectively, σ_c is the uniaxial compressive strength, $m = \sigma_c/\sigma_a$, where σ_a is the apex stress, see figure 2, and n is a curvature parameter, $0 \leqq n \leqq 1$. For $n = 1$ the Mohr-Coulomb criterion is obtained.

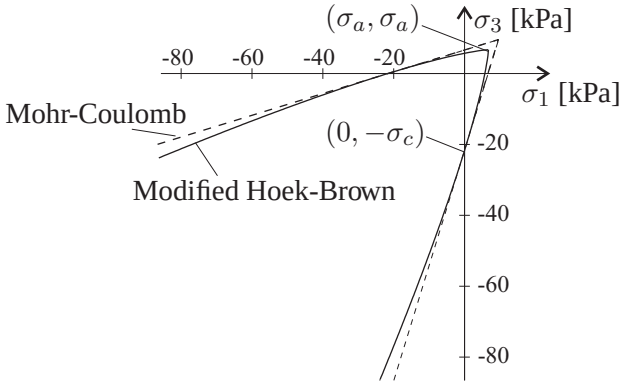

Figure 2: Plane strain Mohr-Coulomb and modified Hoek-Brown yield criterion in principal stresses.

Stress update in principal stresses

In the finite element calculations the slope soil is treated as a perfectly plastic material, and an associated flow rule is applied. The plastic stress integration is carried out using a return mapping scheme. The general return mapping scheme is outlined by Crisfield [6] for general yield criteria. For this method to be applicable the yield criterion must be expressed in the general six-dimensional stress space, or in the stress invariants I_1, I_2, I_3 or I_1, J_2, J_3. To express the modified Hoek-Brown yield criterion in this manner will be very complicated. But as the criterion is expressed in principal stresses the return mapping scheme can be carried out in a simple fashion with respect to the principal axes. This is a further development of the method outlined in references [7, 8].

Safety factor of a slope

Usually in geotecnical engineering the safety factor expresses the ratio of the actual shear strength to the shear strength needed to maintain equilibrium. For the Mohr-Coulomb criterion this can be expressed as

$$r_{\mathrm{MC}} = \frac{c - \sigma \tan\varphi}{c_r - \sigma \tan\varphi_r} \tag{3}$$

where c and φ are the cohesion and the friction angle of the soil, respectively. The reduced parameters c_r and φ_r are the strength parameters needed to maintain equilibrium of the slope. One way to estimate the safety factor is the $\varphi - c$ reduction scheme, see e.g. reference [9]. The parameters c and $\tan\varphi$ are reduced proportionally, which corresponds to a fixed apex point and a reduced friction angle.

After establishing equilibrium of self-weight and externally applied loads c and $\tan\varphi$ are gradually reduced until equilibrium can no longer be satisfied. The last values before failure are then used to calculate the factor of safety.

In the example the parameter n is an independent parameter, and the rest of the parameters of the Hoek-Brown criterion are fitted to the Mohr-Coulomb criterion such that the envelopes in principal stress space as well as the tangents coincide at the point $(\sigma_1, \sigma_3) = (0, \sigma_c)$. This gives

$$m = \frac{k-1}{n} \qquad \text{and} \qquad \sigma_c = 2c\sqrt{k} \tag{4}$$

where $k = \frac{1+\sin\varphi}{1-\sin\varphi}$ is a friction parameter.

The Hoek-Brown parameters are reduced by reducing the Mohr-Coulomb envelope proportionally as explained in the above. The curvature parameter n is kept constant throughout the parameter reduction.

Computational example

A slope is modelled with finite elements as shown on figure 3. The slope has a height of 10 m and is 20 m wide. The domain has a height of 15 m and a width of 40 m. The domain is modelled using six-noded triangular LST-elements. The left and right boundaries are constrained horizontally and the lower boundary is fixed. Plane strain conditions apply. The soil has a selfweight of $\gamma = 20$ kN/m^3. The strength parameters for $n = 1$ are $\varphi = 32°$ and $c = 6$ kPa, which complies with the values fitted from test results shown in figure 1. Four analyses have been carried out with

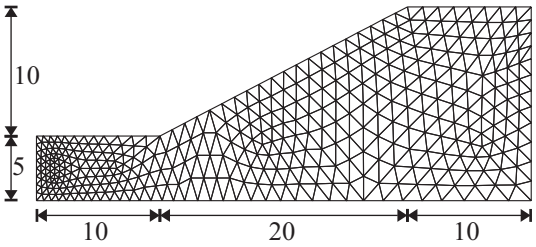

Figure 3: Geometry and finite element mesh. Length unit is m.

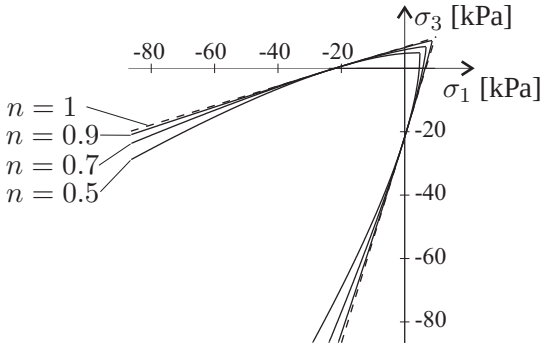

Figure 4: Hoek-Brown yield criteria with different n-values in plane strain.

different curvature parameters, $n = 1, 0.9, 0.7, 0.5$, respectively. The different yield criteria can be seen in figure 4.

The result of the computation can be seen in table 1. As expected the safety level decreases with decreasing n.

Table 1: Safety factors calculated by the finite element method. $n = 1$ is equivalent to a Mohr-Coulomb material.

Material	Safety factor
$n = 1$	1.81
$n = 0.9$	1.73
$n = 0.7$	1.47
$n = 0.5$	1.24

Conclusion

Slope safety factors has been calculated on the basis of a non-linear Mohr-envelope. The non-linear envelope fits test results better than the classical Mohr-Coulomb criterion, especially at low confinement pressures, which are the stress states predominantly present on the slip surfaces of a slope collapse. The safety factors are calculated with the finite element method, using return mapping in principal stress space for the plastic integration.

References

[1] R. Baker. Nonlinear mohr envelopes based on triaxial data. *Journal of Geotechnical and Geoenvironmental Engineering*, 130(5):498–506, 2004.

[2] J.C. Jiang, R. Baker, and T. Yamagami. The effect of strength envelope nonlinearity on slope stability computations. *Canadian Geotechnical Journal*, 40:308–325, 2003.

[3] Xiao-Li Yang and Jian-Hua Yin. Slope stability analysis with nonlinear failure criterion. *Journal of Engineering Mechanics*, 130(3), 2004.

[4] Evert Hoek and Edwin T. Brown. Empirical strength criterion for rock masses. *Journal of Geotecnical Engineering*, 106:1013–1035, 1980.

[5] J. Perry. A technique for defining non-linear shear strength envelopes an their incorporation in a slope stability method of analysis. *Quarterly Journal of Engineering Geology and Hydrogeology*, 27(3):231–241, 1994.

[6] M.A. Crisfield. *Non-Linear Finite Element Analysis of Solids and Structures*, volume 2: Advanced Topics. John Wiley & Sons, 1997.

[7] Johan Clausen, Lars Damkilde, and Lars Andersen. One-step direct return method for mohr-coulomb plasticity. In *Proceedings of the 17th Nordic Seminar on Computational Mechanics*, pages 156–159. KTH Mechanics, Royal Institute of Technology, Sweden, 2004.

[8] Johan Clausen, Lars Damkilde, and Lars Andersen. Efficient return algorithms for associated plasticity with multiple yield planes. *Submitted to International Journal of Numerical Methods in Engineering*, 2005.

[9] R.B.J. Brinkgreve and P.A. Vermeer. *Plaxis, Finite element Code for Soil and Rock Analyses, Version 7*. A.A. Balkema, Rotterdam, 1998.

Shape Optimisation of Core Interfaces in Sandwich Structures

J. Jakobsen*, and L.S. Johansen
Institute of Mechanical Engineering Aalborg University
Pontoppidanstræde 101, DK-9220 Aalborg, Denmark
E–mail: jja@ime.aau.dk

E. Lund, and O.T. Thomsen
Institute of Mechanical Engineering Aalborg University
Pontoppidanstræde 101, DK-9220 Aalborg, Denmark

Summary A numerical approach for shape optimisation was used to improve the structural performance of a sandwich component. The objective was to reduce a failure index in the vicinity of a core interface by modifying its shape. This was successfully achieved, and a reduction in the failure index of 37% was obtained by the use of shape optimisation.

Introduction

Structural sandwich elements have gained widespread acceptance within the aerospace, marine, automotive, building and sustainable energy industries as an excellent way to obtain extremely lightweight components and structures with very high bending stiffness, high strength and high buckling resistance. Other advantages include good acoustic damping, thermal insulations and corrosion resistance.

However, for practical as well as structural reasons the use of sandwich structures frequently involves the use of different cores in the same sandwich element [1]. Various core inserts (stiffeners, backing plates, etc.), which substitute a part of the original core in sandwich panels, are also used often in sandwich structures.

It is well known that the joining of different cores in sandwich beams and panels leads to local effects at the core junctions [1]. The local effects are caused by the mismatch of the elastic properties of the adjoining core materials, and they manifest themselves by a rise of the in-plane stresses in the sandwich faces as well as of the shear and through-the-thickness stresses in the adjacent cores. Depending on the properties of the materials chosen for such a sandwich configuration, the stress concentrations may cause local fracture of the core materials, but severe face damage is also a highly possible scenario. This may jeopardize the structural integrity of a sandwich structure and cause failure under quasi-static as well as fatigue loading conditions [2].

Recently it has been shown [3], that stress concentrations associated with the local effects described above can be reduced significantly by modifying the shape of the core interfaces [3]. In addition, it has been shown that crack initiation depends on the shape of the core interfaces [4], and that the inclination angle of the interfaces influences the location of crack initiation [4].

None of the previous works dealing with the design of core junction interfaces, including the references cited above, have attempted a rigorous systematic approach to shape optimisation of core junction interfaces using mathematical programming and design sensitivity analysis. Thus, the objective of this paper is to propose an improved core junction design for a particular sandwich configuration based on design sensitivity analysis and a systematic optimisation technique.

Shape Optimisation Method

The design optimization problem is solved in an iterative loop based on finite element analysis, analytic design sensitivity analysis and mathematical programming. In this case the mathematical programming problem is solved using SLP (Sequential Linear Programming).
Two approaches can be used to evaluate the structural response of a model. One is a local criterion approach, which in this case concerns the stresses in the structure. A global criterion is another method to evaluate the structural response. The compliance of a structure is one example of a global criterion. It is decided to formulate a local criterion as objective function for the optimisation problem as the cause of fracture is assumed to be an increased stress level at the core junction.

The objective thus is to minimize stress concentrations in and around the junction by minimizing the maximum value of a failure index, $F_{principal}$, which is defined as the ratio of the first principal stress, σ_1, to the allowable tensile stress in the material, S_T, i.e. $F_{principal} = \sigma_1/S_T$. The shape design variables, x_i, are the positions of a set of points describing the interface curve, and these are restrained to vary between the limits $\underline{x} \le x_i \le \overline{x}$. Thus, the optimization problem may be stated as:

$$\begin{aligned} &\text{Objective function:} \quad \min\left(\max(F_{principal}(x_i))\right) \\ &\text{Constraints:} \qquad \underline{x} \le x_i \le \overline{x} \end{aligned} \tag{1}$$

The framework for solving the optimisation problem in Eq. 1, is the structural design optimisation system ODESSY (Optimum DESign SYstem), developed at the Institute of Mechanical Engineering, Aalborg University [5 and 6].

Finite Element Model

The problem considered is a three-material interface, which occurs in sandwich panels with multiple core materials or inserts, see details in [7]. A sandwich beam designed with two different core materials and aluminium face sheets is subjected to three-point bending, see Figure 1. The beam has a total length of 500mm and consists of two 1mm face sheets of aluminium 7075T-6 and a 25mm core made from DIAB Divinycell H60 and H200. The materials are assumed to be isotropic and exert linear elastic behaviour. The mechanical properties of the three materials are summated in Figure 1.

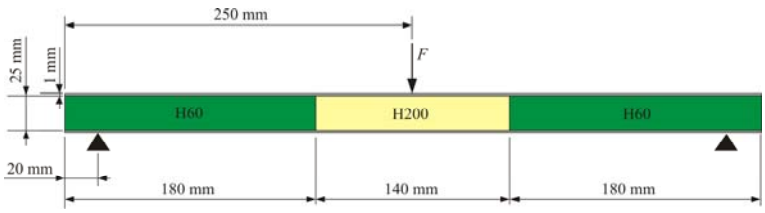

Material	E [MPa]	ν	S_T [MPa]
H60	60	0.32	1.4
H200	310	0.32	4.8
Aluminium	73000	0.33	503

Figure 1 Sandwich beam model with butt junction-type interfaces. Two different core materials are used: DIAB Divinycell H60 and H200**.** Their properties are given in the table. E is the modulus of elasticity, ν Poisson's ratio and S_T tensile strength of the material.

To investigate the stress distribution in and around the core junction interface, a plane stress finite element model is made. According to symmetry only half of the beam is examined. The finite element model consists of a total of 20519 6- and 9-node isoparametric 2D elements.
The element size near the interfaces is 0.30mm. At the core interface the elements have an even smaller side length of 0.08mm (see Figure 2). This refined mesh accurately predicts the stress situation in close vicinity of the three-material interfaces.

The applied load (F) is 2200N and is uniformly distributed over a length of 2mm. To obtain the failure index at this load level for the initial configuration, i.e. vertical core junction interfaces, an initial analysis is performed. The failure index is defined as shown in Eq. 2.

$$F_{principal} = \left(\frac{\sigma_{1,H60}}{S_{T,H60}}, \frac{\sigma_{1,H200}}{S_{T,H200}}, \frac{\sigma_{1,AL}}{S_{T,AL}} \right) \tag{2}$$

Fig. 2 illustrates the failure index distribution $F_{principal}$ for the beam in initial configuration. At the upper interface corner, considerable stress concentrations are observed in the core material. As singularities arise in the point where the three materials are joined, nodes at a representative distance from the singularity are chosen for reference. Convergence tests show that at the current mesh resolution, a distance of d_c=0.2mm is sufficient to ensure convergence of the model.

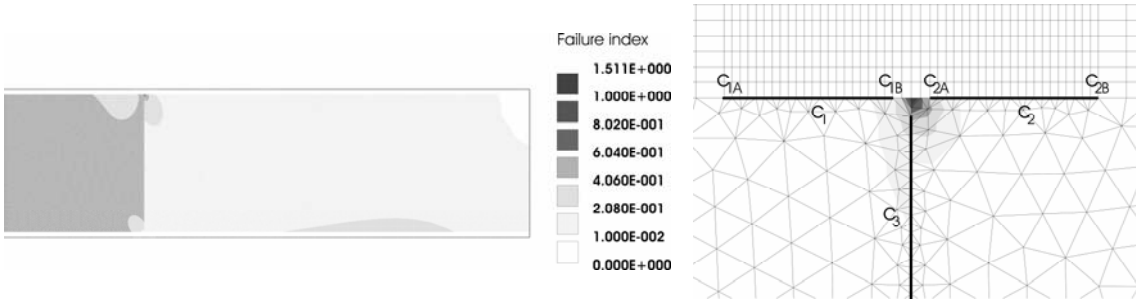

Figure 2: Left: Plot of the failure index $F_{principal}$ in the beam. Right: indication of the interface lines c_1, c_2 and c_3 used for evaluating the failure index. The points c_{1A}, c_{1B}, c_{2A} and c_{2B} are indicated.

The shape optimization problem is formulated with the objective of minimizing the level of $F_{principal}$ in the foam materials. The parameterisation of the problem is shown in Fig. 3.

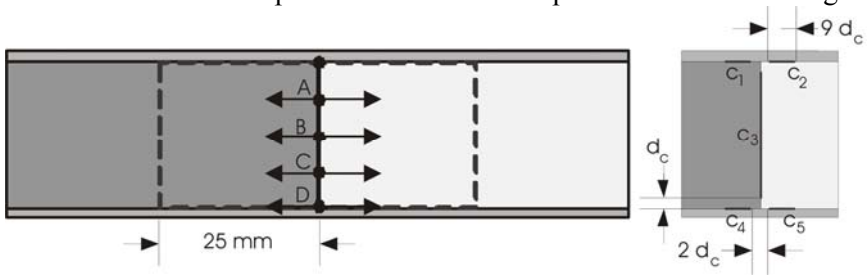

Figure 3: Left: The design boundary is parameterised as a five point cubic B-spline with second order continuity. Vectors indicate the move directions for the four control points (A-D). The area meshed with 6-node triangular elements is indicated with a rectangle. Right: The objective function is evaluated in both core materials along lines placed at characteristic distances d_c away from the singular corner points of the butt junction.

The four control points A-D are allowed to translate horizontally, each controlled by a design variable x_i, as indicated in Fig. 3.
The shape optimisation problem is formulated as a min-max problem using a bound formulation and the objective of minimizing the local failure index for the two core materials evaluated at the interface lines c_1, c_2, c_3, c_4 and c_5 indicated in Fig. 5. In order to save computational time only those failure indices which have a value above 80% of the highest failure index are taken into account (a failure index is a number between zero and one, where one indicates that failure will occur).

Results

The optimised result can be seen in Fig. 4. The largest failure level has been relocated to the central part of the junction interface, and the failure index level has been reduced from 0.76 to 0.48, a reduction of 37%.

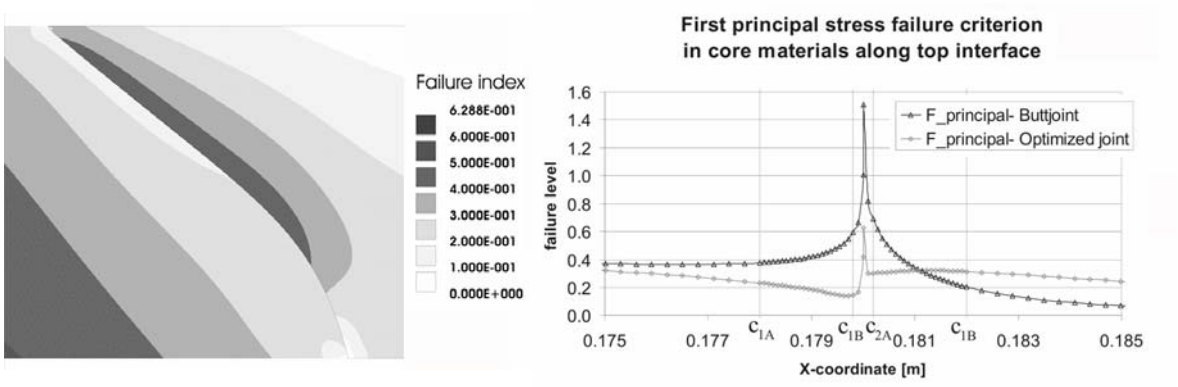

Figure 4 Left: Failure index distribution for the optimised core interface. Right: Failure index level for the original and optimised interface along the top interface. As expected a reduction of the failure index is obtained.

Comparing the results in Fig. 2 and 4 it can be observed that the heightened failure level, which previously occurred near the top three-material interface, has been significantly reduced.

Discussion and Conclusion

It has been shown, that it is possible to obtain a significant improvement in the performance of a sandwich structure, even with singular stress states present in the initial design.
The largest failure index of the original design is reduced by 37% relative to the new design. A first principal stress criterion is used as objective for the optimisation problem. It can be discussed if this choice is sufficient to improve the structural performance of a sandwich component. Some remarks can after all be stated regarding the optimisation of the core interface. One is that the interface should be critical to the structure, meaning that failure should initiate in the vicinity of the interface. Another regards the use of a first principal stress criterion. This decision is based on the assumption that if small cracks appear near or in the interface they will most likely propagate in mode-I. However it should be mentioned that other stress based criteria have been tried out as well.

References

[1] E. Bozhevolnaya, O. T. Thomsen, A. Kildegaard and V. Skvortsov (2003). Local effects across core junctions in sandwich panels. *Composites Part B: Engineering, Volume* **34**, Issue 6, 509-517

[2] Elena Bozhevolnaya and Ole Thybo Thomsen (2005). Structurally graded core junctions in sandwich beams: fatigue loading conditions. *Composite Structures, Volume* **70**, Issue 1, 12-23

[3] A. Lyckegaard, E. Bozhevolnaya, and O.T. Thomsen (2005). Parametric study of structurally graded core junctions, 7th International Confernce on Sandwich Structures, pp 67-76, Springer

[4] S. Ribeiro-Ayeh and S. Hallström (2003). Strength prediction of beams with bi-material butt-joints. *Engineering Fracture Mechanics, Volume* **70**, Issue 12, 1491-1507,

[5] ODESSY (2005). Institute of Mechanical Engineering, Aalborg University, Denmark. www.ime.aau.dk.

[6] Lund, E. (1994). *Finite element based design sensitivity analysis and optimization*. Ph.D. Thesis, Institute of Mechanical Engineering, Aalborg University, Denmark. Special report no. 23, available at: www.ime.aau.dk/~el.

[7] L. Johansen and J. Jakobsen (2005). *Local effects in sandwich structures.* Master thesis, Institute of Mechanical Engineering, Aalborg University, available at:

http://www.ime.aau.dk/People/employees/jja

On wave attenuation in sandwich plates loaded by a layer of viscous fluid

S.V. Sorokin
Institute of Mechanical Engineering
Aalborg University, Denmark
e-mail: svs@ime.aau.dk

A.V. Chubinskij
Department of Mathematics
State Marine Technical University of St. Petersburg, Russia
e.mail: alex_chub@freemail.ru

Summary: This paper addresses free wave propagation in an unbounded elastic sandwich plate loaded by a layer of a viscous compressible fluid. The dispersion equation is derived for this coupled wave guide and the influence of various parameters of a sandwich plate composition and of the heavy fluid loading on the viscosity-induced attenuation of waves is studied.

Introduction

The time harmonic linear wave propagation in elastic structures with heavy fluid loading is traditionally considered within the framework of a theory of a compressible inviscid fluid (the classical model of an acoustic medium). This model is perfectly valid for analysis of vibrations of elastic structures submerged into an unbounded volume of a fluid (e.g., a ship hull in water) or vibrations of thin-walled fluid-conveying structures (e.g., a water-filled tube). However, in some situations, which are rather common for various industrial applications, propagation of an acoustic wave in a narrow gap between, say, two elastic plates or shells should be considered and the attenuation effect produced by viscosity of a fluid cannot be ignored. The paper addresses exactly this case.

A model of dynamics of a viscous fluid

Linearised Navier-Stokes equations are formulated as

$$\rho_{fl}\frac{\partial\vec{v}}{\partial t}-\mu\Delta\vec{v}+\vec{\nabla}p-(\lambda+\mu)\vec{\nabla}(\vec{\nabla}\cdot\vec{v})=0\,, \tag{1a}$$

$$\frac{\partial\rho}{\partial t}+\rho_{fl}\vec{\nabla}\cdot\vec{v}=0\,, \tag{1b}$$

$$\hat{\sigma}=(-p+\lambda\vec{\nabla}\cdot\vec{v})\hat{E}+2\mu\hat{e}\,, \tag{1c}$$

$$2\hat{e}=\vec{\nabla}\vec{v}+(\vec{\nabla}\vec{v})^{T}\,, \tag{1d}$$

$$\frac{\partial p}{\partial\rho}=c_{fl}^{\,2} \tag{1e}$$

Here ρ_{fl} and c_{fl} are density and sound speed in a quiescent fluid ; p is pressure; $\vec{v}$ - velocity, $\hat{\sigma}$ and $\hat{e}$ - stress tensor and strain rate tensor; $\hat{E}$ - identity tensor; μ and ν - dynamic and kinematic coefficients of viscosity; $\mu=\rho_{fl}\nu$; λ - second coefficient of viscosity, which has the following value $\lambda=-\frac{2}{3}\mu$ (the volume viscosity is negligible).

The velocity field is sought in the following form:

$$\vec{v} = \vec{\nabla}\varphi + \vec{\nabla} \times \vec{\psi} \tag{2}$$

Thus, in the coordinate frame, where z is vertical axis and x is horizontal axis,

$$v_x = \frac{\partial \varphi}{\partial x} + \frac{\partial \psi}{\partial z}; \quad v_z = \frac{\partial \varphi}{\partial z} - \frac{\partial \psi}{\partial x} \ . \tag{3}$$

The potentials φ and $\vec{\psi}$ [1], satisfy uncoupled equations:

$$\left[\left(1 + \frac{4\hat{\mu}}{3\rho_{fl} c_{fl}^{\ 2}} \frac{\partial}{\partial t}\right)\Delta - \frac{1}{c_{fl}^{\ 2}} \frac{\partial^2}{\partial t^2}\right]\varphi = 0, \tag{4}$$

$$\left(\nu\Delta - \frac{\partial}{\partial t}\right)\vec{\psi} = 0. \tag{5}$$

Then a pressure is expressed only via scalar potential:

$$p = \rho_{fl}\left(\frac{4\hat{\mu}}{3\rho_{fl}}\Delta - \frac{\partial}{\partial t}\right)\varphi. \tag{6}$$

Normal and shear stresses are formulated as

$$\sigma_{xx} = -\rho_{fl}\left(\frac{4\nu}{3}\Delta - \frac{\partial}{\partial t}\right)\varphi + 2\rho_{fl}\nu\left(\frac{\partial^2 \varphi}{\partial x^2} + \frac{\partial^2 \psi}{\partial x \partial z}\right) \tag{7}$$

$$\tau_{zx} = \rho_{fl}\nu\left(2\frac{\partial^2 \varphi}{\partial x \partial z} + \frac{\partial^2 \psi}{\partial z \partial z} - \frac{\partial^2 \psi}{\partial x \partial x}\right) \tag{8}$$

These stresses act at the plate and they are accounted for in its equations of motion. This model of a viscous fluid naturally merges the classical model of an acoustic medium as viscosity coefficients vanish. It also merges the classical model of linear elasto-dynamics as the constitute law linking the stress tensor and the strain rate tensor is replaced by the conventional in elasticity relation between the stress tensor and the strain tensor, which involves a shear modulus.

A model of a sandwich plate loaded by a layer of viscous compressible fluid

An infinitely long sandwich plate is loaded by a layer of viscous compressible fluid. This layer has a thickness $2H$ and it is bounded by a rigid wall at the opposite to a plate side. The sandwich plate consists of two symmetrical relatively thin, stiff skin plies and thick, soft core ply. Dimensionless parameters are introduced to describe the internal structure of a sandwich plate: $\varepsilon = \frac{h_{skin}}{h_{core}}$ as a thickness parameter (a ratio of thickness of each individual skin ply to a thickness of a core ply), $\delta = \frac{\rho_{core}}{\rho_{skin}}$ as a density parameter, $\gamma = \frac{E_{core}}{E_{skin}}$ as a stiffness parameter. Hereafter, subscripts denoting parameters of skin plies are omitted. The deformation of a sandwich plate is governed by two independent variables: a displacement of the mid-surface of the whole element w (which are the same for all plies) and a shear angle between the mid-surfaces of skin plies θ. Motion of a plate with heavy fluid loading is governed by the following equations [2]:

$$D_1 \frac{\partial^4 w}{\partial x^4} - \Gamma\left(\frac{\partial \theta}{\partial x} + \frac{\partial^2 w}{\partial x^2}\right) + M\frac{\partial^2 w}{\partial t^2} - I_1 \frac{\partial^4 w}{\partial x^2 \partial t^2} = -\sigma_{xx} + N_1 \frac{\partial \tau_{zx}}{\partial x} \tag{9}$$

$$-D_2 \frac{\partial^2 \theta}{\partial x^2} + \Gamma\left(\theta + \frac{\partial w}{\partial x}\right) + I_2 \frac{\partial^2 \theta}{\partial t^2} = -N_1 \tau_{zx} \tag{10}$$

Formulas for the elastic parameters in Eqs. (9-10) are quite cumbersome. They are presented in reference [3].
Dynamics of the fluid is governed by Eqs. (4-5) and (7-8), with continuity conditions at the fluid-structure interface written as:

$$\begin{cases} v_x = \dfrac{\partial \varphi}{\partial x} + \dfrac{\partial \psi}{\partial z} = N_1 \left(\dfrac{\partial^2 w}{\partial t \partial x} + \dfrac{\partial \theta}{\partial t} \right) \\ v_z = \dfrac{\partial \varphi}{\partial z} - \dfrac{\partial \psi}{\partial x} = \dfrac{\partial w}{\partial t} \end{cases} \tag{11}$$

The second pair of conditions at the rigid 'bottom' is:

$$\begin{cases} v_x = \dfrac{\partial \varphi}{\partial x} + \dfrac{\partial \psi}{\partial z} = 0 \\ v_z = \dfrac{\partial \varphi}{\partial z} - \dfrac{\partial \psi}{\partial x} = 0 \end{cases} \tag{12}$$

The problem in free wave propagation is solved and the dispersion equation is derived. This equation formulates a relation between $K = kH$ and $\Omega = \dfrac{\omega H}{c_{fl}}$. Due to the viscosity of a fluid, all wave numbers *K* acquire a real part, which characterizes the rate of decay of 'almost' propagating waves.

Numerical examples

A water-loaded sandwich plate is considered and the depth of its layer is characterized by the ratio $\chi = \dfrac{H}{h_{skin}}$ (the depth parameter). Let a free incident wave have the amplitude A_{in}. As it passes along the plate, it's amplitude decreases to A_{out}, then: $\dfrac{A_{out}}{A_{in}} \sim \exp\left(\mathrm{Re} \dfrac{L}{H} K \right)$, $\mathrm{Re}\, K < 0$.

Hence, wave attenuation is quantified by the real part of K. In Figures 1-3, the following notations are used: Curves A – the structure-originated flexural modes, B – the structure-originated shear modes, C – the first fluid-originated modes, D – the second fluid-originated modes.

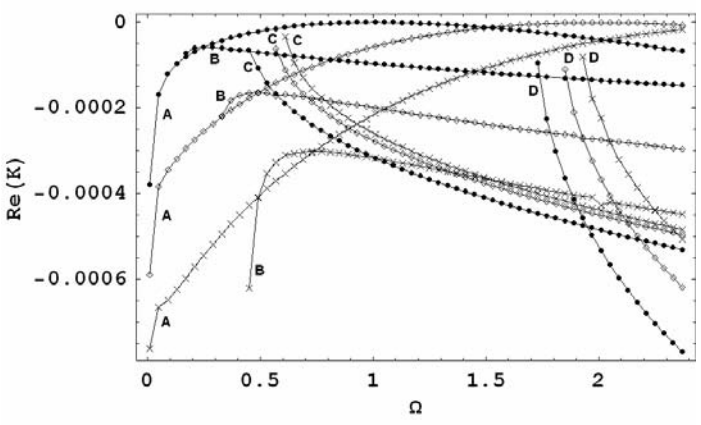

Figure 1

Curves denoted by dots correspond to $\chi = 10$, by boxes to $\chi = 20$ and by daggers to $\chi = 30$ in Figure 1. Other parameters are $\varepsilon = 0.25$, $\gamma = 0.0001$, $\delta = 0.1$. Depth parameter χ has a

significant influence on attenuation of structure-originated mode (an increase in χ, which corresponds to a decrease in plate's thickness, leads to more intensive attenuation). However, it has a weaker influence on attenuation of fluid-originated modes.

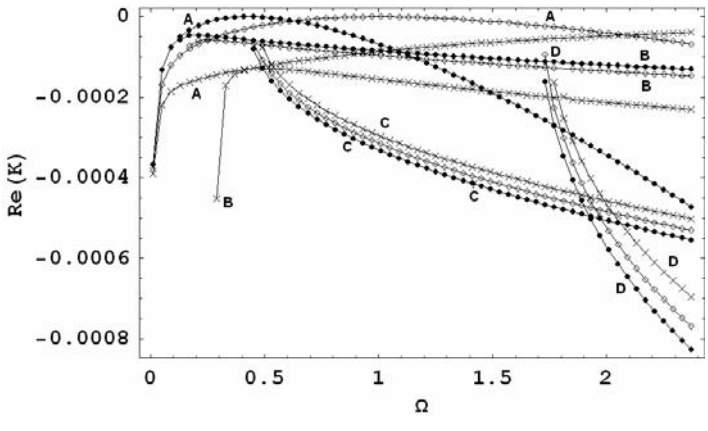

Figure 2

In Figure 2, curves denoted by dots correspond to $\varepsilon = 0.15$, by boxes to $\varepsilon = 0.25$ and by daggers to $\varepsilon = 1$. Other parameters are $\chi = 20$, $\gamma = 0.0001$, $\delta = 0.1$. The thickness parameter has the strongest influence on structure-originated shear modes.

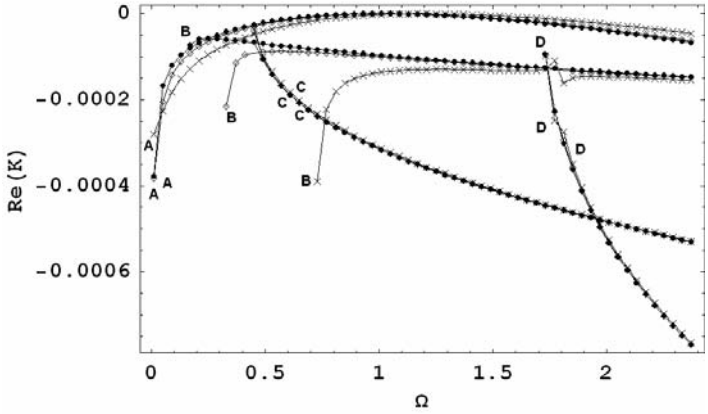

Figure 3

In Figure 3, curves denoted by dots correspond to $\gamma = 0.0001$, by boxes to $\gamma = 0.0005$ and by daggers to $\gamma = 0.0025$. Other parameters are $\chi = 20$, $\varepsilon = 0.25$, $\delta = 0.1$. The influence of this parameters is relatively weak.

Concluding remarks

The reported results suggest that the attenuation of waves in fluid-loaded sandwich plates due to fluid's viscosity may be rather large (even for plates in water) and this effect is strongly 'mode-dependent'.

References

[1] A.N. Guz. Dynamics of solid bodies in a compressible viscous fluid at rest *Prikladnaya Mekhanika* **18**, 3-22, (1981)

[2] S.V. Sorokin. Analysis of wave propagation in sandwich plates with and without heavy fluid loading, *Journal of Sound and Vibration*, **271**(3), 1039-1062, (2004)

[3] A.V. Chubinskij, S.V. Sorokin Wave propagation in a sandwich plate loaded by a viscous compressible fluid In O.T. Thomsen et al.., editors, *Sandwich Structures 7: Advancing with Sandwich Structures and Materials*, pages 605-615, Springer, (2005)

Flexibility Evaluation of Prestressed Kinematically Indeterminate Frameworks

A. Gunnar Tibert
KTH Mechanics
Royal Institute of Technology, Stockholm, Sweden
e–mail: gunnar.tibert@mech.kth.se

Summary The recent interest in tensegrity structures for various applications has increased the need for simple and robust analysis methods. This work presents a method, which is closely connected to the generalised Maxwell's rule, for evaluating the softening effect due to all internal mechanisms in a prestressed, kinematic indeterminate assembly.

Introduction

The recent interest for tensegrity structures in mechanics and biology has increased the research on simple and robust analysis methods [3, 4]. The present work follows the work on distributed static indeterminacy, [8], which can be used to investigate the influence of element length imperfections on the prestress. First, the connection between the force density, force and finite element methods is outlined. Then, two methods for evaluating the softening effect of the internal mechanism are described.

Relationships between equilibrium matrices and the tangent stiffness matrix

Consider a general three-dimensional pin-jointed assembly with b bars, j joints and c kinematic constraints. The static and kinematic properties are described by the generalised Maxwell's rule [2]:

$$3j - b - c = m - s \tag{1}$$

where m is the number of mechanisms (rigid body or internal) and s the number of states of self-stress.

Force density method versus force method

The equilibrium equation in the x-direction for a node i where three bars meet is

$$q_{ih}(x_i - x_h) + q_{ij}(x_i - x_j) + q_{ik}(x_i - x_k) = f_{ix} \tag{2}$$

where $q = t/l$ is the force density or tension coefficient for each bar. In the force density formulation, the nodal coordinates are the unknowns:

$$(-q_{ih} \quad q_{ih} + q_{ij} + q_{ik} \quad -q_{ij} \quad -q_{ik}) \begin{pmatrix} x_h \\ x_i \\ x_j \\ x_k \end{pmatrix} = f_{ix} \tag{3}$$

whereas in the force method it is the element forces that are the unknowns:

$$\begin{pmatrix} \dfrac{x_i - x_h}{l_{ih}} & \dfrac{x_i - x_j}{l_{ij}} & \dfrac{x_i - x_k}{l_{ik}} \end{pmatrix} \begin{pmatrix} t_{ih} \\ t_{ij} \\ t_{ik} \end{pmatrix} = f_{ix} \tag{4}$$

The connectivity for a pin-jointed assembly is written as a $b \times j$ connectivity matrix $\mathbf{C}$. For a bar n which connects nodes i and j:

$$C_{n,p} = \begin{cases} +1 & \text{for} \quad p = i, \\ -1 & \text{for} \quad p = j, \\ 0 & \text{otherwise.} \end{cases} \tag{5}$$

Force density matrix
For a complete assembly, the equilibrium equations in the x-direction with the nodal coordinates as unknowns are

$$\mathbf{D}\mathbf{x} = \mathbf{f}_x \tag{6}$$

where $\mathbf{D} = \mathbf{C}^{\mathrm{T}}\mathbf{Q}\mathbf{C}$ and $\mathbf{Q} = \mathrm{diag}(\mathbf{q})$. Equations identical in form to (6) can be written in terms of the y- and z-directions.

Equilibrium matrix
If the forces are the unknowns the equilibrium equations is written as

$$\mathbf{H}\mathbf{t} = \mathbf{f} \tag{7}$$

where the equilibrium matrix is conveniently formed as [6]:

$$\mathbf{H} = \begin{bmatrix} \mathbf{C}^{\mathrm{T}}\mathrm{diag}(\mathbf{C}\mathbf{x})\mathbf{L}^{-1} \\ \mathbf{C}^{\mathrm{T}}\mathrm{diag}(\mathbf{C}\mathbf{y})\mathbf{L}^{-1} \\ \mathbf{C}^{\mathrm{T}}\mathrm{diag}(\mathbf{C}\mathbf{z})\mathbf{L}^{-1} \end{bmatrix} \tag{8}$$

The nullspace of $\mathbf{H}$ contains the states of self-stress and its left nullspace contains the mechanisms.

Tangent stiffness matrix
The previous equilibrium formulations only include the geometry of the framework and not the material properties. The equilibrium equations in a finite element setting is written as

$$\mathbf{K}\mathbf{d} = \mathbf{f} \tag{9}$$

where the tangent stiffness matrix $\mathbf{K}$ is composed of the elastic and geometric stiffness matrices, which for the pin-jointed assembly is written as [7, 4]:

$$\mathbf{K} = \underbrace{\mathbf{H}\widetilde{\mathbf{\Phi}}\mathbf{H}^{\mathrm{T}}}_{\mathbf{K}_E} + \underbrace{\mathbf{I}_3 \otimes \mathbf{D}}_{\mathbf{K}_G} \tag{10}$$

Note that the diagonal matrix $\widetilde{\mathbf{\Phi}}$ contains the modified axial stiffness of the bars. For bar i with cross-sectional area a_i, modulus of elasticity e_i and unstrained length $l_{0,i}$, the modified axial stiffness is [1, 4]

$$\widetilde{\phi}_{ii} = \frac{a_i e_i}{l_i} = \frac{a_i e_i}{l_{0,i}}\left(1 - \frac{l_i - l_{0,i}}{l_i}\right) = \frac{a_i e_i}{l_{0,i}} - \frac{t_i}{l_i} \tag{11}$$

which for normal construction materials is only little different from the normal axial stiffness $a_i e_i / l_i$.

Evaluation of the flexibility of kinematic indeterminate assemblies
The bases for the mechanisms can be found from the singular value decomposition of $\mathbf{H}$, as illustrated in [5] and collected in the $3j - c \times m$ matrix $\mathbf{M}$. Certain frameworks, e.g. cable nets and tensegrity structures, have several internal mechanisms. By plotting each mechanism, the individual softening influence can be evaluated, but the accumulated influence of all mechanisms is difficult to estimate from these plot. Therefore, a simple method is proposed, in which the flexibility of each node due to the internal mechanisms is indicated by a single number.

Elastic and geometric redundancy

Ströbel [7] introduced a method with elastic and geometric redundancies for the elements to evaluate the flexibility and stability of prestressed kinematically indeterminate structures. In his method the total indeterminacy of the system is the sum of the elastic and geometric redundancies [7, 9]:

$$r = r_{\text{el}} + r_{\text{geo}} = 4b + c - 3j \tag{12}$$

The geometric stiffness matrix $\mathbf{K}_G$ adds three stiffness parameters in the x-, y- and z-directions to the elastic stiffness matrix, on which the generalised Maxwell's rule was based. For a single element, a geometric redundancy equals to 3 means that the element is stable without the influence of the geometric stiffness. A value lower than 3 describes the part of the geometric stiffness necessary for stabilisation and a value higher than 3 indicates that the element is unstable and has to be stabilised by other elements. In this method a distinction is made between compression and tension elements as the latter is more stable.

Distributed kinematic indeterminacy

The approach by Ströbel [7] is interesting as the effects of the elastic and geometric stiffness can be assigned to each member by two numbers. However, the redundancy factors are difficult to interpret as they are not directly connected to a new counting rule, Eq. (12), and not the widely used generalised Maxwell's rule, Eq. (1). The method proposed in this work is directly connected to the generalised Maxwell's rule and previous work on statically and kinematically indeterminate structures, e.g. [5].

Similar to the distribution of the static indeterminacy s over the elements for kinematically indeterminate frameworks [8], the kinematic indeterminacy m may be distributed over the nodes. In Figure 1, a tensegrity simplex with quadratic base is shown. If all the base nodes are fully fixed $c = 12$, the kinematic indeterminacy $m = 1$ is evenly distributed over the free nodes, Figure 1(a). If, however, the minimum six degrees of freedom is fixed such that the rigid body modes disappear, $m = 3$ is distributed over the nodes as shown in Figure 1(b).

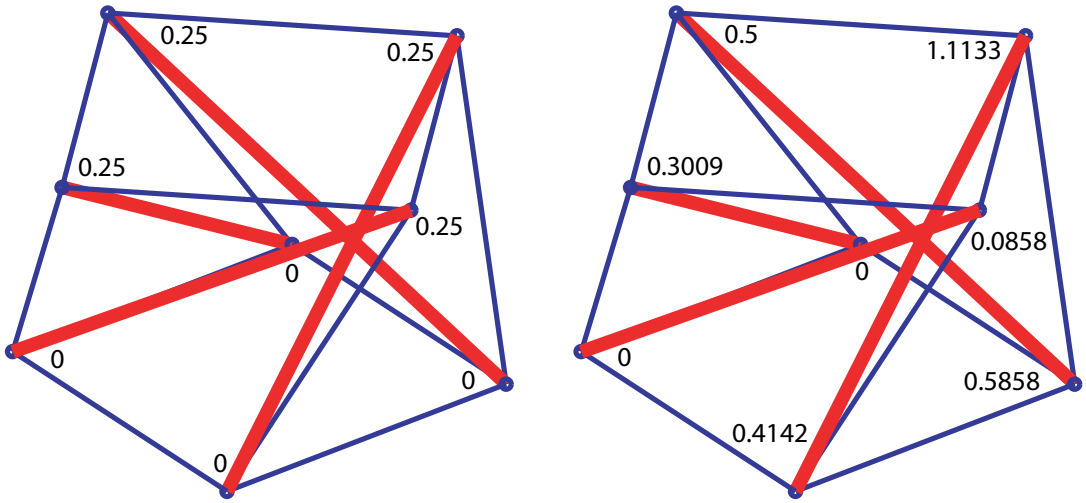

(a) (b)

Figure 1: Distribution of the kinematic indeterminacy m for a tensegrity simplex with square base: (a) $m = 1$ ($c = 12$) and (b) $m = 3$ ($c = 6$).

Conclusions

It has been shown that the equilibrium matrix of the force method is used to create the elastic stiffness matrix whereas the equilibrium matrix of the force density method is used to create the

geometrical stiffness matrix. The degree of kinematic indeterminacy may be distributed over all nodes and used as an indicator for the flexibility of the each node due to all internal mechanisms.

Acknowledgement
Support from the Swedish Research Council (contract 2002-5688) is gratefully acknowledged. Special thanks to Giovani Gomez Estrada for fruitful discussions on the stability of tensegrity structures.

References

[1] J. H. Argyris and D. W. Scharpf. Large deflection analysis of prestressed networks. *J. Struct. Div., ASCE*, **98**, 633–654, (1972).

[2] C. R. Calladine Buckminster Fuller's "tensegrity" structures and Clerk Maxwell's rules for the construction of stiff frames. *Int. J. Solids Structures*, **14**, 161–172, (1978).

[3] G. Gomez Estrada, H.-J. Bungartz, C. Mohrdieck. Numerical form-finding of 2D tensegrity structures. *IASS/IACM 2005—The 5th International Conference on Computation of Shell and Spatial Structures*, Salzburg, Austria, June 1–4, (2005).

[4] S. Guest. The stiffness of prestressed frameworks: a unifying approach. *Int. J. Solids Structures*, In press, (2005).

[5] S. Pellegrino. Structural computations with the singular value decomposition of the equilibrium matrix. *Int. J. Solids Structures*, **30**, 3025–3035, (1993).

[6] H.-J. Schek. The force density method for form finding and computation of general networks. *Comput. Methods Appl. Mech. Engrg.*, **3**, 115–134, (1974).

[7] D. Ströbel. *Die Anwendung der Ausgleichungsrechnung auf elastomechanische Systeme*. Dissertation, Deutsche Geodätische Kommission bei der Bayerischen Akademie der Wissenschaften, Reihe C, Heft 478, München, (1997).

[8] A. G. Tibert. Distributed indeterminacy in frameworks. *IASS/IACM 2005—The 5th International Conference on Computation of Shell and Spatial Structures*, Salzburg, Austria, June 1–4, (2005).

[9] R. Wagner. The virtual world of "tensional integrity". *Textile Roofs 2001—The 6th International Workshop on the Design and Practical Realisation of Architectural Membrane Structures*, Berlin, June 14–16, (2001).

On shape sensitivity analysis with unstructured grids

Jukka I. Toivanen
Department of Mathematical Information Technology
University of Jyväskylä, Jyväskylä, Finland
e-mail: jitoivan@cc.jyu.fi

Summary A simple methodology that enables exact shape sensitivity analysis with unstructured meshes is presented. Method does not involve finite differencing or differentiation of the mesh generator, but is based on deformation of an existing mesh with the aid of the discretized Laplace equation.

Introduction

Design sensitivity analysis is an important step in gradient-based shape optimization [2, 3]. With the aid of automatic differentiation, gradients of highly nonlinear cost functionals can be computed exactly up to numerical precision.

The cost functional to be differentiated is typically implicit function of the control variables: $\mathcal{J}(\alpha) = J(\alpha, \mathrm{u}(\alpha))$. Here α is a vector of control variables and $\mathrm{u}(\alpha) =: u$ is the solution to the set of algebraic equations arising from the finite element discretization of the state equation $r(\alpha, \mathrm{u}(\alpha)) = 0$.

In the classical adjoint method of the optimal control theory the sensitivity is computed from

$$\frac{\partial \mathcal{J}(\alpha)}{\partial \alpha_k} = \frac{\partial J(\alpha, u)}{\partial \alpha_k} - \lambda^T \frac{\partial r(\alpha, u)}{\partial \alpha_k}, \tag{1}$$

where λ is solution to the adjoint equation

$$\left(\frac{\partial r(\alpha, u)}{\partial u} \right)^T \lambda = \nabla_u J(\alpha, u). \tag{2}$$

In this method, we need derivatives of form $\partial f / \partial \alpha_k$ with f being r or J. It is generally not feasible to write these terms as explicit functions of the design variables, since such expressions would be very specific and complex. Assuming f depends on α_k only through the variation in the computational domain, those derivatives can be formally written as

$$\frac{\partial f}{\partial \alpha_k} = \frac{\partial f}{\partial X} \frac{\partial X}{\partial \alpha_k}, \tag{3}$$

where X represents the mesh nodal co-ordinates. This form is more useful in practice, since computation of $\partial f / \partial X$ can be implemented so that the resulting code is independent of shape and mesh parameterization. For details, see for example [3].

The computation of the nodal sensitivities is sometimes considered as the responsibility of the mesh generator [5]. But with unstructured meshes, there exists no algebraic rule for the mesh node locations. Mesh generators can in principle be differentiated with an automatic differentiator such as ADIFOR [1], but many unstructured mesh generation methods include iterative procedures in which nodes are added, relocated and removed, which makes the nodal co-ordinate dependence on the design non-smooth or even discontinuous. Therefore, automatic differentiation of the mesh generator will result in only one-sided derivatives, which are of limited practical value.

Computation of the mesh sensitivities

Shape optimization cycle can include a series of relatively small changes in the design. We would therefore like to avoid remeshing of the whole domain in every optimization step, but instead only deform the existing mesh. The Laplace equation $\Delta v = 0$ is widely used for the mesh deformation [5]. With this equation, there is no coupling of the deformation in different directions, and we can thus look at the computation of the deformation field in one direction.

Discrete form of the equation is $Av = b$, where

$$A = \begin{pmatrix} \mathbb{I} & 0 \\ A_{21} & A_{22} \end{pmatrix}, \; b = \begin{pmatrix} v^b \\ 0 \end{pmatrix}. \tag{4}$$

Here we assume that Dirichlet boundary condition is specified on the whole boundary, and v^b includes the boundary values.

To obtain the deformation in the domain, we simply set v^b to be the boundary deformation and solve for v. The nodal sensitivity $\partial X/\partial \alpha_k$ can now be obtained by using the same equation with v^b being the sensitivity of the boundary nodes $\partial X_b/\partial \alpha_k$. This can be seen in the following way:

The equation can also be written as $v = Lv^b$ where L is a linear transformation whose matrix is formed out of the columns of A^{-1} that correspond to the boundary nodes. The mesh co-ordinates $X = (X_1, \ldots, X_N)$ can therefore be presented in a form

$$X_i = X_{i,0} + L(X_i^b(\alpha) - X_i^b(\alpha_0)) \tag{5}$$

where $X_{i,0}$ are the initial co-ordinates, X_i^b are the boundary co-ordinates and α_0 is the initial design. From this we can obtain the required sensitivities

$$\frac{\partial X_i}{\partial \alpha_k} = L\frac{\partial X_i^b}{\partial \alpha_k}. \tag{6}$$

which is equivalent with solving the system $Av = b$ with v^b being $\partial X_b/\partial \alpha_k$.

Notice, that the matrix A stays the same through the whole sensitivity analysis, and therefore its decomposition has to be done only once, no matter how many design variables we have.

Test problem: fluid flow control

The presented approach is demonstrated with the following fluid flow control problem. We have a channel with fixed inlet height and inlet flow profile. Our target is to produce a given target outflow profile by adjusting the shape of the channel. The configuration can be seen in figure 1. The channel is assumed to symmetric in the x_2 direction.

We used so called CAD-free parameterization [4] and used the x_2 co-ordinates of the nodes on Γ_w as design variables. Since the nodes are allowed to move only in x_2 direction the sensitivities $\partial X_1/\partial \alpha$ are all zero. Sensitivities $\partial X_2/\partial \alpha$ are computed from (6). The required boundary sensitivities $\partial X_2^b/\partial \alpha_k$ are readily obtained: Sensitivity of a node with respect to the design variable that corresponds to the node itself is always one. Sensitivities with respect to other design variables are zero, except for the nodes on Γ_o, which have a sensitivity that is directly proportional to their x_2 co-ordinate with respect to the design variable corresponding to the node on $\Gamma_w \cap \Gamma_o$.

The fluid flow is governed by the steady state Navier-Stokes equations

$$\begin{cases} -\Delta\vec{u} + \nabla p + \rho\vec{u}\cdot\nabla\vec{u} = 0 & \text{in } \Omega \\ \nabla\cdot u = 0 & \text{in } \Omega. \end{cases} \tag{7}$$

Given inlet velocity profile and the target outlet velocity profile have the form of a Poisseuille flow

$$u_1^* = \frac{3}{2}U(1-y^2),\ u_2^* = 0 \tag{8}$$

where $y = 2x_2/h$, h is the height of the channel at that point and U is the characteristic velocity. We wish to accelerate the flow so that U at the outlet will be double the U at the inlet.

Obviously this problem is ill-conditioned (ie. the optimum boundary may be oscillatory). We wish to have a solution where the boundary Γ_w is in some sense as smooth as possible. Therefore, we add to the cost functional a term that penalizes for any nonsmoothness of the boundary. In full the cost functional reads

$$c = \int_{\Gamma_o} (w_1(u_1 - u_1^*)^2 + w_2\, u_2^2)\mathrm{d}s + w_3||r_p||^2. \tag{9}$$

Here w_i are the weighting factors and r_p is the discrete residual of the expression

$$\Delta\delta = 0 \ \text{ on } \Gamma_w \tag{10}$$

where δ is the x_2 deformation of the boundary.

Solver was created on Numerrin software development environment[1], which provides the FE routines, build-in automatic differentiation via operator overloading, and basic optimization routines. We used elementwise constant approximation for the pressure and rotated linear elements for the velocity. Automatic differentiation allowed us to use Newton linearization to solve the state equation efficiently. Optimization was done using sequential quadratic programming (SQP).

The Reynolds number at the inlet was specified to be 100. We started the optimization from a channel with a rectangular profile. Final shape of the channel along with the pressure contours and outlet velocity profile can be seen in figure 1. In figure 2 the velocities at the outlet are plotted. We can see, that the goals are reached very well. The final shape of the channel is influenced by the choice of the penalty term, which tends to minimize the curvature of the moving boundary.

Conclusions

A general methodology that enables exact sensitivity analysis in FE framework with unstructured meshes is presented. The mesh deformation is done using the discretized Laplace equation. This procedure has certain limitations: it is found out that the moving boundary has to be sufficiently smooth at all optimization steps to avoid inverted elements. On the other hand, the nodal coordinate sensitivities with respect to any kind of boundary parameterization can be computed, which enables the exact computation of the cost functional derivative.

Use of the method is demonstrated with a Navier-Stokes control problem using CAD-free shape parameterization, which is a very general method, but may require some kind of smoothing to prevent irregularities on the boundary [4]. Also the number of design variables often becomes large, which may result in slow convergence of the optimization.

[1] Product of Numerola Oy, see www.numerola.fi

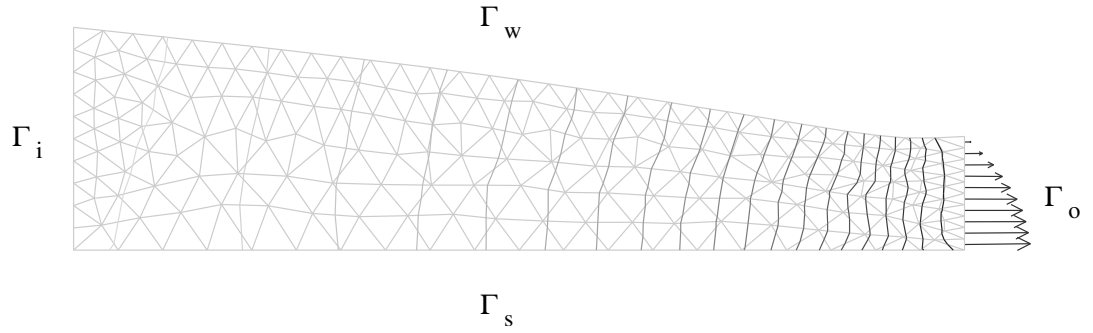

Figure 1: Optimized shape, the pressure contours, and the velocity field of the final solution at the outlet.

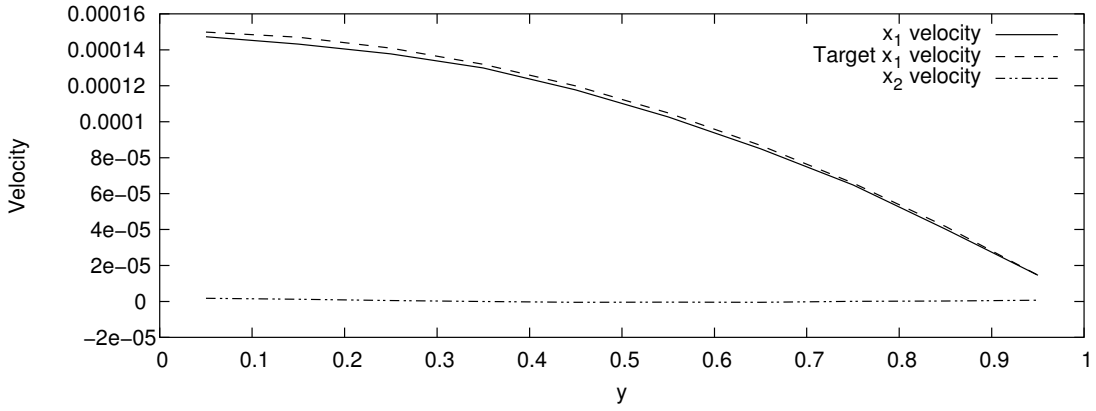

Figure 2: Velocity components and the target velocity profile at the outlet.

References

[1] C. Bischof, P. Khademi, A. Mauer, and A. Carle. Adifor 2.0: automatic differentiation of Fortran 77 programs. *IEEE Computational Science and Engineering*, **3**, 18–32, (1996).

[2] M. D. Gunzburger. *Perspectives in Flow Control and Optimization.* Society for Industrial and Applied Mathematics, (2003).

[3] J. Haslinger and R. A. E. Mäkinen. *Introduction to Shape Optimization: Theory, Approximation and Computation*. Society for Industrial and Applied Mathematics, (2003).

[4] B. Mohammadi and O. Pironneau. *Applied Shape Optimization for Fluids*. Oxford University Press, (2001).

[5] J. A. Samareh. Geometry and grid/mesh generation issues for CFD and CSM shape optimization. *Optimization and Engineering*, **6**, 21–32, (2005).

Space Frame Optimization Using PSO

Jussi Jalkanen
Institute of Applied Mechanics and Optimization
Tampere University of Technology, Tampere, Finland
e–mail: jussi.jalkanen@tut.fi

Summary The topic of this paper is the discrete structural optimization of frames by using heuristic particle swarm optimization (PSO) method. The topology and the shape of the frame are fixed and beams of the frame must be selected from standard RHS-sections. Semi-rigid beam elements are used in the analysis.

Introduction

Tubular structures are common in real life and thus there is a clear need to achieve more economical designs. Structural optimization offers a natural way to go further than just analyzing a few selected candidate structures by finite element method. Since there is only a certain set of profiles available, it leads to nonlinear constrained discrete optimization problem.
Discrete optimization problems are usually much harder to solve than the ones that contain only continuous design variables. Heuristic methods like genetic algorithms (GA) are rather simple and very flexible algorithms and still suitable for solving a variety of hard discrete or combinatorial optimization problems. In this study a new population based heuristic method called Particle Swarm Optimization (PSO) is used to improve the performance of tubular structures.

Particle swarm optimization

The basic idea of stochastic PSO is to model the social behavior of a swarm (e.g. birds or fishes) in nature. A swarm of particles tries to adapt to its environment by using previous knowledge based on the experience of individual particles and the collective experience of the swarm. It is useful for a single member and the whole swarm to share all information in the population.
In PSO the new position $\mathbf{x}_{k+1}^i$ for particle *i* depends on the current position $\mathbf{x}_k^i$ and velocity $\mathbf{v}_{k+1}^i$

$$\mathbf{x}_{k+1}^i = \mathbf{x}_k^i + \mathbf{v}_{k+1}^i \tag{1}$$

where the velocity is calculated as follows

$$\mathbf{v}_{k+1}^i = w\mathbf{v}_k^i + c_1 r_1\left(\mathbf{p}_k^i - \mathbf{x}_k^i\right) + c_2 r_2\left(\mathbf{p}_k^{\mathrm{g}} - \mathbf{x}_k^i\right). \tag{2}$$

$\mathbf{p}_k^i$ is the best ever position for particle *i* and $\mathbf{p}_k^{\mathrm{g}}$ is the best ever position for the whole swarm. *w* is so called inertia, r_1 and r_2 are uniform random numbers $r_1, r_2 \in [0,1]$ and c_1 and c_2 are the scaling parameters. The value of *w* controls how widely the search process is done in the search space. The idea of the last two terms connected to c_1 and c_2 in the Eq. (2) is to direct the optimization process towards good potential areas in the search space. Usually $0{,}8 < w < 1{,}4$ and $c_1 = c_2 = 2$ are selected. The value of *w* can be changed dynamically so that it is bigger during early iteration rounds and becomes smaller later when it is time to focus on promising areas.
Basically PSO is an algorithm for continuous unconstrained optimization problems. Discrete design variables can be taken into account simply rounding each design variable to closest allowed value in Eg. (1). Constraints can be handled by penalizing unfeasible solutions according to the unfeasibility. References [2] and [3] concern the basics of PSO.

Semi-rigid beam element

Usually, for the sake of simplicity, the behavior of the joint in the frame is assumed to be perfectly rigid or pinned. Unfortunately in real life this idealization is not true and joints are semi-rigid. The bending moment causes some rotational deformation in the connection. In order to get a simple linear analysis it is possible to assume that the rotation is proportional to the bending moment.

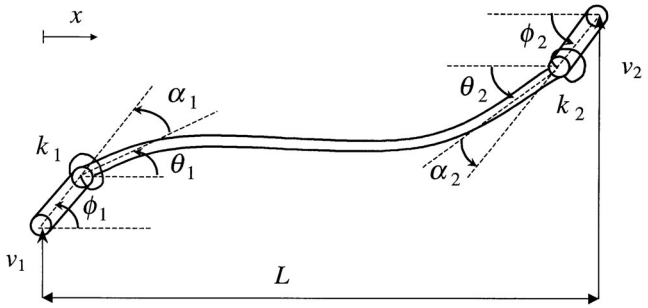

Figure 1: The semi-rigid beam element. v_1, ϕ_1, v_2 and ϕ_2, are the node displacements.

Figure 1 represent four degree of freedom plane beam element with two linear rotational springs at both ends (stiffness factors are k_1 and k_2). The stiffness matrix, the mass matrix and the geometric stiffness matrix of element in Fig. 1 have been presented in ref. [1]. Based on [1] it is straightforward to add the axial degrees of freedoms and to generalize the study to concern the 12 degrees of freedom space beam element which is the element type that has been used in this study.
The value of rotational stiffness k depends on the type of the joint and the dimensions of the profiles connected together. Because it is difficult to determinate the exact values for stiffnesses during the optimization process the fixity factor α can be used instead of it. The fixity factor gets a value $\alpha \in [0,1]$ so that $\alpha = 0$ means perfectly pinned joint and $\alpha = 1$ means perfectly rigid joint. If the value of fixity factor α is known then the actual rotational stiffness is

$$k = \frac{3EI}{L} \cdot \frac{\alpha}{1-\alpha} \tag{3}$$

where E is *Young*'s module, I is the second moment of inertia and L is the length of a beam.

Optimization problem

In the current optimization problem the mass of the space frame is minimized subject to the displacement, strength and buckling constraints. The profiles for the beams should be chosen from a given selection of standard RHS sections that are put in order of magnitude in some sense.
There are total n beams in the frame and m possible profiles for each beam (Fig. 2). The design variable $x_i \in \{1,2,\ldots,m\}$ represents the ordinal number of profile which is chosen for beam i.

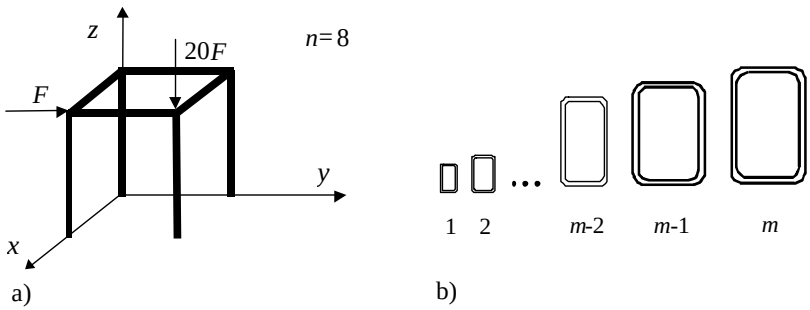

Figure 2: a) A space frame. b) The selection of RHS profiles.

In the standard mathematical form the optimization problem is

$$\begin{aligned} &\min\ m(\mathbf{x}) \\ &g_i^{\mathrm{u}}(\mathbf{x}) \le 0 \qquad i = 1,\ldots,n_{\mathrm{u}} \qquad g_i^{\mathrm{bl}}(\mathbf{x}) \le 0 \qquad i = 1,\ldots,n \\ &g_i^{\mathrm{s}}(\mathbf{x}) \le 0 \qquad i = 1,\ldots,n \qquad g^{\mathrm{bg}}(\mathbf{x}) \le 0 \\ &\mathbf{x} \in \{\mathbf{x}_1, \mathbf{x}_2, \ldots, \mathbf{x}_{\bar{n}}\} \end{aligned} \quad . \tag{4}$$

$m(\mathbf{x})$ is the mass of the frame. The displacement constraints $g_i^{\mathrm{u}}(\mathbf{x}) \le 0$ limit the desired node displacements to be less than the maximum allowed values. The strength constraints $g_i^{\mathrm{s}}(\mathbf{x}) \le 0$ take care that all the beams fulfil the strength requirements of Eurocode 3. The buckling constraints for individual beams $g_i^{\mathrm{bl}}(\mathbf{x}) \le 0$ prevent beams from loosing their stability according to Eurocode 3. The global buckling constraint $g^{\mathrm{bg}}(\mathbf{x}) \le 0$ prevent the whole frame loosing the stability in the sense of linear stability theory. n_{u} is the number of displacement constraints and $\bar{n} = m^n$ is the number of possible candidate solutions.

Example problem

The numerical test problem concerns the space frame of 72 beams in Fig. 3 a). The mass of the frame should be minimized so that the displacements u_1 and u_2 are less than $u^{\max} = 50$ mm, Eurocode 3 strength and buckling requirements which are presented in [4] are fulfilled and the safety factor against global buckling is at least 3. All beams should be chosen from a catalogue [4] that contains 53 different kind of recommended RHS profiles which all belong to the cross section classes 1 or 2. All columns in the corners of tower should have the same cross section as well as all diagonals in each floor and all horizontal beams in each floor. This means that the amount of design variables is 13. Finally diagonal and horizontal beams can not be wider than the columns.
There is one 12 degrees of freedom semi-rigid space beam element per each beam in the FEM-model. Columns are continuous restrained beams which means that for all elements in columns $\alpha = 1$. Diagonals and horizontal beams are connected to columns flexible and for them the constant value $\alpha = 0{,}3$ is used. At the moment all the strength requirements of the structural hollow section joints are ignored.
In PSO the size of the swarm will be increased by one randomly chosen particle every time the best known feasible object function value has not improved during 5 previous iteration rounds. However, if the best known object function value stays the same 20 iteration rounds the increase of swarm stops. The inertia w is changed dynamically by multiplying previous value with factor 0,8 during each iteration round. The initial swarm is selected randomly so that it includes 11 feasible particles. As a result the average decrease of mass is presented in Fig. 3 d). The initial mass is 4541 kg, the mass of the lightest structure is 2972 kg and the median of mass is 3074 kg.

Conclusion

In the discussed discrete optimization problem of tubular structures the global optimum is difficult to find in an arbitrary case. Heuristic PSO can be used to find good solutions that are relatively close to the global optimum. Fortunately this kind of solutions are good enough in many applications and there is no need to find the best solution.
The example problem shows that the number of FEM-analysis is rather big in structural optimization with PSO. This is typical for all heuristic methods. In addition, due to the stochastic nature of PSO, there should be several optimization runs in a single problem in order to get reliable results.

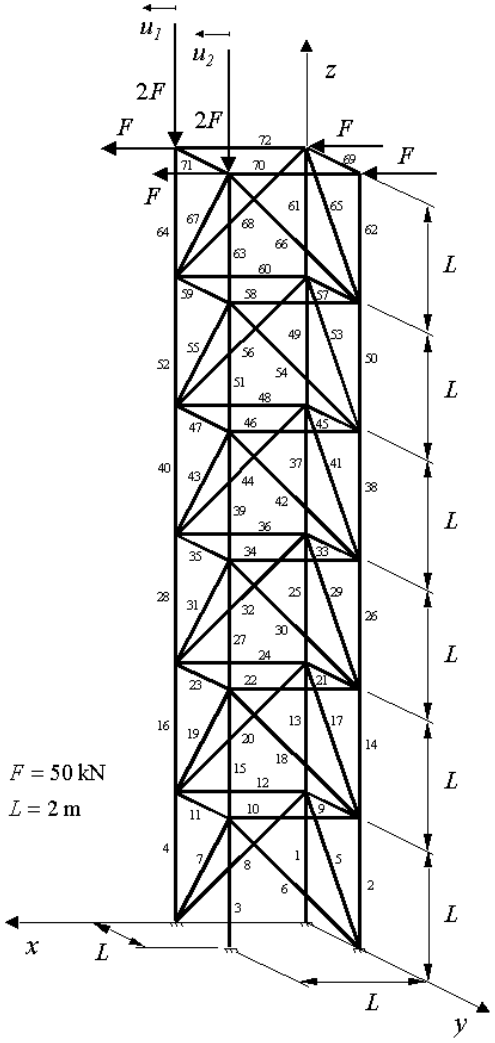

Young's module E	210 GPa
Poisson's ratio ν	0,3
density ρ	7850 kg/m^3
yield limit R_e	355 MPa

b)

Swarm size	40
Iteration rounds	100
Initial inertia w_0	1,4
Penalty	2
Scaling parameters c_1, c_2	2

c)

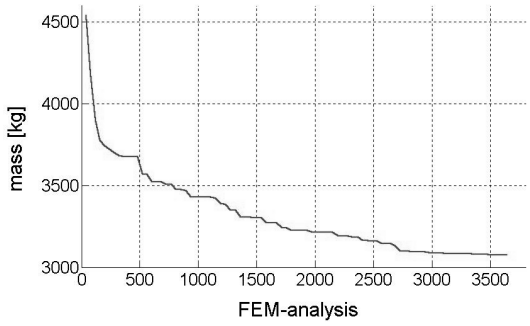

d)

Figure 3: a) The frame of 72 beams. b) Material data. c) Parameter values in PSO. d) The decrease of the mass (median) based on 10 PSO optimization runs.

References

[1] J. Jalkanen. Optimization of frames with semi-rigid connections using tabu search. In: K. M. Mathisen, T. Kvamsdal and K. M. Okstad (eds.) *Proceedings of the 16th Nordic Seminar on Computational Mechanics*, 91-94, (2003).

[2] P.C. Fourie and A. A. Groenwold. The particle swarm optimization algorithm in size and shape optimization. *Structural and Multidisciplinary Optimization*, 23, 259-267, (2002).

[3] G. Venter, and J. Sobieszczanski-Sobieski. Particle Swarm Optimization. *AIAA Journal*, Vol. 41, No 8, 1583-1589, (2003).

[4] Rautaruukki Metform. *Rautaruukin putkipalkkikäsikirja.* (Design Handbook for Rautaruukki Structural Hollow Sections), (1997).

Simulation of Stress Adaptive Bone Remodelling

Bastian Ebbecke* **and Udo Nackenhorst**
Institut of Mechanics and Computational Mechanics IBNM
University of Hannover, Appelstrasse 9A, 30167 Hannover
e–mail: ebbecke@ibnm.uni-hannover.de

Summary Computational techniques for the simulation of stress–adaptive bone–remodelling have been developed and applied for the analysis of the bio–mechanical compatibility of hip–joint endoprosthesis. Numerical simulations are in good agreement with clinical observations and enable parameter studies for the development of optimized prosthesis designs.

Introduction

Hip–joint endoprosthetics has been developed to standard surgery. However, there is a great variety of implant designs and surgery techniques and the question for an optimal solution is still not answered yet. Probably this question has to be answered individually from patient to patient. Computational methods have been developed for the prediction of the mechanical bio–compatibility of endoprostheses. Besides the stress–analysis of implant and the bone remodelling caused from changing mechanical stimulation of bone tissue is simulated. This approach enables studies of the bio–mechanical compatibility of different prosthesis designs under individual constitution and mobility.

Methods and materials

Computational methods for the simulation of stress adaptive bone remodelling are under development since more than 15 years [1, 6, 9]. In this publication we follow up the previous work done by Nackenhorst and coworkers, for details it is referred to [4, 5, 8, 7]. By this approach the bone is modelled in a continuum sense, that means that the network structure of cancellous bone in the proximal region of the femur is smeared by an average mass density ϱ.
Basic assumption of the theory is an equation of evolution

$$\frac{\dot{\varrho}}{\varrho_0} = \tilde{k}\left(\frac{\psi}{\psi_{ref}} - 1\right) \tag{1}$$

where $\tilde{k} = k/\varrho_0$ has the dimension of one over time. (1) is scaled by a reference mass–density ϱ_0, ψ is the strain–energy density in the isotropic case and ψ_{ref} a physiological target value. The computation of the strain–energy density distribution is performed by a linear–elastic finite element analysis, which is an approximate solution of the mechanical equilibrium for arbitrary geometries under consideration of the specific boundary conditions. A standard procedure leads to a system of linear equations

$$\mathbf{K}\mathbf{u} = \mathbf{f} \tag{2}$$

From the solution the strain energy–density is derived by a simple post–processing step, i.e.

$$\psi = \frac{1}{2\varrho}\varepsilon^T \mathbb{C}\varepsilon \tag{3}$$

where $\mathbb{C}$ is the elasticity–matrix and ε the VOIGT–representation of the linear strain tensor, which is easily derived from the displacement–field computed from equation (2).
It is essential to recognize that the elasticity–matrix depends on the spatial mass density distribution. A constitutive relation has to be stated between the YOUNGS–modulus E and mass–density ϱ. Within a thermodynamic consistent framework a relation

$$\frac{E}{E_0} = \left(\frac{\varrho}{\varrho_0}\right)^2 \tag{4}$$

has been proven, [7]. A nonlinear problem consisting the time–discretized version of equation (1), (2), (3) and (4) has to be solved.
The 3D bone is given by [12] and the muscle attachments can be found in [11]. To identify static equivalent muscles and hip joint forces from ct data, the global error

$$\prod(\mathbf{F}) \stackrel{def}{=} \frac{1}{2} \sum_{i=1}^{el} \left[\lambda_i(\mathbf{F}) - \lambda_{i_{opt}}\right]^2 \tag{5}$$

has to minimized with a genetic algorithm, programmed in the MATLAB program code. $\mathbf{F}$ is the unknown vector of the muscles and hip joint forces. A method for the automatic mapping of computed tomography numbers onto finite element models is necessary to solve this equation, [10]. The solution of $\mathbf{F}$ is quite similar to the average of the measured dynamic forces during walking and stairs climbing in [3].

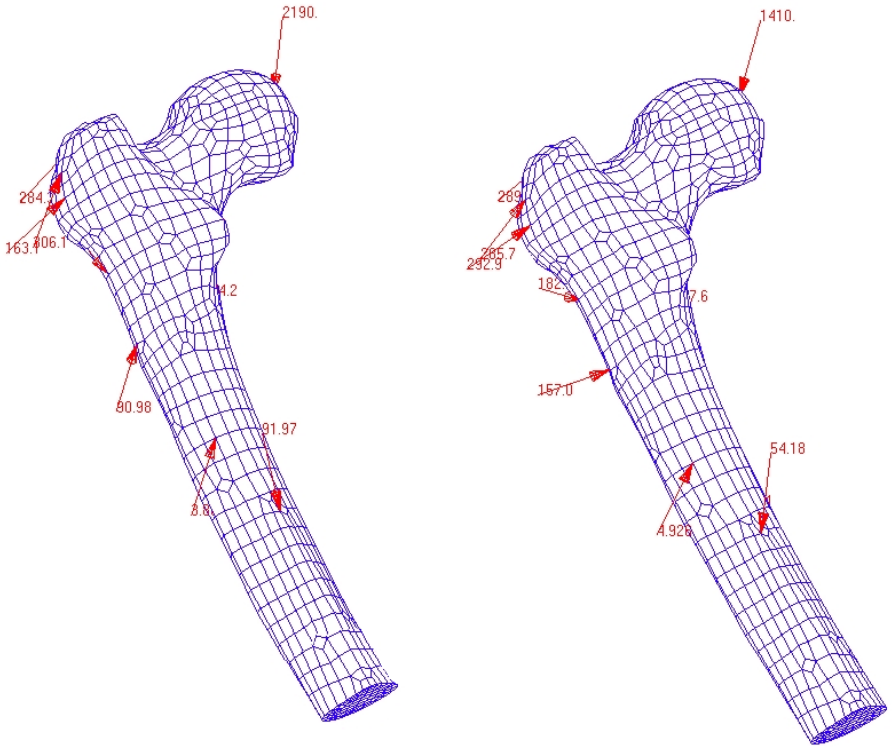

Figure 1: Average measured muscles and hip joint forces during walking and stairs climbing [3], (left) in comparison with calculated forces by minimizing (5), (right)

Finite Element Model and validation
The first step of the computation treats the optimization of the boundary conditions (statically equivalent loads) in the sense that a bio–mechanical equilibrium state is found for a physiologically density distribution. The bone mass density distribution for an equilibrated femur model is depicted in fig. 2. The comparison with CT–data matches well. The hollow bone as well as the characteristic trabecular structure of the cancellous proximal femur is approximated well by the finite element model. The medullary cavity, the trabecula and Ward's triangle can be recognized in the comparison. This equilibrated model is used for the studies on bone remodelling caused from locally changed stress conditions due to hip–joint endoprosthesis.

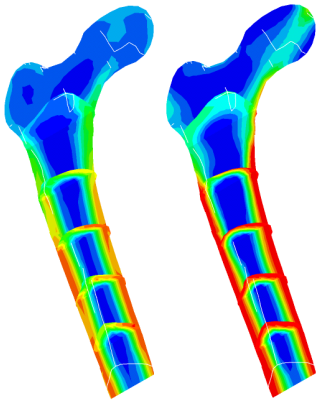

Figure 2: CT data set mapped on FEM mesh [10], (left) in comparison with 3D computed mass density distribution, (right)

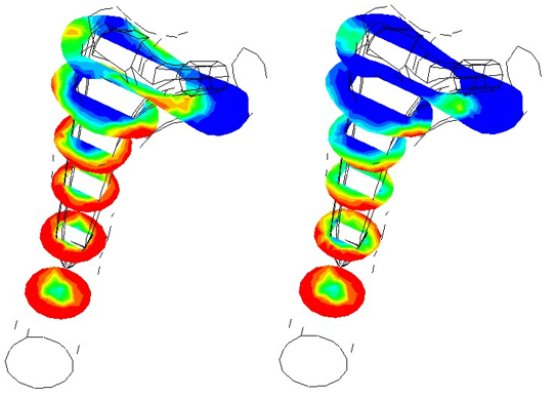

Figure 3: Bone remodelling caused from the Zweymueller–prosthesis.

Prosthesis and results

As an example the bone remodelling caused from a classical stem–prosthesis (Zweymueller) is shown in fig. 3. In the left the immediately post–operative state is plotted whereas in the right the long–term bio–mechanical equilibrium state is shown. These simulations clearly indicate loss of bone density especially in the medial cortical region which is in good agreement with clinical observations.

These investigations of prosthesis are in close cooperations with the Medical Hight School of Hannover (MHH). A new innovative hip joint prosthesis is called Spiron-prosthesis. This prosthesis developed in the year 1999 tries to avoid the risk of a secondary varization and to increase the stability [2]. At the development of this uncemented short-stemmed prosthesis attention was

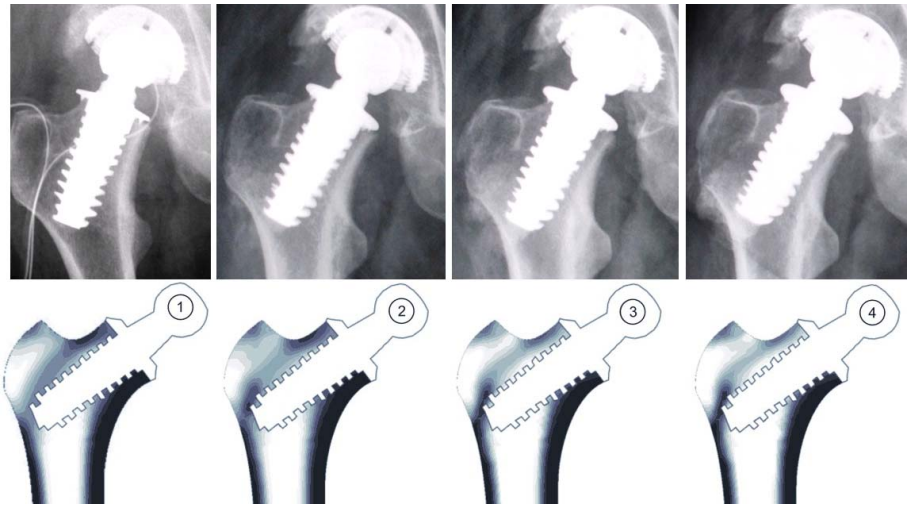

Figure 4: radiograph in comparison with computed mass density distribution: Spiron Prosthesis, postoperativ left site, long therm effect right site

paid on the receipt of the region of the femoral neck since this increases the stability in the primary phase and gets a sufficient bone stock in the revision for a conventional intramedullary prosthesis. Furthermore the use of the femoral neck should receive the mechanic of the natural joint by the unchanged muscular strain. The prosthesis is applied uncemented as a screw with conical

basic body and self-tapping thread and reached by it one considerable surface enlargement in the relatively compact volume of the femoral neck. By the sharp-edged thread formation an osteoinduction is reached in addition to the titanium alloy and bonit coating. The results of the simulation are shown in fig. 4 in comparison with radiographs. The stress-shielding in the area and the bone response at the lateral corticalis in the area of the end of the screw can be proved in the calculation and radiographs.

Conclusions

Computational techniques for qualitative analysis of bone–remodelling are available to assist the surgeons in their choice for an individual prosthesis design. Future work will focus onto the development of more challenging prosthesis designs. Thus, metaphyseal anchored devices seem to be promising alternatives.

References

[1] Beaupre, G.S. and Orr, T.E. and Carter, D.R. An Approach for Time-Dependent Bone Modeling and Remodeling-Application: A Preliminary Remodeling Simulation. *Journal of Orthopaedic Research*, **8**, 662–670, (1990).

[2] Birkenhauer, B. and Kistmacher, H. and Ries, J. Konzepte und erste klinische Ergebnisse der zementfreien Schenkelhalsschraubprothese Typ Spiron. *Der Orthopaede*, **33**, 1259-1266, (2004).

[3] Duda, G. and Heller, M. and Bergmann, G. Musculoskeletal loading database: loading conditions of the proximal femur. *Theoretical Issues in Ergonomics Science*, **6**, 287–292, (2005).

[4] Ebbecke, B. and Nackenhorst, U., Numerical Studies on the Biocompatibility of Innovative Hip-Joint-Prosthesis. *conference paper, The FiniteElement Method in Biomedical Engineering, Biomechanics and Related Fields*. Ulm, 2003

[5] Ebbecke, B. and Nackenhorst, U. Simulation of stress adaptive bone remodelling - towards an individual therapy in endoprosthetics. *PAMM - Proc. in Appl. Mathem. and Mechanics*. Dresden, 2004.

[6] Jacobs, C.R. and Simo, J.C. and Beaupre, G.S. and Carter, D.C. Adaptive Bone Remodeling Incorporating Simultaneous Density and Anisotropy Considerations, *Journal of Biomechanics*, **6**, 603–613, 1997.

[7] Krstin, N. and Nackenhorst, U. and Lammering, R., Zur konstitutiven Beschreibung des anisotropen beanspruchungsadaptiven Knochenumbaus, *Technische Mechanik* **20**, 31–40, 2000.

[8] Nackenhorst, U., Numerical simulation of stress stimulated bone remodeling, *Technische Mechanik* **17**, 31–40, 1997.

[9] Weinans, H. and Huiskes, R. and Gootenboer, H.J., The Behaviour of Adaptive Bone Remodeling Simulation Models, *Journal of Biomechanics* **25**, 1425–1441, 1992.

[10] Taddei, F. and Pancanti, A. and Viceconti, M. An improved method for the automatic mapping of computed tomography numbers onto finite element models. *Medical Engineering and Physics* **26**, 61-69, 2004.

[11] Viceconti, M. and Ansaloni, M. and Baleani, M. and Toni, A. The muscle standardized femur. *Journal of Biomechanics* **36**, 145–146, 2003.

[12] Viceconti, M. and Casali, M. and Massari, B. and Cristofolini, L. The standardized femur program. proposal for a reference geometry to be used for the creation of finite element models of the femur. *Journal of Biomechanics* **29**, 1241-1243, 1996.

Index of authors

List of participants

Clausen	Johan	Denmark
Jacobsen	Johnny	Denmark
Kristensen	Anders	Denmark
Lyckegaard	Anders	Denmark
Walther	Jens Honore	Denmark
Hein	Helle	Estonia
Lellep	Jaan	Estonia
Soomere	Tarmo	Estonia
Aho	Tapio	Finland
Ärölä	Kilwa	Finland
Brandt	Tellervo	Finland
Freund	Jouni	Finland
Herzen von	Raimo	Finland
Jalkanen	Jussi	Finland
Juntunen	Mika	Finland
Karjalainen	Reetta	Finland
Laiho	Antti	Finland
Lyly	Mikko	Finland
Mönkölä	Sanna	Finland
Niemi	Antti	Finland
Niiranen	Jarkko	Finland
Öström	John	Finland
Paavilainen	Jani	Finland
Paavola	Juha	Finland
Peräkylä	Tuomas	Finland
Pitkäranta	Juhani	Finland
Saksala	Timo	Finland
Salonen	Heli	Finland
Toivanen	Jukka	Finland
Tuhkuri	Jukka	Finland
Varpasuo	Pentti	Finland
Vuotikka	Antti-Jussi	Finland
Zuccaro	Ennio	Finland
Battini	Jean-Marc	France
Ebbecke	Bastian	Germany
Lenhof	Berndt	Germany
Rüter	Marcus	Germany
Ivanauskas	Feliksas	Lithuania
Kvamsdal	Trond	Norway
Lie	Knut-Andreas	Norway
Korotov	Sergey	Russia
Sorokin	Sergey	Russia

Bengzon	Fredrik	Sweden
Eriksson	Anders	Sweden
Heintz	Sofia	Sweden
Larson	Mats	Sweden
Larsson	Ragnar	Sweden
Nurhussen	Filli	Sweden
Strömberg	Lena	Sweden
Tibert	Gunnar	Sweden

Thursday 27:th October

15.00-16.30	**Check-in*** (Helsinki)	
15.00-16.00	Registration in Olympia Terminal	**E.Zuccaro**
16.00-16.30	Check-in	
17.00	**DEPARTURE**	
17.00-19.00	**Buffet dinner** (Buffet Serenade)	

Friday 28:th October

07.00-09.30	**Breakfast** (Maxim A La Carte)	
09.30	**ARRIVAL**	
09.45-10.00	**Check-in*** (Stockholm)	
09.45-10.00	Registration (Värtahamnen)	**E. Zuccaro**
10.00-10.15	Check-in	
10.15-10.30	**Seminar opening** (NSCM18/A)**	
10.30-12.00	**Keynote session I** (NSCM18/A)	
10.30-11.15	Discrete Element Simulations in Ice Engineering	**J. Tuhkuri**
11.15-12.00	Numerical Simulation of Nano-, Meso, Macro- and Multiscale Fluid Dynamics	**J.H. Walther**
12.00-13.00	**Buffet lunch** (Buffet Serenade)	
13.00-14.30	**Keynote session II** (NSCM18/A)	
13.00-13.45	Multiscale methods for flow in porous media	**K.A. Lie**
13.45-14.30	Inverse Discontinuity Formulation of Fracture	**R. Larsson**
14.30-15.00	**Coffee break** (Conference center)	
15.00-15.45	**Parallel session I : fracture** (NSCM18/A)	
15.00-15.15	Inelastic conical shells with cracks	**J. Lellep**
15.15-15.30	Simulation of quasi-static crack growth by using the ϑ method	**M. Lyly**
15.30-15.45	Explicit FE-procedure for Numerical Modeling of Rock Fracture under Dynamic Indentation	**T. Saksala**
15.00-15.45	**Parallel session I : applications** (NSCM18/B)	
15.00-15.15	Residual Based Approximations of Fine Scales in Variational Multiscale Approximations of Navier-Stokes Equations	**M. Larson**
15.15-15.30	Adaptive Simulation of Multiphysics Problems	**F. Bengzon**
15.30-15.45	Algorithms for fluid-structure interaction of flow around two or more cylinders with large relative motions	**T. Kvamsdal**
15.45-16.30	**Keynote session III** (NSCM18/A)	
	Lessons in wave theory from the Indian Ocean Tsunami of Millennium and from the Baltic Sea Storm Surge of Century	**T. Soomere**
16.30-16.45	**Break**	
17.00	**DEPARTURE**	
16.45-18.00	**Ordinary session I : modelling** (NSCM18/A)	
16.45-17.00	Finite Element analysis of jar connections: Modeling considerations	**A. Kristensen**
17.00-17.15	Deformation of a Paper Roll Loaded Against a Nip Roller	**K. Ärölä**
17.15-17.30	Comparison between Approaches to Explicit Filtering in Large Eddy Simulation	**T. Brandt**
17.30-17.45	Mathematica Modelling of Biosensors with Perforated and Selective Membranes	**F. Ivanauskas**
17.45-18.00	Modeling Aircraft Ground Behavior into a Flight Simulation	**J. Öström**
18.00-19.00	**Cocktail party** (Conference center)	
20.00-22.00	**Seminar dinner** (Maxim A La Carte)	

Saturday 29:th October

07.30-09.00	**Breakfast** (Maxim A La Carte)	
09.30	**ARRIVAL*** **	
09.30-10.45	**Parallel session II : numerics** (NSCM18/A)	
09.30-09.45	Benchmark study: MITC4-S and boundary layer-type deformations	**A. Niemi**
09.45-10.00	Computational results for the superconvergence and postprocessing of MITC plate elements	**J. Niiranen**
10.00-10.15	Locking-Free Plate Elements at Free Boundary	**J. Pitkäranta**
10.15-10.30	Finding the most efficient rotation-free triangular shell element	**G. Tibert**
10.30-10.45	A Posteriori Error Estimates in Linear Elastic Fracture Mechanics based on Different FE-Solution Spaces for the Primal and the Dual Problem	**M. Rüter**
09.30-10.45	**Parallel session II : applications** (NSCM18/B)	
09.30-09.45	FPK-equation solutions for stochastic structural response	**P. Varpasuo**
09.45-10.00	The Effect of Delamination on the Natural Frequencies of the Composite Beams on Two-Parameter Foundation	**H. Hein**
10.00-10.15	Fatigue life prediction of polymer covered roll	**R. Karjalainen**
10.15-10.30	Extension of ASME regulatory for validation of dynamical calculation when deviations in as-buildt	**L. Strömberg**
10.30-10.45	Forces Between Joined Discrete Particles in Discrete Element Method	**J. Paavilainen**
10.45-11.00	**Break**	
11.00-11.45	**Parallel session III : numerics** (NSCM18/A)	
11.00-11.15	A Finite Element Method for General Boundary Condition	**M. Juntunen**
11.15-11.30	New Tecnologies for Control of Local Errors in Engineering Computations by FEM	**S. Korotov**
11.30-11.45	Solution of the Helmholtz equation with controllability and spectral element methods	**S. Mönkölä**
11.00-11.45	**Parallel session III : education** (NSCM18/B)	
11.00-11.15	Vectors and tensors with matrix manipulations	**J. Freund**
11.15-11.30	Virtual Work, Lagranges Equations and Finite Elements	**J. Paavola**
11.30-11.45	Inertia and related topics of education in mechanics	**L. Strömberg**
11.45-12.30	**Lunch** (Conference center)	
12.30-13.45	**Parallel session IV : materials** (NSCM18/A)	
12.30-12.45	Stress evaluation in sandwich structures near tri-material wedge	**A. Lyckegaard**
12.45-13.00	Identification of Material Parameters of a Polymer	**T. Peräkylä**
13.00-13.15	Nonlocal plasticity model for fibre reinforced concrete	**L. Strömberg**
13.15-13.30	Time-Temperature Superposition Method for Polyester Resin	**A.-J. Vuotikka**
13.30-13.45	Slope safety calculation with a non-linear Mohr criterion using finite element method	**J. Clausen**
12.00-13.15	**Parallel session IV : applications** (NSCM18/B)	
12.30-12.45	Shape Optimisation of Core Interfaces in Sandwich Structures	**J. Jacobsen**
12.45-13.00	On wave attenuation in sandwich plates loaded by a layer of viscous fluid	**S. Sorokin**
13.00-13.15	Flexibility Evaluation of Prestressed Kinematically Indeterminate Frameworks	**G. Tibert**
13.15-13.30	On shape sensitivity analysis with unstructured grids	**J. Toivanen**
13.30-13.45	Space Frame Optimization Using PSO	**J. Jalkanen**
13.45-14.05	**Seminar closure** (NSCM18/A)	
13.45-14.00	Simulation of Stress Adaptive Bone Remodelling	**B. Ebbecke**
14.00-14.30	**Check-out** (Helsinki)	
17.00	**DEPARTURE**	
17.00-19.00	**Buffet dinner** (Buffet Serenade)	

Sunday 30:th October

07.00-09.30	**Breakfast** (Maxim A La Carte)	
09.30	**ARRIVAL**	
09.30-	**Check-out** (Stockholm)	

* You may need to prove your identity (official ID-card with photograph or passport)

** Conference center (deck 6)

*** Hki-Sto-Hki route participants checking-out this day should move luggages etc. to seminar room NSCM18/A after the breakfast. Cabin keys will be inoperable after 10.30 on the arrival day

OHJEITA KIRJOITTAJILLE

Lehti julkaisee rakenteiden mekaniikkaa, maa - ja kallioperän mekaniikkaa, kiinteiden ja nestemäisten aineiden mekaniikkaa, lujuusoppia, rakenteiden ja koneenosien suunnittelua ja mitoitusta, rakennus - ja rakenneaineiden materiaalitekniikkaa ym. vastaavia aiheita käsitteleviä artikkeleita, lyhyitä kommentteja sekä kirjallisuuskatsauksia.
Julkaistavaksi tarjottavat käsikirjoitukset tulee lähettää kahtena kappaleena ja A4-paperille tulostettuna lehden toimitussihteerille. Julkaistavien artikkeleiden maksimipituus on noin 15 sivua. Artikkelin alussa tulee olla tiivistelmä, jonka pituus ei saa olla enempää kuin sata sanaa. Mikäli artikkeli on kirjoitettu suomen kielellä, tulee käsikirjoituksen mukana toimittaa englanninkielinen tiivistelmä erillisellä paperilla. Kuvien piirrosten ja taulukoiden tulee olla sijoitettu tekstin yhteyteen. Käsikirjoituksissa sekä valmiissa artikkeleissa tulee käyttää yksinkertaista riviväliä, fonttikokoa 12 ja mieluiten Times New Roman -fonttia. Tiivistelmässä tulee kuitenkin käyttää riviväliä 0,80 cm. Jokaisen sivun vasempaan ja oikeaan reunaan jätetään 30 mm:n marginaali. Artikkelin nimiösivun ensimmäinen rivi aloitetaan 60 mm yläreunasta, muut sivut 35 mm yläreunasta ja viimeinen rivi lopetetaan 35 mm alareunasta. Lukujen otsikot kirjoitetaan isoilla vahvennetuilla kirjaimilla ilman numerointia. Kaavat, kuvat ja taulukot numeroidaan jatkuvalla numeroinnilla. Lähdeluettelon, kuvien ja tekstin kieliasun suhteen voidaan noudattaa esimerkiksi julkaisun Tirkkonen, K., Teknisen kirjoituksen laatiminen, Suomen Teknillinen Seura STS r.y. & Teknillisten Tieteiden Akatemia, Helsinki 1987 ohjeita. Kirjoittajan tulee huolehtia siitä, ettei tekijänoikeuksia rikota mahdollisten suorien lähdeaineiston lainauksien yhteydessä. Mikäli artikkeliin on otettu kuvia joistakin lähteistä, tulee kirjoittajan itse hankkia kirjallinen lupa lainauksiin.
Lehti julkaisee keskustelupalstallaan lyhyitä (1 -2 sivua) kirjoituksia, jotka sisältävät joko tässä tai jossakin muussa alan lehdessä julkaistuihin artikkeleihin kohdistuvia mielipiteitä ja kritiikkiä tai jonkin mielenkiintoisen lehden toimialaan kuuluvan teknisen menetelmän tai ratkaisun selostuksen.
Artikkelien kirjoittajille lähetetään 5 ylimääräistä lehden numeroa.

NOTES TO CONTRIBUTORS

The journal publishes articles, literature reviews and short notes on theoretical and experimental structural mechanics, soil and rock mechanics, continuum and fluid mechanics, strength of materials, design of structures and machines, structural materials, etc.
Manuscripts should be submitted in duplicate form to the secretary of the journal. The maximum length of an article is about 15 pages including the figures, tables and list of references. The body of the manuscript should be preceded by an abstract of about one hundred words. Manuscripts as well as camera-ready papers should be printed with single line spacing on an A4 paper by using font size 12 and preferably Times New Roman font. However, a 0.80 cm line spacing should be used in the Abstract. The top margin should be 60 mm on the first page and 35 mm on all other pages. A 30 mm left margin, a 30 mm right margin and a 35 mm bottom margin should be used. The chapter headings should be without numbering and typed with capital letters. The formulae, figures and tables should be consecutively numbered. The authors should ensure that the manuscript does not include any material that may be subject to copyright or alternatively get a written permission to use the material subject to copyright.
The journal publishes also short letters containing opinions or critique on articles published in the journal or short letters describing a technical method or a solution having interest in the field of the journal. The length of these letters should not exceed 2 pages.
The authors will receive five copies of the journal free of charge.

R A K E N T E I D E N M E K A N I I K K A
JOURNAL OF STRUCTURAL MECHANICS

TOIMITUS **BOARD OF EDITORS**

JUKKA TUHKURI, päätoimittaja	editor-in-chief
PAAVO HASSINEN	
SEPPO HUOVINEN	
TUOMO KÄRNÄ	
MAURI MÄÄTTÄNEN	
SEPPO ORIVUORI	
JUHA PAAVOLA	
EERO-MATTI SALONEN	
ENNIO ZUCCARO, toimitussihteeri	secretary

ASIANTUNTIJANEUVOSTO EDITORIAL ADVISORY BOARD

JUKKA AALTO, prof.	JARI PUTTONEN, tekn.tri
MATTI HAKALA, prof.	MATTI A RANTA, prof.
MARKKU HEINISUO, tekn.tri	TAPANI RECHARDT, tekn.tri
ESKO HYTTINEN, prof.	OLLI SAARELA, prof.
KARI IKONEN, tekn.tri	RISTO SAJANIEMI, dipl.ins.
PAULI JUMPPANEN, tekn.tri	TAPIO SALMI, prof.
PEKKA KANERVA, prof.	SEPPO SALONEN, dipl.ins.
REIJO KOUHIA, tekn.tri	ASKO SARJA, prof.
MARTTI MIKKOLA, prof.	ROLF STENBERG, prof.
PENTTI MÄKELÄINEN, prof.	MARKKU TUOMALA, prof.
ERKKI NIEMI, prof.	PENTTI VARPASUO, tekn. tri
HERMAN PARLAND, prof.	TOR-ULF WECK, prof.
JOUKO PELLOSNIEMI, dipl.ins.	
VESA PENTTALA, prof.	

Hinnat: vuosikerta 12 EUR kotimaassa, ulkomaille tilattuna 38 EUR ja irtonumero 5 EUR.

OSOITE: Teknillinen korkeakoulu, Rakennus- ja ympäristötekniikan osasto, Rakentajanaukio 4 A, PL 2100, 02015 TKK, puh. (09) 451 3701, telefax (09) 451 3826

ADDRESS: Helsinki University of Technology, Department of Civil and Environmental Engineering, Rakentajanaukio 4 A, P.O.Box 2100, FIN-02015 HUT, Finland, tel. (358-9) 451 3701, telefax (358-9) 451 3826

http://rmseura.tkk.fi/

Julkaisija

RAKENTEIDEN MEKANIIKAN SEURA R.Y.

ISSN 0783-6104 PICASET OY